Modelling and simulation of transient air-water two-phase flows in hydraulic pipes

Charles Demay

THÈSE

pour obtenir le grade de

DOCTEUR DE L'UNIVERSITÉ GRENOBLE ALPES

École doctorale Mathématiques, Sciences et Technologies de l'Information, Informatique

Spécialité : Mathématiques Appliquées

Présentée par

Charles DEMAY

Modélisation et simulation d'écoulements transitoires diphasiques eau-air dans les circuits hydrauliques

Modelling and simulation of transient air-water two-phase flows in hydraulic pipes

---

Soutenue publiquement le 15 novembre 2017 devant le jury composé de

Président	Dr. Jacques Sainte-Marie	INRIA
Rapporteur	Pr. Enrique D. Fernández-Nieto	Université de Séville (Espagne)
Rapporteur	Pr. Nicolas Seguin	Université Rennes 1
Examinateur	Dr. Nicolas Favrie	Université Aix-Marseille
Directeur de thèse	Pr. Christian Bourdarias	Université Savoie Mont Blanc
Co-directeur de thèse	Dr. Stéphane Gerbi	Université Savoie Mont Blanc
Encadrant industriel	Dr. Benoît de Laage de Meux	EDF R&D
Encadrant industriel	Dr. Jean-Marc Hérard	EDF R&D

Résumé

Ce travail est consacré à la modélisation mathématique et numérique des écoulements eau-air en conduite qui interviennent notamment dans les centrales de production d'électricité ou les réseaux d'eaux usées. On s'intéresse particulièrement aux écoulements mixtes caractérisés par la présence de régimes stratifiés pilotés par des ondes gravitaires lentes, de régimes en charge ou secs (conduite remplie d'eau ou d'air) pilotés par des ondes acoustiques rapides, et de poches d'air piégées. Une modélisation précise de ces écoulements est nécessaire afin de garantir le bon fonctionnement du circuit hydraulique sous-jacent. Alors que la plupart des modèles disponibles dans la littérature se concentrent sur la phase eau en négligeant la présence de l'air, un modèle bicouche compressible prenant en compte les interactions eau-air est proposé dans cette thèse. Sa construction réside dans l'intégration des équations d'Euler barotrope sur la hauteur de chaque phase et dans l'application de la contrainte hydrostatique sur le gradient de pression de l'eau. Le modèle obtenu est hyperbolique et satisfait une inégalité d'entropie en plus d'autres propriétés mathématiques notables, telles que l'unicité des relations de saut ou la positivité des hauteurs et densités de chaque phase. Au niveau discret, la simulation d'écoulements mixtes avec le modèle bicouche compressible soulève plusieurs défis en raison de la disparité des vitesses d'ondes caractérisant chaque régime, des processus de relaxation rapide sous-jacents, et de la disparition de l'une des phases dans les régimes en charge ou sec. Une méthode à pas fractionnaires implicite-explicite est alors développée en s'appuyant sur la relaxation rapide en pression et sur le mimétisme avec les équations de Saint-Venant pour la dynamique lente de la phase eau. En particulier, une approche par relaxation permet d'obtenir une stabilisation du schéma en fonction du régime d'écoulement. Plusieurs cas tests sont traités et démontrent la capacité du modèle proposé à gérer des écoulements mixtes incluant la présence de poches d'air piégées.

Mots clés : modèle bicouche, modèle hyperbolique, écoulement eau-air, écoulement mixte, poche d'air piégée, méthode à pas fractionnaires, schéma implicite-explicite.

Abstract

The present work is dedicated to the mathematical and numerical modelling of transient air-water flows in pipes which occur in piping systems of several industrial areas such as nuclear or hydroelectric power plants or sewage pipelines. It deals more specifically with the so-called mixed flows which involve stratified regimes driven by slow gravity waves, pressurized or dry regimes (pipe full of water or air) driven by fast acoustic waves and entrapped air pockets. An accurate modelling of these flows is necessary to guarantee the operability of the related hydraulic system. While most of available models in the literature focus on the water phase neglecting the air phase, a compressible two-layer model which accounts for air-water interactions is proposed herein. The derivation process relies on a depth averaging of the isentropic Euler set of equations for both phases where the hydrostatic constraint is applied on the water pressure gradient. The resulting system is hyperbolic and satisfies an entropy inequality in addition to other significant mathematical properties, including the uniqueness of jump conditions and the positivity of heights and densities for each layer. Regarding the discrete level, the simulation of mixed flows with the compressible two-layer model raises key challenges due to the discrepancy of wave speeds characterizing each regime combined with the fast underlying relaxation processes and with phase vanishing when the flow becomes pressurized or dry. Thus, an implicit-explicit fractional step method is derived. It relies on the fast pressure relaxation in addition to a mimetic approach with the shallow water equations for the slow dynamics of the water phase. In particular, a relaxation method provides stabilization terms activated according to the flow regime. Several test cases are performed and attest the ability of the compressible two-layer model to deal with mixed flows in pipes involving air pocket entrapment.

Keywords: two-layer model, hyperbolic model, air-water flow, mixed flow, entrapped air pocket, fractional step method, implicit-explicit scheme.

Laboratoire de Mathématiques LAMA
Université Savoie Mont Blanc - UMR CNRS 5127
Bâtiment Le Chablais, Campus Scientifique
73376 Le Bourget-du-Lac Cedex, France

EDF R&D
Département Mécanique des Fluides,
Énergies et Environnement
6 quai Watier Chatou Cedex, France

Remerciements

Je souhaite tout d'abord adresser mes remerciements à Jean-Marc Hérard qui fut un directeur de thèse additionnel et idéal. Sa pédagogie, son expertise, sa disponibilité, ses qualités humaines et son soutien ont été essentiels dans la réalisation de ces travaux. En ce sens, je m'estime privilégié d'avoir pu réaliser ma thèse à ses côtés. Je tiens également à remercier chaleureusement Benoît de Laage de Meux avec qui les échanges réguliers ont toujours été très fructueux. En particulier, son implication en plus de sa vision pertinente et originale du problème m'ont offert un recul important sur mes travaux. J'exprime ensuite ma gratitude envers Christian Bourdarias et Stéphane Gerbi pour leur confiance, leur expertise sur les écoulements mixtes et leur réactivité sans faille. Mes prochains remerciements s'adressent directement aux membres du jury qui ont accepté d'évaluer cette thèse. Ce fut un honneur d'avoir Enrique D. Fernàndez-Nieto et Nicolas Seguin en tant que rapporteurs, Jacques Sainte-Marie en tant que président du jury et Nicolas Favrie en qualité d'examinateur.

Mes remerciements s'adressent maintenant à Vincent Lefebvre, chef du groupe Turbomachines (I8E), pour sa confiance dans mes travaux et pour son soutien concernant la suite de mes aventures au sein du groupe EDF. J'en profite pour remercier Christophe avec qui j'ai beaucoup apprécié partager mon bureau durant ces trois années. Je remercie également vivement les autres membres du groupe I8E, en particulier Antoine (Tonio), Mathieu et Mugurel, qui ont contribué à une ambiance de travail des plus agréables.

Sur le plan personnel, je souhaite remercier mes amis du nord, Charles-Henri (frère), Louise, Maxence et Romain (Vahire), sur lesquels j'ai la chance de pouvoir toujours compter. Je remercie également mes amis parisiens, notamment Anne-Sophie, Marion, Mathieu, Matthieu, Nicolas, Noémie, Pierre, Romain, Sylvain, tous des fous (ou folles) à leur manière que j'ai le privilège de côtoyer. Ensuite, j'aimerais adresser une dédicace spéciale au groupe de jazz-fusion Aèdes (ex. Groovin'Monkeys), dont la composition, le niveau et la renommée ont été en évolution constante durant la thèse, pour aboutir ni plus, ni moins sur un *all-star* composé du fidèle Burks à la basse, du fou Gadel à la guitare et du dernier gars sûr, Maxime aux saxophones. Un bel échappatoire qui n'a pas fini d'affoler les foules en délire. En parlant de foules en délire, j'en profite pour souhaiter l'envol du groupe de Hip-Hop Chapka, fondé durant la thèse avec le non des moindres Ulyx à la production, et qui, après un parcours semé d'embûches, devrait buzzer d'ici peu avec un son encore jamais entendu de ce côté de l'atlantique.

Enfin, je voudrais témoigner de ma profonde gratitude envers mes parents et ma sœur pour leur soutien indispensable tout au long de mes études que j'ai eu la chance de pouvoir orienter à ma guise.

Table des matières

Chapitre 1

Introduction générale

Sommaire

1.1 Contexte industriel

Les circuits hydrauliques sont au cœur de nombreuses installations industrielles appartenant à des secteurs variés tels que la production d'électricité ou les réseaux d'assainissement. Des circuits de sauvegarde interviennent par exemple dans les Réacteurs à Eau Pressurisée (REP) en garantissant un apport d'eau en tant que source froide. Concernant la production hydroélectrique, l'acheminement de l'eau retenue par un barrage vers la turbine d'une centrale située en aval de ce dernier est assuré par des conduites forcées. Dans un registre similaire, les réseaux hydrauliques urbains interviennent dans la gestion des eaux usées et pluviales.

(a) (b) (c)

Figure 1.1: (a) Circuits hydrauliques en centrale, (b) Conduite forcée, (b) Conduite souterraine d'eaux usées.

Dans les exemples d'intérêt énoncés ci-dessus, les écoulements fluides sous-jacents répondent principalement à une **dynamique monophasique** en fonctionnement nominal. On y distingue deux types de régimes : le régime à surface libre et le régime en charge. Le **régime à surface libre**, ou régime stratifié eau-air, est un régime piloté par les ondes gravitaires de la phase eau. Il est caractéristique des réseaux d'eaux usées et pluviales. Le **régime en charge**

correspond quant à lui à une conduite remplie d'eau. Il est piloté par des ondes de pression et correspond au régime nominal des conduites hydrauliques intervenant dans les centrales de production d'énergie. Ces deux types de régimes isolés sont correctement appréhendés dans les installations. Un intérêt particulier est notamment porté sur les coups de bélier qui correspondent à des ondes de pression de forte amplitude pouvant se propager dans une conduite en charge lors d'une variation brutale de la vitesse d'écoulement.

En pratique, les géométries complexes des circuits, associées à des contraintes singulières, telles que le démarrage ou l'arrêt d'une pompe, une modification du débit, la fermeture d'une vanne, de fortes pluies pour les réseaux urbains, peuvent conduire à des **transitions entre ces régimes**. Les écoulements obtenus sont alors tantôt à surface libre, tantôt en charge, ils sont qualifiés d'**écoulements mixtes**, cf. figure 1.2. Dans ce cadre, la présence d'air dans les circuits peut devenir critique et modifier significativement la dynamique de l'écoulement. En particulier, des poches d'air piégées, typiquement dans les points hauts du circuit, conduisent à une **dynamique diphasique** eau-air avec une forte interaction entre les phases.

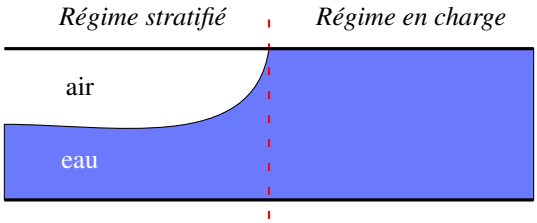

Figure 1.2: Schéma d'une configuration mixte en conduite.

Au regard de la complexité de ce type d'écoulements transitoires, les problématiques soulevées sont fortes. La contrainte principale résulte de la nature mixte des écoulements. Les variations de pression entre les deux régimes peuvent être élevées et devenir la source de dégâts matériels importants. Les poches d'air piégées peuvent également induire des niveaux de pression conséquents ainsi qu'une réduction du débit. Lorsque ces dernières sont transportées par le liquide, leur évacuation du circuit peut conduire à des scénarios dommageables. Le passage d'air dans les systèmes de pompages, notamment sous forme de poches, peut entraîner leur dysfonctionnement. L'évacuation de l'air sous pression par des cheminées dédiées peut quant à elle provoquer la formation de geysers. Le dimensionnement, l'optimisation et le contrôle de ces systèmes en milieu industriel constituent donc un défi important.

En ce sens, de nombreux travaux expérimentaux sont menés depuis plusieurs décennies afin de mieux appréhender la dynamique des écoulements mixtes [17, 16, 70, 65] ainsi que la présence d'air [32, 54, 53, 73]. Plusieurs stratégies sont notamment développées pour réduire l'influence de l'air, telles que la purge des circuits et la mise en place d'évents [56]. Le passage d'air dans les systèmes de pompages est par exemple étudié expérimentalement chez EDF afin de définir des critères d'opérabilité. En parallèle, des modèles analytiques sont développés et les apports de la simulation numérique sont évalués. La modélisation locale multi-dimensionnelle (CFD) est d'une aide précieuse grâce à une description très fine de l'écoulement. Cependant, les échelles spatiales et temporelles caractéristiques des installations industrielles imposent souvent le recours à des ressources de calcul importantes. Une approche intégrée monodimensionnelle (1D) reste donc aujourd'hui incontournable dans un contexte industriel.

Dans ces travaux de thèse, on s'intéresse particulièrement à la **modélisation 1D des écoulements mixtes eau-air en conduite**. Dans un contexte élargi, l'étude des écoulements mixtes est également pertinente pour les interactions d'une surface libre avec un objet flottant tel un iceberg, une bouée ou une éolienne off-shore. Les dynamiques diphasiques complexes en conduite se retrouvent quant à elles dans les circuits primaires et secondaires des Réacteurs à Eau Pressurisée sous forme eau-vapeur ou encore dans les pipelines de l'industrie pétrolière sous forme pétrole-gaz.

1.2 Contexte scientifique

Afin de décrire la dynamique des écoulements mixtes avec un modèle 1D, plusieurs approches dédiées sont proposées dans la littérature, notamment par la communauté hydraulique (conduites forcées, réseaux d'eaux usées et pluviales). Ces approches sont essentiellement monophasiques et se concentrent sur la modélisation des transitions entre les régimes à surface libre et en charge. Certaines d'entre elles sont étendues à la prise en compte de poches d'air pour des configurations simplifiées. Un descriptif de ces approches est proposé ci-dessous en identifiant leurs limites quant à la modélisation diphasique d'écoulements mixtes avec fortes interactions entre les phases. En ce sens, une revue des principaux modèles d'écoulements diphasiques existants, non nécessairement dédiés aux écoulements mixtes, est

ensuite apportée. On commence par rappeler les modèles moyennés usuels permettant de décrire un écoulement à surface libre en conduite ou en charge.

1.2.1 Modélisation des écoulements à surface libre ou en charge

L'objectif de cette section est de présenter les systèmes d'équations usuellement utilisés pour décrire un écoulement à surface libre ou en charge dans une conduite. L'établissement de ces systèmes n'est volontairement pas détaillé ici.

L'écoulement d'un liquide ou d'un gaz peut être décrit localement par les équations d'Euler qui s'écrivent classiquement :

$$\begin{cases} \partial_t \rho + \operatorname{div}(\rho \mathbf{u}) = 0, \\ \partial_t \rho \mathbf{u} + \operatorname{div}(\rho \mathbf{u} \otimes \mathbf{u} + P \mathrm{I_d}) = \rho \mathbf{g}, \end{cases} \tag{1.1}$$

où $(\rho, P, \mathbf{u})$ désignent respectivement la densité, la pression et le vecteur vitesse du liquide en un point donné, $\mathbf{g}$ le champ de gravité et $\mathrm{I_d}$ la matrice identité. Dans ce système, la première équation correspond à la conservation de la masse et la deuxième correspond à la conservation de la quantité de mouvement. Ces équations sont principalement utilisées comme point de départ pour le développement de modèles moyennés. On peut également introduire les effets visqueux en considérant les équations de Navier-Stokes. Dans toute la suite, on considère l'écoulement d'un liquide dans une conduite rectangulaire horizontale d'axe x, de hauteur H, de largeur L et de section constante $S = LH$, cf. figure 1.2.1. Les commentaires et les approches peuvent être aisément étendus au cas des conduites circulaires.

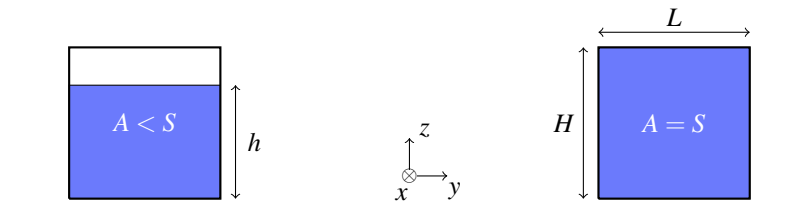

Figure 1.3: Régimes d'écoulement en conduite rectangulaire d'axe x, A : section mouillée, S : section de la conduite.

Dans le **régime à surface libre**, l'écoulement est piloté par les **ondes gravitaires** qui se propagent à la surface du liquide. Afin d'obtenir une description 1D, une série d'hypothèses est faite sur la dynamique de l'écoulement. Une approche classique consiste alors à raisonnablement négliger la compressibilité du liquide dans ce régime (on pose $\rho = \rho_0$ dans (1.1)), les variations dans la direction transverse y, et faire l'hypothèse d'un écoulement en *couche mince*. Cette dernière stipule que l'échelle spatiale caractéristique des phénomènes longitudinaux est grande devant celle des phénomènes verticaux. Dans ce cadre, l'accélération verticale dans l'équation de conservation de quantité de mouvement du système (1.1) est négligée et on obtient une loi de pression hydrostatique qui s'écrit $P(z) = \rho_0 g(h-z)$ (à une constante d'intégration près). En intégrant sur la section mouillée (section occupée par le fluide) l'équation de conservation de masse et de quantité de mouvement projetée selon x, on aboutit alors aux équations de Saint-Venant [9, 38] qui s'écrivent :

$$\begin{cases} \partial_t \rho_0 A + \partial_x \rho_0 Q = 0, \\ \partial_t \rho_0 Q + \partial_x (\rho_0 \dfrac{Q^2}{A} + A\bar{P}) = 0, \end{cases} \tag{1.2}$$

avec $A = Lh$ la section mouillée, Q le débit ($Q = A\bar{u}$ avec $\bar{u}$ la vitesse moyenne sur une section), ρ_0 la densité et $\bar{P}$ la pression moyenne sur une section. En intégrant la loi hydrostatique pour une conduite rectangulaire, on obtient une fermeture pour la pression (à une constante d'intégration près) :

$$\bar{P} = \bar{P}(h) = \rho_0 g \frac{h}{2}. \tag{1.3}$$

La célérité des ondes gravitaires résultantes est alors donnée par $c = \sqrt{gh}$. Les inconnues du système (1.2) sont (A, Q), ou de manière équivalente $(h, \bar{u})$. Il s'agit d'un système hyperbolique largement utilisé pour modéliser les écoulements à surface libre en eaux peu profondes. Des termes sources prenant en compte la pente, le frottement et les variations de section peuvent notamment être introduits, voir [11].

Dans le **régime en charge**, les **ondes acoustiques** se propageant dans le liquide peuvent fortement influencer la dynamique de l'écoulement. Une description compressible est alors pertinente afin de modéliser précisément la

propagation des ondes de pression associées. Une modélisation 1D peut s'obtenir en négligeant les variations dans la direction transverse y et en intégrant, comme précédemment, l'équation de conservation de masse et de quantité de mouvement projetée selon x du système (1.1) sur la section totale. Le système obtenu s'écrit :

$$\begin{cases} \partial_t \bar{\rho} S + \partial_x \bar{\rho} Q = 0, \\ \partial_t \bar{\rho} Q + \partial_x (\bar{\rho} \dfrac{Q^2}{S} + S\bar{P}) = 0, \end{cases} \tag{1.4}$$

avec S la section de la conduite, Q le débit ($Q = S\bar{u}$ avec $\bar{u}$ la vitesse moyenne sur une section), $\bar{\rho}$ la densité moyenne sur une section et $\bar{P}$ la pression moyenne sur une section. Dans un cadre isentropique, une loi de pression barotrope reliant $\bar{P}$ à $\bar{\rho}$ est spécifiée afin de fermer le système :

$$\bar{P} = \bar{P}(\bar{\rho}). \tag{1.5}$$

Les inconnues du système (1.4) sont donc $(\bar{\rho}, Q)$ ou de manière équivalente $(\bar{\rho}, \bar{u})$. La célérité des ondes acoustiques est donnée par $c = \sqrt{\bar{P}'(\bar{\rho})}$ et vaut $c \sim 1500 m.s^{-1}$ pour de l'eau pure. Le système obtenu est hyperbolique et des termes sources prenant en compte la pente, le frottement et les variations de section peuvent être introduits, voir [11]. En pratique, les caractéristiques matérielles de la conduite, telle que son élasticité, peuvent fortement modifier la célérité des ondes de pression. Un autre modèle couramment utilisé pour les écoulements en charge est donné par les équations d'Alliévi qui décrivent la propagation d'ondes acoustiques à célérité c par un système non conservatif en variables $(\bar{P}, Q)$ [71].

Les régimes à surface libre et en charge sont donc de nature très différente et nécessitent une description adaptée. En particulier, il est important de rendre compte de la dynamique gravitaire à surface libre et de la dynamique acoustique en charge. Cela se traduit notamment par une forte disparité dans les célérités d'ondes associées ($\sqrt{gh} \ll c$ en pratique). Dans ce cadre, la modélisation des écoulements mixtes soulève de nombreux défis. Les principales approches proposées dans la littérature sont décrites dans la prochaine section.

1.2.2 Modélisation des écoulements mixtes

Depuis les années 60, de nombreux travaux ont été menés afin de répondre à la problématique des écoulements mixtes, notamment en proposant des modèles permettant de rendre compte des spécificités de chaque régime. Dans la littérature, les différentes approches sont classées parmi trois catégories : *Rigid Water Column*, *Interface Tracking* et *Shock Capturing*. Ces dénominations sont reprises ci-dessous en présentant les principaux modèles associés, voir aussi [14, 66, 46].

1.2.2.a Rigid Water Column

L'approche *Rigid Water Column* a été introduite par Hammam et Mc Corquodale en 1982 [42]. Elle consiste à décomposer l'écoulement en colonnes d'eau rigides ayant une vitesse uniforme. La dynamique de ces colonnes est régie par des équations différentielles ordinaires. En particulier, les colonnes en charge sont séparées par des poches d'air considérées stationnaires mais pouvant se dilater ou se comprimer. La méthode est enrichie par Li et Mc Corquodale [48] en intégrant le mouvement des poches d'air. Cette approche permet de reproduire les résultats expérimentaux de Zhou *et al.* [73] qui considèrent l'interaction entre une colonne d'eau et une poche d'air piégée en bout de conduite. Il s'agit d'une méthode très visuelle et facile à mettre en place sur des configurations simples. Cependant, elle nécessite de connaître précisément la configuration initiale de l'écoulement afin d'établir une décomposition adaptée. De plus, cette décomposition peut devenir ingérable pour des conduites dont la géométrie est complexe.

1.2.2.b Interface Tracking

L'approche dite par *Interface Tracking* consiste à résoudre séparément la dynamique à surface libre et en charge par deux systèmes d'équations aux dérivées partielles différents. Dans ce cadre, il est également nécessaire de modéliser la dynamique de l'interface séparant les régimes afin de coupler ces deux systèmes. Cette modélisation repose notamment sur l'écriture de relations de saut adaptées. L'approche générale a été introduite par Wiggert en 1972 [70] dont les résultats ont été validés expérimentalement. Elle a été reprise par de nombreux auteurs, notamment Song *et al.* [63] et Fuamba [34], avec pour objectif d'améliorer la modélisation de la dynamique d'interface. Cette approche devient toutefois difficile à mettre en œuvre pour un écoulement présentant de nombreux points de transition pouvant éventuellement interagir.

1.2.2.c Shock Capturing

L'approche dite par *Shock Capturing* consiste à utiliser un seul système d'équations canonique permettant de rendre compte *naturellement* des transitions et des spécificités de chaque régime. Il s'agit de l'approche la plus utilisée dont le modèle historique fut introduit par Cunge et Wegner [28] en 1964 en utilisant le concept de la fente de Preissmann proposé par Preissmann et Cunge [55] en 1961. Ce modèle permet notamment de modéliser les transitions entre les régimes à surface libre et en charge avec les célérités d'ondes appropriées dans chaque régime. Il est décrit ci-dessous avant de présenter d'autres modèles plus récents proposant également une description unifiée des deux régimes.

Modélisation des surpressions en charge

Le modèle historique de la fente de Preissmann [28] vise à étendre l'applicabilité du système de Saint-Venant (1.2) au régime en charge en imaginant que la conduite est surmontée d'une fente étroite de largeur ε, cf. figure 1.4. Dans ce cadre, le passage en charge est modélisé par une composante hydrostatique additionnelle positive sur la pression provenant de l'information $A > S$ (ou $h > H$). La célérité des ondes en charge est alors donnée par $c = \sqrt{\frac{gA}{\varepsilon}}$, où la largeur ε peut être ajustée afin d'obtenir le bon ordre de grandeur. Ce modèle est très largement utilisé et validé sur des résultats expérimentaux [36, 16, 65, 7]. Très récemment, Godlewski *et al.* [40] ont proposé un modèle d'écoulements mixtes pour des applications géophysiques qui consiste à contraindre le système de Saint-Venant par la condition $h \leq H$. En s'inscrivant dans un cadre mathématique rigoureux, cette contrainte est ensuite relaxée et se traduit aussi par une composante additionnelle positive sur la pression en charge.

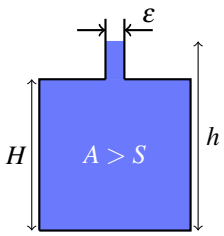

Figure 1.4: Passage en charge avec une fente de Preissmann.

Les modèles décrits ci-dessus ne permettent pas de modéliser des pressions sub-atmosphériques en charge (i.e. les dépressions) qui sont par construction associées à une transition à surface libre. Ces phénomènes, qui interviennent notamment lors d'un coup de bélier où dans les points hauts d'un circuit hydraulique, nécessitent une attention particulière.

Modélisation des dépressions en charge

Afin de modéliser les dépressions en charge, d'autres modèles s'inspirant de l'approche canonique de la fente de Preissmann ont été proposés. Ils utilisent également les équations de Saint-Venant (1.2) à surface libre et interprètent l'information $A > S$ pour modéliser le passage en charge. La modélisation des dépressions repose alors sur deux points, la définition d'un critère discret autorisant ou non le passage à surface libre (la mise à jour d'une cellule en charge dépend de l'état des cellules voisines et de la présence éventuelle d'un évent) et la définition d'une loi de pression en charge permettant effectivement de modéliser des dépressions. Dans le modèle *Two-component Pressure Approach* (TPA) de Vasconcelos *et al.* [68], la loi hydrostatique est complétée par une contribution assimilée à un comportement élastique de la conduite en charge. Dans le modèle *Pressurized Free-Surface* (PFS) de Bourdarias et Gerbi [13], la loi de pression en charge est une loi barotrope. En particulier, la définition d'un jeu de variables équivalent ($A_{eq} = \frac{\bar{\rho}}{\rho_0} S, Q_{eq} = \frac{\bar{\rho}}{\rho_0} Q$) dans (1.4) permet de regrouper les systèmes (1.2) et (1.4) sous un même formalisme. Enfin, dans les travaux de Kerger *et al.* [47], les dépressions sont modélisées par une loi hydrostatique à l'aide d'une fente de Preissmann *négative*. Ces modèles sont validés sur de nombreux résultats expérimentaux et offrent une description satisfaisante de la dynamique monophasique d'un écoulement mixte en conduite. Les auteurs correspondants soulignent toutefois la nécessité d'intégrer la modélisation de la phase air qui peut avoir une influence importante sur la dynamique de l'écoulement, notamment lorsque celle-ci est présente sous forme de poches d'air piégées.

Modélisation des poches d'air

Le modèle TPA de Vasconcelos *et al.* [68] décrit ci-dessus a été étendu à la prise en compte des poches d'air dans [67]. La dynamique de la phase air est calculée uniquement lorsqu'une poche d'air piégée (ou en contact avec un orifice) est détectée à l'aide d'un processus itératif. Deux modélisations sont alors présentées, soit en faisant l'hypothèse d'une pression uniforme dans la poche assortie d'une loi de type gaz parfait et d'une dynamique isotherme,

soit en résolvant un système d'équations exprimant la conservation de la masse et de la quantité de mouvement. La loi de pression hydrostatique utilisée pour la phase eau prend ensuite en compte la pression d'air calculée dans la poche. Un dispositif expérimental représentant l'évacuation d'une poche d'air piégée par un orifice permet de valider les résultats obtenus et d'illustrer l'importance de cette modélisation. Une méthode similaire est développée par León *et al.* [51] à partir du modèle PFS de Bourdarias et Gerbi [13]. Cependant, ces approches itératives simplifient le couplage entre les phases. En particulier, elles ne permettent pas de prendre en compte les interactions eau-air en régime stratifié ni la coalescence de poches.

1.2.2.d Bilan

Les modèles monophasiques proposant une description unifiée d'un écoulement mixte (*Shock Capturing*) ont bénéficié d'une popularité grandissante en raison de leur gestion *naturelle* des transitions entre régimes. En particulier, ils ont fait l'objet de plusieurs améliorations depuis le modèle historique de la fente de Preissmann jusqu'à intégrer l'influence des poches d'air piégées pour des configurations simplifiées. La modélisation des interactions eau-air dans tous les régimes n'est toutefois pas prise en compte. Une approche diphasique permettant également une description unifiée d'un écoulement mixte serait alors pertinente. En ce sens, les différentes familles de modèles d'écoulements diphasiques sont présentées dans la prochaine section en évaluant leur capacité à décrire un écoulement mixte eau-air en conduite.

1.2.3 Modélisation diphasique des écoulements

Dans le but de décrire la dynamique d'un écoulement diphasique, on distingue deux familles de modèles dans la littérature : les modèles homogènes et les modèles bifluide. Les spécificités des deux approches et leurs variantes sont décrites ci-dessous en identifiant les intérêts potentiels pour la modélisation des écoulements mixtes eau-air en conduite.

1.2.3.a Approches homogènes

Les approches homogènes consistent à décrire un écoulement diphasique comme un seul fluide en utilisant des variables de mélange. On écrit alors au moins une équation de conservation de masse pour chaque phase et une équation de conservation de quantité de mouvement pour le mélange. Afin d'en déduire la vitesse de chaque phase, il est nécessaire de faire des hypothèses. On peut considérer un équilibre en vitesse [21] ou imposer une loi de fermeture entre la vitesse du mélange et la vitesse de chaque phase : il s'agit des modèles avec flux de dérive (*drift flux*) [33]. Ces fermetures dépendent notamment du régime d'écoulement [15]. Le taux de présence de chaque phase est également résolu mais il ne permet pas de distinguer la topologie de l'écoulement entre par exemple une configuration stratifiée ou dispersée. Par nature, les modèles résultants sont particulièrement adaptés aux écoulements diphasiques dispersés et conviennent à beaucoup d'applications de l'industrie nucléaire ou pétrolière. Ils s'inscrivent souvent dans un cadre mathématique rigoureux et dégénèrent naturellement vers une description monophasique. Cependant, ils trouvent leurs limites dans la description d'écoulements stratifiés où les vitesses de chaque phase peuvent être fortement décorrélées.

1.2.3.b Approches bifluide

Afin de résoudre indépendamment la vitesse de chaque phase, on écrit une équation de conservation de quantité de mouvement par phase en plus des équations de conservation de masse dans chaque phase. Ces quatre équations constituent la base des modèles bifluide. Dans un contexte 1D, elles résultent typiquement de l'intégration des équations d'Euler (1.1) à l'aide d'un opérateur de moyenne qui peut être spatial, temporel ou statistique. Pour un écoulement liquide-gaz dans une conduite d'axe x, elles prennent la forme canonique suivante :

$$\begin{cases} \partial_t \alpha_l \rho_l + \partial_x \alpha_l \rho_l u_l = TS_{m,l}, \\ \partial_t \alpha_g \rho_g + \partial_x \alpha_g \rho_g u_g = TS_{m,g}, \\ \partial_t \alpha_l \rho_l u_l + \partial_x \alpha_l (\rho_l u_l^2 + P_l) - P_I \partial_x \alpha_l = TS_{q,l}, \\ \partial_t \alpha_g \rho_g u_g + \partial_x \alpha_g (\rho_g u_g^2 + P_g) - P_I \partial_x \alpha_g = TS_{q,g}, \end{cases} \tag{1.6}$$

avec $\alpha_l + \alpha_g = 1$ et $(\alpha_k, \rho_k, P_k, u_k)$ désignant respectivement le taux de présence, la densité moyenne, la pression moyenne et la vitesse moyenne de la phase k sur une section ($k = l$ pour le liquide et g pour le gaz). La variable P_I

désigne la pression à l'interface entre les phases et des termes sources, représentés ici par TS, peuvent être introduits afin de prendre en compte, entre autres, des transferts de masse et de quantité de mouvement. Enfin, des équations de conservation d'énergie peuvent être ajoutés au système (1.6) afin de modéliser les variations d'énergie interne. Dans la suite, on se restreint au cadre isentropique et on s'intéresse particulièrement au cas d'un écoulement stratifié eau-air en conduite. Pour ce dernier, l'utilisation d'un opérateur de moyenne spatiale sur chaque couche est adapté, le taux de présence est alors défini par $\alpha_k = \frac{h_k}{H}$ avec h_k la hauteur de phase k et H la hauteur de conduite.

Le système (1.6) est constitué de quatre équations aux dérivées partielles impliquant huit inconnues données par $(\alpha_l, \rho_l, \rho_g, u_l, u_g, P_l, P_g, P_I)$. Afin d'obtenir des relations de fermeture, il est nécessaire de faire des hypothèses sur la dynamique de l'écoulement. En particulier, la discussion s'effectue autour de la compressibilité des phases et de la modélisation des pressions. Dans notre contexte, la dynamique des poches d'air piégées répond de manière évidente à une dynamique compressible. La compressibilité de la phase eau est quant à elle discutable, notamment en régime stratifié. On distingue alors les modèles *monopression* et *bipression*.

Modèles monopression : eau incompressible/air compressible

Dans cette catégorie de modèles, on considère que les inconnues primitives du système (1.6) sont représentées par quatre inconnues : le taux de présence de l'une des phases, les vitesses de chaque phase et la pression de l'une des phases. L'approche naturelle consiste alors à choisir $(\alpha_l, u_l, u_g, P_l)$ comme inconnues primitives de sorte que la fermeture du système repose sur les hypothèses suivantes : la phase eau est incompressible ($\rho_l = \rho_0$), il y a équilibre instantané en pression entre les phases ($P_g = P_l$, $P_I = P_l$) et la loi d'état de la pression de l'air est barotrope ($\rho_g = \rho_g(P_g)$). Cependant, les effets hydrostatiques qui pilotent le régime stratifié ne sont pas pris en compte. Dans ce but, une deuxième approche consiste à considérer une fermeture hydrostatique pour la loi de pression de l'eau et à choisir $(\alpha_l, u_l, u_g, P_g)$ comme inconnues primitives en gardant les mêmes hypothèses. Cela revient à considérer un modèle type Saint-Venant pour la phase eau. Un modèle bicouche de ce type est développé par Bourdarias *et al.* dans [12] pour les écoulements stratifiés eau-air en conduite circulaire sans étudier le passage en charge. Cette approche est aussi adoptée par Arai et Yamamoto [5] dans le but de modéliser des écoulements mixtes eau-air en conduite, les passages en charge étant représentés par une fente de Preissmann fermée, cf. section 1.2.2.c. Une variante est également proposée par Issa et Kempf dans [44].

Le couplage d'un modèle type Saint-Venant pour la phase eau avec un modèle compressible moyenné pour la phase air via la pression d'interface est une approche pertinente pour modéliser un régime stratifié eau-air. Cependant, au-delà d'envisager une transition vers un régime en charge, ce type de modèle est **conditionnellement hyperbolique**. En particulier, l'hyperbolicité est obtenue uniquement pour une faible ou grande vitesse relative entre les phases [12]. Cette condition peut s'avérer problématique en régime stratifié pour lequel aucune restriction ne peut être *à priori* imposée sur la vitesse relative. L'approche générale hérite en effet des inconvénients *classiques* d'une approche dite *monopression*.

Modèles bipression : eau compressible/air compressible

Dans cette seconde catégorie de modèles, les inconnues primitives du système (1.6) sont représentées par cinq inconnues : $(\alpha_l, u_l, u_g, \rho_l, \rho_g)$. Il est alors nécessaire d'ajouter une équation relative au transport du taux présence qui s'écrit :

$$\partial_t \alpha_l + U_I \partial_x \alpha_l = TS_\alpha, \tag{1.7}$$

avec U_I la vitesse d'interface et TS_α un terme source à fermer. En utilisant une moyenne spatiale par couche, (1.7) correspond au transport matériel de l'interface. Dans le cadre isentropique, deux lois d'états barotropes sont ensuite spécifiées pour chaque phase : $P_g(\rho_g)$ et $P_l(\rho_l)$. Il reste à établir des fermetures pour les termes interfaciaux (U_I, P_I) et les termes sources. Ce type d'approche a notamment été introduit par Ransom et Hicks pour les écoulements stratifiés eau-vapeur dans [58]. Une autre contribution majeure est le modèle proposé par Baer et Nunziato [8] pour les écoulements gaz-particules (moyenne statistique). Il a été largement repris pour la modélisation des écoulements gaz-particules [45] mais aussi liquide-gaz [37]. De nombreuses fermetures pour les termes interfaciaux et les termes sources ont été proposées dans la littérature, par exemple dans [22, 39, 60]. Une caractérisation entropique peut notamment être utilisée [23]. Dans ce cadre, le modèle obtenu est **hyperbolique** et présente des propriétés mathématiques notables. Son application au cas des écoulements mixtes peut être envisagée.

1.2.4 Démarche et objectifs de la thèse

Les modèles d'écoulements mixtes les plus utilisés dans la littérature reposent sur une approche monophasique visant à unifier la description des régimes à surface libre et en charge. Dans ce type d'approche, la prise en compte de la phase air a été relativement peu investiguée, mise à part sur des configurations simplifiées. Ainsi, on se propose de

développer un modèle diphasique 1D pour les écoulements mixtes permettant de rendre compte des spécificités de chaque régime et des interactions entre les phases. En se plaçant dans un cadre mathématique rigoureux, la description des régimes serait également unifiée en portant un intérêt particulier sur (i) la dynamique gravitaire à surface libre, (ii) la dégénérescence du modèle vers une description adaptée aux régimes en charge et sec (conduite remplie d'eau ou d'air) et (iii) les géométries complexes de conduite (section rectangulaire et circulaire variable, rupture de pente).

Dans cette perspective, la classe des modèles bifluide bipression constitue une porte d'entrée intéressante. Ils sont essentiellement utilisés dans la littérature pour la description d'écoulements dispersés eau-vapeur [49] mais le formalisme canonique permet également de décrire une configuration bicouche comme en témoigne le modèle initialement introduit par Ransom et Hicks [58]. Cette configuration bicouche est pertinente pour les écoulements mixtes en conduite puisqu'elle permet de décrire naturellement le régime stratifié, le régime en charge (ou sec) et les poches d'air piégées. Il s'agit alors de répondre aux problématiques (i), (ii) et (iii) en travaillant notamment sur les fermetures du système (termes interfaciaux et termes sources). Dans un second temps, la simulation de ce système doit être envisagée. Des contraintes numériques fortes résultent de la dynamique des écoulements mixtes et de son aspect multi-régime (dynamique *lente* à surface libre et *rapide* en charge, gestion des phases évanescentes). Enfin, une validation du modèle doit être menée en s'appuyant sur des configurations mettant en jeu ou non des interactions entre les phases. Les apports du modèle proposé pourront alors être évalués en comparaison avec les modèles disponibles dans la littérature.

1.3 Synthèse des travaux

Les travaux réalisés dans cette thèse sont regroupés ci-dessous autour de trois grandes parties. La première partie (Chapitre 2) est consacrée à la **modélisation** diphasique des écoulements mixtes en conduite via le développement d'un nouveau modèle. La seconde partie (Chapitres 3,4,5) est dédiée à la **discrétisation** de ce modèle en vue de sa résolution numérique. Dans la dernière partie (Chapitre 6), des cas tests de **validation** du modèle sont présentés. La totalité de ces chapitres est rédigée en anglais car ils font (ou sont destinés à faire) l'objet d'éléments de communications comme précisé en section 1.3.4. En ce sens, ils ont été conçus pour être, dans une certaine mesure, autoporteurs exceptée la partie validation. Une synthèse détaillée de ces travaux est proposée dans cette section.

1.3.1 Partie I : Modélisation

Chapitre 2 : Un modèle bicouche compressible pour les écoulements transitoires gaz-liquide en conduite

Un nouveau modèle 1D d'écoulement mixte liquide-gaz en conduite est proposé dans ce chapitre. Les configurations d'intérêt sont le régime stratifié (une couche de gaz sur une couche de liquide), les régimes en charge ou sec (conduite remplie de liquide ou de gaz) et les poches de gaz piégées. Les transitions entre ces régimes sont également ciblées, on parle alors d'écoulement mixte diphasique. En pratique, ce type d'écoulement peut induire une forte interaction entre les phases sans conduire à un équilibre instantané en vitesse et pression. Ainsi, une description moyennée par couche, bifluide et bipression (une vitesse et une pression thermodynamique par phase), à la manière du modèle de Ransom et Hicks [58] est visée.

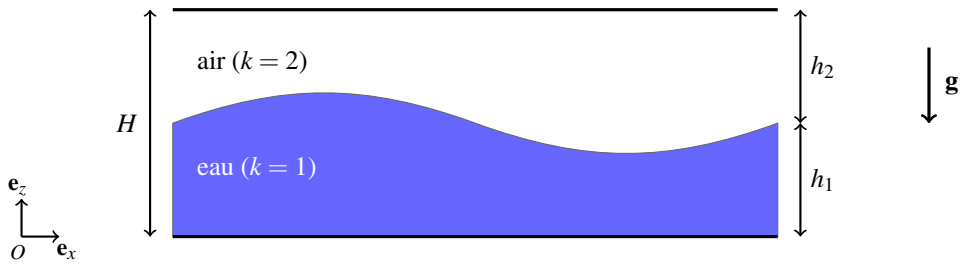

Figure 1.5: Régime stratifié eau-air en conduite.

La configuration canonique pour le développement du modèle correspond à une conduite rectangulaire de hauteur H où l'écoulement liquide-gaz (considéré eau-air dans ce qui suit sans perte de généralité) est stratifié, cf. figure 1.5. La hauteur de chaque de chaque phase est notée h_k, $k=1$ pour l'eau, 2 pour l'air, de telle sorte que $h_1+h_2=H$. La direction longitudinale est notée x, la direction verticale z et le champ de gravité est défini par $\mathbf{g}=-g\mathbf{e_z}$. Les

variations de l'écoulement dans la direction transverse sont négligées. L'évolution locale de chaque phase est ainsi décrite dans le plan (O,x,z) par les équations d'Euler isentropique (modèle compressible). Les transferts de masse éventuels (pertinents dans un contexte liquide-vapeur) ainsi que les transferts de quantité de mouvement (friction entre les phases) sont pris en compte. Sur les parois, la vitesse verticale est supposée nulle localement. Sur l'interface entre les deux phases, la continuité de la vitesse normale et de la pression est imposée localement, les effets dus à la tension de surface sont négligés. Afin d'obtenir un modèle 1D, les équations de conservation de masse ainsi que les équations de conservation de quantité de mouvement projetées selon x sont moyennées sur chaque couche. En y ajoutant l'équation vérifiée par la dynamique de l'interface, le système à cinq équations suivant est obtenu :

$$\begin{cases} \partial_t h_1 + U_I \partial_x h_1 = W_I, \\ \partial_t h_k \rho_k + \partial_x h_k \rho_k u_k = h_k M_k, \ k = 1,2, \\ \partial_t h_k \rho_k u_k + \partial_x h_k (\rho_k u_k^2 + P_k(\rho_k)) - P_I \partial_x h_k = h_k D_k, \ k = 1,2, \end{cases} \tag{1.8}$$

avec $h_1 + h_2 = H$ et (ρ_k, u_k, P_k) désignant respectivement la densité moyenne , la vitesse axiale moyenne et la pression moyenne sur la couche de phase k. Les cinq inconnues du système sont donc données par la hauteur d'eau h_1, la densité moyennée de chaque phase ρ_k, $k = 1,2$, et la vitesse moyennée de chaque phase u_k, $k = 1,2$. Les variables d'interfaces sont notées $\mathbf{u_I} = (U_I, W_I)$ pour la vitesse et P_I pour la pression. Les termes sources M_k et D_k correspondent respectivement aux transferts de masse moyennés et aux transferts de quantité de mouvement moyennés. Afin de fermer le système, il reste à spécifier des lois de pression barotropes $P_k(\rho_k)$ pour chaque phase, et à identifier des lois de fermeture pour les termes interfaciaux et les termes sources.

La structure du système (1.8) est commune aux modèles bifluide bipression, notamment celui introduit dans [58] par Ransom et Hicks mais aussi avec ceux développés dans un cadre statistique et utilisé pour la modélisation d'écoulements dispersés, notamment celui introduit dans [8] par Baer et Nunziato dans sa version isentropique. L'originalité du modèle proposé dans cette thèse réside entre autres dans l'établissement des lois de fermeture pour les termes interfaciaux, en particulier la pression d'interface P_I, et les termes sources. Pour le type d'écoulements considérés, la dynamique de la phase eau en régime stratifiée est pilotée par les effets gravitaires. La fermeture pour P_I est alors obtenue à partir de l'intégration de la **contrainte hydrostatique** imposée sur le système non-moyenné initial. Cette contrainte traduit l'équilibre du gradient de pression vertical de la phase eau avec la gravité, après avoir négligé l'accélération verticale. Elle est utilisée pour fermer la loi de pression dans les équations de Saint-Venant [9, 38] dans un cadre incompressible mais son utilisation dans un cadre compressible est moins commune. On obtient ainsi :

$$P_I = P_1(\rho_1) - \rho_1 g \frac{h_1}{2}, \tag{1.9}$$

qui peut être lue comme une loi de pression hydrostatique moyennée pour la phase eau. Ces effets gravitaires verticaux ne sont pas pris en compte dans le modèle original [58]. Les fermetures de la vitesse interfaciale U_I et des termes sources sont ensuite obtenues par caractérisation entropique en s'inspirant de la démarche initialement proposée dans [23]. Une **inégalité d'entropie** est en ce sens construite à partir des équations du système (1.8). L'entropie sous-jacente correspond à l'énergie totale du système, elle contient l'énergie cinétique et thermodynamique de chaque phase et l'énergie potentielle de pesanteur de la phase eau. En imposant la conservativité de l'équation vérifiée par cette entropie, on obtient :

$$U_I = u_2, \tag{1.10}$$

alors que le caractère dissipatif est assuré dès lors que les termes sources vérifient :

$$\begin{cases} W_I = \lambda_p (P_I - P_2) = \lambda_p (P_1 - \rho_1 g \dfrac{h_1}{2} - P_2), \\ h_k D_k = (-1)^k \lambda_u (u_1 - u_2) + \left(\dfrac{u_1 + u_2}{2} \right) h_k M_k, \ k = 1,2, \\ h_k M_k = (-1)^k \lambda_m \left((\dfrac{P_1 + \rho_1 g \frac{h_1}{2}}{\rho_1} + \Psi_1) - (\dfrac{P_2}{\rho_2} + \Psi_2) \right), \ k = 1,2, \end{cases} \tag{1.11}$$

où λ_p, λ_u et λ_m sont des fonctions bornées positives dépendantes des variables d'état $(h_1, \rho_1, \rho_2, u_1, u_2)$, et $\Psi_k'(\rho_k) = \frac{P_k}{\rho_k^2}$. Pour les écoulements eau-air sans transfert de masse ($M_k = 0$), on obtient un terme de relaxation en pression entre la pression d'interface et la pression de l'air, ainsi qu'un terme de relaxation en vitesse qui correspond à la friction entre les phases.

Le modèle ainsi développé est pertinent pour la modélisation diphasique des écoulements mixtes en conduite. En régime stratifié, la fermeture (1.9) pour P_I combinée à la relaxation en pression permet de retrouver formellement une proximité avec les équations de Saint-Venant [9, 38] pour la phase eau. Lorsque que $h_k \to H$, le système dégénère

par construction vers un modèle Euler monophasique compressible qui est adapté à la description d'un écoulement en charge (ou sec) en conduite. La transition entre ces régimes est donc assurée naturellement au niveau continu par une description unifiée. En particulier, la loi de pression barotrope pour la phase eau est commune aux différents régimes contrairement aux modèles d'écoulements mixtes (monophasiques) les plus utilisés dans la littérature [13, 68, 51].

Les propriétés mathématiques du système (1.8) muni des fermetures (1.9), (1.10) et (1.11) sont étudiées. Elles sont héritées du cadre bifluide bipression étudié par exemple dans [35] et sont notables. La partie convective du modèle est **hyperbolique** sous la condition de non-résonance $|u_1 - u_2| \neq c_1$, où $c_1 \sim 1500 m.s^{-1}$ correspond à la célérité des ondes acoustiques dans la phase eau. Dans les cas pratiques, cette condition n'est pas restrictive contrairement à d'autres modèles bicouche [12, 6] dont l'hyperbolicité n'est assurée que pour de faibles ou grandes vitesses relatives entre les phases. De plus, la structure propre du système est facilement explicitée, les valeurs propres sont notamment données par :

$$\lambda_1 = u_2,\ \lambda_2 = u_1 - c_1,\ \lambda_3 = u_1 + c_1,\ \lambda_4 = u_2 - c_2,\ \lambda_5 = u_2 + c_2, \tag{1.12}$$

où $c_k = \sqrt{P_k'(\rho_k)},\ k = 1,2$. L'étude du problème de Riemann est ensuite menée. La **nature des champs caractéristiques** est obtenue accompagnée des **invariants de Riemann** correspondants. Le champ associé à la valeur propre $\lambda_1 = u_2$ est linéairement dégénéré alors que ceux associés aux valeurs propres $\lambda_p,\ p = 2,..,5$, sont vraiment non-linéaires. On s'intéresse particulièrement à la **définition et l'unicité des relations de saut** pour les solutions discontinues. Ces relations sont établies classiquement à partir des relations de Rankine-Hugoniot malgré la présence de termes non-conservatifs. En effet, ces derniers sont portés par la variable h_1 qui subit une discontinuité uniquement au passage de la 1-onde ($\lambda_1 = u_2$) associée à un champ linéairement dégénéré. Par conséquent, le problème de Riemann est explicitement bien défini et il est possible de construire des solutions analytiques associées à la partie convective de (1.8) qui permettent la vérification de méthodes numériques. Enfin, la **positivité des hauteurs et des densités** de chaque phase est assurée en imposant des paramètres de relaxation λ_p et λ_m pondérés par $m_1 m_2$ où $m_k = h_k \rho_k$. Cette propriété qui garantit $h_k \in [0, H]$, $k = 1,2$, au niveau continu est particulièrement intéressante et originale dans le cadre des écoulements mixtes. En effet, la plupart des modèles développés jusqu'alors n'intègre pas la contrainte $h_1 \leq H$ dans leur formulation et s'inspirent de l'idée de la fente Preissmann [28] qui consiste à utiliser l'information $h_1 \geq H$ pour repérer un point de transition et définir une surpression en charge.

Avec pour objectif de traiter des configurations industrielles, la formulation du modèle et son analyse sont par suite étendues au cadre des conduites circulaires inclinées à section variable en temps et en espace.

Finalement, le modèle bicouche compressible proposé ici est en rupture par rapport aux modèles dédiés aux écoulements mixtes disponibles dans la littérature [14]. Cette singularité réside notamment dans la modélisation des deux phases, et ce, avec une approche compressible pour tous les régimes d'écoulements. Ces derniers incluent le régime stratifié, les régimes en charge ou sec, et la prise en compte de poches d'air piégées. Dans ce cadre, les transitions entre ces régimes sont continûment assurées et la modélisation des surpressions ou des dépressions en charge est naturelle. De plus, les propriétés mathématiques obtenues sont notables. La prochaine étape consiste à développer une méthode numérique efficace adaptée à la simulation de ces différents régimes avec transitions.

1.3.2 Partie II : Discrétisation

L'objectif de cette partie du travail a été de développer une méthode numérique adaptée à la simulation diphasique d'écoulements mixtes avec le modèle bicouche compressible présenté au second chapitre. Dans ce contexte, plusieurs défis ont été identifiés. Une première méthode numérique dédiée est développée dans le troisième chapitre. Malgré un comportement attendu pour l'approximation de solutions analytiques de la partie convective du système, les résultats obtenus montrent leurs limites lorsque les configurations physiques d'intérêt sont considérées. Fort des enseignements tirés de cette première tentative, une seconde méthode numérique est proposée dans le quatrième chapitre. Des résultats très prometteurs sont alors obtenus sur des configurations canoniques d'écoulements mixtes en conduite. Ils seront confirmés sur des cas tests de validation présentés dans le sixième chapitre (partie III). Enfin, précisons que le développement de conditions limites pour le modèle proposé n'a pas été abordé dans cette thèse. En effet, étant donnée la structure complexe et non ordonnée du système d'ondes associé, il s'agit d'un problème toujours ouvert. Pour les divers cas tests étudiés, des conditions de type Neumann homogène, mur et périodique ont toutefois été implémentées.

Contexte

Le modèle bicouche compressible (1.8), dénommé CTL pour *Compressible Two-Layer*, appartient à la classe des modèles bifluide bipression dont la discrétisation soulève plusieurs difficultés. D'une part, la partie convective du système est dotée d'une **structure d'ondes complexe** à appréhender pour le développement d'un solveur basé sur la

résolution exacte ou approchée du problème de Riemann. D'autre part, le système complet inclut des **termes sources de relaxation** qui sont en interaction forte avec la partie convective, notamment la relaxation en pression associée à des échelles de temps très courtes. En outre, l'application de ce type de modèle aux écoulements mixtes est originale et engendre des défis supplémentaires :

(i) **Écoulements multi-régime.** Les écoulements mixtes sont principalement caractérisés par deux régimes : le régime stratifié et le régime en charge. Le régime stratifié est piloté par des ondes gravitaires *lentes* dont l'ordre de grandeur de célérité est donné par $\sqrt{gh_1}$, alors que le régime en charge est piloté par des ondes acoustiques *rapides* dont la célérité est donnée par $c_1 = \sqrt{P_1'(\rho_1)}$. En pratique, $c_1 \sim 1500 m.s^{-1}$ et $\frac{\sqrt{gh_1}}{c_1} \ll 1$ pour des hauteurs de conduite réalistes. Parmi les cinq ondes caractéristiques du modèle bicouche compressible données en (1.12), une d'entre elles se propage à vitesse matérielle (*lente*) u_2, alors que les quatre autres se propagent à vitesse acoustique (*rapide*), $u_k \pm c_k, k = 1,2$. Ainsi, l'utilisation de schémas explicites classiques conduit à l'établissement de conditions de stabilité très restrictives sur le pas de temps car basées sur les ondes acoustiques rapides. Cela entraîne une diffusion excessive dans le régime stratifié. Le schéma idéal doit être capable de gérer efficacement les deux régimes en plus des transitions associées.

(ii) **Phases évanescentes dans les régimes en charge et sec.** Au niveau continu, les régimes en charge et sec sont caractérisés par la disparition d'une des deux phases qui se traduit par $h_k = 0, k = 1,2$. Au niveau discret, la dynamique des deux phases est calculée dans tous les régimes. Cela implique la gestion de phases évanescentes, i.e. $h_k \to 0, k = 1,2$, qui soulèvent des problèmes de robustesse avec la plupart des méthodes numériques classiques.

De nombreux travaux de la littérature sont consacrés au développement de méthodes explicites pour la discrétisation des modèles bifluide bipression. On peut citer par exemple [2, 3, 4, 50, 30, 62, 64], avec une attention particulière sur les phases évanescentes dans [25, 26]. Cependant, ces travaux existants ne permettent pas de répondre aux contraintes exposées ci-dessus, notamment (i). Sur ce point, une approche possible est le développement d'une **méthode implicite-explicite** (IMEX) avec pour objectif de traiter explicitement la dynamique *lente* et implicitement la dynamique *rapide*. Ce traitement s'effectue généralement par le biais d'un splitting de flux (le flux du système global est décomposé en plusieurs flux) ou d'un **splitting d'opérateur** (le système global est décomposé en plusieurs sous-systèmes). La stratégie mise en place permet alors de gagner en précision et en efficacité sur la dynamique lente grâce en partie à des conditions de stabilité moins restrictives sur le pas de temps. Des résultats intéressants sont notamment obtenus pour le système d'Euler en régime bas Mach, par exemple dans [19, 29, 31, 41, 43, 52], et un schéma à grand pas de temps pour le système de Baer et Nunziato est proposé dans [18].

Dans ce contexte, deux méthodes numériques originales ont été développées dans cette thèse (Chapitres 3 et 4) en s'appuyant sur une approche IMEX avec splitting d'opérateur. Elles sont vérifiées sur des solutions analytiques manufacturées pour la partie convective du système (1.8). Au regard des applications visées, l'intérêt de la méthode est évalué sur une configuration en régime stratifié (rupture de barrage) et sur une configuration en régime mixte (remplissage d'une conduite). Cette deuxième série de cas tests a permis d'identifier les limites de la première méthode (Chapitre 3), ce qui a conduit au développement de la deuxième approche (Chapitre 4). Dans toute la suite, on considère le système (1.8) avec $M_k = 0$ (écoulement eau-air) et muni des fermetures (1.9), (1.10), (1.11).

Chapitre 3 : Simulation numérique d'un modèle bicouche compressible : une première tentative avec un schéma implicite-explicite

Afin de gagner en précision sur l'approximation de la dynamique lente du modèle bicouche compressible par rapport à l'utilisation d'un schéma numérique explicite classique (item (i)), la méthode proposée dans ce chapitre est basée sur un splitting d'opérateur qui s'appuie sur la structure des ondes (1.12) de la partie convective. Celle-ci est décomposée en deux sous-systèmes **hyperboliques**. En notant $m_k = h_k \rho_k$, le premier sous-système est associé à l'onde matérielle lente se propageant à vitesse u_2 :

$$\begin{cases} \partial_t h_1 + u_2 \partial_x h_1 = 0, \\ \partial_t m_k = 0, \ k = 1,2, \\ \partial_t m_k u_k = 0, \ k = 1,2. \end{cases} \tag{1.13}$$

Le deuxième sous-système est associé aux ondes acoustiques rapides se propageant à vitesse $u_k \pm c_k, k = 1,2$:

$$\begin{cases} \partial_t h_1 = 0, \\ \partial_t m_k + \partial_x m_k u_k = 0, \ k = 1,2, \\ \partial_t m_k u_k + \partial_x m_k u_k^2 + \partial_x h_k P_k - P_I \partial_x h_k = 0, \ k = 1,2. \end{cases} \tag{1.14}$$

Les valeurs propres de (1.13) sont en effet données par $\{u_2, 0\}$ et celles de (1.14) sont données par $\{0, u_1 - c_1, u_1 + c_1, u_2 - c_2, u_2 + c_2\}$. Une interprétation physique de ce splitting peut également être donnée en interprétant h_1 comme un champ de porosité. Ce champ est mis à jour en temps et en espace dans le premier système. Il est ensuite figé dans le deuxième système où les vitesses et les densités sont calculées selon cette « porosité ». Au niveau discret, il s'agit d'une méthode à pas fractionnaires en deux étapes. Dans la première étape associée au système (1.13), le traitement est explicite, dans la deuxième étape associée au système (1.14), le traitement est implicite.

Un schéma explicite upwind classique est utilisé pour la discrétisation de l'équation de transport sur h_1 dans la première étape. Afin de garantir la **positivité des hauteurs**, une condition de stabilité sur le pas de temps (condition CFL) est obtenue, elle fait intervenir uniquement la vitesse matérielle u_2. Le traitement implicite de la deuxième étape consiste à coupler les équations de conservation de masse et de quantité de mouvement afin d'aboutir à une équation semi-discrète vérifiée par la densité ou la pression. Le système matriciel ainsi obtenu est tridiagonal et doté d'une structure de M-matrice qui garantit l'unicité de la solution. La **positivité des densités** de chaque phase est alors assurée par deux conditions CFL supplémentaires qui font elles-aussi intervenir uniquement les vitesses matérielles $u_k, k = 1,2$. Une discrétisation semi-implicite des équations de conservation de quantité de mouvement avec un traitement upwind des flux permet finalement de calculer les vitesses de chaque phase.

L'approche décrite ci-dessus pour la partie convective s'étend au système complet (1.8) en incluant les termes sources dans le premier sous-système qui devient :

$$\begin{cases} \partial_t h_1 + u_2 \partial_x h_1 = \lambda_p (P_I - P_2), \\ \partial_t m_k = 0, \ k = 1,2, \\ \partial_t m_k u_k = (-1)^k \lambda_u (u_1 - u_2), \ k = 1,2. \end{cases} \tag{1.15}$$

Le termes sources de relaxation en pression et en vitesse sont traités implicitement sauf pour le paramètre de relaxation associé qui bénéficie d'un traitement explicite. Sachant que les masses partielles m_k sont constantes dans cette étape, la résolution de l'équation sur h_1 se ramène à une équation discrète non linéaire dont l'**existence et l'unicité de la solution** dans l'intervalle $[0, H]$ sont garanties. De plus, la discrétisation des équations sur les vitesses se ramène à un système 2x2 non-singulier dont la résolution est immédiate. Le second sous-système ainsi que sa résolution sont inchangés.

Afin d'évaluer la méthode numérique ainsi construite, des tests numériques sont effectués sur la partie convective et sur le système complet avec termes sources. Les résultats sont comparés avec ceux donnés par un schéma explicite classique de Rusanov [59]. Les pas de temps de ce dernier sont calculés à partir d'une condition CFL impliquant les vitesses d'ondes acoustiques $u_k \pm c_k, \ k = 1,2$. On parle alors d'un pas de temps *acoustique* par opposition au pas de temps *matériel* du schéma proposé. L'influence de cette définition est évaluée sur ce schéma en présentant les résultats obtenus avec les deux variantes de pas temps (*matériel* et *acoustique*).

Pour la partie convective, deux problèmes de Riemann sont considérés. Le premier implique un choc par phase (pas de couplage entre les phases), le deuxième implique les cinq ondes du système via deux chocs par phase et une discontinuité de contact. Cette dernière correspond à l'onde lente portée par u_2 et couple les phases via un saut sur la variable h_1. Dans les deux cas, le schéma de Rusanov et le schéma proposé sont **stables** et **convergent vers les bonnes solutions de choc**. Le schéma proposé affiche la meilleure précision et la meilleure efficacité, en particulier sur la variable h_1 associée à la dynamique lente du système. Le comportement visé est donc obtenu pour la partie convective du système. En particulier, l'utilisation d'un pas de temps matériel est optimale pour la dynamique lente. Pour la dynamique rapide associée aux ondes de chocs, l'utilisation d'un pas de temps acoustique est plus pertinente, en particulier pour la phase eau qui correspond à la phase la plus rapide.

Pour le système complet avec termes sources, un cas test de type rupture de barrage (*dambreak*) est d'abord considéré. Il est représentatif du régime stratifié où la phase eau est principalement pilotée par des ondes gravitaires. Dans le cadre du modèle bicouche compressible, ces ondes de célérité $\sqrt{gh_1}$ sont difficiles à approcher lorsqu'elles sont *lentes* par rapport à la célérité des ondes acoustiques de la phase eau, c'est à dire lorsque $\frac{M_1}{Fr} = \frac{\sqrt{gH}}{c_1} \ll 1$, où M_1 et Fr font référence respectivement au nombre de Mach et au nombre de Froude pour la phase eau. Ainsi, deux configurations de *dambreak* sont envisagées, $\frac{M_1}{Fr} \sim 7.10^{-3}$ et $\frac{M_1}{Fr} \sim 7.10^{-2}$, qui correspondent respectivement à $H = 10\,m$ et $H = 1000\,m$. Les solutions obtenues pour la phase eau sont comparées à une solution de référence donnée par la solution analytique du système de Saint-Venant [9, 38]. Pour les deux configurations, les solutions obtenues avec l'utilisation d'un pas de temps acoustique sont en accord avec la solution de référence mais sont très diffusées malgré l'utilisation d'un maillage relativement fin. Les solutions obtenues avec un pas de temps matériel s'éloignent de la solution de référence sur maillage équivalent.

Un cas test de remplissage de conduite est enfin considéré afin d'évaluer la capacité du schéma proposé à gérer des passages en charge (item (ii)). En pratique, ce type de configuration n'a pas pu être simulé avec le schéma proposé. En

particulier, le système implicite à résoudre dans la deuxième étape devient singulier lorsque $h_k \to 0$, ce qui complique sa résolution numérique.

Malgré une bonne approximation de l'onde matérielle *lente* de la partie convective du modèle bicouche compressible, cette première tentative de schéma n'apporte pas d'amélioration notable par rapport à un schéma explicite classique quant à l'approximation de solutions pilotées par des ondes gravitaires *lentes* (i.e. telles que $\frac{\sqrt{gh_1}}{c_1} \ll 1$). De plus, il souffre d'un manque de robustesse dans les régimes en charge et sec. Suite à ces premiers résultats riches d'enseignements, une deuxième approche est développée dans le Chapitre 4 afin de mieux capturer la dynamique gravitaire (item (i)) tout en garantissant plus de robustesse dans les régimes en charge et sec (item (ii)).

Chapitre 4 : Une méthode à pas fractionnaires adaptée à la simulation diphasique d'écoulements mixtes avec un modèle bicouche compressible

Dans ce chapitre, une seconde méthode numérique originale est développée dans le but de simuler des écoulements mixtes en conduite avec le modèle bicouche compressible proposé au Chapitre 2. Les premiers résultats du Chapitre 3 ont permis d'illustrer les difficultés liées à l'approximation des ondes gravitaires lentes (i.e. telles que $\frac{\sqrt{gh_1}}{c_1} \ll 1$) qui pilotent le régime stratifié. En s'appuyant sur ce constat, un splitting d'opérateur guidé par la **dynamique gravitaire** du système est proposé. En effet, la fermeture utilisée pour la pression d'interface P_I (1.9) permet d'obtenir une réécriture de l'équation de conservation de quantité de mouvement pour la phase eau faisant intervenir un gradient hydrostatique. Cette reformulation présente une proximité forte avec les équations de Saint-Venant où la pression *atmosphérique* serait variable en espace [1]. En tenant compte de la **relaxation rapide en pression**, cette pression *atmosphérique* peut s'interpréter comme la pression de l'air dans notre contexte. Une décomposition du système complet en trois sous-systèmes est alors envisagée. Le premier sous-système concerne les termes de transport à vitesse matérielle, le gradient hydrostatique pour la phase eau et le terme source de relaxation en pression :

$$\begin{cases} \partial_t h_1 + u_2 \partial_x h_1 = \lambda_p (P_I - P_2), \\ \partial_t m_k + \partial_x m_k u_k = 0, \ k = 1,2, \\ \partial_t m_1 u_1 + \partial_x m_1 u_1^2 + \partial_x \rho_1 g \dfrac{h_1^2}{2} = 0, \\ \partial_t m_2 u_2 + \partial_x m_2 u_2^2 = 0. \end{cases} \tag{1.16}$$

Le second sous-système contient la dynamique rapide correspondant aux gradients de pression :

$$\begin{cases} \partial_t h_1 = 0, \\ \partial_t m_k = 0, \ k = 1,2, \\ \partial_t m_1 u_1 + h_1 \partial_x P_I = 0, \\ \partial_t m_2 u_2 + h_2 \partial_x P_2 + (P_2 - P_I) \partial_x h_2 = 0, \end{cases} \tag{1.17}$$

Dans ce sous-système, les termes $h_1 \partial_x P_I$ et $(P_2 - P_I)\partial_x h_2$ bénéficient directement de la relaxation en pression résolue dans le premier sous-système. Enfin, la relaxation en vitesse est résolue dans un dernier sous-système :

$$\begin{cases} \partial_t h_1 = 0, \\ \partial_t m_k = 0, \ k = 1,2, \\ \partial_t m_k u_k = (-1)^k \lambda_u (u_1 - u_2), \ k = 1,2. \end{cases} \tag{1.18}$$

Les deux premiers sous-systèmes (1.16) et (1.17) sont **hyperboliques dégénérés**. Leurs spectres sont donnés respectivement par $\{u_2, u_1 \pm \sqrt{g \frac{h_1}{2}}\}$ et $\{0\}$. Au niveau discret, il s'agit d'une méthode à pas fractionnaires en trois étapes pour laquelle on développe une discrétisation implicite-explicite en temps, explicite pour (1.16) et implicite pour (1.17) et (1.18).

La partie convective de (1.16) est discrétisée en utilisant un schéma explicite avec des flux de Rusanov [59]. Concernant l'équation de transport sur h_1, le terme source est traité implicitement (excepté le paramètre λ_p), ce qui conduit à une équation discrète non linéaire dont **l'existence et l'unicité de la solution** dans l'intervalle $[0, H]$ sont acquises. Afin de garantir la **positivité des hauteurs et des densités**, une condition de stabilité sur le pas de temps (condition CFL) est obtenue, elle est basée sur la vitesse matérielle de chaque phase et sur la célérité d'ondes gravitaires.

La discrétisation de (1.17) est moins classique dans la mesure où le spectre du système est réduit à la valeur propre nulle. Une **approche par relaxation** est proposée. Elle consiste à considérer un système étendu plus facile

à résoudre et qui dégénère vers le système initial [24]. Dans ce cadre, deux variables supplémentaires, appelées variables de relaxation, sont introduites. Elles relaxent vers les pressions de chaque phase en vérifiant chacune une équation inspirée de l'équation vérifiée par la pression dans le système non découpé. Le système à sept équations obtenu est **strictement hyperbolique**. Une discrétisation semi-implicite de ce système permet alors de se ramener à un système à deux équations discrétisées en temps s'identifiant aux équations vérifiées par la vitesse de chaque phase dans le système initial (1.17). L'approche par relaxation s'y traduit par l'obtention d'un terme de diffusion pondéré par un paramètre de relaxation qu'il s'agit de définir pour assurer la stabilité du schéma. En particulier, on utilise la condition dite de Whitham qui permet d'assurer la stabilité de la propagation des ondes acoustiques. Cette condition est appliquée pour la phase air mais concernant la phase eau, elle est appliquée uniquement pour le régime en charge. En effet, le terme $h_1 \partial_x P_I$, couplé à la relaxation rapide en pression, est traité comme un terme source en régime stratifié prenant en compte les variations de pression dans la phase air. Une **stabilisation adaptée au régime d'écoulement** est donc proposée. Les systèmes implicites à résoudre sont tri-diagonaux et sont dotés d'une structure de M-matrice qui garantit l'unicité de la solution. De plus, ces derniers ne sont pas singuliers lorsque $h_k \to 0$, contrairement à la partie implicite du schéma présenté au Chapitre 3. Cette étape ne nécessite pas de condition CFL supplémentaire.

Les termes de relaxation en vitesse du système (1.18) sont traités implicitement (excepté le paramètre λ_u) comme dans le Chapitre 3. En couplant les équations vérifiées par chaque phase, on se ramène à la résolution d'un système 2x2 non-singulier dont la résolution est immédiate.

La stratégie globale décrite ci-dessus a pour objectif de répondre efficacement aux problématiques des écoulements multi-régime (item (i)) et des phases évanescentes (item (ii)). La problématique (i) est traitée en tenant compte explicitement du gradient hydrostatique dans la phase eau et en proposant une stabilisation du schéma adaptée au régime d'écoulement. De plus, le caractère rapide de la relaxation en pression et son interaction avec la partie convective sont pris en compte. La problématique (ii) est traitée en étudiant le comportement du schéma lorsque $h_k \to 0$ et en s'assurant notamment de la robustesse de la partie implicite. Une attention particulière est également portée sur la préservation des phénomènes de relaxation (pression et vitesse) au niveau discret car ils correspondent à des phénomènes dissipatifs qui renforcent la robustesse de la méthode dans les régimes en charge et sec.

Des tests numériques sont effectués sur la partie convective et sur le système complet avec termes sources. Comme dans le chapitre précédent, les résultats sont comparés avec ceux donnés par un schéma explicite classique de Rusanov [59]. Pour la partie convective, un problème de Riemann impliquant les 5 ondes du système est considéré. Le schéma proposé est **stable** et **converge vers les bonnes solutions de choc**. Comme attendu, il est beaucoup plus précis et plus efficace qu'un schéma de Rusanov pour l'approximation de l'onde lente du système. L'approximation des ondes rapides est également satisfaisante, notamment en réduisant le nombre CFL tout en restant intéressant en terme d'efficacité. Sur ce cas, les tendances obtenues sont très similaires à celles obtenues avec la méthode proposée au Chapitre 3.

Un cas test de type rupture de barrage (dambreak) est ensuite considéré pour le système complet. Il permet notamment d'évaluer la pertinence du schéma pour l'approximation d'un régime stratifié piloté par la gravité. Contrairement au schéma développé au Chapitre 3, la nouvelle approche, dénommée SPR dans la suite, reproduit un comportement très proche de la solution de référence donnée par la solution analytique des équations de Saint-Venant, cf. figure 1.6 où $\frac{M_1}{Fr} \sim 7.10^{-3}$. De plus, le gain en efficacité est très important par rapport à la méthode de Rusanov (1 s contre 150 s de temps CPU pour les résultats de la figure 1.6). Enfin, la **stabilité** du schéma SPR en régime stratifié est vérifiée sur ce cas test.

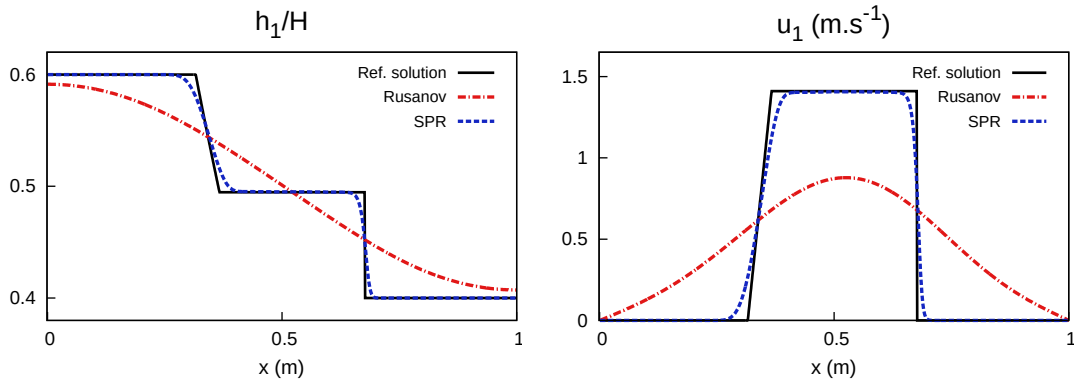

Figure 1.6: Hauteur et vitesse de la phase eau pour le cas *dambreak* à $T = 24.10^{-2}\,s$ avec 1000 cellules.

La **robustesse** du schéma dans les régimes en charge et sec est évaluée dans une dernière section. Trois configurations mettant en jeu des transitions entre régimes sont considérées : un *dambreak* en charge (transition de régime en charge vers stratifié), le remplissage d'une conduite (transition de régime stratifié vers charge) et la vidange d'une conduite (transition de régime stratifié vers sec). Ils permettent de mieux appréhender la stabilisation multi-régime du schéma et d'illustrer l'importance de la dissipation apportée par les termes sources de relaxation en cas de phases évanescentes. Les résultats obtenus sont très prometteurs et permettent d'envisager la validation du modèle bicouche compressible pour la simulation diphasique d'écoulements mixtes en conduite au Chapitre 6. Auparavant, une étude de stabilité linéaire est menée dans le Chapitre 5.

Chapitre 5 : Analyse de stabilité linéaire du schéma SPR

On s'intéresse dans ce chapitre à la stabilité du schéma SPR présenté au Chapitre 4. L'étude de la stabilité d'un schéma dans le cadre non-linéaire soulève généralement beaucoup de difficultés et s'appuie principalement sur deux objectifs : la conservation de domaines invariants (la positivité de grandeurs physiques par exemple) et l'obtention d'une inégalité d'entropie discrète [10]. Le premier point est assuré par le schéma SPR qui garantit la positivité des hauteurs et des densités par une condition CFL basée sur la vitesse matérielle de chaque phase et sur la célérité d'ondes gravitaires. Le deuxième point n'est *à priori* pas vérifié par le schéma, notamment en raison de la décomposition proposée. Cependant, sa stabilité est contrôlée empiriquement par raffinement du maillage et comparaison avec des solutions analytiques ou de référence. Dans cette approche, la seule contrainte sur le nombre CFL correspondant, dit *matériel*, est d'être inférieur à l'unité (ci-après, le nombre CFL mentionné désigne le nombre CFL *matériel*). En pratique, certaines configurations de *dambreak* conduisent à l'apparition d'instabilités lorsque ce nombre CFL est typiquement pris égal à $\frac{1}{2}$. Afin de caractériser cette condition sur le nombre CFL, une étude de stabilité linéaire est menée. Elle est orientée par des travaux récents [61, 72] qui s'intéressent spécifiquement à la stabilité des schémas IMEX. Dans un cadre linéaire, ces travaux montrent que les étapes explicite et implicite d'un schéma IMEX peuvent être individuellement stables sans pour autant garantir la stabilité du schéma global. Le couplage entre les deux parties peut en effet conduire à des conditions de stabilité supplémentaires sur le nombre CFL.

L'étude de stabilité linéaire est conduite au niveau discret en utilisant l'approche de Von Neumann [20, 27]. Elle consiste à décomposer la solution discrète en modes de Fourier et analyser la stabilité de ces modes. En pratique, les trois étapes du schéma SPR sont linéarisées autour d'un état constant et le schéma global est réécrit sous forme matricielle. Cette matrice fait notamment intervenir l'état initial, le nombre d'onde et le nombre CFL. Pour un état initial donné et pour une série de nombres d'ondes, on cherche alors le plus grand nombre CFL garantissant un rayon spectral inférieur à 1. En raison de la complexité de la matrice 5x5 obtenue, cette recherche s'effectue numériquement.

Une série de tests est effectuée sur la version dimensionnée du système en choisissant un état initial source d'instabilités. Les tests sont conduits pour plusieurs hauteurs de conduite H et les corrélations obtenues entre les observations et l'étude de stabilité linéaire sont très satisfaisantes. Plus la hauteur de conduite H est petite, plus le nombre CFL doit être petit pour garantir la stabilité. Afin de mieux caractériser cette dépendance, l'étude est reconduite sur une version adimensionnée du modèle bicouche compressible. Le paramètre d'influence est alors donné par $\frac{M_1}{Fr} = \frac{\sqrt{gH}}{c_1}$. En particulier, le nombre CFL garantissant la stabilité est une fonction croissante de $\frac{\sqrt{gH}}{c_1}$. Par exemple, pour des applications pratiques où $0.1\,m \leq H \leq 10\,m$, le nombre CFL noté ν doit vérifier $0.086 \leq \nu \leq 0.67$. Cette contrainte supplémentaire permet toutefois d'obtenir des pas de temps plus grands par rapport à ceux requis par un schéma totalement explicite.

1.3.3 Partie III : Validation

Chapitre 6 : Simulations d'écoulements mixtes et de poches d'air piégées en conduite avec un modèle bicouche compressible

Ce dernier chapitre se consacre à la validation du modèle bicouche compressible proposé au Chapitre 2 sur des configurations représentatives d'écoulements mixtes en conduite en utilisant le schéma développé au Chapitre 4. Trois cas tests sont considérés. En particulier, une **validation expérimentale** est proposée ainsi qu'une configuration impliquant l'influence de **poches d'air piégées**.

Le premier cas test correspond au remplissage d'une conduite inclinée. Il s'agit d'une configuration caractéristique d'un écoulement mixte qui implique des transitions entre le régime stratifié et les régimes en charge ou sec. La présence de l'air n'a pas d'influence ici. Dans un premier temps, une étude de sensibilité au maillage est menée. Les champs de hauteur et de vitesse convergent rapidement alors que le champ de pression de la phase eau présente des oscillations non désirées dans la partie en charge. Ces oscillations sont couramment rencontrées avec les modèles

d'écoulements mixtes de la littérature [69]. Elles sont associées à la transition brutale en terme de célérité d'ondes entre la partie stratifiée et la partie en charge, qui se traduit par un rapport $\frac{\sqrt{gH}}{c_1} \ll 1$, où H est la hauteur de conduite et c_1 la célérité des ondes acoustiques dans l'eau. Une stratégie fréquemment utilisée consiste alors à prendre une célérité c_1 plus faible, i.e. $c_1 < 1500 m.s^{-1}$. Dans notre cas avec $c_1 = 1500 m.s^{-1}$, les oscillations disparaissent lorsque le maillage est raffiné. En prenant $c_1 = 200 m.s^{-1}$, qui reste une célérité *physiquement* admissible lorsque l'on tient compte de l'élasticité de la conduite et de la présence d'air dans l'eau, elles sont d'autant plus atténuées sur les maillages grossiers. Concernant ce champ de pression, on obtient le bon équilibre entre son gradient et la gravité ainsi qu'une bonne approximation du choc relatif à la transition entre les régimes. De plus, la période des ondes acoustiques se propageant dans la partie en charge est précisément captée. La robustesse du schéma est également illustrée sur ce cas où le taux de présence d'air en charge atteint 10^{-9} sur le maillage le plus fin. Dans un second temps, les résultats sont comparés avec ceux donnés par un modèle validé d'écoulements mixtes monophasiques, le modèle PFS [13] qui couple les équations de Saint-Venant à surface libre avec les équations d'Euler compressible moyennées en charge. Les comparaisons sont concluantes. En particulier, sur maillage fin à célérité donnée ($c_1 = 200 m.s^{-1}$), le modèle bicouche compressible ne présente pas d'oscillations parasites contrairement au modèle PFS. La dissipation apportée par les termes sources de relaxation semble en effet apporter plus de stabilité et de robustesse. En ce sens, la simulation de phase air est profitable. Enfin, les temps de calcul sont comparables même si la diminution de la célérité c_1 est avantageuse pour le modèle PFS qui est associé à un schéma explicite.

Une validation expérimentale est présentée dans le second cas test. Il s'agit d'une configuration récemment proposée dans [7] spécifiquement pour la validation de modèles d'écoulements mixtes. Une conduite circulaire en forme de 'V' est considérée avec une masse d'eau initialement retenue en amont par une vanne. Lorsque cette vanne est ouverte, la masse d'eau se propage dans la partie de conduite initialement vide en décrivant des mouvements de ballottements qui s'accompagnent de transitions entre les régimes stratifiés et en charge. Il y a des zones sèches à tout instant et des évents sont présents dans le dispositif expérimental afin de minimiser l'influence de l'air. Des mesures de vitesse et de pression sont effectuées le long de la conduite. De par les dimensions réalistes de la conduite ($19.2 cm$ de diamètre et $12.12 m$ de longueur), les multiples transitions et le caractère hautement transitoire de l'écoulement, il s'agit d'un cas discriminant pour la validation de modèles. En utilisant un maillage grossier de 300 cellules, les résultats obtenus avec le modèle bicouche compressible sont très satisfaisants. En particulier, les transitions entre les régimes sont correctement prédites ainsi que les niveaux de pression en charge et les niveaux de vitesse. Le temps de calcul est également compétitif (25 minutes pour 30 secondes de simulation). Enfin, la robustesse du modèle et du schéma vis à vis des valeurs attribuées à la célérité c_1 des ondes acoustiques dans l'eau est illustrée. En effet, les résultats présentés correspondent à des ordres de grandeur *physiquement* admissibles ($c_1 = 300 m.s^{-1}$ et $c_1 = 1500 m.s^{-1}$) alors que les résultats proposés dans l'article [7] avec les modèles de la fente de Preissmann [28] et PFS [13] nécessitent l'utilisation de célérités plus *faibles*, typiquement $c_1 = 12 m.s^{-1}$, sous peine d'obtenir des oscillations parasites importantes lors des passages en charge.

Le dernier cas test aborde la problématique des poches d'air piégées. On considère ainsi une conduite décrivant une forme de 'U' fermée aux extrémités et remplie partiellement dans chaque branche. Un manomètre oscillant est obtenu dont la dynamique dépend du niveau de pressurisation des poches d'air piégées aux extrémités. Ce cas peut également être conduit sans influence de l'air en ouvrant la conduite, comme proposé par Ransom dans [57]. Afin de valider les résultats numériques en configuration fermée (et ouverte), on développe une solution de référence donnant l'évolution temporelle de la pression des poches d'air et du niveau d'eau. Plusieurs configurations mettant en jeu des niveaux de pressurisation différents sont alors considérés et les résultats obtenus avec le modèle bicouche compressible sont très satisfaisants. En particulier, la période du phénomène ainsi que les amplitudes sont bien captées, comme illustré sur la figure 1.7 par exemple. La configuration ouverte sans influence de l'air est également correctement simulée. Ce cas test permet d'illustrer l'importance de l'influence des poches d'air piégées sur la dynamique de l'écoulement. En effet, selon le niveau de pressurisation, la période et les amplitudes caractéristiques peuvent être radicalement différentes. Le modèle bicouche compressible est capable de rendre compte de ces différences qui résultent de fortes interactions entre la phase eau et la phase air.

Ces trois cas tests accompagnés des résultats obtenus permettent de valider le modèle bicouche compressible sur des configurations d'écoulements mixtes monophasiques et diphasiques. Le modèle proposé constitue ainsi une contribution originale. Contrairement aux modèles disponibles dans la littérature, sa formulation n'impose aucune restriction quant à la gestion de configurations diphasiques plus complexes telles que le transport forcé ou la coalescence de poches d'air, ou encore le transfert de masse entre phases liquide et vapeur. Cette étape de validation supplémentaire, de même que le développement de conditions limites adaptées, comptent parmi les perspectives premières de ces travaux.

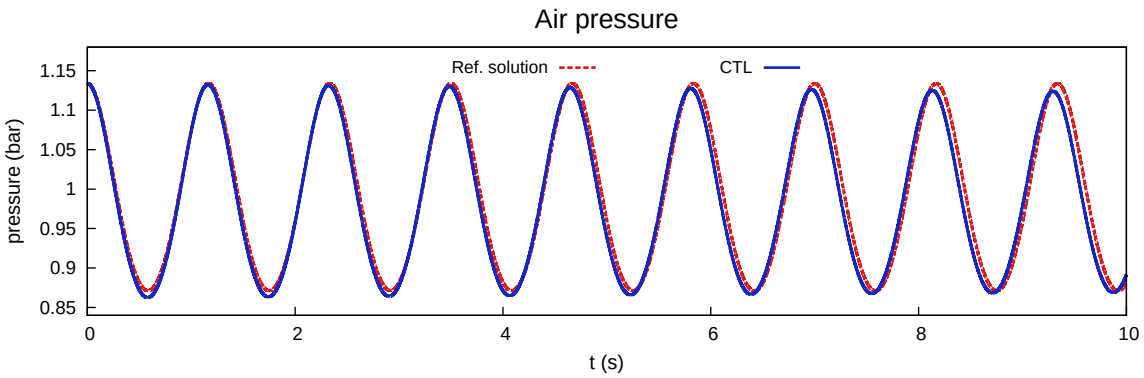

Figure 1.7: Évolution temporelle de la pression d'une poche d'air piégée pour un cas de tube en U fermé.

1.3.4 Valorisation des travaux

Les travaux effectués dans cette thèse ont fait l'objet des éléments de valorisation suivants :

- Les travaux du Chapitre 2 ont été acceptés pour publication dans la revue *Continuum Mechanics and Thermodynamics* dont la référence est :

  - C. Demay and J.-M. Hérard. A compressible two-layer model for transient gas-liquid flows in pipes, *Continuum Mechanics and Thermodynamics*, 29(2):385-410, 2017.

  Ils ont été présentés au congrès international *WONAPDE 2016* (Concepción, Chili, janvier 2016) ainsi qu'aux Groupes de Recherche (GdR) *FILMS* (Aussois, France, décembre 2015) et *EGRIN* (Piriac-sur-mer, France, mai 2016).

- Les travaux du Chapitre 3 ont été soumis dans une revue internationale avec comité de lecture. Ils ont également été déposé sur HAL sous la référence :

  - C. Demay, C. Bourdarias, B. de Laage de Meux, S. Gerbi, and J.-M. Hérard. Numerical simulation of a compressible two-layer model: a first attempt with an implicit-explicit splitting scheme, *Preprint*. URL: https://hal.archives-ouvertes.fr/hal-01421889.

  Ils ont été présentés au congrès international *ECCOMAS 2016* (Hersonissos, Grèce, mai 2016).

- Les travaux du Chapitre 4, accompagnés des résultats du Chapitre 6, font l'objet d'un article en préparation pour soumission dans une revue internationale avec comité de lecture. Une version partielle a été publiée sous forme d'un proceeding dont la référence est :

  - C. Demay, C. Bourdarias, B. de Laage de Meux, S. Gerbi, and J.-M. Hérard. A fractional step method to simulate mixed flows in pipes with a compressible two-layer model, *Springer Proceedings in Mathematics and Statistics*, 200:33-41, 2017.

  Ils ont été présentés au congrès international *FVCA VIII* (Lille, France, juin 2017) ainsi qu'au GdR *EGRIN* (Cargèse, France, mai 2017).

Références

[1] V.I. Agoshkov, D. Ambrosi, V. Pennati, A. Quarteroni, and F. Saleri. Mathematical and numerical modelling of shallow water flow. *Computational Mechanics*, 11(5):280–299, 1993.

[2] A. Ambroso, C. Chalons, F. Coquel, and T. Galié. Relaxation and numerical approximation of a two-fluid two-pressure diphasic model. *ESAIM: Mathematical Modelling and Numerical Analysis*, 43(6):1063–1097, 2009.

[3] A. Ambroso, C. Chalons, and P.-A. Raviart. A Godunov-type method for the seven-equation model of compressible two-phase flow. *Computers & Fluids*, 54:67–91, 2012.

[4] A. Andrianov and G. Warnecke. The Riemann problem for the Baer-Nunziato two-phase flow model. *Journal of Computational Physics*, 195(2):434–464, 2004.

[5] K. Arai and K. Yamamoto. Transient analysis of mixed free- surface-pressurized flows with modified slot model (part 1: Computational model and experiment). *Proc. FEDSM03 4th ASME-JSME Joint Fluids Engineering Conf.*, pages 2907–2913, 2003.

[6] E. Audusse. A multilayer Saint-Venant system : Derivation and numerical validation. *Discrete Contin. Dyn. Syst. Ser. 5*, 5(2):189–214, 2005.

[7] F. Aureli, A. Dazzi, A. Maranzoni, and P. Mignosa. Validation of single- and two-equation models for transient mixed flows: a laboratory test case. *Journal of Hydraulic Research*, 53(4):440–451, 2015.

[8] M. R. Baer and J. W. Nunziato. A two phase mixture theory for the deflagration to detonation (DDT) transition in reactive granular materials. *International Journal of Multiphase Flow*, 12(6):861–889, 1986.

[9] A.J.C. Barré de Saint Venant. Théorie du mouvement non-permanent des eaux avec application aux crues des rivières et à l'introduction des marées dans leur lit. *C.R. Acad. Sc. Paris.*, 73:147–154, 1871.

[10] F. Bouchut. *Nonlinear stability of finite volume methods for hyperbolic conservation laws, and well-balanced schemes for sources*. Birkhauser, 2004.

[11] C. Bourdarias, M. Ersoy, and S. Gerbi. A mathematical model for unsteady mixed flows in closed water pipes. *Science China Mathematics*, 55(2):221–244, 2012.

[12] C. Bourdarias, M. Ersoy, and S. Gerbi. Air entrainment in transient flows in closed water pipes : a two-layer approach. *ESAIM: Mathematical Modelling and Numerical Analysis*, 47(2):507–538, 2013.

[13] C. Bourdarias and S. Gerbi. A finite volume scheme for a model coupling free surface and pressurised flows in pipes. *Journal of Computational and Applied Mathematics*, 209:1–47, 2007.

[14] S. Bousso, M. Daynou, and M. Fuamba. Numerical modeling of mixed flows in storm water systems: Critical review of literature. *Journal of Hydraulic Engineering*, 139(4):385–396, 2013.

[15] C. Brennen. *Fundamentals of Multiphase Flows*. Cambridge University Press, 2005.

[16] H. Capart, X. Sillen, and Y. Zech. Numerical and experimental water transients in sewer pipes. *Journal of Hydraulic Research*, 35(5):659–672, 1997.

[17] J.A. Cardle, C.C.S. Song, and M. Yuan. Measures of mixed transient flows. *Journal of Hydraulic Engineering*, 115(2):169–182, 1989.

[18] C. Chalons, F. Coquel, S. Kokh, and N. Spillane. Large time-step numerical scheme for the seven-equation model of compressible two-phase flows. *Springer Proceedings in Mathematics and Statistics*, 4:225–233, 2011.

[19] C. Chalons, M. Girardin, and S. Kokh. Large time-step and asymptotic preserving numerical schemes for the gas dynamics equations with source terms. *SIAM Journal on Scientific Computing*, 35(6):a2874–a2902, 2013.

[20] J.-G. Charney, R. Fjörtoft, and J. Von Neumann. Numerical integration of the barotropic vorticity equation. *Tellus*, 2:237–254, 1950.

[21] M.H. Chaudhry, S.M. Bhallamudi, C.S. Martin, and M. Naghash. Analysis of transient pressures in bubbly, homogeneous, gas-liquid mixtures. *Journal of Fluids Engineering*, 112(2):225–231, 1990.

[22] A. Chinnayya, E. Daniel, and R. Saurel. Modelling detonation waves in heterogeneous energetic materials. *Journal of Computational Physics*, 196(2):490–538, 2004.

[23] F. Coquel, T. Gallouët, J.-M. Hérard, and N. Seguin. Closure laws for a two-fluid two-pressure model. *C. R. Acad. Sci. Paris*, 334(I):927–932, 2002.

[24] F. Coquel, E. Godlewski, and N. Seguin. Relaxation of fluid systems. *Mathematical Models and Methods in Applied Sciences*, 22(8), 2012.

[25] F. Coquel, J.-M. Hérard, and K. Saleh. A positive and entropy-satisfying finite volume scheme for the Baer-Nunziato model. *Journal of Computational Physics*, 330:401–435, 2017.

[26] F. Coquel, J.-M. Hérard, K. Saleh, and N. Seguin. A robust entropy-satisfying finite volume scheme for the isentropic Baer-Nunziato model. *ESAIM: Mathematical Modelling and Numerical Analysis*, 48:165–206, 2013.

[27] J. Crank and P. Nicolson. A practical method for numerical evaluation of solutions of partial differential equations of the heat-conduction type. *Mathematical Proceedings of the Cambridge Philosophical Society*, 43:50–67, 1947.

[28] J.-A. Cunge and M. Wegner. Numerical integration of barré de Saint-Venant's flow equations by means of an implicit scheme of finite differences. *La Houille Blanche*, 1:33–39, 1964.

[29] P. Degond and M. Tang. All speed scheme for the low Mach number limit of the isentropic Euler equation. *Communications in Computational Physics*, 10:1–31, 2011.

[30] V. Deledicque and M.V. Papalexandris. An exact Riemann solver for compressible two-phase flow models containing non-conservative products. *Journal of Computational Physics*, 222(1):217–245, 2007.

[31] G. Dimarco, R. Loubère, and M.-H. Vignal. Study of a new asymptotic preserving scheme for the Euler system in the low Mach number limit. *Preprint*, 2016. URL: `https://hal.archives-ouvertes.fr/hal-01297238`.

[32] M. Escarameia. Investigating hydraulic removal of air from water pipelines. *Proceedings of the Institution of Civil Engineers-Water Management.*, 160(1):25–34, 2007.

[33] I. Faille and E. Heintze. A rough finite volume scheme for modeling two-phase flow in a pipeline. *Computers & Fluids*, 28(2):213–241, 1999.

[34] M. Fuamba. Contribution on transient flow modelling in storm sewers. *Journal of Hydraulic Research*, 40(6):685–693, 2002.

[35] T. Gallouët, J.-M. Hérard, and N. Seguin. Numerical modeling of two-phase flows using the two-fluid two-pressure approach. *Mathematical Models and Methods in Applied Sciences*, 14(05):663–700, 2004.

[36] P. Garcia-Navarro, F. Alcrudo, and A. Priestley. An implicit method for water flow modelling in channels and pipes. *Journal of Hydraulic Research*, 32(5):721–742, 1994.

[37] S.L. Gavrilyuk and R. Saurel. Mathematical and numerical modeling of two-phase compressible flows with micro-inertia. *Journal of Computational Physics*, 175(1):326–360, 2002.

[38] J.-F. Gerbeau and B. Perthame. Derivation of viscous Saint-Venant system for laminar shallow water; numerical validation. *Discrete Contin. Dyn. Syst. Ser. B*, 1:89–102, 2001.

[39] J. Glimm, D. Saltz, and D. H. Sharp. Two phase flow modelling of a fluid mixing layer. *Journal of Fluid Mechanics*, 378:119–143, 1999.

[40] E. Godlewski, M. Parisot, J. Saint-Marie, and F. Wahl. Congested shallow water type model: roof modelling in free surface flow. *Preprint*, 2017. URL: `https://hal.archives-ouvertes.fr/hal-01368075v2`.

[41] J. Haack, S. Jin, and J.G. Liu. An all-speed asymptotic preserving method for the isentropic Euler and navier-stokes equations. *Communications in Computational Physics*, 12:955–980, 2012.

[42] M.A. Hamam and J.A. McCorquodale. Transient conditions in the transition from gravity to surcharged sewer flow. *Canadian Journal of Civil Engineering*, 9(2):189–196, 1982.

[43] D. Iampietro, F. Daude, P. Galon, and J.-M. Hérard. A Mach-sensitive implicit-explicit scheme adapted to compressible multi-scale flows. *Preprint*, 2017. URL: `https://hal.archives-ouvertes.fr/hal-01531306`.

[44] R.I. Issa and M.H.W. Kempf. Simulation of slug flow in horizontal and nearly horizontal pipes with the two-fluid model. *International Journal of Multiphase Flow*, 29:69–95, 2003.

[45] A. K. Kapila, S. F. Son, J. B. Bdzil, R. Menikoff, and D. S. Stewart. Two-phase modeling of DDT: Structure of the velocity-relaxation zone. *Physics of Fluids*, 9(12):3885–3897, 1997.

[46] F. Kerger. *Modelling transient air-water flows in civil and environmental engineering*. PhD thesis, University of Liège, Liège, Belgium, 2010.

[47] F. Kerger, P. Archambeau, Erpicum S., B.J. Dewals, and M. Pirotton. An exact Riemann solver and a Godunov scheme for simulating highly transient mixed flows. *Journal of Computational and Applied Mathematics*, 235(8):2030–2040, 2011.

[48] J. Li and J.A. McCorquodale. Modeling mixed flow in storm sewers. *Journal of Hydraulic Engineering*, 125(11):1170–1180, 1999.

[49] H. Lochon, F. Daude, P. Galon, and J.-M. Hérard. Comparison of two-fluid models on steam-water transients. *ESAIM: Mathematical Modelling and Numerical Analysis*, 50(6):1631–1657, 2016.

[50] H. Lochon, F. Daude, P. Galon, and J.-M. Hérard. HLLC-type Riemann solver with approximated two-phase contact for the computation of the Baer-Nunziato two-fluid model. *Journal of Computational Physics*, 326:733–762, 2016.

[51] A.S. Léon, M.S. Ghidaoui, A.R. Schmidt, and M.H. Garcia. A robust two-equation model for transient-mixed flows. *Journal of Hydraulic Research*, 48(1):44–56, 2010.

[52] S. Noelle, G. Bispen, K. Arun, M. Lukacova-Medvidova, and C.D. Munz. A weakly asymptotic preserving all Mach number scheme for the Euler equations of gas dynamics. *SIAM Journal on Scientific Computing*, 36:B989–B1024, 2014.

[53] I.W.M. Pothof and F.H.L.R. Clemens. Experimental study of air-water flow in downward sloping pipes. *International Journal of Multiphase Flow*, 37(3):278–292, 2011.

[54] O Pozos, C. Gonzalez, J. Giesecke, W. Marx, and E. Rodal. Air entrapped in gravity pipeline systems. *Journal of Hydraulic Research*, 48(3):338–347, 2010.

[55] A. Preissmann and J.A. Cunge. Calcul des intumescences sur machines électroniques. *IX^e Assemblée Générale de l'A.I.R.H.*, Dubrovnik, 1961.

[56] L. Ramezani, B. Karney, and A. Malekpour. Encouraging effective air management in water pipelines: A critical review. *Journal of Water Resources Planning and Management*, 142(12), 2016.

[57] V. H. Ransom. Numerical benchmark test no. 2.2: Oscillating manometer. *Multiphase Science and Technology*, 3:468–470, 1987.

[58] V. H. Ransom and D. L. Hicks. Hyperbolic two-pressure models for two-phase flow. *Journal of Computational Physics*, 53:124–151, 1984.

[59] V. V. Rusanov. Calculation of interaction of non-steady shock waves with obstacles. *Zh. Vychisl. Mat. Mat. Fiz.*, 1(2):267–279, 1961.

[60] R. Saurel and R. Abgrall. A simple method for compressible multifluid flows. *SIAM Journal on Scientific Computing*, 21(3):1115–1145, 1999.

[61] J. Schütz and S. Noelle. Flux splitting for stiff equations: A notion on stability. *SIAM Journal on Scientific Computing*, 64:522–540, 2015.

[62] D. W. Schwendeman, C. W. Wahle, and A. K. Kapila. The Riemann problem and a high-resolution Godunov method for a model of compressible two-phase flow. *Journal of Computational Physics*, 212(2):490–526, 2006.

[63] C. Song, J. Cardle, and K. Leung. Transient mixed-flow models for storm sewers. *Journal of Hydraulic Engineering*, 109(11):1487–1504, 1983.

[64] S.-A. Tokareva and E.-F. Toro. HLLC-type Riemann solver for the Baer-Nunziato equations of compressible two-phase flow. *Journal of Computational Physics*, 229(10):3573–3604, 2010.

[65] B. Trajkovic, M. Ivetic, F. Calomino, and A. D'Ippolito. Investigation of transition from free surface to pressurized flow in a circular pipe. *Water science and technology*, 39(9):105–112, 1999.

[66] B.C. Trindade. Air pocket modeling in water mains with an air valve. Master's thesis, Auburn University, 2012.

[67] B.C. Trindade and J.G. Vasconcelos. Modeling of water pipeline filling events accounting for air phase interactions. *Journal of Hydraulic Engineering*, 139(9):921–934, 2013.

[68] J.G. Vasconcelos, S.J. Wright, and P.L. Roe. Improved simulation of flow regime transition in sewers: Two-component pressure approach. *Journal of Hydraulic Engineering*, 132(6):553–562, 2006.

[69] J.G. Vasconcelos, S.J. Wright, and P.L. Roe. Numerical oscillations in pipe-filling bore predictions by shock-capturing models. *Journal of Hydraulic Engineering*, 135(4):296–305, 2009.

[70] D.C. Wiggert. Transient flow in free surface, pressurized systems. *Journal of the Hydraulics Division*, 98(1):11–27, 1972.

[71] B.E. Wylie and V.L. Streeter. *Fluid transients in systems*. McGraw-Hill, 1993.

[72] H. Zakerzadeh and S. Noelle. A note on the stability of implicit-explicit flux splittings for stiff hyperbolic systems. *IGPM report 449*, 2016.

[73] F. Zhou, F. E. Hicks, and P. M. Steffler. Transient flow in a rapidly filling horizontal pipe containing trapped air. *Journal of Hydraulic Engineering*, 128(3):625–634, 2002.

Chapter 2

A compressible two-layer model for transient gas-liquid flows in pipes

Abstract: This work is dedicated to the modelling of gas-liquid flows in pipes. As a first step, a new two-layer model is proposed to deal with the stratified regime. The starting point is the isentropic Euler set of equations for each phase where the classical hydrostatic assumption is made for the liquid. The main difference with the models issued from the classical literature is that the liquid as well as the gas is assumed compressible. In that framework, an averaging process results in a five-equation system where the hydrostatic constraint has been used to define the interfacial pressure. Closure laws for the interfacial velocity and source terms such as mass and momentum transfer are provided following an entropy inequality. The resulting model is hyperbolic with non-conservative terms. Therefore, regarding the homogeneous part of the system, the definition and uniqueness of jump conditions is studied carefully and acquired. The nature of characteristic fields and the corresponding Riemann invariants are also detailed. Thus, one may build analytical solutions for the Riemann problem. In addition, positivity is obtained for heights and densities. The overall derivation deals with gas-liquid flows through rectangular channels, circular pipes with variable cross section and includes vapor-liquid flows.

Note: The content of this chapter has been published under the reference:

- C. Demay and J.-M. Hérard. A compressible two-layer model for transient gas-liquid flows in pipes, *Continuum Mechanics and Thermodynamics*, 29(2):385-410, 2017.

Contents

2.1 Introduction

The present work focuses on the modelling of transient gas-liquid flows in pipes, especially air-water flows. This type of flow occurs in piping systems of several industrial areas such as nuclear power plants, petroleum industries or sewage pipelines. The presence of air in such facilities is usually unwanted as it may induce for instance pressure surges and traveling air pockets, leading to reduced efficiency and damages for pumping systems, see [34, 36] ; an accurate modelling is thus necessary to improve performances and reliability. Although being studied since many years, the macroscopic description of those flows is still complex to assess as they may display different regimes such as dispersed flow, stratified flow, pressurized flow (pipe full of water), slug flow and transitions between them, see [30] for details. On the one hand, experimental studies have provided many interesting data on key points such as transition from stratified to pressurized regime [14] and air entrainment [17, 22, 35, 37]. On the other hand, mathematical and numerical modelling still raise many challenges as pointed out in the recent literature review [13]. In particular, the free-surface regime is usually described by an incompressible flow with surface waves, while the pressurized regime is described by a compressible flow with acoustic waves. Thus, most of existing 1D models focus on this transition without computing the air phase which increases the modelling difficulties, see [12]. However, air-water interactions may greatly affect the flow behavior regarding hydraulic jumps or traveling air pockets. Thus, the purpose of the model presented herein is to account for air-water interactions in addition to regime transitions occurring in air-water pipe flows.

As a first step, we consider in this paper the 1D modelling of stratified air-water flows in pipes. Seeing this regime as a free-surface flow, a common way to deal with it is to use the Saint-Venant system [6], also called shallow water equations, which results from a depth averaging process on the Euler set of equations and assumes a thin layer of incompressible fluid (liquid phase) with hydrostatic pressure law. It may also include friction and viscosity, see [28]. Following this classical approach, the model proposed in [12] computes the water layer, and strict hyperbolicity is acquired with mathematical entropy. In addition, the transition to the pressurized regime is handled including a switching from an incompressible to a compressible description for water and a discontinuity of the pressure gradient. With the aim of computing the air phase, one may rather consider the extension of the Saint-Venant system to a multilayer system, one layer being associated with one height, one velocity and constant density, see [3]. The air

layer is thus added in [11] with variable density and perfect gas pressure law, the compressibility of air playing a key role in our framework. This process results in a two-layer model with incompressible liquid and compressible gas, referred hereafter as the incompressible/compressible two-layer model. Nonetheless, the latter is hyperbolic only for small or large relative speed between both phases. In fact, this system inherits the difficulties from the common incompressible/incompressible two-layer systems, such as non-conservative terms, non-explicit eigenstructure and conditional hyperbolicity, see [1, 9]. Note that a multilayer Saint-Venant system which accounts for mass exchanges between the layers is proposed in [4] and is strictly hyperbolic in its two-layer version when the total water height is strictly positive. Dealing with two-fluid flows, the homogeneous model [16] or the drift-flux model [23] may also be proposed as candidates. However, the first one considers one velocity field for the two phases, while the second one imposes velocity profiles for the relative motion. Thus, those models are unable to restore the complexities of the flow such as entrapped air pockets with unpredictable velocity. Another approach may be the two-velocity two-pressure models where compressibility is assumed for both phases with an associated barotropic pressure law. In that context, interesting mathematical properties are obtained such as hyperbolicity as well as entropy inequality. It was first introduced for separated flows with depth averaging in [38] and mainly used afterward in a statistical framework for bubbly or granular flows, see [5, 25, 29, 31]. This class of models can also been obtained from a variational approach as in [27] and may be extended to multi-component fluids, see [33]. Nonetheless, the statistical framework is not relevant for stratified flows as the height and the relative position of each phase are not given by the model.

Combining the interesting properties of the two-layer and the two-velocity two-pressure frameworks, the model proposed herein is a compressible/compressible two-layer model as in [38]. Thus, water is considered compressible and does not follow the classical hydrostatic pressure law but a barotropic pressure law, such as stiffened gas law. The starting point is the isentropic Euler set of equations for both phases where the classical hydrostatic assumption is made for water (vertical acceleration is neglected). Adding a kinetic boundary condition at the interface between the liquid and gas layers, an averaging process results in a five-equation model in which the hydrostatic constraint is used to define the interfacial pressure. Following an entropy inequality, closure laws are provided for the interfacial velocity and source terms such as mass and momentum transfer. Contrary to the incompressible/incompressible or incompressible/compressible two-layer frameworks, the eigenstructure can be easily detailed and the hyperbolicity is acquired except for resonance conditions which may not occur for realistic air-water flows. Regarding the Riemann problem associated with the homogeneous problem (i.e., without any source terms), the nature of characteristic fields and the associated Riemann invariants can also be detailed. Furthermore, since non-conservative terms exist, the uniqueness of jump conditions is an important feature that is studied and acquired. Thus, one may build analytical solutions for the Riemann problem. In addition, positivity is guaranteed for heights and densities. Finally, note that when dealing with regime transitions, this framework includes a uniform description of water as a compressible flow without any switching on the pressure law.

The document is organized as follows. For the sake of clarity, the model is presented first in the 2D framework with a 1D averaging process where a vertical depth averaging process is used in the classical way of shallow water two-layer equations. Thus, plane channels with constant width are implicitly considered in Section 2.2 neglecting the spanwise variations of the flow. Closure laws for the interfacial velocity and source terms are provided in Section 2.3 and the resulting closed system is commented in Section 2.4 regarding its consistency with other well-known models. Its ability to deal with more complex pipes configurations such as sloping pipes or pressurized flows is also studied. Section 2.5 details significant mathematical properties of the model. In a second step, the 3D framework with a 2D averaging process is handled in Section 2.6 with the aim of considering circular pipes with variable cross section in time and space. The derivation is done following the same approach as in Section 2.2. Air-water flows are considered throughout the paper but the model can applied in the general framework of gas-liquid flows and vapor-liquid flows.

2.2 Model development

2.2.1 Local governing equations

Throughout this section, a two-layer air-water flow through an horizontal pipe of height H is considered. Index k is attributed to each phase, 1 for water, 2 for air. Thus, as h_k refers to the height of phase k, one has $h_1 + h_2 = H$. A 2D description of the flow is used such that all local variables depend on (x,z,t) excepting $h_k(x,t)$. In this framework, we implicitly deal with rectangular channels homogeneous in the spanwise direction. The extension to circular pipes with variable cross section will be investigated in Section 2.6. The geometric description is given in cartesian coordinates $(0,x,z)$ on Figure 2.1.

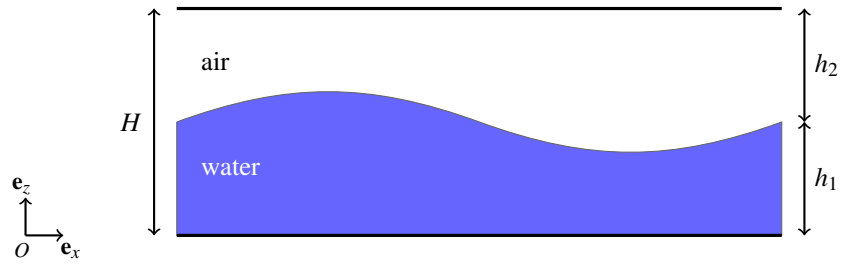

Figure 2.1: Geometric description for horizontal channels.

The set of local governing equations is given by the 2D isentropic Euler set of equations for both phases. In that context, both phases are assumed compressible and the pressure P_k of phase k depends on density ρ_k. Denoting $\mathbf{u}_k = (u_k, w_k)$ the velocity vector of phase k, mass and momentum conservation equations write:

$$\frac{\partial \rho_k}{\partial t} + \mathrm{div}(\rho_k \mathbf{u}_k) = M_k, \qquad k = 1,2, \tag{2.1}$$

$$\frac{\partial \rho_k \mathbf{u}_k}{\partial t} + \mathrm{div}(\rho_k \mathbf{u}_k \otimes \mathbf{u}_k + P_k \mathrm{I_d}) = \mathbf{D}_k + \rho_k \mathbf{g}, \qquad k = 1,2, \tag{2.2}$$

where M_k and $\mathbf{D}_k = D_k \mathbf{e}_x$ stand, respectively, for mass and momentum transfer between phases, $\mathbf{g} = -g\mathbf{e}_z$ denotes the gravity field and $\mathrm{I_d}$ is the identity matrix. Note that mass transfer terms are introduced here for generality, considering single-component vapor-liquid flows for instance, but may be neglected for most of air-water flows. In addition, mass and momentum conservation of the mixture yields $M_1 + M_2 = 0$ and $D_1 + D_2 = 0$.

Dealing with stratified flows in pipes, the classical hydrostatic assumption is made for water (i.e., vertical acceleration is neglected), so that (2.2) along z for $k = 1$ yields:

$$\frac{\partial P_1(\rho_1)}{\partial z} = -\rho_1 g, \tag{2.3}$$

which will be referred to as the hydrostatic constraint. Note that in the framework of barotropic pressure laws, this constraint implies that the density $\rho_1(x,z,t)$ is not homogeneous along the vertical coordinate z.

As the phases are compressible, state equations are required for pressures. For instance, perfect gas law may be used for air and isentropic stiffened gas law for water:

$$P_1(\rho_1) = (P_{1,\mathrm{ref}} + \Pi_1)\Big(\frac{\rho_1}{\rho_{1,\mathrm{ref}}}\Big)^{\gamma_1} - \Pi_1,$$
$$P_2(\rho_2) = P_{2,\mathrm{ref}}\Big(\frac{\rho_2}{\rho_{2,\mathrm{ref}}}\Big)^{\gamma_2},$$

with some reference density $\rho_{k,\mathrm{ref}}$ and pressure $P_{k,\mathrm{ref}}$. Classical thermodynamic considerations impose $\gamma_k > 1$, $\Pi_1 \geq 0$ and $P_k'(\rho_k) > 0$ so that $c_k = \sqrt{P_k'(\rho_k)}$ defines the celerity of acoustic waves. For air, γ_2 is set to 7/5 (diatomic gas) while γ_1 and Π_1 are fitted according to a reference state. Note that the development herein is independent of the chosen pressure laws.

An additional interfacial kinetic boundary condition may be added on the interface separating air and water writing:

$$\varphi(x,z,t) = z - h_1(x,t) = 0,$$

so that:

$$\frac{d\varphi}{dt} = 0,$$

and thus:

$$\frac{\partial \varphi}{\partial t} + \mathbf{u}_I . \underline{\nabla}_{x,z} \varphi = 0,$$

where $\mathbf{u}_I = \begin{pmatrix} U_I \\ W_I \end{pmatrix}$ denotes the interfacial velocity. Using the expression of φ, it finally writes:

$$\frac{\partial h_1}{\partial t} + U_I \frac{\partial h_1}{\partial x} = W_I. \tag{2.4}$$

Boundary conditions may be applied to both phases. On the walls, impermeability imposes:

$$w_1(x,z=0,t) = w_2(x,z=H,t) = 0. \tag{2.5}$$

On the interface, the continuity of the normal velocity is assumed:

$$(\mathbf{u}_1(x,z=h_1^-,t) - \mathbf{u}_2(x,z=h_1^+,t)).\mathbf{n}_I = 0, \tag{2.6}$$

with $\mathbf{n}_I = \frac{(-\frac{\partial h_1}{\partial x} \quad 1)^T}{\sqrt{1+(\frac{\partial h_1}{\partial x})^2}}$, the unit normal vector at the interface. As a dynamic boundary condition, a pressure equilibrium is imposed on the interface neglecting surface tension effects:

$$P_1(x,z=h_1^-,t) = P_2(x,z=h_1^+,t) = P_I(x,t), \tag{2.7}$$

where P_I denotes the interfacial pressure.

Finally, we assume that the interfacial velocity satisfies:

$$\mathbf{u}_I(x,t) = \beta \mathbf{u}_1(x,z=h_1^-,t) + (1-\beta)\mathbf{u}_2(x,z=h_1^+,t),\ \beta \in [0,1]. \tag{2.8}$$

2.2.2 Averaging process

Following the shallow water modelling approach, a vertical average across the layer depth is performed using the operator:

$$\overline{f_k(x,t)} = \frac{1}{h_k}\int_{z_k}^{h_k+z_k} f_k(x,z,t)dz \text{ with } \begin{cases} z_1 = 0, \\ z_2 = h_1, \end{cases} \tag{2.9}$$

where f_k is a function depending on the state variables. The density weighted averaging operator is also introduced:

$$\widehat{f_k(x,t)} = \frac{\overline{\rho_k f_k}}{\overline{\rho}_k}. \tag{2.10}$$

In addition, the interface value of each variable is denoted f_k^* such that:

$$\begin{cases} f_1^*(x,t) = f_1(x,z=h_1^-,t), \\ f_2^*(x,t) = f_2(x,z=h_1^+,t). \end{cases} \tag{2.11}$$

Mass conservation

Vertical integration of (2.1) gives:

$$\int_{z_k}^{h_k+z_k} \frac{\partial \rho_k}{\partial t}dz + \int_{z_k}^{h_k+z_k} \frac{\partial \rho_k u_k}{\partial x}dz + \int_{z_k}^{h_k+z_k} \frac{\partial \rho_k w_k}{\partial z}dz = \int_{z_k}^{h_k+z_k} M_k dz.$$

Using Leibniz's integral rule for non-constant bounds in the first two terms of the left-hand side and kinetic boundary condition (2.5) for the third one, one gets:

$$\frac{\partial h_k \overline{\rho}_k}{\partial t} + \frac{\partial h_k \overline{\rho_k u_k}}{\partial x} - B_k = h_k \overline{M}_k,$$

with:

$$\begin{aligned} B_k &= \rho_k^*(\tfrac{\partial h_1}{\partial t} + u_k^* \tfrac{\partial h_1}{\partial x} - w_k^*) \\ &= \rho_k^*((u_k^* - U_I)\tfrac{\partial h_1}{\partial x} + (W_I - w_k^*)) \text{ according to (2.4)} \\ &= \rho_k^*(\mathbf{u}_I - \mathbf{u}_k^*).(-\tfrac{\partial h_1}{\partial x} \quad 1)^T \\ &= 0, \end{aligned} \tag{2.12}$$

using (2.6) and the colinearity between $\mathbf{u}_I - \mathbf{u}_k^*$ and $\mathbf{u}_1^* - \mathbf{u}_2^*$ given by (2.8).

Finally, using the definition $\overline{\rho_k u_k} = \overline{\rho}_k \widehat{u_k}$, the averaged mass conservation equations write:

$$\frac{\partial h_k \overline{\rho}_k}{\partial t} + \frac{\partial h_k \overline{\rho}_k \widehat{u_k}}{\partial x} = h_k \overline{M}_k. \tag{2.13}$$

Momentum conservation

Dealing with the streamwise component of (2.2), vertical integration writes:

$$\int_{z_k}^{h_k+z_k}\frac{\partial \rho_k u_k}{\partial t}dz+\int_{z_k}^{h_k+z_k}\frac{\partial \rho_k u_k^2}{\partial x}dz+\int_{z_k}^{h_k+z_k}\frac{\partial \rho_k u_k w_k}{\partial z}dz+\int_{z_k}^{h_k+z_k}\frac{\partial P_k}{\partial x}dz=\int_{z_k}^{h_k+z_k}D_k dz.$$

Using Leibniz's integral rule and kinetic boundary condition (2.5), the first three terms of the left-hand side write:

$$\frac{\partial h_k\overline{\rho_k u_k}}{\partial t}+\frac{\partial h_k\overline{\rho_k u_k^2}}{\partial x}-u_k^* B_k,$$

where $B_k=0$ according to (2.12). Concerning the pressure gradient term, it comes:

$$\int_{z_k}^{h_k+z_k}\frac{\partial P_k}{\partial x}dz=\frac{\partial h_k\overline{P}_k}{\partial x}-P_I\frac{\partial h_k}{\partial x}.$$

At first order, the turbulence of the flow is neglected, such that the closure law $\overline{\rho_k u_k^2}=\overline{\rho}_k\widehat{u}_k^2$ is chosen. Thus, the averaged momentum equations considered are:

$$\frac{\partial h_k\overline{\rho}_k\widehat{u}_k}{\partial t}+\frac{\partial h_k(\overline{\rho}_k\widehat{u}_k^2+\overline{P}_k)}{\partial x}-P_I\frac{\partial h_k}{\partial x}=h_k\overline{D}_k. \tag{2.14}$$

Hydrostatic constraint

In [38], the averaged system for 1D stratified flows gathers the averaged mass conservation equations (2.13), the averaged momentum equations (2.14) and the kinetic boundary condition (2.4). However, as gravitational effects have a leading role in the dynamics of stratified flows, it is proposed here to account for the so-called hydrostatic constraint (2.3) in the averaged system. Some approaches have already been studied in the literature, see [21, 32], but an original one is proposed below. The starting point is to integrate the hydrostatic constraint (2.3) between z and h_1:

$$P_1(\rho_1(x,z,t))=P_I(x,t)+\int_z^{h_1}\rho_1(x,s,t)g ds. \tag{2.15}$$

Performing a second integration between 0 and h_1 it yields:

$$\int_0^{h_1}P_1(\rho_1(x,z,t))dz=h_1P_I(x,t)+g\int_0^{h_1}\Big(\int_z^{h_1}\rho_1(x,s,t)ds\Big)dz. \tag{2.16}$$

Then, using an integration by parts of the double integral it comes:

$$\begin{aligned}\int_0^{h_1}P_1(\rho_1(x,z,t))dz&=h_1P_I(x,t)+g\left[z\int_z^{h_1}\rho_1(x,s,t)ds\right]_0^{h_1}+g\int_0^{h_1}\rho_1(x,z,t)zdz,\\&=h_1P_I(x,t)+\overline{\rho_1 z}gh_1.\end{aligned}$$

At this point, it is proposed to neglect the correlation between ρ_1 and z, such that the closure law for $\overline{\rho_1 z}$ writes:

$$\overline{\rho_1 z}=\overline{\rho}_1\overline{z}=\overline{\rho}_1\frac{h_1}{2}. \tag{2.17}$$

Remark 2.1. *As detailed in Appendix 2.A, the validity of (2.17) can be clarified when choosing a linear pressure law for phase 1. Indeed, assuming that $\varepsilon=\frac{gh_1}{c_1^2}\ll 1$, one obtains the following estimate:*

$$\left|\frac{\overline{\rho_1 z}-\overline{\rho}_1\overline{z}}{\overline{\rho}_1\overline{z}}\right|=\frac{\varepsilon}{6}+\mathscr{O}(\varepsilon^2),$$

which justifies (2.17) as in practice, $c_1\sim 1500\ m.s^{-1}$, $H\sim 1\ m$ and $|\varepsilon|\leq 10^{-5}$.

Thus, (2.16) yields:

$$P_I=\overline{P}_1-\overline{\rho}_1 g\frac{h_1}{2}. \tag{2.18}$$

In the isentropic framework, the above expression provides the closure law for P_I regarding $\overline{P}_1$ as a function of $\overline{\rho}_1$. Moreover, (2.18) may be read as an averaged hydrostatic pressure law for $\overline{P}_1$ used with the averaged density $\overline{\rho}_1$. Therefore, the averaged momentum equations under hydrostatic constraint write:

$$\frac{\partial h_k\overline{\rho}_k\widehat{u}_k}{\partial t}+\frac{\partial h_k(\overline{\rho}_k\widehat{u}_k^2+\overline{P}_k)}{\partial x}-(\overline{P}_1-\overline{\rho}_1 g\frac{h_1}{2})\frac{\partial h_k}{\partial x}=h_k\overline{D}_k. \tag{2.19}$$

2.2.3 Resulting averaged system

Adding the interfacial kinetic boundary condition (2.4), a five-equation system corresponding to the five unknowns $(h_1, \overline{\rho}_1, \overline{\rho}_2, \widehat{u}_1, \widehat{u}_2)$ is obtained:

$$\frac{\partial h_1}{\partial t} + U_I \frac{\partial h_1}{\partial x} = W_I, \tag{2.20a}$$

$$\frac{\partial h_k \overline{\rho}_k}{\partial t} + \frac{\partial h_k \overline{\rho}_k \widehat{u}_k}{\partial x} = h_k \overline{M}_k, \tag{2.20b}$$

$$\frac{\partial h_k \overline{\rho}_k \widehat{u}_k}{\partial t} + \frac{\partial h_k (\overline{\rho}_k \widehat{u}_k^2 + \overline{P}_k)}{\partial x} - (\overline{P}_1 - \overline{\rho}_1 g \frac{h_1}{2}) \frac{\partial h_k}{\partial x} = h_k \overline{D}_k, \tag{2.20c}$$

where $k = 1,2$ and $h_1 + h_2 = H$. This system is relevant for two-layer gas-liquid or vapor-liquid flows in horizontal channels and relies on a vertical average across the layer depth. Compressibility is considered for both layers with barotropic pressure laws. Dealing with the averaged source terms, conservation of mass and momentum of the mixture impose:

$$h_1 \overline{D}_1 + h_2 \overline{D}_2 = 0, \tag{2.21a}$$

$$h_1 \overline{M}_1 + h_2 \overline{M}_2 = 0. \tag{2.21b}$$

In practice, the averaged pressure laws $\overline{P_k(\rho_k)}$ are classically expressed in terms of $\overline{\rho}_k$ so that the closure $\overline{P_k(\rho_k)} = P_k(\overline{\rho}_k)$ is chosen. Consequently, the celerity of acoustic waves in the averaged framework is defined by:

$$\overline{c}_k = \sqrt{P_k'(\overline{\rho}_k)}. \tag{2.22}$$

The interfacial pressure P_I is defined by the averaged hydrostatic constraint (2.18) whereas the interfacial velocity U_I and source terms still need closure laws. In the following section, an entropy inequality is used to close the system.

2.3 Entropy inequality and closure laws

System (2.20) may develop discontinuous solutions even with continuous initial conditions. Therefore, an entropy inequality which allows to select the physically relevant solution is obtained in this section; closure laws will be proposed following with this inequality.

From now on, the operator notations are omitted until Section 2.6. Let us define:

$$m_k = h_k \rho_k, \; E_{c,k} = \frac{1}{2} m_k u_k^2, \; E_{t,k} = m_k \Psi_k(\rho_k), \tag{2.23}$$

with Ψ_k some function of ρ_k. Notice that $E_{c,k}$ and $E_{t,k}$ respectively stand for the integrated kinetic energy and thermodynamic energy of phase k over the layer of height h_k.

Considering smooth solutions of (2.20) and combining (2.20a) with (2.20b), the equation for ρ_k writes:

$$\frac{\partial \rho_k}{\partial t} + u_k \frac{\partial \rho_k}{\partial x} + \rho_k \frac{\partial u_k}{\partial x} + \frac{\rho_k}{h_k}(u_k - U_I) \frac{\partial h_k}{\partial x} = (-1)^k \frac{\rho_k}{h_k} W_I + M_k.$$

Multiplying the last equation by $m_k \Psi_k'$, we get for $E_{t,k}$:

$$\frac{\partial E_{t,k}}{\partial t} + \frac{\partial u_k E_{t,k}}{\partial x} + m_k \rho_k \Psi_k' \frac{\partial u_k}{\partial x} + \rho_k^2 (u_k - U_I) \Psi_k' \frac{\partial h_k}{\partial x} = (-1)^k \rho_k^2 \Psi_k' W_I + (\rho_k \Psi_k' + \Psi_k) h_k M_k. \tag{2.24}$$

Multiplying (2.20c) by u_k and combining with (2.20b) we get for $E_{c,k}$:

$$\frac{\partial E_{c,k}}{\partial t} + \frac{\partial}{\partial x}(u_k E_{c,k} + u_k h_k P_k) - h_k P_k \frac{\partial u_k}{\partial x} - u_k P_1 \frac{\partial h_k}{\partial x} + u_k \rho_1 g \frac{h_1}{2} \frac{\partial h_k}{\partial x} = u_k h_k D_k - \frac{u_k^2}{2} h_k M_k. \tag{2.25}$$

For phase 1, the term $u_1 \rho_1 g \frac{h_1}{2} \frac{\partial h_1}{\partial x}$ in (2.25) may be used to introduce the gravitational potential energy:

$$E_{p,1} = \rho_1 g \frac{h_1^2}{2}. \tag{2.26}$$

After calculations, one obtains:

$$u_1\rho_1 g\frac{h_1}{2}\frac{\partial h_1}{\partial x} = \frac{\partial E_{p,1}}{\partial t} + \frac{\partial u_1 E_{p,1}}{\partial x} + U_I\rho_1 g\frac{h_1}{2}\frac{\partial h_1}{\partial x} - \rho_1 g\frac{h_1}{2}W_I - g\frac{h_1^2}{2}M_k. \tag{2.27}$$

The energy equation for the whole system is then obtained adding (2.24) with (2.25) for $k = 1,2$. Using (2.27) and the following consistency relations:

$$\frac{\partial h_1}{\partial x} + \frac{\partial h_2}{\partial x} = 0,\ h_1 D_1 + h_2 D_2 = 0,\ h_1 M_1 + h_2 M_2 = 0,$$

it yields:

$$\begin{aligned}\frac{\partial}{\partial t}\Big(E_{c,1}+E_{t,1}+E_{p,1}+E_{c,2}+E_{t,2}\Big) + \frac{\partial}{\partial x}\Big(u_1(E_{c,1}+E_{p,1}+E_{t,1}) + u_2(E_{c,2}+E_{t,2}) + u_1h_1P_1 + u_2h_2P_2\Big)\\ + \kappa_{u_1}\frac{\partial u_1}{\partial x} + \kappa_{u_2}\frac{\partial u_2}{\partial x} + \kappa_{h_1}\frac{\partial h_1}{\partial x} = \kappa_{w_I}W_I + \kappa_{D_1}h_1D_1 + \kappa_{M_1}h_1M_1,\end{aligned} \tag{2.28}$$

where:

$$\begin{aligned}\kappa_{u_k} &= h_k\rho_k^2\Psi_k' - h_kP_k,\\ \kappa_{h_1} &= (u_1-U_I)\rho_1^2\Psi_1' - (u_2-U_I)(\rho_2^2\Psi_2' - \rho_1 g\frac{h_1}{2}) + (u_2-u_1)P_1,\\ \kappa_{w_I} &= \rho_2^2\Psi_2' - \rho_1^2\Psi_1' + \rho_1 g\frac{h_1}{2},\\ \kappa_{D_1} &= u_1 - u_2,\\ \kappa_{M_1} &= (\rho_1\Psi_1' + \Psi_1 + g\frac{h_1}{2}) - (\rho_2\Psi_2' + \Psi_2) + \frac{1}{2}(u_2^2 - u_1^2).\end{aligned}$$

In order to obtain a conservative equation, the contribution of non-conservative terms is canceled out. Thus, we define $\Psi_k(\rho_k)$ such that:

$$\Psi_k'(\rho_k) = \frac{P_k(\rho_k)}{\rho_k^2}. \tag{2.30}$$

This closure yields $\kappa_{u_k} = 0$ and one obtains the consistency with the definition of thermodynamic energy when dealing with single-phase flows and the Euler system. Setting $\kappa_{h_1} = 0$ and using (2.30), one obtains:

$$(u_2 - U_I)(P_1 - P_2 + \rho_1 g\frac{h_1}{2}) = 0,\ \forall(h_1,\rho_1,\rho_2),$$

which gives the closure for U_I:

$$U_I = u_2. \tag{2.31}$$

To conclude, one can state the following proposition:

Proposition 2.1. *Smooth solutions of system (2.20) comply with the entropy inequality:*

$$\frac{\partial \mathscr{E}}{\partial t} + \frac{\partial \mathscr{G}}{\partial x} \leq 0, \tag{2.32}$$

where the entropy $\mathscr{E}$ and the entropy flux $\mathscr{G}$ are defined by:

$$\mathscr{E} = E_{c,1} + E_{p,1} + E_{t,1} + E_{c,2} + E_{t,2}, \tag{2.33a}$$
$$\mathscr{G} = u_1(E_{c,1} + E_{p,1} + E_{t,1}) + u_2(E_{c,2} + E_{t,2}) + u_1h_1P_1 + u_2h_2P_2, \tag{2.33b}$$

with:

$$E_{c,k} = \frac{1}{2}h_k\rho_k u_k^2,\ E_{t,k} = h_k\rho_k\Psi_k(\rho_k),\ E_{p,1} = \rho_1 g\frac{h_1^2}{2},$$

and:

$$\Psi_k'(\rho_k) = \frac{P_k(\rho_k)}{\rho_k^2},$$

as soon as the following closure laws are used for the interfacial variables:

$$U_I = u_2, \tag{2.34a}$$

$$P_I = P_1 - \rho_1 g \frac{h_1}{2}, \tag{2.34b}$$

and for the source terms:

$$W_I = \lambda_p(P_I - P_2) = \lambda_p(P_1 - \rho_1 g \frac{h_1}{2} - P_2), \tag{2.35a}$$

$$h_k D_k = (-1)^k \lambda_u (u_1 - u_2) + \Big(\frac{u_1+u_2}{2}\Big) h_k M_k, \tag{2.35b}$$

$$h_k M_k = (-1)^k \lambda_m \Big((\frac{P_1 + \rho_1 g \frac{h_1}{2}}{\rho_1} + \Psi_1) - (\frac{P_2}{\rho_2} + \Psi_2) \Big), \tag{2.35c}$$

where λ_p, λ_u and λ_m are positive bounded functions which depend on the state variable $(h_1, \rho_1, \rho_2, u_1, u_2)$.

Proof. (2.32) is obtained from (2.28) where the source terms are chosen to ensure that the inequality is verified. Indeed, the right-hand side of (2.28) writes:

$$S = h_1 D_1 (u_1 - u_2) + h_1 M_1 \Big((\frac{P_1 + \rho_1 g \frac{h_1}{2}}{\rho_1} + \Psi_1) - (\frac{P_2}{\rho_2} + \Psi_2) + \frac{u_2^2 - u_1^2}{2} \Big) + W_I (P_2 - P_1 + \rho_1 g \frac{h_1}{2}),$$

so that choosing $h_k D_k = h_k D_k^{'} + (\frac{u_1+u_2}{2}) h_k M_k$, one obtains:

$$S = h_k D_k^{'} (u_1 - u_2) + h_1 M_1 \Big((\frac{P_1 + \rho_1 g \frac{h_1}{2}}{\rho_1} + \Psi_1) - (\frac{P_2}{\rho_2} + \Psi_2) \Big) + W_I (P_2 - P_1 + \rho_1 g \frac{h_1}{2}),$$

and the corresponding expressions for W_I, $h_k D_k^{'}$ and $h_k M_k$ are chosen such that $S \leq 0$. □

Therefore, the closed system writes:

$$\frac{\partial W}{\partial t} + \frac{\partial F(W)}{\partial x} + B(W) \frac{\partial W}{\partial x} = C(W), \tag{2.36}$$

where:

$$W = (h_1, h_1\rho_1, h_2\rho_2, h_1\rho_1 u_1, h_2\rho_2 u_2)^T,$$

$$F(W) = \begin{pmatrix} 0 \\ h_1\rho_1 u_1 \\ h_2\rho_2 u_2 \\ h_1(\rho_1 u_1^2 + P_1) \\ h_2(\rho_2 u_2^2 + P_2) \end{pmatrix}, \; B(W)\frac{\partial W}{\partial x} = \begin{pmatrix} u_2 \frac{\partial h_1}{\partial x} \\ 0 \\ 0 \\ -(P_1 - \rho_1 g \frac{h_1}{2}) \frac{\partial h_1}{\partial x} \\ -(P_1 - \rho_1 g \frac{h_1}{2}) \frac{\partial h_2}{\partial x} \end{pmatrix},$$

and:

$$C(W) = \begin{pmatrix} \lambda_p (P_1 - \rho_1 g \frac{h_1}{2} - P_2) \\ -\lambda_m \Big((\frac{P_1 + \rho_1 g \frac{h_1}{2}}{\rho_1} + \Psi_1) - (\frac{P_2}{\rho_2} + \Psi_2) \Big) \\ \lambda_m \Big((\frac{P_1 + \rho_1 g \frac{h_1}{2}}{\rho_1} + \Psi_1) - (\frac{P_2}{\rho_2} + \Psi_2) \Big) \\ -\lambda_u (u_1 - u_2) - (\frac{u_1+u_2}{2}) \lambda_m \Big((\frac{P_1 + \rho_1 g \frac{h_1}{2}}{\rho_1} + \Psi_1) - (\frac{P_2}{\rho_2} + \Psi_2) \Big) \\ \lambda_u (u_1 - u_2) + (\frac{u_1+u_2}{2}) \lambda_m \Big((\frac{P_1 + \rho_1 g \frac{h_1}{2}}{\rho_1} + \Psi_1) - (\frac{P_2}{\rho_2} + \Psi_2) \Big) \end{pmatrix},$$

where λ_p, λ_u and λ_m are positive bounded functions which depend on the state variable $(h_1, \rho_1, \rho_2, u_1, u_2)$.

2.4 Comments on the closed system

2.4.1 Consistency with the shallow water equations

When it comes to free-surface flows, the well-known (incompressible) shallow water equations are usually considered in the literature. It is thus interesting to check the consistency of the present model with that classical description.

Regarding the closed system (2.36) without mass nor momentum transfers between the layers, averaged mass and momentum conservation equations for the water phase write:

$$\begin{aligned}
&\frac{\partial h_1\rho_1}{\partial t}+\frac{\partial h_1\rho_1 u_1}{\partial x}=0,\\
&\frac{\partial h_1\rho_1 u_1}{\partial t}+\frac{\partial h_1\rho_1 u_1^2}{\partial x}+\frac{\partial h_1 P_1}{\partial x}-P_I\frac{\partial h_1}{\partial x}=0,
\end{aligned}$$

where $P_1 = P_I + \rho_1 g\frac{h_1}{2}$ (averaged hydrostatic constraint). Focusing on the pressure gradient and smooth solutions, it comes:

$$\frac{\partial h_1 P_1}{\partial x}=\frac{\partial \rho_1 g\frac{h_1^2}{2}}{\partial x}+h_1\frac{\partial P_I}{\partial x}+P_I\frac{\partial h_1}{\partial x},$$

and the water layer system reads:

$$\frac{\partial h_1\rho_1}{\partial t}+\frac{\partial h_1\rho_1 u_1}{\partial x}=0, \tag{2.37a}$$

$$\frac{\partial h_1\rho_1 u_1}{\partial t}+\frac{\partial h_1\rho_1 u_1^2}{\partial x}+\frac{\partial \rho_1 g\frac{h_1^2}{2}}{\partial x}+h_1\frac{\partial P_I}{\partial x}=0. \tag{2.37b}$$

Thus, if ρ_1 is considered as a constant in (2.37), one obtains *formally* the classical (incompressible) shallow water model with varying atmospheric pressure $P_I(x,t)$, see [2] for instance.

Furthermore, regarding the surface dynamic equation (3.14a), its interpretation is given in terms of pressure relaxation. Indeed, considering static fluids without mass transfer, one can write:

$$\begin{aligned}
&\frac{\partial h_1}{\partial t}=\lambda_p(P_I-P_2)=\lambda_p\Pi(x,t),\\
&\frac{\partial h_k\rho_k}{\partial t}=0,
\end{aligned}$$

where $\Pi(x,t)=P_I-P_2=P_1-\rho_1 g\frac{h_1}{2}-P_2$. The second equation gives $h_k\frac{\partial \rho_k}{\partial t}=(-1)^k\rho_k\frac{\partial h_1}{\partial t}$ and $\Pi(x,t)$ verifies:

$$\begin{aligned}
\frac{\partial \Pi}{\partial t}&=-\frac{\partial h_1}{\partial t}\left(\frac{c_1^2\rho_1}{h_1}+\frac{c_2^2\rho_2}{h_2}\right),\\
&=-\lambda_p\left(\frac{c_1^2\rho_1}{h_1}+\frac{c_2^2\rho_2}{h_2}\right)\Pi(x,t),
\end{aligned}$$

which yields:

$$\Pi(x,t)=\Pi(x,0)\exp\left(-\int_0^t\lambda_p\left(\frac{c_1^2\rho_1}{h_1}+\frac{c_2^2\rho_2}{h_2}\right)dt\right).$$

As λ_p is a positive bounded function, one obtains the following asymptotic behavior:

$$P_I\underset{t\to+\infty}{\longrightarrow}P_2. \tag{2.38}$$

In practice, dealing with water for phase 1 and pipe radii of about 1 m, $\frac{c_1^2\rho_1}{h_1}\sim 10^9$ Pa.m^{-1} and the relaxation is very fast. Consequently, the atmospheric pressure in (2.37b) quickly converges toward the pressure of the air phase, which makes sense regarding the layered configuration. Note that an explicit form for the pressure relaxation term λ_p is proposed in [26] for bubbly flows and might be extended to our model.

The consistency of the proposed model with the incompressible shallow water model deserves also a deep investigation considering an asymptotic low Mach number development in the liquid, but this study lies beyond the scope of the work exposed herein.

2.4.2 Consistency with pressurized flows

The case where the pipe is full of phase 1 is referred to as *pressurized flow*. In practice, transitions from stratified to pressurized regime often occur in industrial facilities so that one may wonder if this configuration will be correctly handled by our model. Formally, considering $h_1 = H$, one obtains:

$$\begin{aligned}
&\frac{\partial \rho_1}{\partial t} + \frac{\partial \rho_1 u_1}{\partial x} = 0, \\
&\frac{\partial \rho_1 u_1}{\partial t} + \frac{\partial (\rho_1 u_1^2 + P_1)}{\partial x} = 0,
\end{aligned}$$

as soon as the source terms vanish when $h_1 = H$. This system gives the expected averaged equations to describe a rectangular channel full of phase 1 where compressibility effects provide the correct velocity of acoustic waves. Therefore, the model presented herein for stratified air-water flows degenerates correctly to the pressurized regime without any switching on the pressure law, contrary to the model presented in [12]. Note also that the above comments hold for a pipe full of phase 2, referred as a dry flow.

2.4.3 Comparison with the two-fluid two-pressure models

By construction, the model presented herein may be seen as a two-fluid two-pressure model. Indeed, looking at the system (2.36), one may recognize a two-velocity two-pressure model as developed in [5, 18, 25, 29, 31] without the energy equations. The first difference relies on the averaging process; in the literature, one may find time averages, space averages or statistical averages, resulting in the same system structure. Another difference is given by the closure laws (2.34). In the overall framework, see [18], several closure laws are possible for (U_I, P_I) to get both a linearly degenerated field for the 1-wave and an entropy inequality, whereas in our case, there is only one possibility satisfying the additional hydrostatic constraint (2.3). That being said, most of the good properties such as hyperbolicity (see next section) or entropy inequality have been inherited directly from the overall framework. One may also find similarities with the model developed in [24] where granular flows have been described in the statistical framework. Particularly, reading h_k as the statistical fraction, similarities are found regarding the source terms: W_I includes the granular stress contribution, $h_k D_k$ the classical friction effects and $h_k M_k$ the disequilibrium of Gibbs enthalpy.

2.4.4 Sloping pipes

Sloping pipes are frequently encountered in industrial configurations. Considering a constant slope of angle θ, a description of the geometry is presented on Figure 2.2.

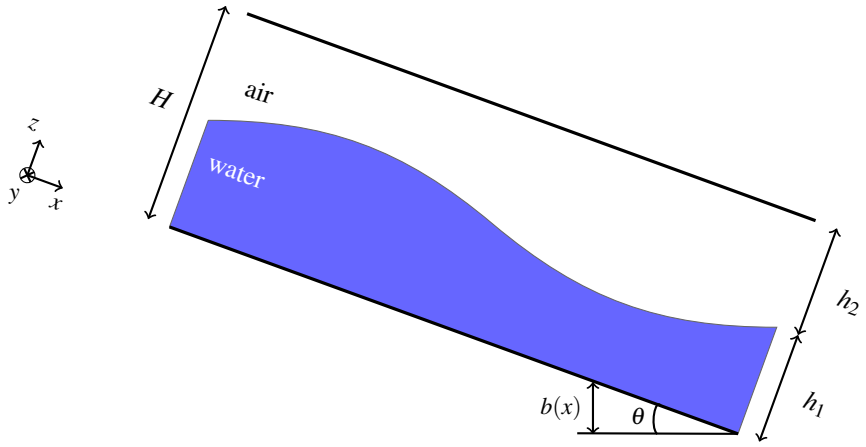

Figure 2.2: Geometric description for sloped pipes.

In the (O, x, y, z) frame of reference, the hydrostatic constraint writes:

$$\frac{\partial P_1}{\partial z} = -\rho_1 g \cos\theta, \tag{2.39}$$

and one may easily demonstrate that the closing relations for the interfacial variables are exactly the same as those presented in the previous section, replacing g by $g\cos\theta$:

$$U_I = u_2,$$
$$P_I = P_1 - \rho_1 g \frac{h_1}{2}\cos\theta,$$

and for the source terms:

$$W_I = \lambda_p(P_1 - \rho_1 g\frac{h_1}{2}\cos\theta - P_2),$$
$$h_k D_k = (-1)^k \lambda_u(u_1 - u_2) + \Big(\frac{u_1+u_2}{2}\Big)h_k M_k,$$
$$h_k M_k = (-1)^k \lambda_m\Big((\frac{P_1 + \rho_1 g(\frac{h_1}{2}\cos\theta + b)}{\rho_1} + \Psi_1) - (\frac{P_2}{\rho_2} + \Psi_2)\Big).$$

The entropy inequality being equivalent to (2.32) where $E_{p,1}$ now writes:

$$E_{p,1} = \rho_1 g\frac{h_1^2}{2}\cos\theta + \rho_1 g h_1 b,$$

with $\frac{db}{dx} = sin\theta$. Note that there is no approximation required on θ to get these relations. The only implicit assumption is that phases stay layered with phase 1 below. The validity of this system is thus questionable when θ gets close to $\frac{\pi}{2}$.

To conclude, one may easily deal with sloped pipes where θ is constant. The case with variable slopes is not considered here although it can a priori be handled considering the curvilinear formulation of Euler equations as in [7, 8, 10, 32].

2.5 Mathematical properties

Dealing with the closed system (2.36), the homogeneous problem is studied through the eigenstructure and hyperbolicity analysis, the nature of characteristic fields and the associated Riemann invariants. Furthermore, as non-conservative terms exist, uniqueness of jump conditions is then studied carefully. Finally, positivity is obtained for the physical variables h_k and ρ_k, $k = 1, 2$.

2.5.1 Eigenstructure and hyperbolicity

Regarding the convective part of (2.36):

$$\frac{\partial h_1}{\partial t} + u_2\frac{\partial h_1}{\partial x} = 0, \tag{2.42a}$$
$$\frac{\partial h_k\rho_k}{\partial t} + \frac{\partial h_k\rho_k u_k}{\partial x} = 0, \tag{2.42b}$$
$$\frac{\partial h_k\rho_k u_k}{\partial t} + \frac{\partial h_k(\rho_k u_k^2 + P_k)}{\partial x} - (P_1 - \rho_1 g\frac{h_1}{2})\frac{\partial h_k}{\partial x} = 0, \tag{2.42c}$$

where $h_1 + h_2 = H$, and recalling that $c_k = \sqrt{P_k'(\rho_k)}$ denotes the celerity of acoustic waves, the following proposition holds:

Proposition 2.2. *The homogeneous problem (2.42) is hyperbolic under the condition:*

$$|u_1 - u_2| \neq c_1. \tag{2.43}$$

Its eigenvalues are unconditionally real and given by:

$$\lambda_1 = u_2,\ \lambda_2 = u_1 - c_1,\ \lambda_3 = u_1 + c_1,\ \lambda_4 = u_2 - c_2,\ \lambda_5 = u_2 + c_2. \tag{2.44}$$

Defining the vector:

$$Y = (h_1, \rho_1, u_1, \rho_2, u_2)^T, \tag{2.45}$$

the corresponding right eigenvectors write in column:

$$R(Y) = \begin{pmatrix} 1 & 0 & 0 & 0 & 0 \\ \eta_1 & \rho_1 & \rho_1 & 0 & 0 \\ \eta_2 & -c_1 & c_1 & 0 & 0 \\ \eta_3 & 0 & 0 & \rho_2 & \rho_2 \\ 0 & 0 & 0 & -c_2 & c_2 \end{pmatrix},$$

where:

$$\eta_1 = \frac{\rho_1}{c_1^2-(u_1-u_2)^2}\Big(\frac{(u_1-u_2)^2}{h_1} - \frac{g}{2}\Big),\ \eta_2 = \frac{u_1-u_2}{c_1^2-(u_1-u_2)^2}(-\frac{c_1^2}{h_1}+\frac{g}{2}),$$

$$\eta_3 = \frac{P_2-P_1+\rho_1 g\frac{h_1}{2}}{h_2 c_2^2}.$$

Proof. (2.42) may be written with respect to Y, which gives, for regular solutions:

$$\frac{\partial Y}{\partial t} + C(Y)\frac{\partial Y}{\partial x} = 0, \tag{2.46}$$

where

$$C(Y) = \begin{pmatrix} u_2 & 0 & 0 & 0 & 0 \\ \frac{\rho_1}{h_1}(u_1-u_2) & u_1 & \rho_1 & 0 & 0 \\ \frac{g}{2} & \frac{c_1^2}{\rho_1} & u_1 & 0 & 0 \\ 0 & 0 & 0 & u_2 & \rho_2 \\ \frac{P_1-\rho_1 g\frac{h_1}{2}-P_2}{\rho_2 h_2} & 0 & 0 & \frac{c_2^2}{\rho_2} & u_2 \end{pmatrix}.$$

The eigenvalues and the eigenvectors are then easily computed using the block structure of $C(Y)$. As $c_k \neq 0$, the eigenvectors are linearly independent and span $\mathbb{R}^5$ as soon as $\lambda_1 = u_2$ is different from the other eigenvalues, which may be rewritten under the condition (2.43). □

Note that the hyperbolicity is not strictly verified everywhere since some eigenvalues may coincide if (2.43) is violated, leading to the so-called resonant behavior. However, in the context of air-water flows, $c_1 \approx 1500\ m.s^{-1}$, and the resonant situation is clearly out of the scope of interest and the model is not devoted to this unrealistic flow regime. Finally, looking at $C(Y)$ and $R(Y)$, phases 1 and 2 are only coupled by the first column which means that they evolve independently on each side of the 1-wave $\lambda_1 = u_2$. Moreover, the system may be symmetrized using the Y variable, see [19] for some counterpart.

2.5.2 Study of the Riemann problem

In this section, we focus on the Riemann problem associated with (2.42) in order to verify that the parametrization of waves λ_k, $k = 1,..,5$, is well defined. Using the conservative variable:

$$W = (h_1, h_1\rho_1, h_2\rho_2, h_1\rho_1 u_1, h_2\rho_2 u_2)^T,$$

the Riemann problem writes:

$$W(t=0,x) = \begin{cases} W_L, & \text{if } x < 0, \\ W_R, & \text{if } x > 0, \end{cases}$$

where W_L and W_R are some constant states. After studying the nature of characteristic fields, one turns to Riemann invariants and jump conditions which need careful consideration regarding non-conservative terms.

Nature of characteristic fields and Riemann invariants

Considering the eigenstructure of (2.42) detailed in Proposition 2.2, the following proposition can be stated:

Proposition 2.3. *The field associated with the 1-wave λ_1 is linearly degenerate while the fields associated with the waves λ_k, $k = 2,..,5$, are genuinely nonlinear. Moreover, denoting $I^k(W)$ the vector of k-Riemann invariants associated with the k-wave, one obtains:*

$$I^1(W) = \left(u_2, m_1(u_1-u_2), m_1u_1(u_1-u_2)+h_1P_1+h_2P_2, \frac{P_1+\rho_1 g\frac{h_1}{2}}{\rho_1}+\Psi_1+\frac{(u_1-u_2)^2}{2}\right)^T,$$

$$I^2(W) = \left(h_1, \rho_2, u_2, u_1+\int \frac{c_1(\rho_1)}{\rho_1}d\rho_1\right)^T,$$

$$I^3(W) = \left(h_1, \rho_2, u_2, u_1-\int \frac{c_1(\rho_1)}{\rho_1}d\rho_1\right)^T,$$

$$I^4(W) = \left(h_1, \rho_1, u_1, u_2+\int \frac{c_2(\rho_2)}{\rho_2}d\rho_2\right)^T,$$

$$I^5(W) = \left(h_1, \rho_1, u_1, u_2-\int \frac{c_2(\rho_2)}{\rho_2}d\rho_2\right)^T.$$

Proof. One may readily see that:

$$\underline{\nabla}_Y\lambda_1(Y).\mathbf{r}_1(Y) = 0,$$

where $\mathbf{r}_k(Y)$ denotes the k^{th} column of $R(Y)$. Thus, the 1-wave field is linearly degenerate. Moreover, a classical result derived from the Euler system with perfect gas law or stiffened gas law gives:

$$\underline{\nabla}_Y\lambda_k(Y).\mathbf{r}_k(Y) \neq 0,\ k = 2,...,5.$$

Thus, the associated fields are genuinely nonlinear. Regarding the matrix $R(Y)$ in Proposition 2.2, the definition of the k-Riemann invariants, $k = 2,..,5$, is also a classical result derived from the Euler system. Concerning the linearly degenerate field, $\lambda_1 = u_2$ is a 1-Riemann invariant by definition. The three remaining 1-Riemann invariants may be obtained using three conservation laws on which Rankine-Hugoniot jump conditions are applied with $\sigma = \lambda_1$ as speed of discontinuity. Mass conservation and momentum conservation summed on both phases provide the first two, while the last one is the entropy equality without source terms (see Proposition 2.1). Then, denoting I^1_k the k^{th} component of I^1, checking that $\underline{\nabla}_Y I^1_k(Y).\mathbf{r}_1(Y) = 0$ is straightforward though tedious. □

This result emphasizes the fact that the phases evolve independently on each side of the 1-wave. In those regions, h_1 is constant and one may notice that the system (2.42) reduces locally to two conservative Euler systems.

Jump conditions

System (2.42) contains two non-conservative products, $u_2\partial_x h_1$ and $(P_1-\rho_1 g\frac{h_1}{2})\partial_x h_1$. Regarding discontinuous solutions, one has to make sure that those products are well defined across genuinely nonlinear and linearly degenerate fields. As h_1 is constant through the genuinely nonlinear fields, the system (2.42) can be considered locally conservative. Thus, one may state the following proposition:

Proposition 2.4. *For all genuine nonlinear fields corresponding to the k-waves, $k = 2,...,5$, the Rankine-Hugoniot jump conditions across a single discontinuity of speed σ write:*

$$\begin{aligned}
&[h_k] = 0,\\
&[m_k(u_k-\sigma)] = 0,\\
&[m_ku_k(u_k-\sigma)+h_kP_k] = 0,
\end{aligned}$$

where brackets $[.]$ denote the difference between the states on both sides of the discontinuity.

Furthermore, as the field associated with the jump of h_1 is linearly degenerate, the non-conservative products $u_2\partial_x h_1$ and $(P_1-\rho_1 g\frac{h_1}{2})\partial_x h_1$ are well defined. Indeed, one may use the available 1-Riemann invariants detailed in Proposition 2.3 to write explicitly the 1-wave parametrization.

Finally, no ambiguity holds in the definition of jump relations and non-conservative products. In addition, one can build analytical solutions for system (2.42) which may be used to validate numerical schemes. Nonetheless, the great complexity of (2.42) seems to prohibit the exact resolution of Riemann problems.

2.5.3 Positivity

Considering variables with physical meaning such as h_k or ρ_k, ensuring their positivity is a major requirement. Focusing on smooth solutions, the result is classical regarding the system (2.36) if one assumes that λ_p and λ_m may be written under the form $\lambda_p = m_1 m_2 \tilde{\lambda}_p$ and $\lambda_m = m_1 m_2 \tilde{\lambda}_m$, where $\tilde{\lambda}_p$ and $\tilde{\lambda}_m$ are positive bounded functions depending on the state variable (see Proposition 2.B.1 in Appendix 2.B). In addition, one can demonstrate that the positivity requirements hold for discontinuous solutions of the Riemann problem associated with the homogeneous system (2.42). It relies on an explicit writing of elementary waves parametrizations.

2.6 Extension to circular pipes with variable cross section

As mentioned earlier, the 1D averaging operator proposed in (2.9) implicitly deals with the case of homogeneous channels. As most of pipes are actually circular in industrial facilities, the case of horizontal circular pipes is now considered. The analysis is also extended to variable cross section in space and in time corresponding to geometric constraint and pipe elasticity. To this end, a 2D averaging operator is applied on 3D Euler system following the same approach as in Section 2.2. Note that the variable cross section case is developed in [15] considering open channels and two incompressible layers.

2.6.1 Local governing equations and geometric description

The framework is the set of 3D isentropic Euler equations with the same hypothesis as in Section 2.2, that is the classical hydrostatic assumption for water. Denoting $\mathbf{u}_k = (u_k, v_k, w_k)$ the velocity vector of phase k and $\mathbf{v}_k = (0, v_k, w_k)$, the system along the longitudinal direction writes:

$$\frac{\partial \rho_k}{\partial t} + \frac{\partial \rho_k u_k}{\partial x} + \mathrm{div}_{y,z}(\rho_k \mathbf{v}_k) = M_k, \tag{2.47a}$$

$$\frac{\partial \rho_k u_k}{\partial t} + \frac{\partial \rho_k u_k^2}{\partial x} + \mathrm{div}_{y,z}(\rho_k u_k \mathbf{v}_k) + \frac{\partial P_k(\rho_k)}{\partial x} = D_k, \tag{2.47b}$$

with the hydrostatic constraint for phase 1:

$$\frac{\partial P_1(\rho_1)}{\partial z} = -\rho_1 g. \tag{2.48}$$

It is assumed that the flow is homogeneous in the spanwise direction y, so that (ρ_k, u_k) are functions of (x,z,t) and the interface level $\eta_1(x,t)$ is constant along the y direction, see Figure 2.3 for a sketch of the problem. The pipe is assumed to have a symmetry axis $\mathscr{C}$ which coincides with the x axis. In the *cross section planes* (Oyz), $\mathbf{e}_z$ and $\mathbf{e}_r$ denote, respectively, the unit normal vector to the interface and the outward unit normal vector to the wall, $\sigma(x,z,t)$ is the width of the cross section and $R(x,t)$ the radius of the pipe. $A_k(x,t)$ refers to the area filled by phase k such that $A_1(x,t) + A_2(x,t) = S(x,t)$, the area of the cross section. The normal vector to the interface is given by $\mathbf{n_I}$, which differs from $\mathbf{e}_z$ except when the height profile is horizontal.

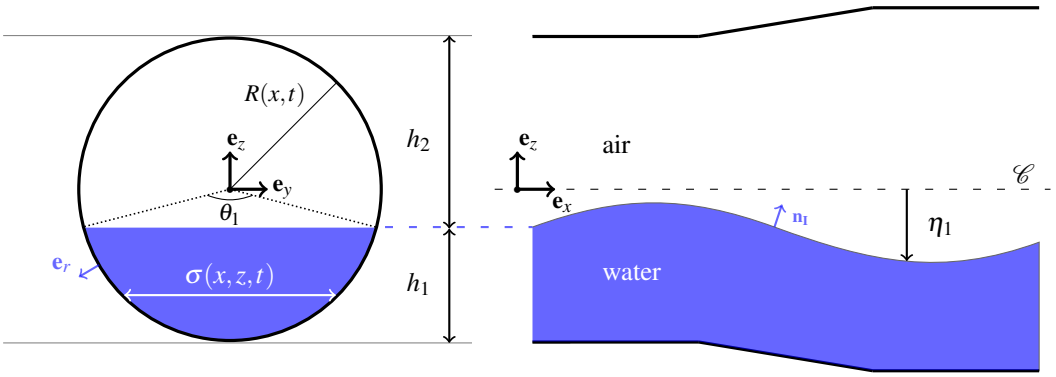

Figure 2.3: Geometric description for circular pipes with variable cross section.

In that framework, the position of the interface is determined from the symmetry axis $\mathscr{C}$ and given by $\eta_1(x,t)$

which verifies the following kinetic boundary condition:

$$\frac{\partial \eta_1}{\partial t} + U_I \frac{\partial \eta_1}{\partial x} = W_I, \tag{2.49}$$

where $\mathbf{u}_I = (U_I, V_I, W_I)^T$ is the interfacial velocity.

On the interface, the following boundary conditions still apply:

$$(\mathbf{u}_1(x, z = \eta_1^-, t) - \mathbf{u}_2(x, z = \eta_1^+, t)).\mathbf{n}_I = 0, \tag{2.50a}$$
$$P_1(x, z = \eta_1^-, t) = P_2(x, z = \eta_1^+, t) = P_I(x, t), \tag{2.50b}$$

and we will assume that the interfacial velocity still satisfies:

$$\mathbf{u}_I(x,t) = \beta \mathbf{u}_1(x, z = \eta_1^-, t) + (1-\beta)\mathbf{u}_2(x, z = \eta_1^+, t),\ \beta \in [0,1]. \tag{2.51}$$

On the walls, we will consider a contact boundary condition between phase k and the wall, which may be written as:

$$\left.\frac{d\mathbf{OM}_b}{dt}\right|_{wall} = \mathbf{u}_{k,wall}, \tag{2.52}$$

where $M_b(x,y,z)$ is a material point belonging to the contour of the area filled by phase k in the cross section and defined as:

$$\mathbf{OM}_b = x\mathbf{e}_x + R\mathbf{e}_r, \text{ on the wall,} \tag{2.53a}$$
$$= x\mathbf{e}_x + y\mathbf{e}_y + \eta_1(x,t)\mathbf{e}_z, \text{ on the interface.} \tag{2.53b}$$

Note that the impermeability condition (2.5) used in Section 2.2 is consistent with (2.52).

2.6.2 Averaging process

Let us define $\Omega_k(x,t)$ the integration domain for phase k,

$$\Omega_k(x,t) = \{(y,z) \in \mathbb{R}^2; -\frac{\sigma(x,z,t)}{2} \leq y \leq \frac{\sigma(x,z,t)}{2},\ -R(x,t) + z_k \leq z \leq -R(x,t) + z_k + h_k(x,t)\},$$

with $z_1 = 0,\ z_2 = h_1(x,t)$, so that the averaging operator writes:

$$\overline{f_k(x,t)} = \frac{1}{A_k(x,t)} \int_{\Omega_k(x,t)} f_k(x,z,t) d\Omega \tag{2.54}$$

where $A_k(x,t)$ is the area filled by phase k in the cross section at abscissa x and time t:

$$A_k(x,t) = \int_{\Omega_k(x,t)} d\Omega. \tag{2.55}$$

Applying the operator (2.54) to (2.47), one will use the Reynolds transport theorem in time and space given below:

$$\int_{\Omega_k(x,t)} \frac{\partial f_k}{\partial t} d\Omega = \frac{\partial A_k \overline{f_k}}{\partial t} - \int_{\partial\Omega_k} f_k \frac{\partial \mathbf{OM}_b}{\partial t}.\mathbf{n}_k dl, \tag{2.56a}$$
$$\int_{\Omega_k(x,t)} \frac{\partial f_k}{\partial x} d\Omega = \frac{\partial A_k \overline{f_k}}{\partial x} - \int_{\partial\Omega_k} f_k \frac{\partial \mathbf{OM}_b}{\partial x}.\mathbf{n}_k dl, \tag{2.56b}$$

and the divergence theorem:

$$\int_{\Omega_k(x,t)} \mathrm{div}_{y,z}(f_k \mathbf{v}_k) d\Omega = \int_{\partial\Omega_k} f_k \mathbf{v}_k.\mathbf{n}_k dl, \tag{2.57}$$

where $\mathbf{OM}_b$ is defined in (2.53) and $\mathbf{n}_k$ denotes the outward unit normal vector to $\partial\Omega_k$.

$\partial\Omega_k$ includes two different parts, a first part Γ_I on the interface and a second part $\Gamma_{w,k}$ on the wall such that:

$$\partial\Omega_k = \Gamma_I + \Gamma_{w,k}. \tag{2.58}$$

Thus, regarding the contour integral in (2.56b) and using the definition (2.53) of $\mathbf{OM}_b$, one writes for the wall part:

$$\int_{\Gamma_{w,k}} f_k \frac{\partial \mathbf{OM}_b}{\partial x}.\mathbf{n}_k dl = \int_{\Gamma_{w,k}} f_k \frac{\partial R}{\partial x} R d\theta = \widetilde{f}_k \frac{\theta_k}{2\pi}\frac{\partial S}{\partial x}, \tag{2.59}$$

where:

$$\widetilde{f}_k = \frac{1}{\theta_k}\int_{\Gamma_{w,k}} f_k d\theta, \qquad \theta_k = \int_{\Gamma_{w,k}} d\theta, \tag{2.60}$$

and $S(x,t) = \pi R(x,t)^2$ is the area of the cross section. Note that $\widetilde{f}_k$ corresponds to the linear average of f_k along the wet ($k=1$) or dry circular contour ($k=2$).

In addition, note that the kinematic boundary condition (2.49) may be written with A_1. Indeed, using (2.56b) and (2.59) with $f_k = 1$, one obtains:

$$\frac{\partial A_k}{\partial x} = \sigma_I (-1)^{k+1}\frac{\partial \eta_1}{\partial x} + \frac{\theta_k}{2\pi}\frac{\partial S}{\partial x}, \tag{2.61}$$

where σ_I is the width of the cross section at the interface. The same calculations with (2.56a) yield:

$$\frac{\partial A_k}{\partial t} = \sigma_I (-1)^{k+1}\frac{\partial \eta_1}{\partial t} + \frac{\theta_k}{2\pi}\frac{\partial S}{\partial t},$$

and it follows:

$$\frac{\partial A_1}{\partial t} + U_I \frac{\partial A_1}{\partial x} = \sigma_I W_I + \frac{\theta_1}{2\pi}\left(\frac{\partial S}{\partial t} + U_I \frac{\partial S}{\partial x}\right). \tag{2.62}$$

Mass conservation

The 2D averaging of (2.47a) using (2.56) and (2.57) yields:

$$\frac{\partial A_k \overline{\rho}_k}{\partial t} + \frac{\partial A_k \overline{\rho_k u_k}}{\partial x} - \int_{\partial\Omega_k} \rho_k \left(\frac{\partial \mathbf{OM}_b}{\partial t} + u_k \frac{\partial \mathbf{OM}_b}{\partial x} - \mathbf{v}_k\right).\mathbf{n}_k dl = A_k \overline{M}_k.$$

On the interface, $\mathbf{n}_k = (-1)^{k+1}\mathbf{e}_z$ and the definition (2.53) of $\mathbf{OM}_b$ gives for the Γ_I part:

$$\int_{\Gamma_I} \rho_k (-1)^{k+1}\left(\frac{\partial \eta_1}{\partial t} + u_k \frac{\partial \eta_1}{\partial x} - w_k\right) dl = \int_{\Gamma_I} B_k dl = 0,$$

the nullity of B_k being provided by the kinetic boundary condition (2.49) combined with the continuity of the normal velocity on the interface (2.50a), see (2.12) for details. On the wall, $\mathbf{n}_k = \mathbf{e}_r$ and the definition (2.53) of $\mathbf{OM}_b$ gives for the $\Gamma_{w,k}$ part:

$$\int_{\Gamma_{w,k}} \rho_k \left(\frac{\partial \mathbf{OM}_b}{\partial t} + u_k \frac{\partial \mathbf{OM}_b}{\partial x} - \mathbf{v}_k\right).\mathbf{e}_r dl = \int_{\Gamma_{w,k}} \rho_k \left(\frac{d\mathbf{OM}_b}{dt}\Big|_{wall} - \mathbf{u}_{k,wall}\right).\mathbf{e}_r dl = 0,$$

noticing that $\mathbf{v}_k.\mathbf{e}_r = \mathbf{u}_k.\mathbf{e}_r$, $\left(v_k \frac{\partial \mathbf{OM}_b}{\partial y} + w_k \frac{\partial \mathbf{OM}_b}{\partial z}\right).\mathbf{e}_r = 0$ on the wall, and using the contact boundary condition (2.52).

Finally, the contour integral on $\partial\Omega_k$ is zero and using the notation $\overline{\rho_k u_k} = \overline{\rho}_k \widehat{u}_k$, the averaged mass conservation equations write:

$$\frac{\partial A_k \overline{\rho}_k}{\partial t} + \frac{\partial A_k \overline{\rho}_k \widehat{u}_k}{\partial x} = A_k \overline{M}_k. \tag{2.63}$$

Note that this equation is correct for all geometries of pipes, even for non-circular ones, as the nullity of the contour integral does not require a circular section.

Momentum conservation

The 2D averaging of (2.47b) yields:

$$\frac{\partial A_k \overline{\rho_k u_k}}{\partial t} + \frac{\partial A_k (\overline{\rho_k u_k^2} + \overline{P}_k)}{\partial x} - \int_{\partial\Omega_k} \rho_k u_k \left(\frac{\partial \mathbf{OM}_b}{\partial t} + u_k \frac{\partial \mathbf{OM}_b}{\partial x} - \mathbf{v}_k\right).\mathbf{n}_k dl - \int_{\partial\Omega_k} P_k \frac{\partial \mathbf{OM}_b}{\partial x}.\mathbf{n}_k dl = A_k \overline{D}_k.$$

The first contour integral is zero using the same decomposition as for the mass conservation. The contour integral on P_k provides:

$$\begin{aligned}\int_{\partial\Omega_k} P_k \frac{\partial \mathbf{OM}_b}{\partial x}.\mathbf{n}_k dl &= \int_{\Gamma_I} (-1)^{k+1} P_k \frac{\partial \mathbf{OM}_b}{\partial x}.\mathbf{e}_z dl + \int_{\Gamma_{w,k}} P_k \frac{\partial \mathbf{OM}_b}{\partial x}.\mathbf{e}_r dl,\\ &= P_I \sigma_I (-1)^{k+1} \frac{\partial \eta_1}{\partial x} + \widetilde{P}_k \frac{\theta_k}{2\pi}\frac{\partial S}{\partial x},\\ &= P_I \frac{\partial A_k}{\partial x} + (\widetilde{P}_k - P_I)\frac{\theta_k}{2\pi}\frac{\partial S}{\partial x},\end{aligned}$$

using (2.61). Recall that $\widetilde{P}_k$ corresponds to the linear average of P_k along the wet ($k=1$) or dry circular contour ($k=2$). Neglecting the turbulence of the flow at first order, the closure law $\overline{\rho_k u_k^2} = \overline{\rho}_k \widehat{u}_k^2$ is chosen and one obtains:

$$\frac{\partial A_k \overline{\rho}_k \widehat{u}_k}{\partial t} + \frac{\partial A_k (\overline{\rho}_k \widehat{u}_k^2 + \overline{P}_k)}{\partial x} - P_I \frac{\partial A_k}{\partial x} = A_k \overline{D}_k + (\widetilde{P}_k - P_I)\frac{\theta_k}{2\pi}\frac{\partial S}{\partial x}. \tag{2.64}$$

Hydrostatic constraint

As in Section 2.2, one has to account for gravitational effects for phase 1 coupling (2.64) with the hydrostatic constraint (2.48). An original approach is proposed below.

An integration of (2.48) between z and η_1 writes:

$$P_1(\rho_1(x,z,t)) = P_I(x,t) + \int_z^{\eta_1} \rho_1(x,z,t) g ds,$$

which gives:

$$A_1 \overline{P}_1 = \int_{\Omega_1} P_I d\Omega + \int_{\Omega_1} \Big(\int_z^{\eta_1} \rho_1 g ds \Big) d\Omega, \tag{2.65a}$$

$$= A_1 P_I + \int_{-R}^{\eta_1} \Big(\int_z^{\eta_1} \rho_1 g ds \Big) \sigma dz, \tag{2.65b}$$

as $\rho_1(x,z,t)$ and $P_I(x,t)$ do not depend on y.

Let us define $\mathscr{A}(x,z,t)$ the primitive function of $\sigma(x,z,t)$ along z which cancels out in $-R$:

$$\mathscr{A}(x,z,t) = \int_{-R}^{z} \sigma(x,z,t) dz.$$

An integration by parts provides:

$$\begin{aligned}\int_{-R}^{\eta_1} \Big(\int_z^{\eta_1} \rho_1 g ds \Big) \sigma dz &= \Big[\Big(\int_z^{\eta_1} \rho_1 g ds \Big) \mathscr{A} \Big]_{-R}^{\eta_1} + \int_{-R}^{\eta_1} \rho_1 g \mathscr{A} dz,\\ &= \int_{-R}^{\eta_1} \rho_1 g \mathscr{A} dz,\\ &= g \overline{\rho_1 \frac{\mathscr{A}}{\sigma}}.\end{aligned}$$

As in the depth-averaged case, it is proposed to neglect the correlation between ρ_1 and $\frac{\mathscr{A}}{\sigma}$ (see Appendix 2.A for details), such that the closure law for $\overline{\rho_1 \frac{\mathscr{A}}{\sigma}}$ writes:

$$\overline{\rho_1 \frac{\mathscr{A}}{\sigma}} = \overline{\rho}_1 \overline{\Big(\frac{\mathscr{A}}{\sigma} \Big)},$$

with:

$$\begin{aligned}\overline{\left(\frac{\mathscr{A}}{\sigma}\right)} &= \frac{1}{A_1}\int_{-R}^{\eta_1} \mathscr{A}\, dz,\\ &= \frac{1}{A_1}\Big([(z-\eta_1)\mathscr{A}]_{-R}^{\eta_1} + \int_{-R}^{\eta_1}(\eta_1 - z)\sigma dz\Big),\\ &= \frac{1}{A_1}\int_{-R}^{\eta_1}(\eta_1 - z)\sigma dz,\\ &= \overline{\eta_1 - z}.\end{aligned}$$

Thus, (2.65b) yields:

$$P_I = \overline{P}_1 - \overline{\rho}_1 g \ell_1, \tag{2.66}$$

where:

$$\ell_1(x,t) = \overline{\eta_1(x,t) - z} \tag{2.67}$$

represents the distance between the interface and the center of mass of the wet section.

(2.66) provides the closure law for P_I regarding $\overline{P}_1$ as a function of $\overline{\rho}_1$. Moreover, the latter may be read as a section-averaged hydrostatic pressure law for $\overline{P}_1$ used with the averaged density $\overline{\rho}_1$. Therefore, the averaged momentum equations under hydrostatic constraint write:

$$\frac{\partial A_k \overline{\rho}_k \widehat{u}_k}{\partial t} + \frac{\partial A_k(\overline{\rho}_k \widehat{u}_k^2 + \overline{P}_k)}{\partial x} - (\overline{P}_1 - \overline{\rho}_1 g\ell_1)\frac{\partial A_k}{\partial x} = A_k \overline{D}_k + \Big(\widetilde{P}_k - (\overline{P}_1 - \overline{\rho}_1 g\ell_1)\Big)\frac{\theta_k}{2\pi}\frac{\partial S}{\partial x}. \tag{2.68}$$

2.6.3 Resulting averaged system

Adding the interfacial kinetic boundary condition (2.62), one obtains a five-equation system corresponding to the five unknowns $(A_1, \overline{\rho}_1, \overline{\rho}_2, \widehat{u}_1, \widehat{u}_2)$:

$$\frac{\partial A_1}{\partial t} + U_I \frac{\partial A_1}{\partial x} = \sigma_I W_I + \frac{\theta_1}{2\pi}\Big(\frac{\partial S}{\partial t} + U_I \frac{\partial S}{\partial x}\Big), \tag{2.69a}$$

$$\frac{\partial A_k \overline{\rho}_k}{\partial t} + \frac{\partial A_k \overline{\rho}_k \widehat{u}_k}{\partial x} = A_k \overline{M}_k, \tag{2.69b}$$

$$\frac{\partial A_k \overline{\rho}_k \widehat{u}_k}{\partial t} + \frac{\partial A_k(\overline{\rho}_k \widehat{u}_k^2 + \overline{P}_k)}{\partial x} - (\overline{P}_1 - \overline{\rho}_1 g\ell_1)\frac{\partial A_k}{\partial x} = A_k \overline{D}_k + \Big(\widetilde{P}_k - (\overline{P}_1 - \overline{\rho}_1 g\ell_1)\Big)\frac{\theta_k}{2\pi}\frac{\partial S}{\partial x}, \tag{2.69c}$$

where $k = 1,2$ and $A_1 + A_2 = S$, $\theta_1 + \theta_2 = 2\pi$. Dealing with the source terms, conservation of mass and momentum of the mixture impose:

$$A_1 \overline{D}_1 + A_2 \overline{D}_2 = 0, \tag{2.70a}$$

$$A_1 \overline{M}_1 + A_2 \overline{M}_2 = 0. \tag{2.70b}$$

As in Subsection 2.2.3, the closure $\overline{P_k(\rho_k)} = P_k(\overline{\rho}_k)$ is chosen and the celerity of acoustic waves in the averaged framework is defined by:

$$\overline{c}_k = \sqrt{P_k'(\overline{\rho}_k)}. \tag{2.71}$$

Note that the structure of (2.69) is the same as (2.20) obtained with 1D averaging, replacing A_k by h_k. Moreover, considering rectangular pipes of constant width L, one has $A_k = Lh_k$, $\ell_1 = \frac{h_1}{2}$, and both systems are equivalent. Dealing with circular pipes, ℓ_1 is given by the formula (2.67) which may be detailed as:

$$\ell_1 = \frac{R^3}{A_1}\Big(\frac{2}{3}\sin^3\frac{\theta_1}{2} - \frac{1}{2}\cos\frac{\theta_1}{2}(\theta_1 - \sin\theta_1)\Big), \tag{2.72}$$

where $\theta_1 = 2\arccos(1 - \frac{h_1}{R})$.

$S(x,t)$ is a given function which accounts for cross section variations and as in Section 2.2, P_I is closed by the averaged hydrostatic constraint (2.66). The interfacial velocity U_I and the source terms, including $\widetilde{P}_k$, still need closure laws. To this end, an entropy characterization is detailed in the following section.

2.6.4 Closure laws and system properties

From now on, the operator notations are omitted. As (2.69) and (2.20) are structurally identical, the calculations will not be detailed in this section.

Proposition 2.5. *System* (2.69) *admits the entropy inequality:*

$$\frac{\partial \mathscr{E}}{\partial t} + \frac{\partial \mathscr{G}}{\partial x} + \mathscr{S}_t \frac{\partial S}{\partial t} \leq 0, \tag{2.73}$$

where the entropy $\mathscr{E}$*, the entropy flux* $\mathscr{G}$ *and* $\mathscr{S}_t$ *are defined by:*

$$\mathscr{E} = E_{c,1} + E_{p,1} + E_{t,1} + E_{c,2} + E_{t,2}, \tag{2.74a}$$
$$\mathscr{G} = u_1(E_{c,1} + E_{p,1} + E_{t,1}) + u_2(E_{c,2} + E_{t,2}) + u_1 A_1 P_1 + u_2 A_2 P_2, \tag{2.74b}$$
$$\mathscr{S}_t = \frac{\theta_1}{2\pi}(P_1 + \rho_1 g(\widetilde{\eta_1 - z} - \ell_1)) + \frac{\theta_2}{2\pi} P_2, \tag{2.74c}$$

with:

$$E_{c,k} = \frac{1}{2} A_k \rho_k u_k^2,\ E_{t,k} = A_k \rho_k \Psi_k(\rho_k),\ E_{p,1} = A_1 \rho_1 g(\eta_1 - \ell_1),$$

and:

$$\Psi_k'(\rho_k) = \frac{P_k(\rho_k)}{\rho_k^2},$$

as soon as the following closure laws are used for the interfacial variables:

$$U_I = u_2, \tag{2.75a}$$
$$P_I = P_1 - \rho_1 g \ell_1, \tag{2.75b}$$

and for the source terms:

$$\widetilde{P_1} = P_1 + \rho_1 g(\widetilde{\eta_1 - z} - \ell_1), \tag{2.76a}$$
$$\widetilde{P_2} = P_2, \tag{2.76b}$$
$$\sigma_I W_I = \lambda_p(P_I - P_2) = \lambda_p(P_1 - \rho_1 g \ell_1 - P_2), \tag{2.76c}$$
$$A_k D_k = (-1)^k \lambda_u (u_1 - u_2) + \Big(\frac{u_1 + u_2}{2}\Big) A_k M_k, \tag{2.76d}$$
$$A_k M_k = (-1)^k \lambda_m \Big((\frac{P_1 + \rho_1 g(\eta_1 - \ell_1)}{\rho_1} + \Psi_1) - (\frac{P_2}{\rho_2} + \Psi_2) \Big), \tag{2.76e}$$

where λ_p*,* λ_u *and* λ_m *are positive bounded functions which may depend on the state variable* $(A_1, \rho_1, \rho_2, u_1, u_2)$*.*

Proof. Developing similar calculations as in Section 2.2 and using the closure laws (2.76c), (2.76d), (2.76e), one ends up with the following entropy inequality:

$$\frac{\partial \mathscr{E}}{\partial t} + \frac{\partial \mathscr{G}}{\partial x} + \mathscr{S}_t \frac{\partial S}{\partial t} + \mathscr{S}_x \frac{\partial S}{\partial x} \leq 0,$$

where $\mathscr{E}, \mathscr{G}, \mathscr{S}_t$ are defined in (2.74) and:

$$\mathscr{S}_x = u_1 \frac{\theta_1}{2\pi}(P_1 + \rho_1 g(\widetilde{\eta_1 - z} - \ell_1) - \widetilde{P_1}) + u_2 \frac{\theta_2}{2\pi}(P_2 - \widetilde{P_2}).$$

Thus, the suggested closure laws (2.76a) and (2.76b) for $\widetilde{P_1}$ and $\widetilde{P_2}$ cancel out the $\mathscr{S}_x$ contribution and yield a decreasing entropy when dealing with section area constant in time. In addition, the latter are also consistent with the single-phase steady state at rest, see Remark 2.3. □

Remark 2.2. *In order to clarify* (2.74c) *and* (2.76a), $\widetilde{\eta_1 - z}$ *may be detailed as follows:*

$$\widetilde{\eta_1 - z} = \frac{1}{\theta_1} \int_{\Gamma_{w,1}} (\eta_1 - z) d\theta = \eta_1 - \frac{2R}{\theta_1} \sin(\frac{\theta_1}{2}).$$

Thus, when $\eta_1 = R$ *and* $A_1 = S$*,* $\widetilde{R - z} = \ell_1 = R$ *and* $\widetilde{P_1} = P_1$*. Moreover, note that* $A_k = S$ *yields* $\mathscr{S}_t \frac{\partial S}{\partial t} = P_k \frac{\partial S}{\partial t}$ *in* (2.73)*, which is consistent with the single-phase case.*

Remark 2.3. *The suggested closure laws (2.76a) and (2.76b) are consistent with the single-phase steady state at rest. Indeed, regarding the averaged momentum equation (2.69c) with $u_k = 0$, one obtains:*

$$\frac{\partial A_k P_k}{\partial x} - (P_1 - \rho_1 g \ell_1)\frac{\partial A_k}{\partial x} = A_k D_k + \left(\widetilde{P}_k - (P_1 - \rho_1 g \ell_1)\right)\frac{\theta_k}{2\pi}\frac{\partial S}{\partial x}.$$

Considering uniform pressure and single-phase flow, that is $\frac{\partial P_k}{\partial x} = 0$, $A_k = S$, $\theta_k = 2\pi$ and $D_k = 0$, the above equation reads:

$$(P_k - \widetilde{P}_k)\big|_{A_k = S}\frac{\partial S}{\partial x} = 0,$$

and the single-phase steady state at rest yields:

$$\widetilde{P}_k\big|_{A_k=S} = P_k\big|_{A_k=S},$$

which is verified by (2.76b) and (2.76a), see Remark 2.2.

The closed system describing compressible two-layer flows in circular pipes with variable cross section writes:

$$\frac{\partial W}{\partial t} + \frac{\partial F(W)}{\partial x} + B(W)\frac{\partial W}{\partial x} = C(W) + D(W), \tag{2.77}$$

where:

$$W = (A_1, A_1\rho_1, A_2\rho_2, A_1\rho_1 u_1, A_2\rho_2 u_2)^T,$$

$$F(W) = \begin{pmatrix} 0 \\ A_1\rho_1 u_1 \\ A_2\rho_2 u_2 \\ A_1(\rho_1 u_1^2 + P_1) \\ A_2(\rho_2 u_2^2 + P_2) \end{pmatrix}, \quad B(W)\frac{\partial W}{\partial x} = \begin{pmatrix} u_2\frac{\partial A_1}{\partial x} \\ 0 \\ 0 \\ -(P_1 - \rho_1 g\ell_1)\frac{\partial A_1}{\partial x} \\ -(P_1 - \rho_1 g\ell_1)\frac{\partial A_2}{\partial x} \end{pmatrix},$$

$$C(W) = \begin{pmatrix} \lambda_p(P_1 - \rho_1 g\ell_1 - P_2) \\ -\lambda_m\Big(\big(\frac{P_1 + \rho_1 g(\eta_1 - \ell_1)}{\rho_1} + \Psi_1\big) - \big(\frac{P_2}{\rho_2} + \Psi_2\big)\Big) \\ \lambda_m\Big(\big(\frac{P_1 + \rho_1 g(\eta_1 - \ell_1)}{\rho_1} + \Psi_1\big) - \big(\frac{P_2}{\rho_2} + \Psi_2\big)\Big) \\ -\lambda_u(u_1 - u_2) - \big(\frac{u_1+u_2}{2}\big)\lambda_m\Big(\big(\frac{P_1 + \rho_1 g(\eta_1 - \ell_1)}{\rho_1} + \Psi_1\big) - \big(\frac{P_2}{\rho_2} + \Psi_2\big)\Big) \\ \lambda_u(u_1 - u_2) + \big(\frac{u_1+u_2}{2}\big)\lambda_m\Big(\big(\frac{P_1 + \rho_1 g(\eta_1 - \ell_1)}{\rho_1} + \Psi_1\big) - \big(\frac{P_2}{\rho_2} + \Psi_2\big)\Big) \end{pmatrix},$$

and:

$$D(W) = \begin{pmatrix} \frac{\theta_1}{2\pi}\big(\frac{\partial S}{\partial t} + u_2\frac{\partial S}{\partial x}\big) \\ 0 \\ 0 \\ \rho_1 g\widetilde{\eta_1 - z}\frac{\theta_1}{2\pi}\frac{\partial S}{\partial x} \\ (P_2 - (P_1 - \rho_1 g\ell_1))\frac{\theta_2}{2\pi}\frac{\partial S}{\partial x} \end{pmatrix},$$

where λ_p, λ_u and λ_m are positive bounded functions which depend on the state variable $(A_1, \rho_1, \rho_2, u_1, u_2)$. The hyperbolicity of the homogeneous problem associated with (2.77) is readily obtained following the same approach as in Section 2.5, the eigenvalues being unchanged.

Proposition 2.6. *The homogeneous problem associated with (2.77) is hyperbolic under the condition:*

$$|u_1 - u_2| \neq c_1. \tag{2.78}$$

Its eigenvalues are unconditionally real, given by:

$$\lambda_1 = u_2,\ \lambda_2 = u_1 - c_1,\ \lambda_3 = u_1 + c_1,\ \lambda_4 = u_2 - c_2,\ \lambda_5 = u_2 + c_2. \tag{2.79}$$

Dealing with the Riemann problem, the same analysis as in Section 2.5 leads to same results for (2.77). Thus, the nature of characteristic fields associated with the k-waves, $k = 1, .., 5$, and Riemann invariants can be detailed, as well as positivity properties and definition of jump conditions.

Remark 2.4. *The comments of Section 2.4 apply to the system (2.77). Particularly, taking $A_1(x,t) = S(x,t)$ in (2.77), one obtains the following system:*

$$\frac{\partial S\rho_1}{\partial t} + \frac{\partial S\rho_1 u_1}{\partial x} = 0, \tag{2.80}$$

$$\frac{\partial S\rho_1 u_1}{\partial t} + \frac{\partial S(\rho_1 u_1^2 + P_1)}{\partial x} = P_1 \frac{\partial S}{\partial x}, \tag{2.81}$$

as soon as the source terms vanish when $A_1 = S$. This resulting system correctly models a pressurized flow in a circular pipe with variable cross section where the pipe elasticity, taken into account here with the function $S(x,t)$, has a great influence on the speed of acoustic waves.

2.7 Conclusion

A new model is proposed herein to deal with stratified gas-liquid or vapor-liquid flows in pipes with variable cross section. It is a compressible two-layer model which results from an averaging process of the isentropic Euler set of equations with hydrostatic constraint on the liquid phase. The main difference with the two-layer models issued from the classical literature is that both phases are assumed compressible. Consequently, it more or less enters in the class of two-fluid two-pressure models and significant mathematical properties are obtained. The latter include hyperbolicity, entropy inequality and positivity. Regarding closure laws, the isentropic framework with hydrostatic constraint implies that the interfacial pressure is defined to satisfy this constraint although the interfacial velocity and source terms are provided by the entropy inequality. It is then observed that this closed system may correctly deal with pressurized flows without any switching on the pressure law. Indeed, this feature results from the compressible description of the stratified regime and opens the door, at least formally, to the modeling of transitions from stratified to pressurized flows and entrapped air pockets. In practice, note that industrial flows include low Mach velocities for both phases verifying $|u_k| \ll c_k$. Thus, with the aim of performing numerical simulations with the model presented herein, the current work involves the development of a numerical scheme regarding the asymptotic low Mach number behavior of the system. This approach will be validated building analytical solutions thanks to the detailed Riemann invariants and jump conditions of the homogeneous part. The overall mathematical/numerical model will be then assessed using experimental data. Secondly, the robustness of the scheme will be studied regarding pressurized flows and vanishing phases, see [20] for details.

2.A Error estimate for the closure $\overline{\rho_1 z} = \overline{\rho}_1 \overline{z}$

One considers the following linear pressure law for phase 1:

$$P_1(\rho_1) = P_{1,\text{ref}} + c_{1,\text{ref}}^2(\rho_1 - \rho_{1,\text{ref}}), \tag{2.A.1}$$

where $P_{1,\text{ref}}$, $\rho_{1,\text{ref}}$ and $c_{1,\text{ref}}$ are constant values fitted according to a reference state. In practice, one has $P_{1,\text{ref}} \sim 1$ bar, $\rho_{1,\text{ref}} \sim 1000$ kg.m^{-3} and $c_{1,\text{ref}} \sim 1500$ m.s^{-1}. Note that (2.A.1) is as relevant as the isentropic stiffened gas law proposed in Section 2.2 for water pipe flows and simplifies the analysis below. Thus, the hydrostatic constraint (2.3) reads:

$$\frac{\partial P_1(\rho_1)}{\partial z} = c_{1,\text{ref}}^2 \frac{\partial \rho_1}{\partial z} = -\rho_1 g, \tag{2.A.2}$$

and yields:

$$\rho_1(x,z,t) = r_1(x,t)\exp(-\frac{gz}{c_{1,\text{ref}}^2}), \tag{2.A.3}$$

where $r_1(x,t) = \rho_1(x,0,t)$. Using (2.A.3) and denoting $\varepsilon = \frac{gh_1}{c_{1,\text{ref}}^2}$, one obtains:

$$\overline{\rho_1 z} = \frac{1}{h_1}\int_0^{h_1} r_1(x,t)\exp(-\frac{gz}{c_{1,\text{ref}}^2})z dz = \frac{r_1 h_1}{\varepsilon^2}\Big(1 - (1+\varepsilon)\exp(-\varepsilon)\Big), \tag{2.A.4}$$

$$\overline{\rho}_1 \overline{z} = \frac{1}{h_1}\int_0^{h_1} r_1(x,t)\exp(-\frac{gz}{c_{1,\text{ref}}^2})dz\frac{h_1}{2} = \frac{r_1 h_1}{2\varepsilon}\Big(1 - \exp(-\varepsilon)\Big). \tag{2.A.5}$$

Regarding realistic configurations where $H \sim 1$ m, one has $\varepsilon \ll 1$ so that asymptotic expansions of (2.A.4) and (2.A.5) write:

$$\overline{\rho_1 z} = r_1 \frac{h_1}{2}\left(1 - \frac{2}{3}\varepsilon + \mathscr{O}(\varepsilon^2)\right), \tag{2.A.6}$$

$$\overline{\rho}_1 \overline{z} = r_1 \frac{h_1}{2}\left(1 - \frac{1}{2}\varepsilon + \mathscr{O}(\varepsilon^2)\right). \tag{2.A.7}$$

Therefore, one ends up with the following estimate:

$$\left|\frac{\overline{\rho_1 z} - \overline{\rho}_1 \overline{z}}{\overline{\rho}_1 \overline{z}}\right| = \frac{\varepsilon}{6} + \mathscr{O}(\varepsilon^2), \tag{2.A.8}$$

which justifies the closure $\overline{\rho_1 z} = \overline{\rho}_1 \overline{z}$. Note that this development is extended to the section-averaged case presented in Section 2.6.

2.B Positivity for heights and densities

Proposition 2.B.1. *Let L and T be two positive and real constants. Assume that u_k, $\partial_x u_k$ and the first two right-hand sides of (2.36) belong to $L^\infty([0,L]\times[0,T])$ for $k = 1,2$. Then, the latter equations associated with admissible inlet boundary conditions lead to:*

$$h_k(x,t) \in [0,H], \quad \forall (x,t) \in [0,L]\times[0,T], \tag{2.B.1}$$

$$\rho_k(x,t) \geq 0, \quad \forall (x,t) \in [0,L]\times[0,T], \tag{2.B.2}$$

when restricting ourselves to regular solutions.

Proof. We place ourselves in the general case and we consider a function Φ from $[0,L]\times[0,T]$ to $\mathbb{R}$ which verifies an equation of the form:

$$\frac{\partial \Phi}{\partial t} + a\frac{\partial \Phi}{\partial x} + \Phi\frac{\partial b}{\partial x} = \Phi m, \tag{2.B.3}$$

where a, b, m are smooth functions from $[0,L]\times[0,T]$ to $\mathbb{R}$ and a, $\partial_x a$, b, $\partial_x b$, m belong to $L^\infty([0,L]\times[0,T])$. Assume that Φ verifies positive inlet boundary conditions, that is $\Phi(x=0,t)$ and $\Phi(x=L,t)$ positive for all t in [0,T]. Let introduce the decomposition $\Phi = \Phi^+ - \Phi^-$, with $\Phi^+ \geq 0$, $\Phi^- \geq 0$ and $\Phi^+\Phi^- = 0$. Multiplying (2.B.3) by $-\Phi^-$ yields:

$$-\Phi^-\frac{\partial}{\partial t}(\Phi^+ - \Phi^-) - a\Phi^-\frac{\partial}{\partial x}(\Phi^+ - \Phi^-) - \Phi^-(\Phi^+ - \Phi^-)\frac{\partial b}{\partial x} = -\Phi^-(\Phi^+ - \Phi^-)m.$$

Defining the norm $\| \, . \, \| = (\int_0^L | \, . \, |^2 \, dx)^{1/2}$, one may obtain by integration over $[0,L]$:

$$\frac{\partial}{\partial t}(\| \, \Phi^- \, \|^2) + \int_0^L a\frac{\partial}{\partial x}(\Phi^-)^2 dx + 2\int_0^L (\Phi^-)^2\frac{\partial b}{\partial x}dx = 2\int_0^L (\Phi^-)^2 m dx.$$

Integrating by parts the second term of the left-hand side gives:

$$\frac{\partial}{\partial t}(\| \, \Phi^- \, \|^2) + [a(\Phi^-)^2]_0^L = \int_0^L (\Phi^-)^2(2m - 2\frac{\partial b}{\partial x} + \frac{\partial a}{\partial x})dx.$$

The positive inlet boundary conditions give $\Phi^-(x=0,t) = \Phi^-(x=L,t) = 0$, and thus, one can write:

$$\frac{\partial}{\partial t}(\| \, \Phi^- \, \|^2) \leq \int_0^L (\Phi^-)^2 |2m - 2\frac{\partial b}{\partial x} + \frac{\partial a}{\partial x}| dx \leq \| \, \Phi^- \, \|^2 \sup_{x\in[0,L]} |2m - 2\frac{\partial b}{\partial x} + \frac{\partial a}{\partial x}|.$$

Since the initial data on Φ is positive, the Gronwall's lemma gives for any time t in $[0,T]$:

$$\| \, \Phi^- \, \| \, (t) = 0.$$

Therefore, Φ^- is null and Φ remains positive on the whole domain $[0,L]\times[0,T]$. Finally, consider $\Phi = h_k$ and $\Phi = H - h_k$ to get (2.B.1), while $\Phi = m_k$ provides (2.B.2). □

References

[1] R. Abgrall and S. Karni. Two-layer shallow water system: a relaxation approach. *SIAM Journal on Scientific Computing*, 31(3):1603–1627, 2009.

[2] V.I. Agoshkov, D. Ambrosi, V. Pennati, A. Quarteroni, and F. Saleri. Mathematical and numerical modelling of shallow water flow. *Computational Mechanics*, 11(5):280–299, 1993.

[3] E. Audusse. A multilayer Saint-Venant system : Derivation and numerical validation. *Discrete Contin. Dyn. Syst. Ser. 5*, 5(2):189–214, 2005.

[4] E. Audusse, M.-O. Bristeau, B. Perthame, and J. Sainte-Marie. A multilayer Saint-Venant system with mass exchanges for shallow water flows. derivation and numerical validation. *ESAIM: Mathematical Modelling and Numerical Analysis*, 45:169–200, 2011.

[5] M. R. Baer and J. W. Nunziato. A two phase mixture theory for the deflagration to detonation (DDT) transition in reactive granular materials. *International Journal of Multiphase Flow*, 12(6):861–889, 1986.

[6] A.J.C. Barré de Saint Venant. Théorie du mouvement non-permanent des eaux avec application aux crues des rivières et à l'introduction des marées dans leur lit. *C.R. Acad. Sc. Paris.*, 73:147–154, 1871.

[7] F. Bouchut, E.D. Fernández-Nieto, A. Mangeney, and P.-Y. Lagrée. On new erosion models of Savage-Hutter type for avalanches. *Acta Mechanica*, 199(1):181–208, 2008.

[8] F. Bouchut, A. Mangeney-Castelnau, B. Perthame, and J.-P. Vilotte. A new model of Saint Venant and Savage-Hutter type for gravity driven shallow water flows. *C. R. Acad. Sci. Paris, Ser. I*, 336:531–536, 2003.

[9] F. Bouchut and T. Morales de Luna. An entropy satisfying scheme for two-layer shallow water equations with uncoupled treatment. *ESAIM: Mathematical Modelling and Numerical Analysis*, 42(4):683–698, 2008.

[10] C. Bourdarias, M. Ersoy, and S. Gerbi. A mathematical model for unsteady mixed flows in closed water pipes. *Science China Mathematics*, 55(2):221–244, 2012.

[11] C. Bourdarias, M. Ersoy, and S. Gerbi. Air entrainment in transient flows in closed water pipes : a two-layer approach. *ESAIM: Mathematical Modelling and Numerical Analysis*, 47(2):507–538, 2013.

[12] C. Bourdarias and S. Gerbi. A finite volume scheme for a model coupling free surface and pressurised flows in pipes. *Journal of Computational and Applied Mathematics*, 209:1–47, 2007.

[13] S. Bousso, M. Daynou, and M. Fuamba. Numerical modeling of mixed flows in storm water systems: Critical review of literature. *Journal of Hydraulic Engineering*, 139(4):385–396, 2013.

[14] H. Capart, X. Sillen, and Y. Zech. Numerical and experimental water transients in sewer pipes. *Journal of Hydraulic Research*, 35(5):659–672, 1997.

[15] M.J. Castro, J.A. García-Rodríguez, J.M. González-Vida, J. Macás, C. Parés, and Vásquez-Cendón M.E. Numerical simulation of two-layer shallow water flows through channels with irregular geometry. *Journal of Computational Physics*, 195(1):202–235, 2004.

[16] M.H. Chaudhry, S.M. Bhallamudi, C.S. Martin, and M. Naghash. Analysis of transient pressures in bubbly, homogeneous, gas-liquid mixtures. *Journal of Fluids Engineering*, 112(2):225–231, 1990.

[17] C. D. Chosie, T. M. Hatcher, and J. G. Vasconcelos. Experimental and numerical investigation on the motion of discrete air pockets in pressurized water flows. *Journal of Hydraulic Engineering*, 140(8):25–34, 2014.

[18] F. Coquel, T. Gallouët, J.-M. Hérard, and N. Seguin. Closure laws for a two-fluid two-pressure model. *C. R. Acad. Sci. Paris*, 334(I):927–932, 2002.

[19] F. Coquel, J.-M. Hérard, K. Saleh, and N. Seguin. Two properties of two-velocity two-pressure models for two-phase flows. *Communications in Mathematical Sciences*, 12(3):593–600, 2014.

[20] C. Demay. *Modelling and simulation of transient two-phase air-water flows in hydraulic pipes*. PhD thesis, Université Savoie Mont Blanc, in preparation.

[21] M. Diémé. *Etudes théorique et numérique de divers écoulements en couche mince*. PhD thesis, Université Laval, Québec, 2012.

[22] M. Escarameia. Investigating hydraulic removal of air from water pipelines. *Proceedings of the Institution of Civil Engineers-Water Management.*, 160(1):25–34, 2007.

[23] I. Faille and E. Heintze. A rough finite volume scheme for modeling two-phase flow in a pipeline. *Computers & Fluids*, 28(2):213–241, 1999.

[24] T. Gallouët, P. Helluy, J.-M. Hérard, and J. Nussbaum. Hyperbolic relaxation models for granular flows. *ESAIM: Mathematical Modelling and Numerical Analysis*, 44(2):371–400, 2010.

[25] T. Gallouët, J.-M. Hérard, and N. Seguin. Numerical modeling of two-phase flows using the two-fluid two-pressure approach. *Mathematical Models and Methods in Applied Sciences*, 14(05):663–700, 2004.

[26] S.L. Gavrilyuk. The structure of pressure relaxation terms : one-velocity case. *EDF report H-I83-2014-00276-EN*, 2014.

[27] S.L. Gavrilyuk and R. Saurel. Mathematical and numerical modeling of two-phase compressible flows with micro-inertia. *Journal of Computational Physics*, 175(1):326–360, 2002.

[28] J.-F. Gerbeau and B. Perthame. Derivation of viscous Saint-Venant system for laminar shallow water; numerical validation. *Discrete Contin. Dyn. Syst. Ser. B*, 1:89–102, 2001.

[29] J. Glimm, D. Saltz, and D. H. Sharp. Two phase flow modelling of a fluid mixing layer. *Journal of Fluid Mechanics*, 378:119–143, 1999.

[30] M. Ishii. *Thermo-fluid dynamic theory of two-phase flow*. Paris, Eyrolles (Collection de la Direction des Etudes et Recherches d'Electricite de France), 1975.

[31] A. K. Kapila, S. F. Son, J. B. Bdzil, R. Menikoff, and D. S. Stewart. Two-phase modeling of DDT: Structure of the velocity-relaxation zone. *Physics of Fluids*, 9(12):3885–3897, 1997.

[32] T. Morales de Luna. A Saint Venant model for gravity driven shallow water flows with variable density and compressibility effects. *Mathematical and Computer Modelling*, 47(3):436–444, 2008.

[33] S. Müller, M. Hantke, and P. Richter. Closure conditions for non-equilibrium multi-component models. *Continuum Mechanics and Thermodynamics*, 28(4):1157–1189, 2016.

[34] M. Murakami and K. Minemura. Effects of entrained air on the performance of a horizontal axial-flow pump. *Journal of Fluids Engineering*, 105(4):382–388, 1983.

[35] I.W.M. Pothof and F.H.L.R. Clemens. Experimental study of air-water flow in downward sloping pipes. *International Journal of Multiphase Flow*, 37(3):278–292, 2011.

[36] A. Poullikkas. Effects of two-phase liquid-gas flow on the performance of nuclear reactor cooling pumps. *Progress in Nuclear Energy*, 42(1):3–10, 2003.

[37] O Pozos, C. Gonzalez, J. Giesecke, W. Marx, and E. Rodal. Air entrapped in gravity pipeline systems. *Journal of Hydraulic Research*, 48(3):338–347, 2010.

[38] V. H. Ransom and D. L. Hicks. Hyperbolic two-pressure models for two-phase flow. *Journal of Computational Physics*, 53:124–151, 1984.

Chapter 3

Numerical simulation of a compressible two-layer model: a first attempt with an implicit-explicit splitting scheme

Abstract: This work is devoted to the numerical simulation of the Compressible Two-Layer model developed in [15]. The latter is an hyperbolic two-fluid two-pressure model dedicated to gas-liquid flows in pipes, especially stratified air-water flows. Using explicit schemes, one obtains a CFL condition based on the celerity of (fast) acoustic waves which typically brings large numerical diffusivity for the (slow) material waves and small time steps. In order to overcome these drawbacks, the proposed scheme involves an operator splitting and an implicit-explicit time discretization. Thus, the full system is split into two hyperbolic sub-systems. The first one deals with the transport equation on the liquid height using an explicit scheme and upwind fluxes. The second one deals with the averaged mass and momentum conservation equations of both phases using an implicit scheme which handles the propagation of acoustic waves. At last, the positivity of heights and densities is ensured under a CFL condition which involves material velocities. Numerical experiments are performed using acoustic as well as material time steps. Adding the Rusanov scheme for comparison, the best accuracy is obtained with the proposed scheme used with acoustic time steps. When used with material time steps, efficiency on the slow waves and stability are obtained regarding analytical solutions of the convective part.

Note: The content of this chapter has been submitted to an international journal. It is also available on HAL under the reference:

- C. Demay, C. Bourdarias, B. de Laage de Meux, S. Gerbi, and J.-M. Hérard. Numerical simulation of a compressible two-layer model: a first attempt with an implicit-explicit splitting scheme, *Preprint*. URL: https://hal.archives-ouvertes.fr/hal-01421889.

Contents

3.1 Introduction

The Compressible Two-Layer model proposed in [15] deals with transient gas-liquid flows in pipes, especially stratified air-water flows which occur in several industrial areas such as nuclear power plants, petroleum industries or sewage pipelines. It is a five-equation system which results from a depth averaging of the isentropic Euler set of equations for each phase where the classical hydrostatic assumption is applied to the liquid. This system is composed by a transport equation on the liquid height in addition to averaged mass and averaged momentum conservation equations for both phases. The derivation process presents similarities with the work exposed in [23]. Thus, the resulting model is a two-fluid two-pressure model and displays the same structure as an isentropic Baer-Nunziato model which provides a statistical description of two-phase flows, especially granular flows or bubbly flows (see for instance [3, 16]). In this context, interesting mathematical properties are obtained such as hyperbolicity, entropy inequality, explicit eigenstructure as well as Riemann invariants and uniqueness of jump conditions. Note that the numerical discretization of the Compressible Two-Layer model has not been considered yet in the literature such that the work presented in the sequel is a first attempt.

From a numerical point of view, the Compressible Two-Layer model, as the isentropic Baer-Nunziato model, are complex to deal with for several reasons. The first difficulty arises from the large size of the system which makes the Riemann problem difficult to solve regarding the convective part and Godunov-type methods. The second difficulty is linked to the presence of non-conservative products in the governing equations such that the model does not admit a full conservative form. However, the non-conservative products vanish and the system reduces to two decoupled isentropic Euler-type systems on both sides of a linearly degenerate field which is parametrized using the corresponding Riemann invariants. The third difficulty results from the non-linearity in pressure laws which renders even more difficult the derivation of Riemann solvers. When dealing with the full system, one also has to account for relaxation processes, in particular pressure relaxation and velocity relaxation given by the source terms, which bring numerical issues regarding the involved time scales.

Despite the mentioned difficulties, some successful solvers are proposed in the literature focusing on the convective part of the Baer-Nunziato system. They are mainly time-explicit Godunov-type methods such as Roe-like scheme, HLL or HLLC scheme and relaxation scheme, see [11, 27, 2, 1, 14, 25] among others. For stability reasons, such methods have to comply with the usual Courant-Friedrichs-Lewy (CFL) condition on the time step which involves

the celerity of (fast) acoustic waves and can be very restrictive. In our framework of two-layer pipe flows, even if we are interested in the accurate description of fast waves when the pipe is full of water (in water hammer situation for instance), we are also interested in the dynamics of slow waves associated to material velocities. Thus, an additional difficulty relies in the mix of two types of waves, namely the (fast) acoustic and the (slow) material waves. A possible way to tackle this issue is to use a fractional step method or equivalently an operator splitting. It consists in a multi-step algorithm where each step deals with a system containing exclusively acoustic or material waves. This approach is developed in [4, 6] for the Euler model and in [10] for the isentropic Baer-Nunziato model, among others. Note also that some similarities may be found with the so-called flux splitting approach used in [29] for the Euler model and recently in [28] for the Baer-Nunziato model. However, the above-mentioned references are explicit in time and the CFL condition on the time step still relies on the celerity of fast waves. In order to obtain a less restrictive CFL condition, an implicit-explicit scheme may be used where the fast waves are treated implicitly and the slow waves explicitly to preserve accuracy. Combining the splitting approach and the implicit-explicit treatment, one obtains a CFL condition based on material velocities and consequently a large time-step scheme. This was initially proposed in the context of the Euler model, see [12, 8], and an extension to the Baer-Nunziato model was proposed in [7]. Particularly, the latter references use a Lagrange-Projection approach that consists in approximating the gas dynamics equation using the Lagrange coordinates and then remapping the solution onto an Eulerian mesh. Note that implicit-explicit strategies are also used to derive all speed or all Mach schemes with asymptotic preserving properties regarding the compressible Euler model and its incompressible limit, see [19, 13, 22, 8]. Thus, one can obtain accurate schemes in the low Mach regime with large time steps. Nonetheless, such low Mach properties are still difficult to acquire for two-fluid two-pressure models as the limit model is not clearly defined.

The work presented herein provides numerical results regarding the Compressible Two-Layer model and the related challenges exposed above. Thus, in addition to consider a classical explicit Rusanov scheme known for its robustness, see [24], we propose a large time-step implicit-explicit scheme relying on an operator-splitting approach. The five-equation system is split into two hyperbolic sub-systems. The first one deals with the transport equation on the liquid height using an explicit scheme and upwind fluxes. The second one deals with the averaged mass and momentum conservation equations using an implicit scheme which handles the propagation of acoustic waves. The positivity of heights and densities is ensured under a CFL condition which involves material velocities. Numerical experiments with grid convergence studies are performed with both schemes using analytical solutions for the convective part of the system. The source terms are then handled accounting for the interactions between the convective dynamics and relaxation processes. The dambreak test case is first considered where the numerical solutions are compared with a reference solution given by the incompressible one-layer shallow-water system. Secondly, one considers a so-called mixed flow test case which involves a transition to the pressurized regime (pipe full of water) through a pipe filling.

The paper is organized as follows. The governing equations of the model under consideration are recalled in Section 3.2 as well as its main mathematical properties. Focusing on the convective part of the system, the splitting approach and the associated implicit-explicit scheme are presented in Section 3.3. Numerical experiments are then performed in Section 3.4 building analytical solutions thanks to the available jump conditions and Riemann invariants. In the last part, the full model with the source terms is handled and tested against the dambreak problem and a mixed-flow configuration.

3.2 The Compressible Two-Layer model

The Compressible Two-Layer model, referred to as the CTL model hereafter, has been introduced in [15] to deal gas-liquid flows in pipes, see Figure 3.1 for a typical configuration. The governing equations of the model and its main mathematical properties are exposed below. In the sequel, we focus on air-water flows but the general approach applies to gas-liquid flows.

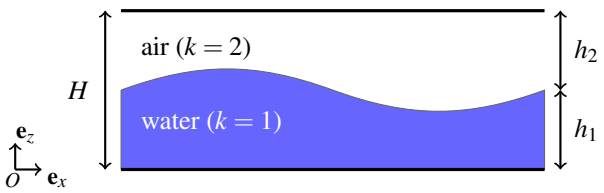

Figure 3.1: Geometric description for horizontal channels.

3.2.1 Governing equations

The CTL model belongs to the class of two-fluid two-pressure models introduced by Ransom & Hicks in [23]. It results from a depth-averaging of the isentropic Euler set of equations for each phase, see [15] for details. Considering a two-layer air-water flow through an horizontal rectangular pipe of height H, see Figure 3.1, the model reads:

$$\frac{\partial h_1}{\partial t} + U_I \frac{\partial h_1}{\partial x} = \lambda_p (P_I - P_2(\rho_2)), \tag{3.1a}$$

$$\frac{\partial h_k \rho_k}{\partial t} + \frac{\partial h_k \rho_k u_k}{\partial x} = 0,\ k = 1,2, \tag{3.1b}$$

$$\frac{\partial h_k \rho_k u_k}{\partial t} + \frac{\partial h_k (\rho_k u_k^2 + P_k(\rho_k))}{\partial x} - P_I \frac{\partial h_k}{\partial x} = (-1)^k \lambda_u (u_1 - u_2),\ k = 1,2, \tag{3.1c}$$

where $k = 1$ for water, $k = 2$ for air, and $h_1 + h_2 = H$. Here, h_k, ρ_k, $P_k(\rho_k)$ and u_k denote respectively the height, the mean density, the mean pressure and the mean velocity of phase k. The interfacial variables, namely the interfacial pressure and the interfacial velocity, are denoted P_I and U_I respectively. The interface dynamics is represented by (3.1a) while mass and momentum conservation for each phase are given respectively by (3.1b) and (3.1c).

The main originality of the CTL model comes from the integration of the hydrostatic constraint applied to the water phase which results in a closure law for P_I. This constraint is essential in order to account for water gravity waves in the stratified regime. The closure law for the interfacial velocity is obtained using an entropy inequality as in [9]. The resulting closures read:

$$(U_I, P_I) = (u_2, P_1 - \rho_1 g \frac{h_1}{2}), \tag{3.2}$$

where g is the gravity field magnitude. As the phases are compressible, state equations are required for gas and liquid pressures. For instance, perfect gas law may be used for air and linear law for water:

$$P_1(\rho_1) = (\rho_1 - \rho_{1,\text{ref}}) c_{1,\text{ref}}^2 + P_{1,\text{ref}}, \tag{3.3a}$$

$$P_2(\rho_2) = P_{2,\text{ref}} \Big(\frac{\rho_2}{\rho_{2,\text{ref}}} \Big)^{\gamma_2}, \tag{3.3b}$$

with some reference density $\rho_{k,\text{ref}}$ and pressure $P_{k,\text{ref}}$. The celerity of acoustic waves is defined by:

$$c_k = \sqrt{P_k'(\rho_k)}, \tag{3.4}$$

where $P_k'(\rho_k) > 0$. For air, γ_2 is set to 7/5 (diatomic gas) and for water, c_1 is constant and equals to a reference celerity denoted $c_{1,\text{ref}}$.

In the following, the thermodynamic reference state is chosen to deal with air-water flows at $20^o C$: $P_{k,\text{ref}} = 1$ bar, $\rho_{1,\text{ref}} = 998.1115$ kg.m^{-3}, $c_{1,\text{ref}} = 1500$ m.s^{-1}, $\rho_{2,\text{ref}} = 1.204$ kg.m^{-3} and $c_2 = 350$ m.s^{-1}. Note that phase 1 inherits from the *fastest* pressure waves. Regarding the source terms, λ_p and λ_u are positive bounded functions which account for relaxation time scales, see Appendix 3.A for details.

Denoting W the state variable defined as:

$$W = (h_1, h_1\rho_1, h_1\rho_1 u_1, h_2\rho_2, h_2\rho_2 u_2)^T, \tag{3.5}$$

and using (3.2), the system (3.1) may be written under the following condensed form:

$$\frac{\partial W}{\partial t} + \frac{\partial F(W)}{\partial x} + B(W)\frac{\partial W}{\partial x} = C(W), \tag{3.6}$$

where:

$$F(W) = \begin{bmatrix} 0 \\ h_1\rho_1 u_1 \\ h_2\rho_2 u_2 \\ h_1(\rho_1 u_1^2 + P_1) \\ h_2(\rho_2 u_2^2 + P_2) \end{bmatrix},\ B(W)\frac{\partial W}{\partial x} = \begin{bmatrix} u_2 \frac{\partial h_1}{\partial x} \\ 0 \\ 0 \\ -(P_1 - \rho_1 g \frac{h_1}{2}) \frac{\partial h_1}{\partial x} \\ -(P_1 - \rho_1 g \frac{h_1}{2}) \frac{\partial h_2}{\partial x} \end{bmatrix},$$

and:

$$C(W) = \begin{bmatrix} \lambda_p (P_1 - \rho_1 g \frac{h_1}{2} - P_2) \\ 0 \\ 0 \\ -\lambda_u (u_1 - u_2) \\ \lambda_u (u_1 - u_2) \end{bmatrix}.$$

As discussed in [15], note that this model is consistent with the shallow water equations as well as the depth-averaged single-phase Euler equations used for pressurized flows. Moreover, its formulation is very close to the isentropic Baer-Nunziato model suited for dispersed flows. Thus, the numerical method exposed in the sequel applies to this other model.

3.2.2 Mathematical properties

In this section, the main mathematical properties of (3.6) are recalled. Details and proofs are available in [15].

Property 3.1 (Entropy inequality)**.** *Smooth solutions of system* (3.6) *comply with the entropy inequality*

$$\frac{\partial \mathscr{E}}{\partial t} + \frac{\partial \mathscr{G}}{\partial x} \leq 0$$

where the entropy $\mathscr{E}$ *and the entropy flux* $\mathscr{G}$ *are defined by:*

$$\begin{aligned}
&\mathscr{E} = E_{c,1} + E_{p,1} + E_{t,1} + E_{c,2} + E_{t,2},\\
&\mathscr{G} = u_1(E_{c,1} + E_{p,1} + E_{t,1}) + u_2(E_{c,2} + E_{t,2}) + u_1 h_1 P_1 + u_2 h_2 P_2,
\end{aligned}$$

with:

$$E_{c,k} = \frac{1}{2} h_k \rho_k u_k^2,\ E_{t,k} = h_k \rho_k \Psi_k(\rho_k),\ E_{p,1} = \rho_1 g \frac{h_1^2}{2},$$

and:

$$\Psi_k'(\rho_k) = \frac{P_k(\rho_k)}{\rho_k^2},\ k = 1,2.$$

Property 3.2 (Hyperbolicity and structure of the convective system)**.** *The convective part of* (3.6) *is hyperbolic under the condition:*

$$|u_1 - u_2| \neq c_1.$$

Its eigenvalues are unconditionally real and given by:

$$\lambda_1 = u_2,\ \lambda_2 = u_1 - c_1,\ \lambda_3 = u_1 + c_1,\ \lambda_4 = u_2 - c_2,\ \lambda_5 = u_2 + c_2. \tag{3.7}$$

The field associated with the 1-wave λ_1 *is linearly degenerate while the fields associated with the waves* λ_k, $k = 2,..,5$, *are genuinely nonlinear. Moreover, all the Riemann invariants can be detailed.*

Property 3.3 (Uniqueness of jump conditions)**.** *Unique jump conditions hold within each isolated field. For all genuine non-linear fields corresponding to the k-waves,* $k = 2,...,5$*, the Rankine-Hugoniot jump conditions across a single discontinuity of speed* σ *write:*

$$\begin{aligned}
&[h_k] = 0,\\
&[h_k \rho_k (u_k - \sigma)] = 0,\\
&[h_k \rho_k u_k (u_k - \sigma) + h_k P_k] = 0,
\end{aligned}$$

where brackets $[.]$ *denote the difference between the states on both sides of the discontinuity.*

Furthermore, as the field associated to the jump of h_1 is linearly degenerate, the non-conservative products $u_2 \partial_x h_1$ and $(P_1 - \rho_1 g \frac{h_1}{2}) \partial_x h_1$ in (3.6) are well defined. Indeed, one may use the available 1-Riemann invariants to write explicitly the 1-wave parametrisation.

Property 3.4 (Positivity)**.** *Focusing on smooth solutions, the positivity of* h_k *and* ρ_k *is verified, as soon as* λ_p *may be written under the form* $\lambda_p = m_1 m_2 \tilde{\lambda}_p$*, where* $\tilde{\lambda}_p$ *is a positive bounded function depending on the state variable. The positivity requirements hold for discontinuous solutions of the Riemann problem associated to the homogeneous system* (3.6)*.*

As the jump conditions and the Riemann invariants can be detailed, recall that one can build analytical solutions for the convective part of (3.6) including the contact discontinuity, shock waves and rarefaction waves. This approach is used in Section 3.4 to verify the numerical scheme exposed in the next section.

3.3 Splitting method and implicit-explicit scheme for the convective part

In this section, we focus on the convective part of (3.6):

$$\begin{cases} \dfrac{\partial h_1}{\partial t} + u_2 \dfrac{\partial h_1}{\partial x} = 0, \\ \dfrac{\partial m_k}{\partial t} + \dfrac{m_k u_k}{\partial x} = 0, \ k = 1,2, \\ \dfrac{\partial m_k u_k}{\partial t} + \dfrac{\partial m_k u_k^2}{\partial x} + \dfrac{\partial h_k P_k}{\partial x} - P_I \dfrac{\partial h_k}{\partial x} = 0, \ k = 1,2, \end{cases} \tag{$\mathscr{S}_0$}$$

where $m_k = h_k \rho_k$ and $h_1 + h_2 = H$. More precisely, the goal is to approximate the weak solutions of the associated Cauchy problem with discontinuous initial data:

$$\begin{cases} \dfrac{\partial W}{\partial t} + \dfrac{\partial F(W)}{\partial x} + B(W) \dfrac{\partial W}{\partial x} = 0, \ x \in \mathbb{R}, \ t > 0, \\ W(x,0) = W_0(x). \end{cases} \tag{3.8}$$

Using classical explicit schemes to discretize ($\mathscr{S}_0$) and regarding its eigenvalue in (3.7), one obtains a typical CFL condition driven by the fast waves which writes formally:

$$\frac{\Delta t}{\Delta x} \max(|u_2|, |u_1 \pm c_1|, |u_2 \pm c_2|) < 1, \tag{3.9}$$

where Δx and Δt denote respectively the space step and the time step. Dealing with low speed flow, that is $|u_k| \ll |u_k \pm c_k|$, (3.9) may be very constraining and may induce low precision on the material wave (slow wave) which has a leading role in this regime. Thus, the goals of this work is to propose an implicit-explicit scheme more accurate than a classical Rusanov explicit scheme and to examine its ability to relax the CFL condition (3.9). The overall strategy is to split ($\mathscr{S}_0$) between the material wave λ_1 and the acoustic waves λ_k, $k = 2,..,5$, in order to adapt the numerical treatment: roughly speaking, explicit scheme for the slow wave, implicit scheme for the fast waves. As detailed below, this approach results in CFL conditions which rely on material velocities.

3.3.1 Splitting approach

It is proposed to split the system ($\mathscr{S}_0$) into two sub-systems ($\mathscr{S}_1$) and ($\mathscr{S}_2$):

$$\begin{cases} \dfrac{\partial h_1}{\partial t} + u_2 \dfrac{\partial h_1}{\partial x} = 0, \\ \dfrac{\partial m_k}{\partial t} = 0, \ k = 1,2, \\ \dfrac{\partial m_k u_k}{\partial t} = 0, \ k = 1,2. \end{cases} \tag{$\mathscr{S}_1$}$$

$$\begin{cases} \dfrac{\partial h_1}{\partial t} = 0, \\ \dfrac{\partial m_k}{\partial t} + \dfrac{\partial m_k u_k}{\partial x} = 0, \ k = 1,2, \\ \dfrac{\partial m_k u_k}{\partial t} + \dfrac{\partial m_k u_k^2}{\partial x} + \dfrac{\partial h_k P_k}{\partial x} - P_I \dfrac{\partial h_k}{\partial x} = 0, \ k = 1,2. \end{cases} \tag{$\mathscr{S}_2$}$$

A physical interpretation of this splitting can be given in the context of porous flows where h_1 would stand for the porosity. In the first step, one updates the porosity in time and space. In the second step, the porosity is frozen w.r.t. time and the densities and velocities are updated according to this porosity field. In practice, it leads to a splitting of eigenvalues between ($\mathscr{S}_1$) which contains the material wave and ($\mathscr{S}_2$) which contains the acoustic waves, with the following properties:

- ($\mathscr{S}_1$) *is unconditionally hyperbolic*. Its eigenvalues are unconditionally real and given by:

$$\eta_1 = u_2,$$
$$\eta_p = 0, \ p = 2,..,5.$$

All the characteristic fields are linearly degenerate.

- ($\mathscr{S}_2$) *is unconditionally hyperbolic*. Its eigenvalues are unconditionally real and given by:

$$\begin{aligned} \mu_1 &= 0, \\ \mu_2 = u_1 - c_1,\ \mu_3 &= u_1 + c_1, \\ \mu_4 = u_2 - c_2,\ \mu_5 &= u_2 + c_2. \end{aligned}$$

The field associated with the 1-wave $\mu_1 = 0$ is linearly degenerate while the fields associated with $\mu_p,\ p = 2,..,5$, are genuinely nonlinear.

The numerical strategy is then to use an explicit scheme for ($\mathscr{S}_1$) and an implicit scheme for ($\mathscr{S}_2$).

3.3.2 Numerical approximation

In the following, we use the operator splitting method in order to derive a fractional-step numerical scheme. The space step Δx is assumed to be constant for simplicity in the notations such that the space is partitioned into cells:

$$\mathbb{R} = \bigcup_{i\in\mathbb{N}^*} C_i \text{ with } C_i = [x_{i-\frac{1}{2}}, x_{i+\frac{1}{2}}[,\ \forall i \in \mathbb{N}^*,$$

where $x_{i+\frac{1}{2}} = (i+\frac{1}{2})\Delta x$ are the cell interfaces. The time step is denoted Δt and is calculated at each iteration. For the iteration n, the solution of (3.8) is approximated on each cell C_i by a constant value denoted by:

$$W_i^n = \Big((h_1)_i^n, (h_1\rho_1)_i^n, (h_1\rho_1 u_1)_i^n, (h_2\rho_2)_i^n, (h_2\rho_2 u_2)_i^n\Big)^T.$$

The following notation is also introduced:

$$\begin{cases} f^+ = \max(f,0), \\ f^- = \min(f,0), \end{cases}$$

such that $f = f^+ + f^-$ and $|f| = f^+ - f^-$.

The first step of the proposed numerical scheme is associated to ($\mathscr{S}_1$) and updates W_i from W_i^n to W_i^* while the second step is associated to ($\mathscr{S}_2$) and updates W_i from W_i^* to W_i^{n+1}, each step being associated to the discrete time Δt. The overall numerical scheme is detailed in the next two subsections.

3.3.3 First step: water height update

In this step, one updates W_i from W_i^n to W_i^*. Regarding the last two equations of ($\mathscr{S}_1$), one obtains:

$$m_{k,i}^* = m_{k,i}^n, \tag{3.10}$$

$$(m_k u_k)_i^* = (m_k u_k)_i^n. \tag{3.11}$$

Consequently, $m_{k,i}$ and the velocity $u_{k,i}$ are constant but the density $\rho_{k,i}$ may vary as $h_{k,i}$ may vary.

Writing the transport equation on h_1 under the equivalent form $\frac{\partial h_1}{\partial t} + \frac{\partial u_2 h_1}{\partial x} - h_1\frac{\partial u_2}{\partial x} = 0$, an explicit first order upwind scheme is proposed:

$$\frac{h_{1,i}^* - h_{1,i}^n}{\Delta t} + \frac{(u_2h_1)_{i+\frac{1}{2}}^n - (u_2h_1)_{i-\frac{1}{2}}^n}{\Delta x} - (h_1)_i^n \frac{u_{2,i+\frac{1}{2}}^n - u_{2,i-\frac{1}{2}}^n}{\Delta x} = 0,$$

with:

$$\begin{cases} (u_2h_1)_{i+\frac{1}{2}}^n &= u_{2,i+\frac{1}{2}}^{n,+} h_{1,i}^n + u_{2,i+\frac{1}{2}}^{n,-} h_{1,i+1}^n, \\ u_{2,i+\frac{1}{2}}^n &= \frac{1}{2}(u_{2,i}^n + u_{2,i+1}^n), \end{cases}$$

such that one obtains:

$$h_{1,i}^* = \Big(1 - \frac{\Delta t}{\Delta x}(u_{2,i-\frac{1}{2}}^{n,+} - u_{2,i+\frac{1}{2}}^{n,-})\Big)h_{1,i}^n + \frac{\Delta t}{\Delta x}u_{2,i-\frac{1}{2}}^{n,+} h_{1,i-1}^n - \frac{\Delta t}{\Delta x}u_{2,i+\frac{1}{2}}^{n,-} h_{1,i+1}^n. \tag{3.12}$$

Proposition 3.1 (Positivity of heights)**.** *Regarding* (3.12)*, the positivity of $h_{k,i}^*$ is ensured as soon as the following CFL condition holds:*

$$\frac{\Delta t}{\Delta x}\max_i(u_{2,i-\frac{1}{2}}^{n,+} - u_{2,i+\frac{1}{2}}^{n,-}) \le 1. \tag{3.13}$$

As expected, this CFL condition only depends on material velocities.

3.3.4 Second step: densities and velocities update

In this step, one updates W_i from W_i^* to W_i^{n+1}. Regarding ($\mathscr{S}_2$), the first equation directly yields:

$$h_{1,i}^{n+1} = h_{1,i}^*. \tag{3.14}$$

The proposed time discretization for mass and momentum conservation equations reads:

$$\frac{m_k^{n+1} - m_k^*}{\Delta t} + \frac{\partial (m_k u_k)}{\partial x}^{n+1} = 0, \tag{3.15a}$$

$$\frac{(m_k u_k)^{n+1} - (m_k u_k)^*}{\Delta t} + \frac{\partial (m_k u_k)^{n+1} u_k^*}{\partial x} + h_k^{n+1} \frac{\partial (P_k)}{\partial x}^{n+1} + (P_k - P_I)^{n+1} \frac{\partial (h_k)}{\partial x}^{n+1} = 0. \tag{3.15b}$$

This approach is proposed in order to obtain an implicit equation on ρ_k, or equivalently P_k, and avoid a CFL condition which would involve the celerity of acoustic waves. The current step is divided into two sub-steps where the densities are updated first before updating the velocities using (3.15b).

3.3.4.a Densities update

At this stage, it is proposed to neglect the terms $\frac{\partial m_k u_k^2}{\partial x}$ and $(P_k - P_I)\frac{\partial h_k}{\partial x}$ in (3.15b) as they may not be leading terms regarding pressure effects. Thus, (3.15b) becomes:

$$\frac{(m_k u_k)^{n+1} - (m_k u_k)^*}{\Delta t} + h_k^{n+1} \frac{\partial (P_k)}{\partial x}^{n+1} = 0, \tag{3.16}$$

and combining it with (3.15a), one obtains the implicit governing equation of ρ_k which accounts for the propagation of acoustic waves:

$$h_k^{n+1} \rho_k^{n+1} - \Delta t^2 \frac{\partial}{\partial x}\left(h_k^{n+1} \frac{\partial P_k(\rho_k)}{\partial x}^{n+1} \right) = m_k^* - \Delta t \frac{\partial (m_k u_k)}{\partial x}^*. \tag{3.17}$$

After integration on a cell $C_i = [x_{i-\frac{1}{2}}, x_{i+\frac{1}{2}}[$ and using (3.14), it comes:

$$h_{k,i}^* \rho_{k,i}^{n+1} - \frac{\Delta t^2}{\Delta x}\left((h_k^* \frac{\partial (P_k)}{\partial x}^{n+1})_{i+\frac{1}{2}} - (h_k^* \frac{\partial (P_k)}{\partial x}^{n+1})_{i-\frac{1}{2}} \right) = m_{k,i}^* - \frac{\Delta t}{\Delta x}\left((m_k u_k)_{i+\frac{1}{2}}^* - (m_k u_k)_{i-\frac{1}{2}}^* \right),$$

with the corresponding fluxes:

$$\begin{cases} (h_k^* \frac{\partial (P_k)}{\partial x}^{n+1})_{i+\frac{1}{2}} = h_{k,i+\frac{1}{2}}^* \left(\frac{P_{k,i+1}^{n+1} - P_{k,i}^{n+1}}{\Delta x} \right), \\ (m_k u_k)_{i+\frac{1}{2}}^* = u_{k,i+\frac{1}{2}}^{*,+} m_{k,i}^* + u_{k,i+\frac{1}{2}}^{*,-} m_{k,i+1}^*. \end{cases}$$

The implicit system to solve finally writes:

$$\left(h_{k,i}^* \frac{\rho_k(P_{k,i}^{n+1})}{P_{k,i}^{n+1}} + \left(\frac{\Delta t}{\Delta x}\right)^2 (h_{k,i+\frac{1}{2}}^* + h_{k,i-\frac{1}{2}}^*) \right) P_{k,i}^{n+1} - \left(\frac{\Delta t}{\Delta x}\right)^2 h_{k,i-\frac{1}{2}}^* P_{k,i-1}^{n+1} - \left(\frac{\Delta t}{\Delta x}\right)^2 h_{k,i+\frac{1}{2}}^* P_{k,i+1}^{n+1} = S_{k,i}^*, \tag{3.18}$$

where:

$$S_{k,i}^* = \frac{\Delta t}{\Delta x} u_{k,i-\frac{1}{2}}^{*,+} m_{k,i-1}^* + \left(1 - \frac{\Delta t}{\Delta x}(u_{k,i+\frac{1}{2}}^{*,+} - u_{k,i-\frac{1}{2}}^{*,-}) \right) m_{k,i}^* - \frac{\Delta t}{\Delta x} u_{k,i+\frac{1}{2}}^{*,-} m_{k,i+1}^*. \tag{3.19}$$

In practice, the interface values $h_{k,i+\frac{1}{2}}^*$ and $u_{k,i+\frac{1}{2}}^*$ are defined by $h_{k,i+\frac{1}{2}}^* = \frac{1}{2}(h_{k,i}^* + h_{k,i+1}^*)$ and $u_{k,i+\frac{1}{2}}^* = \frac{1}{2}(u_{k,i}^* + u_{k,i+1}^*)$. At last, one obtains a non-linear system to solve which is linearized below regarding the choice of the pressure law $P_k(\rho_k)$. As exposed in (3.3), a perfect gas law is used for phase 2 while a linear pressure law is used for phase 1 which applies to air-water flows. In particular, an optimized approach regarding linear pressure laws is used to get the least restrictive CFL condition.

Nonlinear pressure laws
Using the relation $\frac{\partial P_2}{\partial t} = c_2^2(\rho_2)\frac{\partial \rho_2}{\partial t}$, one obtains:

$$\rho_{2,i}^{n+1} = \rho_{2,i}^{*} + \frac{P_{2,i}^{n+1} - P_{2,i}^{*}}{c_{2,i}^{*2}}. \tag{3.20}$$

Using (3.20), (3.18) is linearized and reads in matrix form:

$$A_2^{*}\mathbb{P}_2^{n+1} = \mathbb{S}_2^{*}, \tag{3.21}$$

with:

$$A_{2,ij}^{*} = \begin{cases} \frac{h_{2,i}^{*}}{c_{2,i}^{*2}} + \left(\frac{\Delta t}{\Delta x}\right)^2 (h_{2,i+\frac{1}{2}}^{*} + h_{2,i-\frac{1}{2}}^{*}) & \text{if } i = j, \\ -\left(\frac{\Delta t}{\Delta x}\right)^2 h_{2,i+\frac{1}{2}}^{*} & \text{if } j = i+1, \\ -\left(\frac{\Delta t}{\Delta x}\right)^2 h_{2,i-\frac{1}{2}}^{*} & \text{if } j = i-1, \\ 0 & \text{elsewhere,} \end{cases}$$

and:

$$\begin{aligned} \mathbb{P}_{2,i}^{n+1} &= P_{2,i}^{n+1}, \\ \mathbb{S}_{2,i}^{*} &= S_{2,i}^{*} - \left(1 - \frac{1}{\gamma_2}\right) m_{2,i}^{*}, \end{aligned}$$

where $\gamma_2 = \frac{P_{2,i}^{*}}{\rho_{2,i}^{*} c_{2,i}^{*2}} = \frac{7}{5}$ is related to the perfect gas law (3.3b). Note that once (3.21) is solved, one has to use (3.20) to compute $\rho_{2,i}^{n+1}$ instead of the pressure law for consistency reasons.

Linear pressure laws
Using the linearity of the pressure law for phase 1, see (3.3a), (3.18) is already linear. Thus, using $\rho_{1,i}^{n+1}$ instead of $P_{1,i}^{n+1}$ as an unknown, it reads in matrix form:

$$A_1^{*}\mathbb{R}_1^{n+1} = \mathbb{S}_1^{*}, \tag{3.22}$$

with:

$$A_{1,ij}^{*} = \begin{cases} h_{1,i}^{*} + \left(c_1 \frac{\Delta t}{\Delta x}\right)^2 (h_{1,i+\frac{1}{2}}^{*} + h_{1,i-\frac{1}{2}}^{*}) & \text{if } i = j, \\ -\left(c_1 \frac{\Delta t}{\Delta x}\right)^2 h_{1,i+\frac{1}{2}}^{*} & \text{if } j = i+1, \\ -\left(c_1 \frac{\Delta t}{\Delta x}\right)^2 h_{1,i-\frac{1}{2}}^{*} & \text{if } j = i-1, \\ 0 & \text{elsewhere,} \end{cases}$$

and:

$$\begin{aligned} \mathbb{R}_{1,i}^{n+1} &= \rho_{1,i}^{n+1}, \\ \mathbb{S}_{1,i}^{*} &= S_{1,i}^{*}. \end{aligned}$$

Therefore, the densities are updated solving (3.21) and (3.22), the positivity being ensured under the CFL conditions exposed below.

Proposition 3.2 (Positivity of densities)**.** *The positivity of ρ_1^{n+1} is ensured under the following CFL condition:*

$$\frac{\Delta t}{\Delta x} \max_i \left(u_{1,i+\frac{1}{2}}^{*,+} - u_{1,i-\frac{1}{2}}^{*,-} \right) \leq 1, \tag{3.23}$$

while the positivity of P_2^{n+1} (and thus ρ_2^{n+1}) is ensured under the following CFL condition:

$$\frac{\Delta t}{\Delta x} \max_i \left((u_{2,i+\frac{1}{2}}^{*,+} - u_{2,i-\frac{1}{2}}^{*,-})\gamma_2 \right) \leq 1, \tag{3.24}$$

where $\gamma_2 = \frac{\rho_{2,i}^{*} c_{2,i}^{*2}}{P_{2,i}^{*}} = \frac{7}{5}$ is related to the perfect gas law (3.3b).

Proof. Noting that A_k^* is a M-Matrix:

$$A_{k,ii}^* > 0, \qquad A_{k,i\neq j}^* \leq 0, \qquad |A_{k,ii}^*| - \sum_{j\neq i} |A_{k,ij}^*| > 0, \tag{3.25}$$

one obtains that A_k^* is non-singular and $(A_k^{*^{-1}})_{ii} > 0$, which provides:

$$\rho_{k,i}^{n+1} > 0, \forall i \iff \mathbb{S}_k^* > 0. \tag{3.26}$$

Thus, regarding nonlinear pressure laws and $\mathbb{S}_2^*$, one obtains the CFL condition (3.24). Regarding linear pressure laws, the condition $\mathbb{S}_1^* > 0$ yields (3.23). □

Finally, dealing with air-water flows, one has to solve (3.21) and (3.22) without violating the CFL conditions (3.24) and (3.23) which involves material velocities.

Remark 3.1. *If (3.24) would apply to phase 1 associated to the linearized pressure law (3.3a), one obtains:*

$$\frac{\rho_{1,i}^* c_{1,i}^{*2}}{P_{1,i}^*} = \frac{P_{1,i}^* + \Pi_1}{P_{1,i}^*},$$

where $\Pi_1 = \rho_{1,ref} c_{1,ref}^2 - P_{1,ref}$. When dealing with water and $P_1 \sim 1$ bar, $\frac{P_{1,i}^* + \Pi_1}{P_{1,i}^*} \sim 10^4$ and (3.24) would be very restrictive on $\frac{\Delta t}{\Delta x}$. It is thus profitable to use $\rho_{1,i}^{n+1}$ instead of $P_{1,i}^{n+1}$ as an unknown.

Remark 3.2. *Regarding (3.18), one may also propose the approximation $\frac{\rho_k(P_{k,i}^{n+1})}{P_{k,i}^{n+1}} P_{k,i}^{n+1} \approx \frac{\rho_k(P_{k,i}^*)}{P_{k,i}^*} P_{k,i}^{n+1}$ as a linearization process. Thus, one ends up with the following CFL condition:*

$$\frac{\Delta t}{\Delta x} \max_i \left(u_{k,i+\frac{1}{2}}^{*,+} - u_{k,i-\frac{1}{2}}^{*,-} \right) \leq 1,$$

which applies to both phases, independently of the pressure law. Note also that (3.18) may be treated as a nonlinear system to solve but it will not be considered here for computational efficiency reasons.

Remark 3.3. *One may estimate the condition number $\kappa(A_k)$ of A_k assuming constant heights. Indeed, one obtains a positive-definite matrix whose condition number scales roughly as:*

$$\kappa(A_k) \sim \frac{1 + 4(c_k \frac{\Delta t}{\Delta x})^2}{1 + \frac{4}{n^2}(c_k \frac{\Delta t}{\Delta x})^2},$$

where n denotes the number of grid points. Under the CFL conditions (3.24) and (3.23), one obtains $\kappa(A_k) \sim n^2$, which is a classical result dealing with the acoustic operator. In the general case, preconditioning techniques may be used to improve the efficiency of the linear solver.

3.3.4.b Velocities update

Integrating (3.15a) and (3.15b) on a cell $C_i = [x_{i-\frac{1}{2}}, x_{i+\frac{1}{2}}[$, one obtains:

$$m_{k,i}^{n+1} - m_{k,i}^* + \frac{\Delta t}{\Delta x} \left((m_k u_k)_{i+\frac{1}{2}}^{n+1} - (m_k u_k)_{i-\frac{1}{2}}^{n+1} \right) = 0, \tag{3.27}$$

$$(m_k u_k)_i^{n+1} - (m_k u_k)_i^* + \frac{\Delta t}{\Delta x} \left(((m_k u_k)^{n+1} u_k^*)_{i+\frac{1}{2}} - ((m_k u_k)^{n+1} u_k^*)_{i-\frac{1}{2}} \right)$$
$$+ \frac{\Delta t}{\Delta x} \left((h_k P_k)_{i+\frac{1}{2}}^{n+1} - (h_k P_k)_{i-\frac{1}{2}}^{n+1} - P_{I,i}^{n+1} (h_{k,i+\frac{1}{2}}^{n+1} - h_{k,i-\frac{1}{2}}^{n+1}) \right) = 0, \tag{3.28}$$

where the pressure gradient has been used under its conservative form. At this point, the fluxes $(m_k u_k)_{i+\frac{1}{2}}^{n+1}$ are known using (3.27) but one needs to compute the cell value $(m_k u_k)_i^{n+1}$. To this aim, one considers (3.28) using a first order upwind scheme for $((m_k u_k)^{n+1} u_k^*)_{i+\frac{1}{2}}$ which writes:

$$((m_k u_k)^{n+1} u_k^*)_{i+\frac{1}{2}} = (m_k u_k)_{i+\frac{1}{2}}^{n+1,+} u_{k,i}^* + (m_k u_k)_{i+\frac{1}{2}}^{n+1,-} u_{k,i+1}^*, \tag{3.29}$$

while centered fluxes are used for $(h_k P_k)_{i+\frac{1}{2}}^{n+1}$ and $h_{k,i+\frac{1}{2}}^{n+1}$.

This final step closes the numerical strategy for ($\mathscr{S}_0$) as all the variables are now updated.

3.4 Numerical experiments

In this section, we consider two test cases which are Riemann problems built using the available Riemann invariants and the jump conditions. Thus, the analytical solution is known and we compare it with the approximate solution obtained with the proposed implicit-explicit splitting scheme, which is denoted **SP** hereafter. In addition, we add for comparison a classical Rusanov explicit scheme applied on ($\mathscr{S}_0$).

3.4.1 Time and space step configurations

3.4.1.a Time step profiles

Regarding the Rusanov scheme, the associated CFL condition to guarantee the positivity of densities and heights classically writes:

$$\frac{\Delta t_a}{\Delta x}\max_i\left(\frac{r_{i+\frac{1}{2}}+r_{i-\frac{1}{2}}}{2}\right)=\frac{1}{2}, \tag{3.30}$$

where $r_{i+\frac{1}{2}}=\max\limits_{k\in\{1,..,5\}}(|\lambda^n_{k,i}|,|\lambda^n_{k,i+1}|)$, λ_k denoting the eigenvalues of ($\mathscr{S}_0$), see (3.7). Note that the CFL number has been chosen to be $\frac{1}{2}$. In our framework, Δt_a will be referred to as the *acoustic* time step as it contains the celerity of acoustic waves given by $u_k \pm c_k$.

Gathering the CFL conditions (3.13), (3.24), (3.23), the **SP** scheme guarantees the positivity of densities and heights under the condition:

$$\frac{\Delta t_m}{\Delta x}\max_i\left(u^{n,+}_{2,i-\frac{1}{2}}-u^{n,-}_{2,i+\frac{1}{2}},u^{*,+}_{1,i+\frac{1}{2}}-u^{*,-}_{1,i-\frac{1}{2}},(u^{*,+}_{2,i+\frac{1}{2}}-u^{*,-}_{2,i-\frac{1}{2}})\gamma_2\right)=\frac{1}{2}, \tag{3.31}$$

where the CFL number has been chosen to be $\frac{1}{2}$. In our framework, Δt_m will be referred to as the *material* time step as it contains only material speeds, which consequently yields $\Delta t_a < \Delta t_m$.

In order to evaluate the influence of the time step on the approximated solutions, one introduces two variants for the **SP** scheme:

- SP$_a$: **SP** scheme with the *acoustic* time step Δt_a defined in (3.30).
- SP$_m$: **SP** scheme with the *material* time step Δt_m defined in (3.31).

The two variants are compared with the Rusanov scheme whose time step is necessarily the *acoustic* one. To summarize, the time step profiles are sketched on Figure 3.2. Note that a ramp on the CFL number is used in the first iterations to start the calculations.

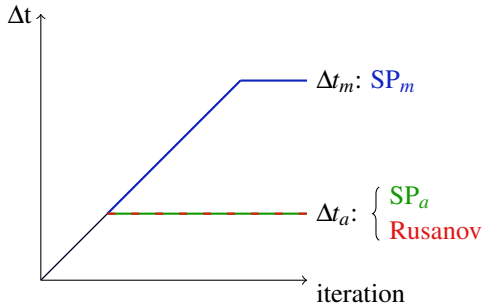

Figure 3.2: Time step profiles.

3.4.1.b Mesh refinement

The solutions are computed on the domain $[0,1]$ of the x-space where homogeneous Neumann conditions are imposed at the inlet and outlet. A mesh refinement is performed in order to check the numerical convergence of the method. For

this purpose, the discrete L^1-error between the approximate solution and the exact one at the final time T, normalized by the discrete L^1-norm of the exact solution, is computed:

$$\text{error}(\Delta x, T) = \frac{\sum_j |\mathscr{U}_j^n - \mathscr{U}_{ex}(x_j, T)|}{\sum_j |\mathscr{U}_{ex}(x_j, T)|}, \tag{3.32}$$

where $\mathscr{U}$ denotes the state vector in non conservative variables:

$$\mathscr{U} = (\alpha_1, \rho_1, u_1, \rho_2, u_2),$$

and $\mathscr{U}_{ex}$ stands for the exact solution. Note that Δt is defined from Δx through (3.30) or (3.31). In the refinement process, the coarser mesh is composed of 100 cells and the most refined one contains 200000 cells. Hereafter, the fields are plotted with 1000 cells and the error is plotted against Δx using a $log - log$ scale.

3.4.2 Numerical results

3.4.2.a Test case 1: one shock within each phase

In this first test case, one considers one shock within each phase. One shock on phase 2 is traveling at $\lambda_4 = u_2 - c_2$ and linking the left state $\mathscr{U}_L$ to the state $\mathscr{U}_C$. One shock on phase 1 is traveling at $\lambda_3 = u_1 + c_1$ and linking the state $\mathscr{U}_C$ to the right state $\mathscr{U}_R$. In particular, there is no contact discontinuity since the initial condition for h_1 is uniform. Thus, it consists in solving two decoupled isentropic Euler systems, see the wave structure and initial conditions on Figure 3.3. The fields at $T = 16.10^{-5}\,s$ with 1000 cells and the errors are displayed respectively on Figures 3.4 and 3.5.

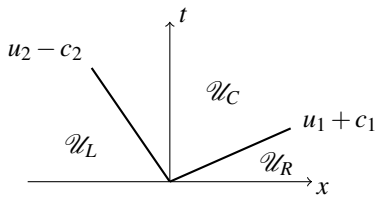

Variable	$\mathscr{U}_L$	$\mathscr{U}_C$	$\mathscr{U}_R$
h_1	0.5	0.5	0.5
ρ_1	998.11150	998.11150	997.11339
u_1	15	15	13.508384
ρ_2	1.204	1.3244	1.3244
u_2	10.0	-23.061466	-23.061466

Figure 3.3: Wave structure, initial conditions ($\mathscr{U}_L$, $\mathscr{U}_R$) and intermediate state ($\mathscr{U}_C$) for test case 1.

As a first comment, one can see on Figure 3.4 that the different methods approximate the relevant shock solutions. Regarding the fields and the errors for phase 1, the results for SP_a and Rusanov are similar. As phase 1 is the fastest one, Rusanov is in its optimal regime regarding the shock waves and compares well with SP_a. One observes a loss of accuracy with SP_m which is more diffusive around the shock location. Regarding the fields and the errors for phase 2, the best accuracy is obtained with SP_a which is partly due to the centered pressure gradient in the implicit equation (3.18). However, overshoots are observed on the fields but the latter are bounded in L^∞-norm and do not preclude the convergence. Regarding coarser meshes, SP_m is more accurate than Rusanov and both are comparable when the mesh is refined.

Dealing with isolated shock waves, one would expect to reach a first order convergence rate. This order is obtained for phase 2 but not for phase 1 which displays order $\frac{1}{2}$, see Figure 3.5. As an explanation, note that the shock on density is far weaker for phase 1 (water) than for phase 2 (air). Such configurations are realistic and make the shock more difficult to capture for phase 1.

Errors in L^1-norm against CPU time are displayed on Figure 3.6 for u_1 and u_2 (ρ_1 and ρ_2 respectively present the same trends). Considering a given error, one observes that SP_a is the most efficient scheme. Even if SP_m is more efficient than Rusanov on phase 2, it suffers from a lack of accuracy on the fastest phase (i.e phase 1) and the use of material time steps is not appropriate for this test case. Indeed, one considers only fast waves so that the optimal regime is obtained with acoustic time steps.

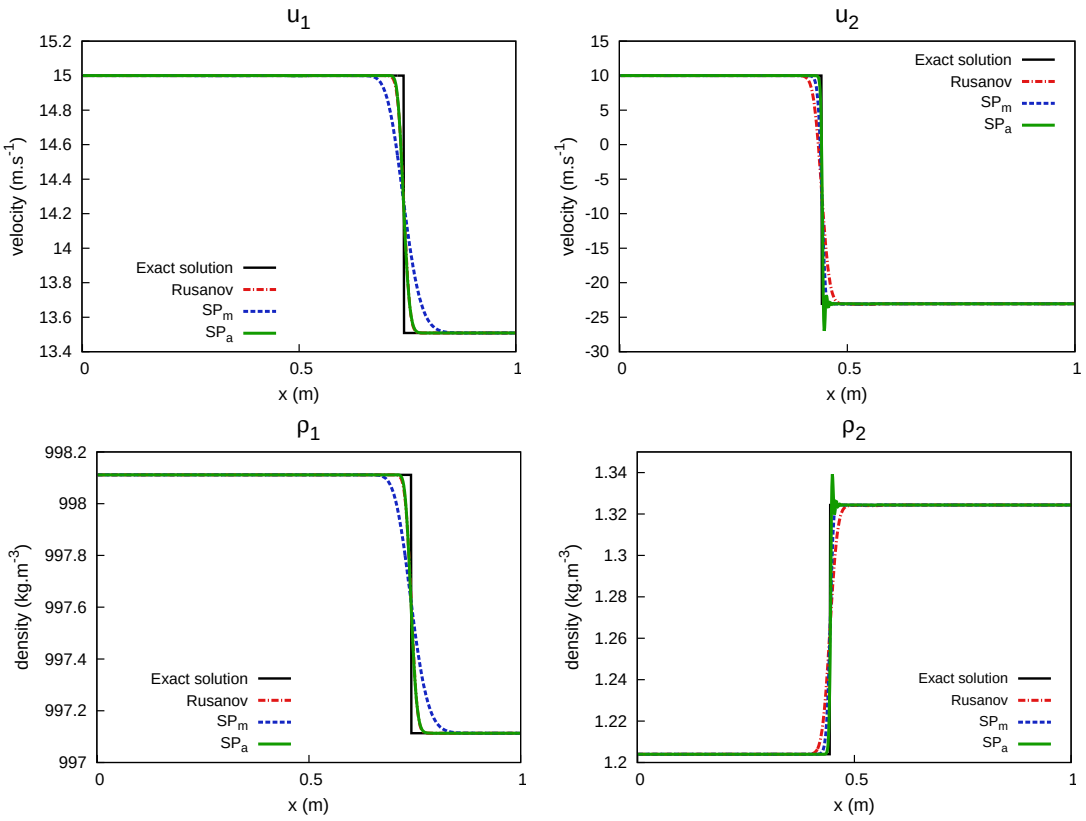

Figure 3.4: Approximate solution for test case 1 at $T = 16.10^{-5}\,s$ with 1000 cells.

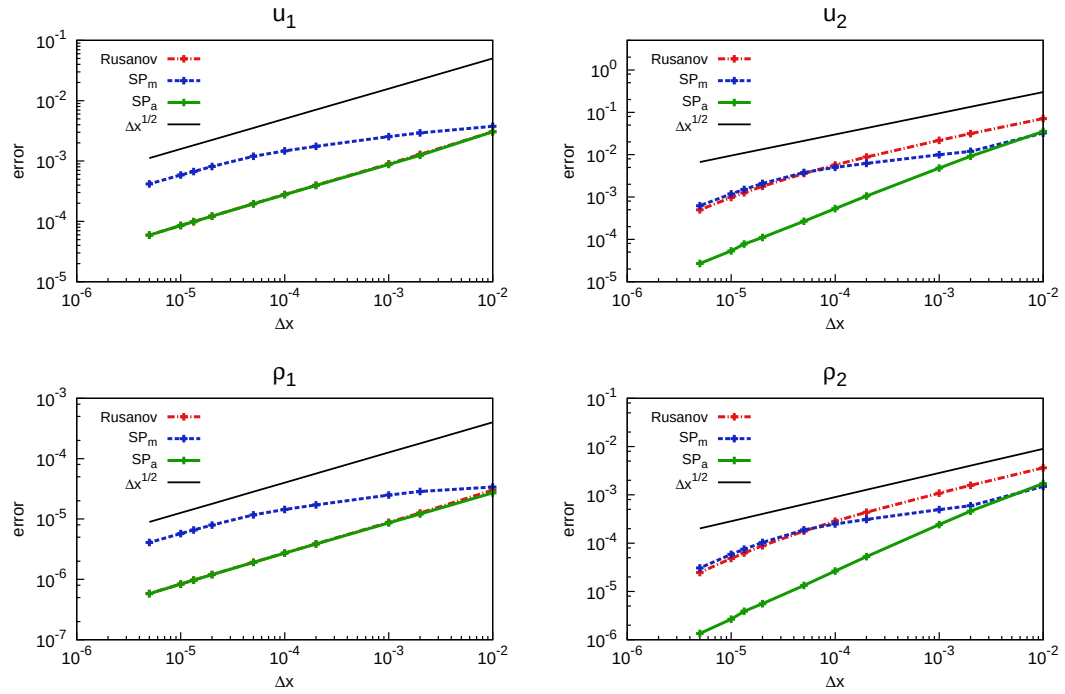

Figure 3.5: Errors in L^1-norm for test case 1.

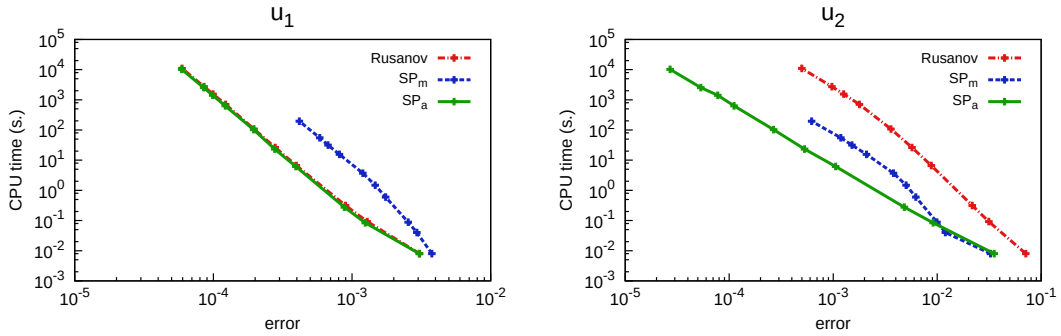

Figure 3.6: Error in L^1-norm against CPU time for test case 1.

3.4.2.b Test case 2: a complete case with all the waves

In this case, all the waves are considered. The analytical solution contains two shocks for each phase traveling with the acoustic waves and one contact discontinuity in $\lambda_1 = u_2$ where h_1 jumps, see Figures 3.7 and 3.8.

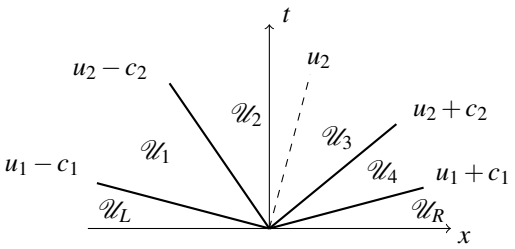

Variable	$\mathscr{U}_L$	$\mathscr{U}_1$	$\mathscr{U}_2$	$\mathscr{U}_3$	$\mathscr{U}_4$	$\mathscr{U}_R$
h_1	0.5	0.5	0.5	0.5023747	0.5023747	0.5023747
ρ_1	998.11150	998.16140	998.16140	998.16240	998.16240	998.06259
u_1	10.0	9.9254584	9.9254584	9.8225555	9.82255555	9.6734610
ρ_2	1.204	1.204	1.2642	1.2601362	1.2349335	1.2349335
u_2	5.0	5.0	-11.838960	-11.838960	-18.826134	-18.826134

Figure 3.7: Wave structure, initial conditions ($\mathscr{U}_L$, $\mathscr{U}_R$) and intermediate states $(\mathscr{U}_k)_{k=1,4}$ for test case 2.

The fields at $T = 23.10^{-5}\,s$ with 1000 cells and the errors are displayed respectively on Figures 3.8 and 3.9. Despite the great complexity of this second test case, one observes that the intermediate states are correctly captured. The same trends as in the previous test case are observed. SP_a presents the best accuracy for both phases while SP_m is more diffusive for phase 1 and behaves slightly better than Rusanov for phase 2. In particular, the contact discontinuity traveling at material speed is better captured using the implicit-explicit scheme. Overshoots are still observed with SP_a on the fields but they are bounded in L^∞-norm and do not preclude the convergence. Regarding the order of convergence on Figure 3.9, the expected convergence rate $\frac{1}{2}$ is obtained.

The test case is a mix between the (slow) material wave in $\lambda_1 = u_2$ and the fast acoustic waves in $\lambda_k = u_k \pm c_k$. On one hand, focusing on h_1 which is (in theory) directly affected by the slow wave, Figure 3.10 shows that SP_m is the most efficient. As expected, the use of material time steps is the best choice to approximate material waves. On the other hand, regarding u_1, the velocity of the fastest phase which is affected by all the waves, SP_m yields the worst efficiency while the use of acoustic time steps through SP_a is the best choice. Regarding u_2, the best efficiency is still obtained with SP_a while SP_m is more efficient that Rusanov. Thus, the efficiency results strongly depend on the wave under consideration and consequently on the related variables.

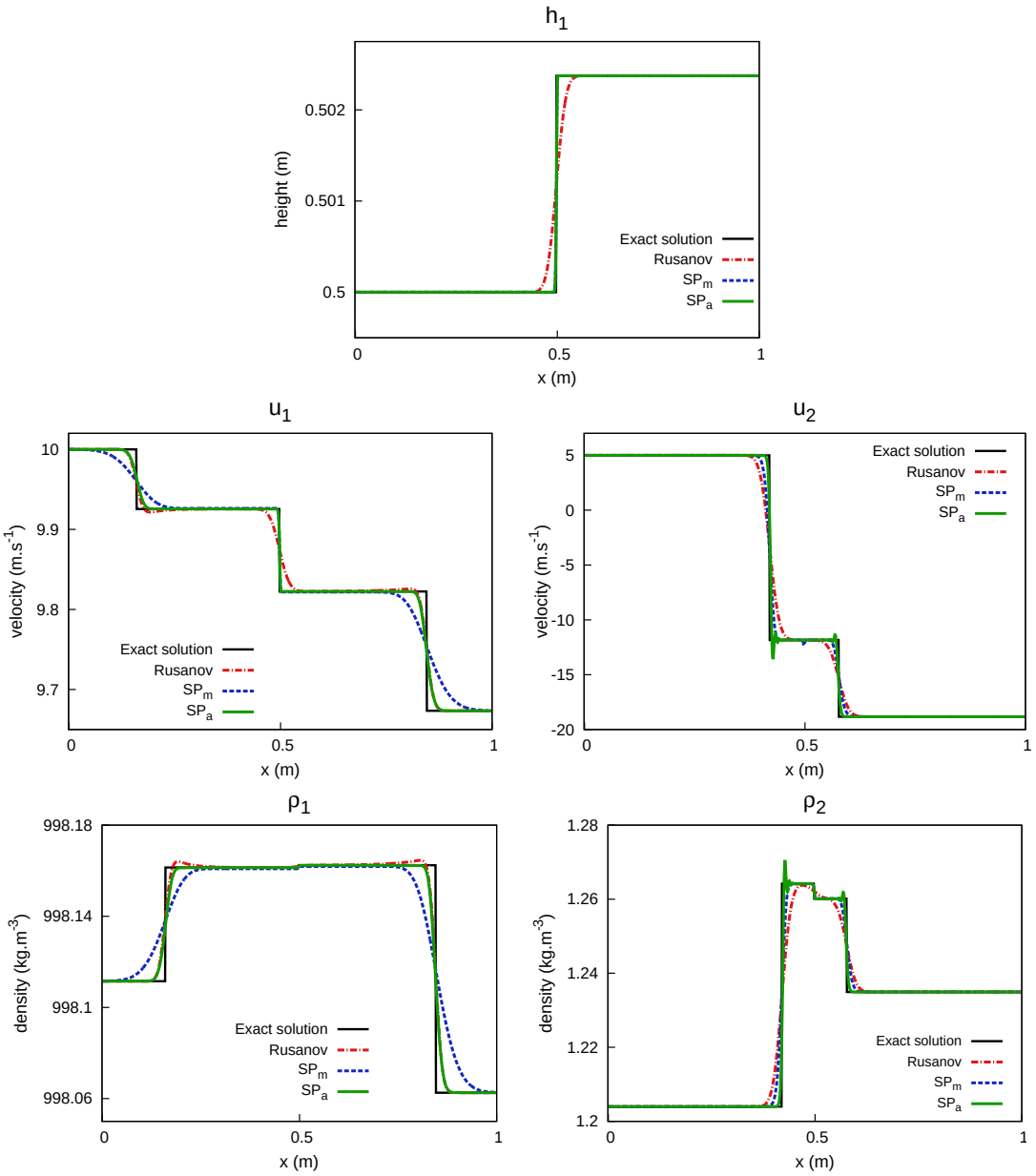

Figure 3.8: Approximate solution for test case 2 at $T = 23.10^{-5}\,s$ with 1000 cells.

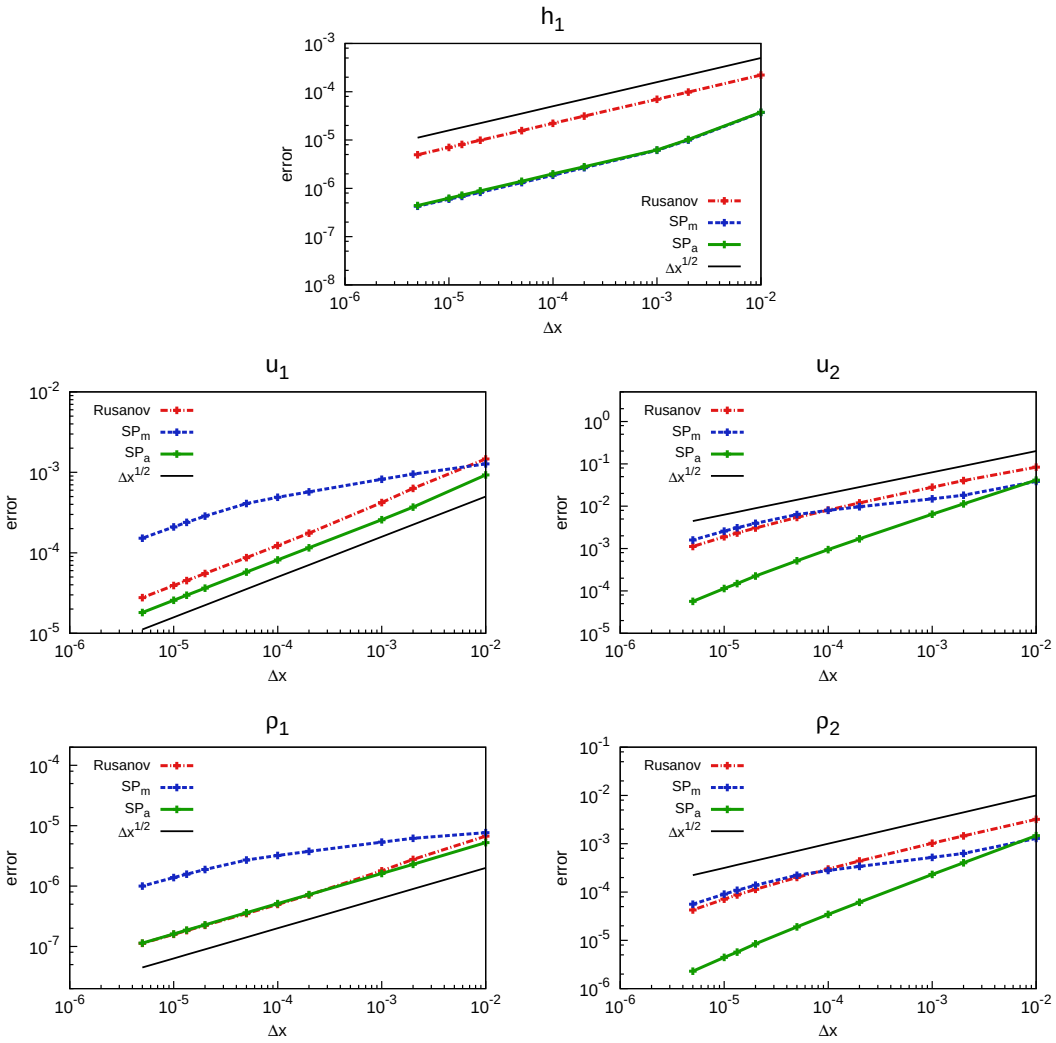

Figure 3.9: Errors in L^1-norm for test case 2.

3.4.3 Comments

The results presented in this section deal with an implicit-explicit splitting scheme, namely **SP**, regarding the convective part of the CTL model. **SP** is used with *acoustic* time steps as well as *material* time steps and compared with a classical explicit Rusanov scheme which requires *acoustic* time steps. The considered test cases highlight the following comments:

- Stability and convergence towards relevant shock solutions are obtained for **SP** and Rusanov.
- **SP** with acoustic time steps (SP_a) is the most efficient regarding the (fast) acoustic waves.
- **SP** with material time steps (SP_m) is the most efficient regarding the (slow) material wave.

Lastly, the best accuracy is obtained with SP_a while a competition in terms of variables is observed regarding the efficiency: best efficiency on the variables $(\rho_1, u_1, \rho_2, u_2)$ given by SP_a or best efficiency on the variable h_1 given by SP_m. Thus, one has to determine the most profitable variant regarding all the fields and the considered test case.

Those comments focus on the convective part of the model. In order to pursue this analysis, the full CTL model is considered in the next section with the aim of including the source terms in the **SP** framework. Indeed, relaxation phenomena encountered in physical configurations may have great influence regarding the system behavior.

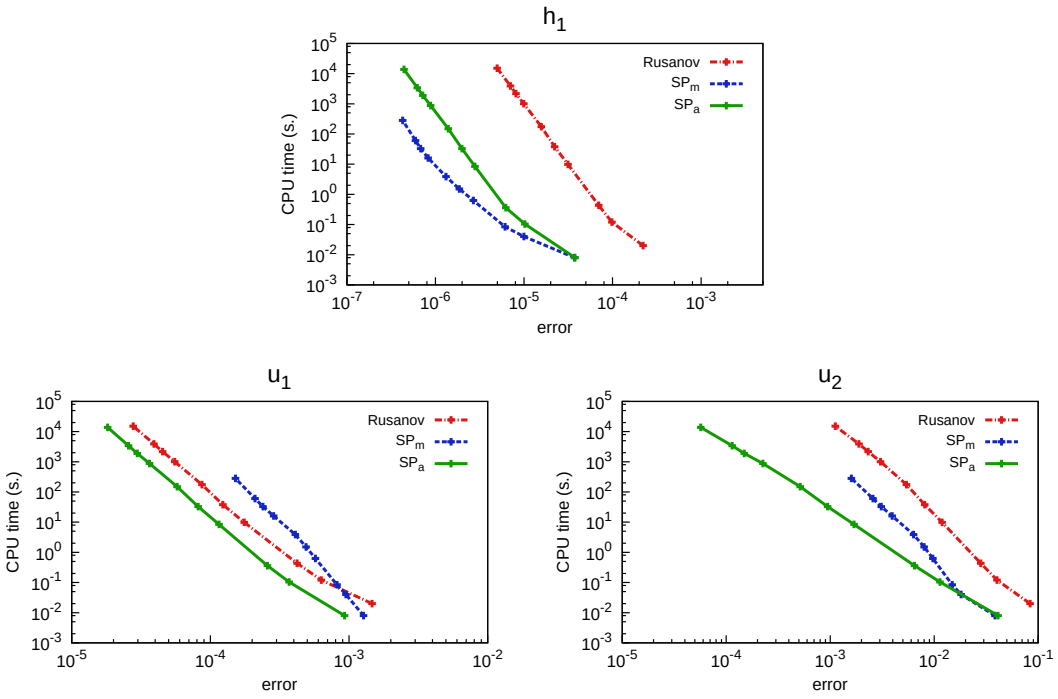

Figure 3.10: Error in L^1-norm against CPU time for test case 2.

3.5 Extension to the full system with source terms

In this section, one deals with the source terms of the CTL model detailed in (3.1), namely the pressure relaxation and the velocity relaxation. Numerical experiments are performed considering a dambreak problem in addition to a mixed flow test case which involves a transition to the pressurized regime through a pipe filling.

3.5.1 Splitting approach

Regarding the pressure relaxation term, $\lambda_p(P_I - P_2)$, one may easily demonstrate that the associated relaxation process, i.e $P_I \underset{t\to\infty}{\to} P_2$, is very fast for air-water flows. The proposed approach is driven by this behavior and consists in plugging the source terms in ($\mathscr{S}_1$) which becomes ($\mathscr{S}_1^s$). Thus, ($\mathscr{S}_2$) is unchanged and the proposed splitting reads:

$$\begin{cases} \dfrac{\partial h_1}{\partial t} + u_2 \dfrac{\partial h_1}{\partial x} = \lambda_p(P_I - P_2), \\ \dfrac{\partial m_k}{\partial t} = 0,\ k = 1,2, \\ \dfrac{\partial m_k u_k}{\partial t} = (-1)^k \lambda_u (u_1 - u_2),\ k = 1,2. \end{cases} \tag{$\mathscr{S}_1^s$}$$

$$\begin{cases} \dfrac{\partial h_1}{\partial t} = 0, \\ \dfrac{\partial m_k}{\partial t} + \dfrac{\partial m_k u_k}{\partial x} = 0,\ k = 1,2, \\ \dfrac{\partial m_k u_k}{\partial t} + \dfrac{\partial m_k u_k^2}{\partial x} + \dfrac{\partial h_k P_k}{\partial x} - P_I \dfrac{\partial h_k}{\partial x} = 0,\ k = 1,2. \end{cases} \tag{$\mathscr{S}_2$}$$

The overall scheme which includes the source terms is denoted $\mathbf{SP}^s$. The latter slightly differs from **SP** regarding the first sub-system ($\mathscr{S}_1^s$) which as before, updates the state variable W_i from W_i^n to W_i^*. The associated numerical scheme is detailed below. Note that ($\mathscr{S}_2$) is treated as in Subsection 3.3.4 such that no details are provided in the current section.

3.5.2 Numerical treatment of the source terms

3.5.2.a Pressure relaxation

The transport equation on h_1 is discretized as in subsection 3.3.3, see (3.12), where the source term is added implicitly except for the λ_p parameter. It writes:

$$h_{1,i}^* - h_{1,i}^n + \Delta t \int_{x_{i-\frac{1}{2}}}^{x_{i+\frac{1}{2}}} u_2^n \frac{\partial h_1^n}{\partial x} dx = \Delta t \lambda_{p,i}^n (P_{I,i}^* - P_{2,i}^*), \tag{3.33}$$

where upwind fluxes are used for the convection term. As m_k is constant w.r.t. time in $(\mathscr{S}_1^s)$, it yields $P_{2,i}^* = P_2(\rho_{2,i}^*) = P_2(\frac{m_{2,i}^n}{H - h_{1,i}^*})$, $P_{I,i}^* = P_1(\frac{m_{1,i}^n}{h_{1,i}^*}) - m_{1,i}^n \frac{g}{2}$ and (3.33) is equivalent to:

$$f(h_{1,i}^*) = 0 \tag{3.34}$$

where:

$$f(y) = y - h_{1,i}^n + \Delta t \int_{x_{i-\frac{1}{2}}}^{x_{i+\frac{1}{2}}} u_2^n \frac{\partial h_1^n}{\partial x} dx - \Delta t \lambda_{p,i}^n \left(P_1\left(\frac{m_{1,i}^n}{y}\right) - m_{1,i}^n \frac{g}{2} - P_2\left(\frac{m_{2,i}^n}{H-y}\right)\right). \tag{3.35}$$

One may easily demonstrate that f is strictly increasing on $[0;H]$ with the limits $f \underset{0^+}{\to} -\infty$ and $f \underset{H^-}{\to} +\infty$, such that (3.34) admits a unique solution $h_{1,i}^*$ on $[0;H]$. Thus, $h_{1,i}^*$ can be obtained using classical numerical methods devoted to nonlinear equations such as the bisection or Newton's method. In addition, note that in this framework, there is no need for CFL conditions to ensure the positivity of $h_{k,i}^*$.

3.5.2.b Velocity relaxation

Once $h_{k,i}^*$ is obtained, the remaining unknown is $u_{k,i}^*$, given by the last equation of $(\mathscr{S}_1^s)$. As for the pressure relaxation, the source term is treated implicitly except for the λ_u parameter. Indeed, the latter may include complex functions depending on the state variable and accounting for friction effects, see Appendix 3.A.2. Using the fact that m_k is constant w.r.t. time, the proposed implicit scheme writes:

$$m_{k,i}^n (u_{k,i}^* - u_{k,i}^n) = (-1)^k \Delta t \lambda_{u,i}^n (u_{1,i}^* - u_{2,i}^*). \tag{3.36}$$

Combining (3.36) for $k = 1,2$, one obtains the following non-singular 2×2 system:

$$\begin{pmatrix} m_{1,i}^n + \Delta t \lambda_{u,i}^n & -\Delta t \lambda_{u,i}^n \\ -\Delta t \lambda_{u,i}^n & m_{2,i}^n + \Delta t \lambda_{u,i}^n \end{pmatrix} \begin{pmatrix} u_{1,i}^* \\ u_{2,i}^* \end{pmatrix} = \begin{pmatrix} (m_1 u_1)_i^n \\ (m_2 u_2)_i^n \end{pmatrix}. \tag{3.37}$$

This system can be solved directly and one obtains an explicit relation for $u_{k,i}^*$.

At this point, $(\mathscr{S}_1^s)$ is solved accounting for the relaxation processes. $(\mathscr{S}_2)$ is then solved as in Section 3.3.4 to obtain the updated state variable W_i^{n+1}. In order to assess this method, two test cases are considered in the next subsection.

3.5.3 Numerical results

In the sequel, numerical tests are performed with SP_a^s and SP_m^s which denote respectively the $\mathbf{SP}^s$ scheme with *acoustic* and *material* time steps. As in Section 3.4, the acoustic time step is denoted Δt_a and defined in (3.30). The material time step is denoted Δt_m and defined in (3.31) except that the CFL condition regarding the positivity of h_k, see (3.13), can be ignored when including the pressure relaxation term. In addition, one considers the Rusanov scheme applied to $(\mathscr{S}_0)$ where the source terms are classically treated in a second step involving only ODEs, see [20]. The latter scheme is denoted Rusanov^s hereafter to be consistent in the notations.

3.5.3.a Dambreak test case

A common way to deal with free-surface flows is to use the well-known Saint-Venant or shallow-water equations, see [18]. In a few words, this model is a *one-layer* model resulting from a depth averaging process on the Euler

set of equations and assuming a thin layer of incompressible fluid (water for instance) with hydrostatic pressure law. Particularly, it admits an analytical solution for the so-called dambreak problem detailed below. Note that this classical approach is used in [5] to model the free-surface regime in pipe flows without computing the air phase.

In the following, it is proposed to consider the dambreak test case for the CTL model and to compare the results with the reference solution provided by the Saint-Venant system for the single water layer. Indeed, one can expect to obtain the same kind of solution as the derivation processes are very close and the compressibility of water as well as the additional air layer should have a minor influence here.

The dambreak problem

The dambreak problem is a Riemann problem where the initial condition is a discontinuity on h_1 with constant density and zero speed, see Figure 3.11. Regarding the water layer, the analytical solution of the incompressible shallow-water system, denoted SW_{ref} hereafter, provides the evolution in time and space for h_1 and u_1 which contains a rarefaction wave propagating to the left and a shock wave propagating to the right.

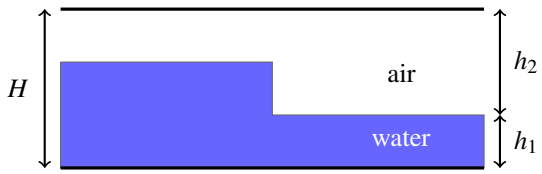

Variable	$0 \leq x \leq 2$	$2 < x \leq 4$
h_1/H	0.6	0.4
ρ_1	998.1115	998.1115
u_1	0	0
ρ_2	1.204	1.204
u_2	0	0

Figure 3.11: Initial conditions for the dambreak problem.

The dynamics of this test case is driven by water gravity waves whose typical celerity is given by $\sqrt{gh_1}$. The CTL model focuses *by construction* on the dynamics of acoustic waves whose celerity is given by $c_1 = \sqrt{P_1'(\rho_1)}$ for the water phase. Thus, when $\frac{\sqrt{gh_1}}{c_1} \ll 1$, the approximation of water gravity waves with the CTL model is challenging. Consequently, defining the water Mach number as $M_1 = \frac{|u_1|}{c_1}$ and the Froude number as $Fr = \frac{|u_1|}{\sqrt{gH}}$, a dimensionless number of interest is given by:

$$\frac{M_1}{Fr} = \frac{\sqrt{gH}}{c_1}, \tag{3.38}$$

as soon as $h_1 \sim H$ in the applications.

Implementation

The solutions are computed on the domain [0,4] of the x-space where the initial conditions are given on Figure 3.11. Regarding the boundary conditions, one imposes homogeneous Neumann conditions at the inlet and outlet. The fields are presented on a 4000 cells mesh at time $T = 0.11\,s$. Two pipe heights are considered, $H = 10\,m$ and $H = 1000\,m$, which yields $\frac{M_1}{Fr} \sim 7.10^{-3}$ and $\frac{M_1}{Fr} \sim 7.10^{-2}$ respectively.

Results

On Figure 3.12, SP_a^s is compared with Rusanov^s with $\frac{M_1}{Fr} \sim 7.10^{-3}$. As a first comment, note that both schemes seem to follow the SW_{ref} solution regarding h_1 and u_1, which is the expected trend for the CTL model since the air layer has minor influence here. In addition, admitting SW_{ref} as a reference solution, one observes that SP_a^s is more accurate than Rusanov^s as for the homogeneous test cases presented in Section 3.4.

On Figure 3.13, SP_m^s is compared with Rusanov^s at $\frac{M_1}{Fr} \sim 7.10^{-3}$. In practice $\Delta t_m \sim 100\Delta t_a$ and one observes that SP_m^s is unable to restore the SW_{ref} solution. The solution obtained for h_1 is totally inaccurate so that the comments given in Subsection 3.4.3 cannot be extended to SP_m^s. Refining the mesh, one obtains the expected structure but SP_m^s is inefficient for all the variables compared to SP_a^s and Rusanov^s. Consequently, the use of material time steps with the proposed implicit-explicit splitting scheme seems to be too sharp regarding such a gravity driven test case.

When the dimensionless number $\frac{\sqrt{gH}}{c_1}$ is multiplied by a factor 10, $\frac{M_1}{Fr} \sim 7.10^{-2}$, and SP_m^s is able to restore the structure of the SW_{ref} solution although the profiles are very diffusive, see Figure 3.14. SP_a^s is still more accurate than Rusanov^s but diffusivity is also observed. At last, those results illustrate the difficulties to approximate slow gravity waves with the CTL model with even more challenges at large time steps.

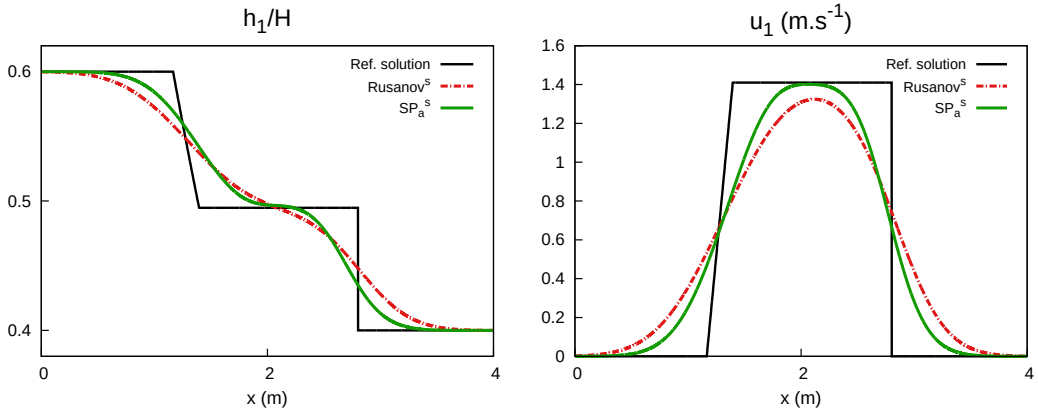

Figure 3.12: Approximate solution at $T = 0.11\,s$ with $\frac{M_1}{Fr} \sim 7.10^{-3}$ and 4000 cells (Rusanov^s and SP^s_a).

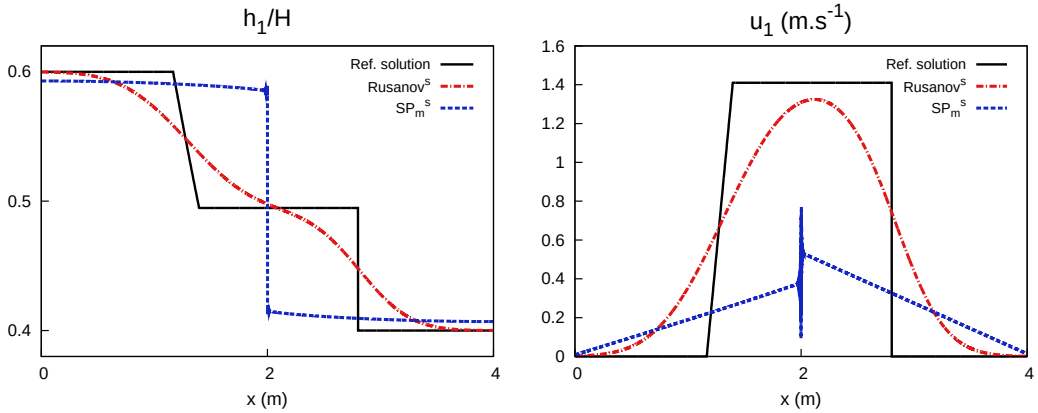

Figure 3.13: Approximate solution at $T = 0.11\,s$ with $\frac{M_1}{Fr} \sim 7.10^{-3}$ and 4000 cells (Rusanov^s and SP^s_m).

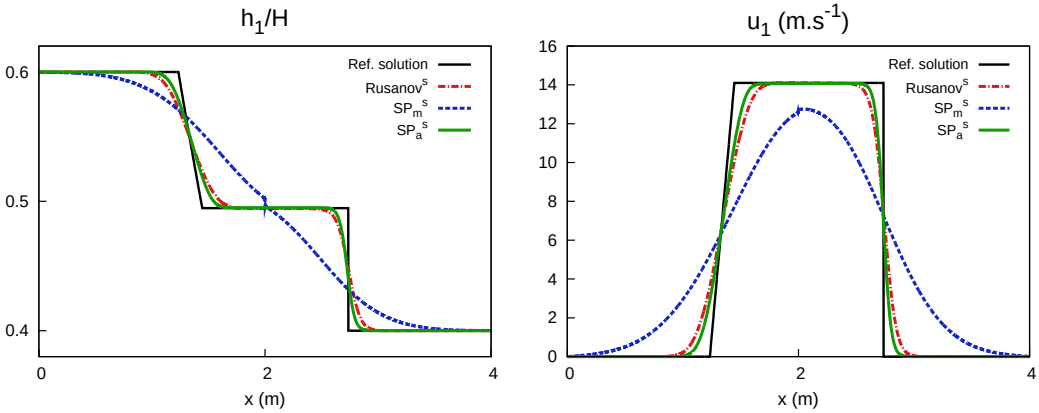

Figure 3.14: Approximate solution at $T = 0.11\,s$ with $\frac{M_1}{Fr} \sim 7.10^{-2}$ and 4000 cells.

3.5.3.b A first attempt to deal with mixed flows: pipe filling test case

In this test case, one considers a more complex configuration which involves a transition from the free-surface regime to the pressurized regime, namely a mixed flow. As exposed in [15], the CTL model degenerates correctly towards an isentropic Euler set of equations for the water phase when the height of the air phase goes to zero. The latter equations

are commonly used to describe pressurized flows but in our framework, one has to handle numerically the vanishing air phase which may be a tough challenge.

In order to enable a transition to the pressurized regime, one considers a sloping pipe with a wall boundary condition at the outlet and a classical homogeneous Neumann boundary condition at the inlet. The initial conditions are the same as the ones used for the dambreak test case, see Figure 3.11, except that the pipe is inclined by 20 degrees to the horizontal. The computations are still done on the domain [0,4] of the x-space with a 4000 cells mesh. There is no analytical solution but the idea is to obtain *qualitative* results. Note that the exposed results mainly involve ongoing work.

On Figure 3.15, one displays a snapshot w.r.t. time regarding the height of the water phase. The Rusanov^s scheme is used and one obtains encouraging results. Indeed, the vanishing air phase configuration seems to be handled providing a realistic qualitative behavior. However, the **SP**^{s} scheme is not able to reproduce this behavior. As a first explanation, one notices that when the height of the air phase goes to zero, the matrix A_2^* involved in (3.21) to compute the air pressure goes as well to zero and the system becomes hard to solve numerically. In order to cope with that issue, the use of preconditioning techniques could be an area of investigation.

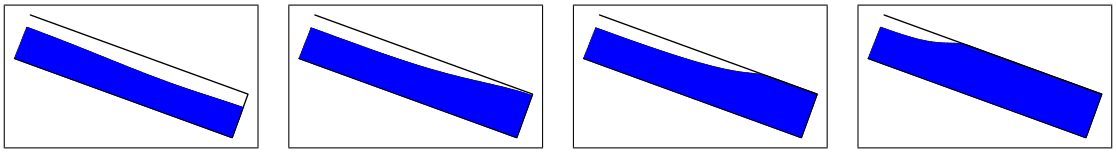

Figure 3.15: Snapshots w.r.t. time for the pipe filling case using the Rusanov^s scheme. Height of the water phase in blue.

This test may illustrate the ability of the CTL model to handle mixed flows at least using a diffusive scheme as the Rusanov^s scheme. Further investigations have to be led in order to adapt the **SP**^{s} scheme to the vanishing phases configuration.

3.6 Conclusion and further works

An implicit-explicit splitting scheme, namely **SP**, is presented to approximate the solutions of the Compressible Two-Layer model developed in [15]. The CFL condition associated to this scheme relies on material velocities but numerical experiments are performed using *acoustic* as well as *material* time steps. In short, adding the Rusanov scheme for comparison, the best accuracy is obtained with the proposed scheme used with *acoustic* time steps. When used with *material* time steps, efficiency on the slow waves and stability are obtained for analytical solutions of the convective part.

More precisely, one obtains convergent approximations of analytical discontinuous solutions regarding the convective part. As expected, the use of *acoustic* time steps leads better efficiency on fast waves while the *material* time steps yield better efficiency on slow waves. When considering the source terms and the dambreak problem, the latter comments cannot be extended. The use of *acoustic* time steps leads to encouraging results which meet the expected behavior of the CTL model. However, the use of *material* time steps in this context yields unsatisfactory results. Indeed, the approximation of slow gravity waves is particularly challenging and the proposed scheme may not be fitted to deal correctly with it.

Dealing with mixed flows, one may also consider vanishing phases occurring in pressurized and dry flows. A first attempt to address this challenge is done herein with the pipe filling test case. The explicit Rusanov scheme displays interesting qualitative results but they are very diffusive. The proposed scheme is unable to compute this configuration due to a lack of robustness in its implicit part.

Thus, the simulation of mixed flows using the CTL model needs further investigations. The implicit-explicit approach seems relevant for the targeted applications but the associated splitting has to better account for slow propagation phenomena and particularly gravity waves. Furthermore, a particular interest has to be paid to vanishing phases introducing for instance preconditioning or threshold techniques to ensure the transition. Taking advantage on the first results exposed herein, further works are conducted in that sense.

3.A Closure laws for the source terms

3.A.1 Pressure relaxation

In order to determine the time scale associated to pressure relaxation, one considers in [17] the evolution of a bubble in an infinite medium using the Rayleigh-Plesset equation. Regarding the source term $\lambda_p(P_I - P_2)$ in (3.1), the latter approach is extended to our framework so that the λ_p function reads:

$$\lambda_p = \frac{3}{4\pi\mu_1}\frac{h_1 h_2}{H}, \tag{3.A.1}$$

where μ_1 is the dynamic viscosity of phase 1. For water, $\mu_1 = 10^{-3}\,Pa.s$ at $T = 20^o C$.

3.A.2 Velocity relaxation

Regarding the averaged momentum conservation equation (3.1c), the source $\lambda_u(u_2 - u_1)$ accounts for friction effects between phases. Therefore, the function λ_u is modeled as a classical interfacial drag force which writes:

$$\lambda_u = \frac{1}{2} f_i \rho_2 |u_1 - u_2|, \tag{3.A.2}$$

where f_i is a friction factor. In order to define f_i, several experimental studies have been led since the pioneer work of Taitel and Dukler in 1976, see [26]. In particular, f_i should ideally depends on the flow regime. In the present work, a constant value relying on experimental results for stratified air-water flows is chosen, that is $f_i \sim 0.015$ (see [21]). Indeed, the performed numerical experiments do not involve strong interfacial shear between the phases. However, note that the numerical scheme proposed hereafter is independent from λ_u such that more complex laws can be implemented.

References

[1] A. Ambroso, C. Chalons, and P.-A. Raviart. A Godunov-type method for the seven-equation model of compressible two-phase flow. *Computers & Fluids*, 54:67–91, 2012.

[2] A. Andrianov and G. Warnecke. The Riemann problem for the Baer-Nunziato two-phase flow model. *Journal of Computational Physics*, 195(2):434–464, 2004.

[3] M. R. Baer and J. W. Nunziato. A two phase mixture theory for the deflagration to detonation (DDT) transition in reactive granular materials. *International Journal of Multiphase Flow*, 12(6):861–889, 1986.

[4] R. Baraille, G. Bourdin, F. Dubois, and A.-Y. Le Roux. A splitted version of the Godunov scheme for hydrodynamic models. *C. R. Acad. Sci. Paris*, 314(1):147–152, 1992.

[5] C. Bourdarias and S. Gerbi. A finite volume scheme for a model coupling free surface and pressurised flows in pipes. *Journal of Computational and Applied Mathematics*, 209:1–47, 2007.

[6] T. Buffard and J.-M. Hérard. A conservative fractional step method to solve non-isentropic Euler equations. *Computer Methods in Applied Mechanics and Engineering*, 144:199–225, 1997.

[7] C. Chalons, F. Coquel, S. Kokh, and N. Spillane. Large time-step numerical scheme for the seven-equation model of compressible two-phase flows. *Springer Proceedings in Mathematics and Statistics*, 4:225–233, 2011.

[8] C. Chalons, M. Girardin, and S. Kokh. Large time-step and asymptotic preserving numerical schemes for the gas dynamics equations with source terms. *SIAM Journal on Scientific Computing*, 35(6):a2874–a2902, 2013.

[9] F. Coquel, T. Gallouët, J.-M. Hérard, and N. Seguin. Closure laws for a two-fluid two-pressure model. *C. R. Acad. Sci. Paris*, 334(I):927–932, 2002.

[10] F. Coquel, J.-M. Hérard, and K. Saleh. A splitting method for the isentropic Baer-Nunziato two-phase flow model. *ESAIM: Proceedings*, 38(3):241–256, 2012.

[11] F. Coquel, J.-M. Hérard, K. Saleh, and N. Seguin. A robust entropy-satisfying finite volume scheme for the isentropic Baer-Nunziato model. *ESAIM: Mathematical Modelling and Numerical Analysis*, 48:165–206, 2013.

[12] F. Coquel, Q.-L. Nguyen, M. Postel, and Q.-H. Tran. Entropy-satisfying relaxation method with large time-steps for Euler ibvps. *Mathematics of Computation*, 79:1493–1533, 2010.

[13] P. Degond and M. Tang. All speed scheme for the low Mach number limit of the isentropic Euler equation. *Communications in Computational Physics*, 10:1–31, 2011.

[14] V. Deledicque and M.V. Papalexandris. An exact Riemann solver for compressible two-phase flow models containing non-conservative products. *Journal of Computational Physics*, 222(1):217–245, 2007.

[15] C. Demay and J.-M. Hérard. A compressible two-layer model for transient gas-liquid flows in pipes. *Continuum Mechanics and Thermodynamics*, 29(2):385–410, 2017.

[16] T. Gallouët, J.-M. Hérard, and N. Seguin. Numerical modeling of two-phase flows using the two-fluid two-pressure approach. *Mathematical Models and Methods in Applied Sciences*, 14(05):663–700, 2004.

[17] S.L. Gavrilyuk. The structure of pressure relaxation terms : one-velocity case. *EDF report H-I83-2014-00276-EN*, 2014.

[18] J.-F. Gerbeau and B. Perthame. Derivation of viscous Saint-Venant system for laminar shallow water; numerical validation. *Discrete Contin. Dyn. Syst. Ser. B*, 1:89–102, 2001.

[19] J. Haack, S. Jin, and J.G. Liu. An all-speed asymptotic preserving method for the isentropic Euler and navier-stokes equations. *Communications in Computational Physics*, 12:955–980, 2012.

[20] J.-M. Hérard and O. Hurisse. A fractional step method to compute a class of compressible flows with micro-inertia. *Computers & Fluids*, 55:57–69, 2012.

[21] A. Line and J. Fabre. Stratified gas liquid flow. *Encyclopedia of Heat Transfer*, pages 1097–1101, 1997.

[22] S. Noelle, G. Bispen, K. Arun, M. Lukacova-Medvidova, and C.D. Munz. A weakly asymptotic preserving all Mach number scheme for the Euler equations of gas dynamics. *SIAM Journal on Scientific Computing*, 36:B989–B1024, 2014.

[23] V. H. Ransom and D. L. Hicks. Hyperbolic two-pressure models for two-phase flow. *Journal of Computational Physics*, 53:124–151, 1984.

[24] V. V. Rusanov. Calculation of interaction of non-steady shock waves with obstacles. *Zh. Vychisl. Mat. Mat. Fiz.*, 1(2):267–279, 1961.

[25] D. W. Schwendeman, C. W. Wahle, and A. K. Kapila. The Riemann problem and a high-resolution Godunov method for a model of compressible two-phase flow. *Journal of Computational Physics*, 212(2):490–526, 2006.

[26] Y. Taitel and A.E. Dukler. A model for predicting flow regime transitions in horizontal and near horizontal gas-liquid flow. *AIChE J.*, 22:47–55, 1976.

[27] S.-A. Tokareva and E.-F. Toro. HLLC-type Riemann solver for the Baer-Nunziato equations of compressible two-phase flow. *Journal of Computational Physics*, 229(10):3573–3604, 2010.

[28] S.-A. Tokareva and E.-F. Toro. A flux splitting method for the Baer–Nunziato equations of compressible two-phase flow. *Journal of Computational Physics*, 323:45–74, 2016.

[29] E.F. Toro and M.E. Vázquez-Cendón. Flux splitting schemes for the Euler equations. *Computers & Fluids*, 70:1–12, 2012.

Chapter 4

A fractional step method adapted to the two-phase simulation of mixed flows with a compressible two-layer model

Abstract: The numerical resolution of the Compressible Two-Layer proposed in Chapter 2 is addressed in this work with the aim of simulating mixed flows and entrapped air pockets in pipes. This five-equation model provides a unified two-phase description of such flows which involve transitions between stratified regimes (air-water herein) and pressurized or dry regimes (pipe full of water or air). In particular, strong interactions between both phases and entrapped air pockets are accounted for. At the discrete level, the coexistence of slow gravity waves in the stratified regime with fast acoustic waves in the pressurized regime is difficult to approximate. Furthermore, the two-phase description requires to deal with vanishing phases in pressurized and dry regimes. In that context, a robust fractional step method combined with an implicit-explicit time discretization is derived. Unlike for the first attempt proposed in Chapter 3, the overall strategy relies on the fast pressure relaxation in addition to a mimetic approach with the shallow water equations for the slow dynamics of the water phase. It results in a three-step scheme which ensures the positivity of heights and densities under a CFL condition based on the celerity of material and gravity waves. In particular, an implicit relaxation approach provides stabilization terms which are activated according to the flow regime. Numerical experiments are performed beginning with a Riemann problem for the convective part. The method is then assessed in the framework of mixed flows considering a dambreak problem relevant for the stratified regime and canonical configurations involving regime transitions and vanishing phases.

Note: A paper in preparation is made up of the content of this chapter associated with the numerical results exposed in Chapter 6. A shorter version of this work has been published in the proceedings of the conference *Finite Volume for Complex Applications VIII* (June 12-16, 2017, Lille, France). The corresponding reference is:

- C. Demay, C. Bourdarias, B. de Laage de Meux, S. Gerbi, and J.-M. Hérard. A fractional step method to simulate mixed flows in pipes with a compressible two-layer model, *Springer Proceedings in Mathematics and Statistics*, 200:33-41, 2017.

Contents

4.1 Introduction

This work is devoted to the simulation of the so-called mixed flows in pipes. The latter are encountered in several industrial areas such as nuclear and hydroelectric power plants or sewage pipelines. They are multi-regime flows featuring stratified regimes (air-water in the sequel) and pressurized or dry regimes (pipe full of water or air). In particular, transitions occur between these regimes which potentially result in entrapped air pockets. This transient nature may lead to strong constraints on industrial facilities. For instance, the transitions between stratified and pressurized regimes induce strong pressure variations. In addition, the presence of air, especially entrapped air pockets, is usually unwanted as it may lead to a reduced efficiency, geysering and damages for pumping systems [45]. In a larger extent, these flows are also involved in the interactions between a free surface and a floating structure such as an iceberg, an off-shore wind turbine or a buoy [39]. Consequently, a particular interest is paid to mixed flows through both modelling and experimental studies.

Regarding the modelling of mixed flows, numerous challenges are raised due to the different nature of each regime. Indeed, the stratified regime is driven by slow gravity waves compared to the fast acoustic waves characterizing the pressurized regime. Furthermore, strong interactions between the water phase and the air phase may also be involved, especially in the presence of entrapped air pockets. Modelling studies have been conducted with the aim of proposing a 1D description adapted to the large time and spatial scales involved in industrial facilities. As presented in a recent literature review [12], see also [52, 37], several approaches have been proposed. They are mainly single-phase models which focus on the transitions between stratified and pressurized regimes neglecting the air phase. Among them, the most natural (and popular) approach relies on a unified description of the different regimes. This approach was introduced in [44, 22] with the so-called Preissmann Slot model. In the latter, the shallow water equations [7, 29], usually dedicated to the modelling of free-surface flows, are used for both stratified and pressurized regimes assuming that there is a narrow slot at the top of the pipe. The width of the slot is then calculated to obtain gravity waves with the same celerity as acoustic waves. This technique is validated against experimental data in [27, 14, 51, 5] for example. Recently, another unified approach has been proposed in [31] where the shallow water equations are supplemented with a constraint on the water height describing a roof, i.e. the top of the pipe in our framework. With these approaches, sub-atmospheric pressures in the pressurized regime cannot be modeled as they are, by construction, associated with a transition to the stratified regime. These sub-atmospheric pressures may nevertheless be involved in some configurations such as high points of an hydraulic circuit or water hammer phenomena. Thus, more sophisticated

models, also based on a unified single-phase description, have been proposed to account for these pressure levels [54, 11, 38]. Some of them have also been extended to the modelling of entrapped air pockets in simplified configurations [53, 42]. Beyond this physical classification, the different nature of each regime and the associated transitions also induce numerical challenges. In the literature, Finite Volume approaches are principally adopted and strategies relying on Godunov-type schemes [38], Roe-type schemes [54, 11] or kinetic schemes [10] may be proposed. However, the transition points are often associated with spurious oscillations due to the discrepancy of wave speeds characterizing each regime, see [55] for a related study. Lastly, even if these models with their associated numerical method may provide a satisfactory single-phase description of mixed flows, they are unable to account for strong interactions between the air and water phase in all the regimes. As recently pointed out in a literature review [12], the development of a 1D model which accounts for these interactions is still needed. Some attempts based on two-fluid models have been proposed assuming an incompressible liquid and a compressible gas, see particularly [35, 4]. However, the resulting models are not hyperbolic and the management of the pressurized regime is not clearly defined nor the associated transitions.

In this context, a two-phase flow model, namely the Compressible Two-Layer model, has been proposed in Chapter 2. The derivation process relies on a depth averaging of the isentropic Euler set of equations for each phase. It leads to a five-equation system composed by a transport equation on the liquid height in addition to averaged mass and averaged momentum conservation equations for both phases. Thus, this model belongs to the class of two-phase two-pressure models and significant mathematical properties such as hyperbolicity are obtained. This class of model was first introduced for separated flows with depth averaging in [46] and mainly used afterward in a statistical framework for bubbly or granular flows, see [6, 26, 30, 36] for instance. The main originality of the Compressible Two-Layer model relies on the closure law of the interfacial pressure which is derived from the hydrostatic constraint applied to the liquid. Therefore, a unified two-phase description of mixed flows is obtained. Indeed, the model is consistent in some sense with the shallow water equations [7, 29] for the water phase (stratified regime) while the whole system degenerates formally towards a single-phase isentropic Euler system when one phase vanishes (pressurized or dry regime). From the numerical point of view, several challenges are raised, above all for mixed flows. The convective part of two-fluid two-pressure models is doted with a complex wave structure which makes difficult the Riemann problem to solve regarding Godunov-type methods. Furthermore, the whole system includes relaxation source terms which strongly interact with the convective part involving various time scales. When dealing with mixed flows, two additional difficulties may be identified. Firstly, one has to approximate the slow dynamics of the stratified regime (gravity waves) as well as the fast dynamics of the pressurized regime (acoustic waves). Secondly, dealing with a two-phase flow model, one has to handle vanishing phases in pressurized and dry regimes which are known to raise robustness issues.

Some successful solvers for two-fluid two-pressure models are proposed in the literature. They focus on the convective part of the system and they are mainly time-explicit methods such as Godunov-type schemes [3], HLLC-type schemes [41, 49] and relaxation schemes [2, 20, 21] with a particular interest paid to vanishing phases in the latter two references. However, these methods have to comply with the usual Courant-Friedrichs-Lewy (CFL) condition on the time step which involves the celerity of fast acoustic waves. Dealing with the water phase, this celerity is about $1500 m.s^{-1}$ so that the resulting CFL condition is very constraining and brings too much diffusion to approximate satisfactorily the slow stratified regime. In order to relax this constraint, a possible approach is to derive an implicit-explicit method (IMEX) where the slow dynamics is treated explicitly while the fast dynamics is treated implicitly. This treatment is associated with a *well-chosen* splitting of the system, which can be a flux splitting or an operator splitting. In this framework, interesting results are obtained for the approximation of low Mach solutions of the Euler system, see [16, 23, 24, 32, 34, 43], and a large time-step scheme for a two-fluid two-pressure model is proposed in [15]. Such an implicit-explicit method is derived in Chapter 3 as a first attempt for the numerical resolution of the Compressible Two-Layer model. However, it fails to approximate satisfactorily slow gravity waves resulting from a classical dambreak problem and presents a lack of robustness with vanishing phases. Very recently, the numerical resolution of a five-equation model which presents similarities with the Compressible Two-Layer model has been addressed in [25]. The aim of this work is to handle slug flows which may also be interpreted as mixed flows as they involve transitions between stratified and pressurized regimes. A Roe-type explicit scheme is proposed and their strategy to handle the transitions consists in artificially switching from a two-phase to a single-phase description removing gradually coupling terms and setting a zero density value to vanishing phases. Interesting features are obtained regarding slug flow capturing but the accuracy of the explicit approach regarding slow gravity waves is not presented and the artificial management of transitions is questionable.

The numerical resolution of the Compressible Two-Layer model is addressed herein with the aim of simulating mixed flows and entrapped air pockets in pipes. The model and its properties are first recalled in Section 4.2 as well as its relevance for the two-phase description of mixed flows. A fractional step method (operator splitting) associated with an implicit-explicit scheme is then proposed in Section 4.3. Contrary to the first attempt proposed

in Chapter 3, the overall strategy relies on the fast pressure relaxation in addition to a mimetic approach with the shallow water equations for the slow dynamics of the water phase. It results in a three-step scheme which ensures the positivity of heights and densities under a CFL condition based on the celerity of material and gravity waves. In particular, an implicit relaxation approach provides stabilization terms which are activated according to the flow regime. Furthermore, the robustness of the method allows to solve both phases in pressurized and dry regimes. Numerical experiments are performed in Section 4.4 beginning with a Riemann problem for the convective part. The method is then assessed in the framework of mixed flows considering a dambreak problem relevant for the stratified regime and canonical configurations involving regime transitions and vanishing phases. Validation test cases are extensively studied in Chapter 6.

4.2 The Compressible Two-Layer model

The Compressible Two-Layer model, referred to as the CTL model hereafter, has been introduced in Chapter 2 to deal with gas-liquid mixed flows in pipes. The latter involve stratified regimes (see Figure 4.1) as well as pressurized or dry regimes (pipe full of liquid or gas). The governing equations of this model and its main properties are exposed below. In the sequel, we focus on air-water flows but the general approach applies to gas-liquid flows.

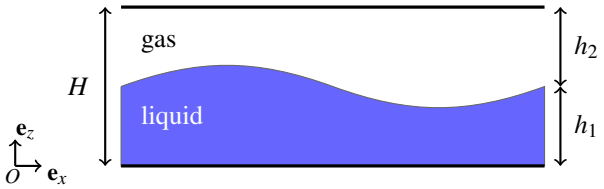

Figure 4.1: Geometric description for horizontal channels.

4.2.1 Governing equations

The CTL model belongs to the class of two-fluid two-pressure models introduced by Ransom & Hicks in [46]. It results from a depth-averaging of the isentropic Euler set of equations for each phase, see Chapter 2 for details. Considering a two-layer air-water flow through an horizontal rectangular pipe of height H, see Figure 4.1, the model reads:

$$\left\{\begin{array}{l} \dfrac{\partial h_1}{\partial t} + U_I \dfrac{\partial h_1}{\partial x} = \lambda_p (P_I - P_2(\rho_2)), \\ \dfrac{\partial m_k}{\partial t} + \dfrac{\partial m_k u_k}{\partial x} = 0, \ k = 1,2, \\ \dfrac{\partial m_k u_k}{\partial t} + \dfrac{\partial m_k u_k^2}{\partial x} + \dfrac{\partial h_k P_k(\rho_k)}{\partial x} - P_I \dfrac{\partial h_k}{\partial x} = (-1)^k \lambda_u (u_1 - u_2), \ k = 1,2, \end{array}\right. \tag{$\mathscr{S}$}$$

where $k = 1$ for water, $k = 2$ for air, $m_k = h_k \rho_k$ and $h_1 + h_2 = H$. Here, h_k, ρ_k, $P_k(\rho_k)$ and u_k denote respectively the height, the mean density, the mean pressure and the mean velocity of phase k. The interfacial variables, namely the interfacial pressure and the interfacial velocity, are denoted P_I and U_I respectively. The interface dynamics is represented by the transport equation on h_1 while the other two equations account for mass and momentum conservation in each phase.

The main originality of the CTL model comes from the integration of the hydrostatic constraint applied to the water phase which results in a closure law for P_I. This constraint is essential in order to account for water gravity waves in the stratified regime. The closure law for the interfacial velocity is obtained using an entropy inequality as in [17]. The resulting closures read:

$$(U_I, P_I) = (u_2, P_1 - \rho_1 g \frac{h_1}{2}), \tag{4.1}$$

where g is the gravity field magnitude. As the phases are compressible, state equations are required for gas and liquid

pressures. For instance, perfect gas law may be used for air and linear law for water:

$$P_1(\rho_1) = (\rho_1 - \rho_{1,\text{ref}})c_{1,\text{ref}}^2 + P_{1,\text{ref}}, \tag{4.2a}$$

$$P_2(\rho_2) = P_{2,\text{ref}}\Big(\frac{\rho_2}{\rho_{2,\text{ref}}}\Big)^{\gamma_2}, \tag{4.2b}$$

with some reference density $\rho_{k,\text{ref}}$ and pressure $P_{k,\text{ref}}$. The celerity of acoustic waves is defined by:

$$c_k = \sqrt{P_k'(\rho_k)}, \tag{4.3}$$

where $P_k'(\rho_k) > 0$. For air, γ_2 is set to 7/5 (diatomic gas) and for water, c_1 is constant and equal to a reference celerity denoted $c_{1,\text{ref}}$.

In the following, the thermodynamic reference state is chosen to deal with air-water flows at $20^o C$: $P_{1,\text{ref}} = 1.0133$ bar, $\rho_{1,\text{ref}} = 998.1115$ kg.m^{-3}, $c_{1,\text{ref}} = 1500$ m.s^{-1}, $P_{2,\text{ref}} = 1$ atm and $\rho_{2,\text{ref}} = 1.204$ kg.m^{-3} which yield $c_{2,\text{ref}} \approx 343$ m.s^{-1}. Note that phase 1 inherits from the *fastest* pressure waves. Regarding the source terms, λ_p and λ_u are positive bounded functions which account for relaxation time scales, see Section 4.2.2 for details.

4.2.2 Relaxation processes

The source terms of the CTL model ($\mathscr{S}$) are represented by relaxation terms, namely pressure and velocity relaxation terms. In the following, the associated relaxation processes at the continuous level as well as the relaxation time scales are detailed.

4.2.2.a Pressure relaxation

The interpretation of the pressure relaxation is given considering a flow homogeneous along x. Thus, ($\mathscr{S}$) yields:

$$\begin{cases} \dfrac{\partial h_1}{\partial t} = \lambda_p(P_I - P_2), \\ \dfrac{\partial m_k}{\partial t} = 0, \ k = 1,2. \end{cases} \tag{4.4}$$

The second equation of (4.4) gives $\frac{\partial \rho_k}{\partial t} = (-1)^k \frac{\rho_k}{h_k}\frac{\partial h_1}{\partial t}$ such that using the closure law (4.1) for P_I and (4.3), one obtains:

$$\begin{aligned} \frac{\partial (P_I - P_2)}{\partial t} &= c_1^2 \frac{\partial \rho_1}{\partial t} - \frac{g}{2}\frac{\partial m_1}{\partial t} - c_2^2 \frac{\partial \rho_2}{\partial t}, \\ &= -(\frac{c_1^2\rho_1}{h_1} + \frac{c_2^2\rho_2}{h_2})\frac{\partial h_1}{\partial t}, \\ &= -(\frac{c_1^2\rho_1}{h_1} + \frac{c_2^2\rho_2}{h_2})\lambda_p(P_I - P_2). \end{aligned}$$

Therefore, $\Pi(t) = \big(P_I - P_2\big)(t)$ satisfies:

$$\Pi(t) = \Pi_0 \exp\Big(-\int_0^t \lambda_p(\frac{c_1^2\rho_1}{h_1} + \frac{c_2^2\rho_2}{h_2})dt\Big), \tag{4.5}$$

where $\Pi_0 = \Pi(t=0)$. As λ_p is a positive bounded function, the following asymptotic behavior is obtained:

$$P_I - P_2 \underset{t\to+\infty}{\longrightarrow} 0. \tag{4.6}$$

Under the light of (4.5), the associated time scale, denoted τ_p, is defined as:

$$\tau_p = \Big(\lambda_p\Big(\frac{c_1^2\rho_1}{h_1} + \frac{c_2^2\rho_2}{h_2}\Big)\Big)^{-1}. \tag{4.7}$$

Regarding λ_p, an analytical expression is developed in [28] describing the oscillations of an isolated bubble (air bubble for instance) in an infinite medium (water for instance) with the Rayleigh-Plesset equation. This approach is adopted for our framework so that λ_p reads:

$$\lambda_p = \frac{3}{4\pi\mu_1}\frac{h_1 h_2}{H}, \tag{4.8}$$

where μ_1 is the dynamic viscosity of phase 1. For water, $\mu_1 = 10^{-3}\,Pa.s$ at $T = 20^o C$. In practice, dealing with air-water flows and choosing $c_k = c_{k,\text{ref}}$, $\rho_k = \rho_{k,\text{ref}}$, $h_k = \frac{H}{2}$ with $H = 1\,m$, (4.7) yields $\tau_p \sim 10^{-12}\,s$. Consequently, the interfacial pressure P_I quickly converges toward the air pressure.

Remark 4.1 (Pressure relaxation with spatial derivatives)**.** *When taking into account spatial derivatives in* (4.4), (4.5) *becomes:*

$$\Pi(t) = \big(\Pi_0 + R\big)\exp\big(-\int_0^t \frac{d\tau}{\tau_p}\big), \tag{4.9}$$

where $R = \int_0^t \mathscr{C}\exp(\int_0^\tau \frac{d\tau'}{\tau_p})d\tau$ *and* $\mathscr{C}$ *includes spatial derivatives due to convection terms. The relaxation effect still exists with the same time scale* τ_p *but is in competition with convection effects. Assuming that* τ_p *is constant and that* $\mathscr{C}$ *is bounded in time by a constant denoted M, one obtains* $|R| \leq \tau_p M(\exp\big(\frac{t}{\tau_p}\big) - 1\big)$ *which provides:*

$$|R\exp\big(-\int_0^t \frac{d\tau}{\tau_p}\big)| \leq |R|\exp(-\frac{t}{\tau_p}) \leq \tau_p M\big(1 - \exp(-\frac{t}{\tau_p})\big).$$

Thus, the additional contribution in (4.9) *vanishes when* $\tau_p \to 0$.

4.2.2.b Velocity relaxation

As in the previous section, a flow constant along x is considered. Thus, ($\mathscr{S}$) yields:

$$\begin{cases} \dfrac{\partial m_k}{\partial t} = 0,\ k = 1,2, \\ \dfrac{\partial m_k u_k}{\partial t} = (-1)^k \lambda_u (u_1 - u_2),\ k = 1,2. \end{cases} \tag{4.10}$$

As m_k is constant w.r.t. time, $\big(u_1 - u_2\big)(t)$ immediately satisfies:

$$\frac{\partial (u_1 - u_2)}{\partial t} = -\lambda_u\big(\frac{1}{m_1} + \frac{1}{m_2}\big)(u_1 - u_2),$$

which gives:

$$\big(u_1 - u_2\big)(t) = \big(u_1 - u_2\big)(0)\exp\Big(-\int_0^t \lambda_u\Big(\frac{m_1 + m_2}{m_1 m_2}\Big)dt\Big). \tag{4.11}$$

As λ_u is a positive bounded function, the following asymptotic behavior is obtained:

$$u_1 - u_2 \underset{t\to+\infty}{\longrightarrow} 0. \tag{4.12}$$

Under the light of (4.11), the associated time scale denoted τ_u verifies:

$$\tau_u = \Big(\lambda_u\Big(\frac{m_1 + m_2}{m_1 m_2}\Big)\Big)^{-1}. \tag{4.13}$$

The function λ_u is modeled as a classical interfacial drag force which writes:

$$\lambda_u = \frac{1}{2} f_i \rho_2 |u_1 - u_2|, \tag{4.14}$$

where f_i is a friction factor. In order to define f_i, several experimental studies have been led since the pioneer work of Taitel and Dukler in 1976 [48]. In particular, f_i should ideally depends on the flow regime. In the present work, a constant value relying on experimental results for stratified air-water flows is chosen, that is $f_i \sim 0.015$ (see [40]). Indeed, the performed numerical experiments do not involve strong interfacial shear between the phases. However, note that the numerical scheme proposed hereafter is independent of λ_u so that more complex laws can be implemented.

In practice, dealing with air-water flows and choosing $\rho_k = \rho_{k,\text{ref}}$, $h_k = \frac{H}{2}$ with $H = 1\,m$, (4.13) yields $\tau_u \sim 7.10^1/|u_1 - u_2|$. With a large speed disparity between the phases, $|u_1 - u_2| \sim 10\,m.s^{-1}$ for instance, one obtains $\tau_u \sim 7\,s$. Therefore, the velocity relaxation time scale is much larger than the pressure relaxation time scale.

4.2.3 Relevance of the CTL model for mixed flows

The CTL model has been developed to deal with mixed flows which involve stratified regimes as well as pressurized or dry regimes (pipe full of water or air). In this section, details are provided regarding its ability to handle these different regimes at the continuous level.

4.2.3.a Consistency with the shallow water equations

When it comes to free-surface flows, the well-known (incompressible) shallow water equations are usually considered in the literature. Considering a variable atmospheric pressure $P_a(x,t)$ without friction terms, the water height h_1 and the water speed u_1 comply with:

$$\begin{cases} \dfrac{\partial \rho_0 h_1}{\partial t} + \dfrac{\partial \rho_0 h_1 u_1}{\partial x} = 0, \\ \dfrac{\partial \rho_0 h_1 u_1}{\partial t} + \dfrac{\partial \rho_0 h_1 u_1^2}{\partial x} + \dfrac{\partial \rho_0 g \frac{h_1^2}{2}}{\partial x} + h_1 \dfrac{\partial P_a}{\partial x} = 0, \end{cases} \tag{4.15}$$

where ρ_0 is a constant accounting for water density, see [1, 29] for instance. It is thus interesting to check the consistency of the present model with that classical description.

Focusing on the momentum conservation equation for the water phase and smooth solutions, the last two terms of the left hand side, i.e. $\frac{\partial h_1 P_1}{\partial x} - P_I \frac{\partial h_1}{\partial x}$, may be rewritten as:

$$\frac{\partial h_1 P_1}{\partial x} - P_I \frac{\partial h_1}{\partial x} = \frac{\partial h_1 (P_1 - P_I)}{\partial x} + h_1 \frac{\partial P_I}{\partial x} = \frac{\partial \rho_1 g \frac{h_1^2}{2}}{\partial x} + h_1 \frac{\partial P_I}{\partial x},$$

using $P_I = P_1 - \rho_1 g \frac{h_1}{2}$. Thus, the water phase complies with the following system:

$$\frac{\partial h_1}{\partial t} + u_2 \frac{\partial h_1}{\partial x} = \lambda_p (P_I - P_2), \tag{4.16a}$$

$$\frac{\partial h_1 \rho_1}{\partial t} + \frac{\partial h_1 \rho_1 u_1}{\partial x} = 0, \tag{4.16b}$$

$$\frac{\partial h_1 \rho_1 u_1}{\partial t} + \frac{\partial h_1 \rho_1 u_1^2}{\partial x} + \frac{\partial \rho_1 g \frac{h_1^2}{2}}{\partial x} + h_1 \frac{\partial P_I}{\partial x} = \lambda_u (u_2 - u_1). \tag{4.16c}$$

If ρ_1 is considered as a constant in (4.16b) and (4.16c), the convective part reads *formally* as the classical (incompressible) shallow water model with an hydrostatic gradient and varying interfacial pressure $P_I(x,t)$, see (4.15). Furthermore, (4.16a) provides the very fast pressure relaxation (4.6) such that this last term can be read as a source term accounting for varying air pressure. In that description, friction effects with the air phase are also taken into account through the velocity relaxation term. The rewriting (4.16) is relevant in the stratified regime and guides the fractional step method developed in Section 4.3.

4.2.3.b Consistency with pressurized and dry flows

The case where the pipe is full of phase k is referred to as pressurized flow ($k = 1$) or dry flow ($k = 2$). In practice, transitions from stratified to pressurized or dry regimes often occur in industrial facilities so that one may wonder if this configuration will be correctly handled by the CTL model. Formally, considering $h_k = H$, $k = 1$ or 2, with H constant, ($\mathscr{S}$) reduces to:

$$\begin{cases} \dfrac{\partial \rho_k}{\partial t} + \dfrac{\partial \rho_k u_k}{\partial x} = 0, \\ \dfrac{\partial \rho_k u_k}{\partial t} + \dfrac{\partial (\rho_k u_k^2 + P_k(\rho_k))}{\partial x} = 0, \end{cases} \tag{4.17}$$

as soon as the source terms vanish when $h_k = H$, $k = 1$ or 2. This system is equivalent to an isentropic Euler system which is usually used to describe a pipe with constant cross-section and full of one phase including compressibility effects. Consequently, when $h_k \to H$, $k = 1$ or 2, the CTL model degenerates *naturally* (actually by construction) towards a relevant model for pressurized and dry flows.

Remark 4.2 (Definition of λ_u in pressurized and dry regimes)**.** *When $h_k = H$, $k = 1$ or 2, the pressure relaxation source term effectively vanishes due to the definition (4.8) of λ_p while the velocity relaxation source term does not necessarily vanish regarding the definition (4.14) of λ_u. This definition is nonetheless chosen to improve the robustness of the scheme proposed in Section 4.3 when dealing with vanishing phases. The corresponding parametric study is presented in Section 4.4.3.*

Thus, the CTL model provides a unified description of stratified, pressurized and dry regimes. In particular, the water phase is assumed compressible in every regime following a barotropic pressure law. Furthermore, significant mathematical properties are obtained as detailed in the next section.

4.2.4 Mathematical properties

In this section, the main mathematical properties of ($\mathscr{S}$) are recalled. Details and proofs are available in Chapter 2.

Property 4.1 (Entropy inequality)**.** *Smooth solutions of system ($\mathscr{S}$) comply with the entropy inequality:*

$$\frac{\partial \mathscr{E}}{\partial t} + \frac{\partial \mathscr{G}}{\partial x} \leq 0,$$

where the entropy $\mathscr{E}$ and the entropy flux $\mathscr{G}$ are defined by:

$$\begin{aligned}
&\mathscr{E} = E_{c,1} + E_{p,1} + E_{t,1} + E_{c,2} + E_{t,2},\\
&\mathscr{G} = u_1(E_{c,1} + E_{p,1} + E_{t,1}) + u_2(E_{c,2} + E_{t,2}) + u_1 h_1 P_1 + u_2 h_2 P_2,
\end{aligned}$$

with:

$$E_{c,k} = \frac{1}{2} h_k \rho_k u_k^2,\ E_{t,k} = h_k \rho_k \Psi_k(\rho_k),\ E_{p,1} = \rho_1 g \frac{h_1^2}{2},$$

and:

$$\Psi_k'(\rho_k) = \frac{P_k(\rho_k)}{\rho_k^2},\ k = 1,2.$$

Property 4.2 (Hyperbolicity and structure of the convective system)**.** *The convective part of ($\mathscr{S}$) is hyperbolic under the non-resonant condition:*

$$|u_1 - u_2| \neq c_1. \tag{4.18}$$

Its eigenvalues are unconditionally real and given by:

$$\lambda_1 = u_2,\ \lambda_2 = u_1 - c_1,\ \lambda_3 = u_1 + c_1,\ \lambda_4 = u_2 - c_2,\ \lambda_5 = u_2 + c_2. \tag{4.19}$$

The characteristic field associated with the 1-wave λ_1 is linearly degenerate while the characteristic fields associated with the waves λ_k, $k = 2,..,5$, are genuinely nonlinear. Moreover, all the Riemann invariants can be detailed.

Note that in our applications, $c_1 = 1500\,m/s$ and (4.18) should not be violated.

Property 4.3 (Uniqueness of jump conditions)**.** *Unique jump conditions hold within each isolated field. For all genuine non-linear fields corresponding to the k-waves, $k = 2,...,5$, the Rankine-Hugoniot jump conditions across a single discontinuity of speed σ write:*

$$\begin{aligned}
&[h_k] = 0,\\
&[h_k \rho_k (u_k - \sigma)] = 0,\\
&[h_k \rho_k u_k (u_k - \sigma) + h_k P_k] = 0,
\end{aligned}$$

where brackets $[.]$ denote the difference between the states on both sides of the discontinuity.

Furthermore, note that as the field associated to the jump of h_1 is linearly degenerate, the non-conservative products $u_2 \partial_x h_1$ and $(P_1 - \rho_1 g \frac{h_1}{2}) \partial_x h_1$ in ($\mathscr{S}$) are well defined. Indeed, one may use the available 1-Riemann invariants to write explicitly the 1-wave parametrisation. Note that as the jump conditions and the Riemann invariants can be detailed, one can build analytical solutions for the convective part of ($\mathscr{S}$) including the contact discontinuity, shock waves and rarefaction waves. This approach is used in Section 4.4 to verify the numerical scheme exposed in Section 4.3.

Property 4.4 (Positivity)**.** *Focusing on smooth solutions, the positivity of h_k and ρ_k is verified, as soon as λ_p may be written under the form $\lambda_p = h_1 h_2 \tilde{\lambda}_p$, where $\tilde{\lambda}_p$ is a positive bounded function depending on the state variable. The positivity requirements hold for discontinuous solutions of the Riemann problem associated to the homogeneous system ($\mathscr{S}$).*

Due to Property 4.4, the height h_k of each layer is naturally kept between the bounds at the continuous level, i.e. $h_k \in [0,H]$, $k = 1,2$, without imposing any constraint. This is an interesting feature when dealing with mixed flow modelling as this fundamental property may be naturally transposed to the discrete level. For comparison, the popular single-phase mixed flow models available in the literature [54, 11, 42, 38] do not satisfy the constraint $h_1 \leq H$ so that they interpret the domain $h_1 \geq H$ as the pressurized regime. In our case, this property comes from the two-phase framework which nonetheless brings numerical challenges when dealing with vanishing phases. In the next section, a numerical method which handles the different regimes and transitions between them is presented.

4.3 A fractional step method adapted to mixed flows

As highlighted in Section 4.2.3 at the continuous level, the CTL model may be an interesting candidate to compute mixed flows with a two-phase description. Nonetheless, difficulties are encountered at the discrete level as listed below. Therefore, a numerical strategy based on a fractional step method combined with an implicit-explicit time discretization is proposed.

4.3.1 Numerical challenges

The CTL model is a two-fluid two-pressure model whose numerical resolution raises several challenges. Firstly, the convective part of the system is doted with a complex wave structure, see Property 4.2, which makes difficult the Riemann problem to solve regarding Godunov-type methods. Secondly, the whole system includes relaxation source terms strongly interacting with the convective part and associated with various time scales. In particular, the pressure relaxation is very fast, see Section 4.2.2. Dealing with mixed flows, the following challenges are added:

(i) *Multi-regime flow*. Mixed flows essentially features two regimes: the stratified and the pressurized regimes. The stratified regime is mainly driven by slow gravity waves in the liquid phase whose typical celerity is $\sqrt{gh_1}$ (see [29]), whereas the pressurized regime is driven by fast acoustic waves whose celerity is given by $c_1 = \sqrt{P_1'(\rho_1)}$. In practice, $c_1 \sim 1500 m.s^{-1}$ for water which leads to $\frac{\sqrt{gh_1}}{c_1} \ll 1$ considering realistic pipe heights. Regarding the characteristic waves of the CTL model, see (4.19), one of them is propagating at slow material speed u_2 whereas the other four are propagating at fast acoustic speeds, $u_k \pm c_k$, $k = 1,2$. Therefore, when using classical explicit schemes, one obtains a CFL condition based on the speed of these fast acoustic waves which brings large numerical diffusion in the slow stratified regime. The ideal scheme should be efficient in both regimes in addition to handle transitions between them.

(ii) *Vanishing phases in pressurized and dry regimes*. At the continuous level, pressurized and dry regimes involve single-phase flows, i.e. $h_k = 0$, $k = 1$ or 2. At the discrete level, both phases are solved in every regime with the CTL model. Thus, one has to deal with vanishing phases, i.e. $h_k \to 0$, $k = 1$ or 2, which raise robustness issues with most of classical numerical solvers.

A numerical scheme is detailed hereafter with the aim of addressing the above challenges. It begins with a splitting approach which particularly accounts for item (i) and for the fast pressure relaxation. A three-step scheme relying on an implicit-explicit time discretization is then derived. As highlighted in the sequel, a particular interest is paid to the robustness of the overall approach with vanishing phases.

4.3.2 Operator splitting

Regarding the CTL model ($\mathscr{S}$), the slow dynamics of the stratified regime is driven by the hydrostatic gradient found in the momentum conservation equation for the water phase while the fast dynamics is driven by pressure gradients in both phases. Therefore, ($\mathscr{S}$) is split into three sub-systems. The slow dynamics of ($\mathscr{S}$) is treated in ($\mathscr{S}_m$) where the

rewriting (4.16c) is used for the water phase:

$$\begin{cases} \partial_t h_1 + u_2 \partial_x h_1 = \lambda_p (P_I - P_2), \\ \partial_t m_k + \partial_x m_k u_k = 0, \ k = 1,2, \\ \partial_t m_1 u_1 + \partial_x m_1 u_1^2 + \partial_x \rho_1 g \dfrac{h_1^2}{2} = 0, \\ \partial_t m_2 u_2 + \partial_x m_2 u_2^2 = 0. \end{cases} \tag{$\mathscr{S}_m$}$$

The second sub-system ($\mathscr{S}_a$) refers to the fast dynamics of ($\mathscr{S}$) including the pressure gradients:

$$\begin{cases} \partial_t h_1 = 0, \\ \partial_t m_k = 0, \ k = 1,2, \\ \partial_t m_1 u_1 + h_1 \partial_x P_I = 0, \\ \partial_t m_2 u_2 + h_2 \partial_x P_2 + (P_2 - P_I) \partial_x h_2 = 0, \end{cases} \tag{$\mathscr{S}_a$}$$

where $P_I = P_1 - \rho_1 g \frac{h_1}{2}$. The last sub-system ($\mathscr{S}_u$) deals with the velocity relaxation source term:

$$\begin{cases} \partial_t h_1 = 0, \\ \partial_t m_k = 0, \ k = 1,2, \\ \partial_t m_k u_k = (-1)^k \lambda_u (u_1 - u_2), \ k = 1,2. \end{cases} \tag{$\mathscr{S}_u$}$$

This splitting has mainly two key features. The first one is the closeness of ($\mathscr{S}_m$) with the shallow water system for the water phase which is relevant regarding the stratified regime. The second one relies on the resolution of the fast pressure relaxation also in the first step. Doing so, the terms linked to this relaxation, namely $h_1 \partial_x P_I$ and $(P_2 - P_I)\partial_x h_2$, are explicitly impacted in the second step. Hyperbolicity properties of systems ($\mathscr{S}_m$) and ($\mathscr{S}_a$) are given in propositions below. The proofs are not detailed herein as they result from straightforward calculations.

Proposition 4.1 (Structure of the convective part of ($\mathscr{S}_m$))**.** *The convective part of ($\mathscr{S}_m$) is weakly hyperbolic. Its eigenvalues belongs to* $\{u_2; u_1 \pm \sqrt{g \frac{h_1}{2}}\}$. *The characteristic fields associated with the eigenvalue u_2 are linearly degenerate while the characteristic fields associated with the eigenvalues* $u_1 \pm \sqrt{g \frac{h_1}{2}}$ *are genuinely nonlinear.*

Proposition 4.2 (Structure of the convective part of ($\mathscr{S}_a$))**.** *The convective part of ($\mathscr{S}_m$) is weakly hyperbolic. Its eigenvalues are* $\{0\}$. *All the characteristic fields are linearly degenerate.*

Remark 4.3 (Eigenvalues and gravity waves)**.** *Regarding the water phase equations in ($\mathscr{S}_m$), one obtains the eigenvalues* $u_1 \pm \sqrt{g \frac{h_1}{2}}$ *instead of* $u_1 \pm \sqrt{g h_1}$ *when dealing with the (incompressible) shallow water system. This result is a straightforward consequence of the water phase compressibility which modifies subsequently the Jacobian structure through the hydrostatic gradient* $\partial_x \rho_1 g \frac{h_1^2}{2}$. *Indeed, the latter yields contribution in $\partial_x \rho_1$ in addition to $\partial_x h_1$ in the compressible framework.*

A three step scheme is then proposed and exposed in the next sections. In particular, a classical explicit scheme with Rusanov fluxes is used for ($\mathscr{S}_m$) while an original implicit relaxation approach is derived to handle the singular spectrum of ($\mathscr{S}_a$). Note that a similar splitting is developed in [19] for the isentropic Baer-Nunziato system but the underlying scheme is fully explicit.

In the discrete setting, the time step is denoted Δt and the space step Δx. The space is partitioned into cells $C_i = [x_{i-\frac{1}{2}}, x_{i+\frac{1}{2}}[$ where $x_{i+\frac{1}{2}} = (i+\frac{1}{2})\Delta x$ are the cell interfaces. At discrete times t^n, the solution is approximated on each cell C_i by:

$$\mathbf{W}_i^n = \left((h_1)_i^n, (m_1)_i^n, (m_2)_i^n, (m_1 u_1)_i^n, (m_2 u_2)_i^n \right)^T. \tag{4.20}$$

4.3.3 Step 1: explicit approach for the slow dynamics

This first step deals with ($\mathscr{S}_m$) and updates $\mathbf{W}_i$ from $\mathbf{W}_i^n$ to $\mathbf{W}_i^*$. A classical explicit finite-volume scheme with Rusanov fluxes is used on the convective part (see [47]) while the pressure relaxation source term is treated implicitly except for the λ_p parameter. It writes:

$$\mathbf{W}_i^* = \mathbf{W}_i^n - \frac{\Delta t}{\Delta x} \left(\mathbf{F}(\mathbf{W}_{i+\frac{1}{2}}^n) - \mathbf{F}(\mathbf{W}_{i-\frac{1}{2}}^n) \right) - \frac{\Delta t}{2\Delta x} \mathbf{B}(\mathbf{W}_i^n) \left(\mathbf{W}_{i+1}^n - \mathbf{W}_{i-1}^n \right) + \Delta t \mathbf{S}(\mathbf{W}_i^*), \tag{4.21}$$

where:

$$\begin{cases} \mathbf{F}(\mathbf{W}) = (0, m_1u_1, m_2u_2, m_1u_1^2 + m_1g\dfrac{h_1}{2}, m_2u_2^2)^T, \\ \mathbf{B}(\mathbf{W}) = (u_2, 0, 0, 0, 0)^T, \\ \mathbf{S}(\mathbf{W}) = (\lambda_p(P_I - P_2), 0, 0, 0, 0)^T. \end{cases}$$

The fluxes are defined by:

$$\begin{cases} \mathbf{F}(\mathbf{W}^n_{i+\frac{1}{2}}) = \dfrac{1}{2}\Big(\mathbf{F}(\mathbf{W}^n_i) + \mathbf{F}(\mathbf{W}^n_{i+1}) - r_{i+\frac{1}{2}}(\mathbf{W}^n_{i+1} - \mathbf{W}^n_i)\Big), \\ r_{i+\frac{1}{2}} = \max\limits_{j\in\{i;i+1\}}\Big(|u^n_{2,j}|; |\big(u_1 \pm \sqrt{g\dfrac{h_1}{2}}\big)^n_j|\Big). \end{cases} \tag{4.22}$$

Note that the time step Δt and the coefficient $r_{i+\frac{1}{2}}$ depend on the iteration and should get a superscript n but it is omitted hereafter for the sake of clarity. Regarding the update of $h^n_{1,i}$, one can state the following proposition:

Proposition 4.3 (Uniqueness and positivity of heights)**.** *There exits a unique $h^*_{1,i} \in [0;H]$ satisfying the discretization (4.21) of ($\mathscr{S}_m$). In addition, this property does not require any condition on the time step.*

Proof. $h^*_{1,i}$ is computed with an implicit treatment of the pressure relaxation source term keeping the relaxation parameter λ_p explicit. The mass terms $m^n_{k,i}$ are updated first and the transport equation (4.16a) is solved under the form $f(h^*_{1,i}) = 0$ where:

$$f(y) = y - h^n_{1,i} + \Delta t \int_{x_{i-\frac{1}{2}}}^{x_{i+\frac{1}{2}}} u_2^n \frac{\partial h_1^n}{\partial x} dx - \Delta t \lambda^n_{p,i}\Big(P_1\Big(\frac{m^*_{1,i}}{y}\Big) - m^*_{1,i}\frac{g}{2} - P_2\Big(\frac{m^*_{2,i}}{H-y}\Big)\Big). \tag{4.23}$$

One may easily demonstrate that f is strictly increasing on $[0;H]$ with the limits $f \underset{0^+}{\to} -\infty$ and $f \underset{H^-}{\to} +\infty$, such that $f(x) = 0$ admits a unique solution $h^*_{1,i}$ on $[0;H]$. This result does not require any condition on Δt and is independent of the space discretization applied to $\int_{x_{i-\frac{1}{2}}}^{x_{i+\frac{1}{2}}} u_2^n \frac{\partial h_1^n}{\partial x} dx$. In practice, this integral is decomposed as $\int_{x_{i-\frac{1}{2}}}^{x_{i+\frac{1}{2}}} u_2^n \frac{\partial h_1^n}{\partial x} dx = \int_{x_{i-\frac{1}{2}}}^{x_{i+\frac{1}{2}}} (\frac{\partial u_2^n h_1^n}{\partial x} - h_1^n \frac{\partial u_2^n}{\partial x}) dx$ where the fluxes are defined with (4.22). □

Therefore, $h^*_{1,i}$ is computed solving $f(h^*_{1,i}) = 0$ where f is defined in (4.23). In practice, the Brent method is used to solve this nonlinear problem, see [13]. The algorithm combines linear interpolation and inverse quadratic interpolation with bisection to get efficiency and robustness. The convergence is superlinear and the solution is kept between the bounds, even when getting close to the boundaries. This choice is important when dealing with vanishing phases. Regarding the positivity of densities, it is ensured through a CFL condition detailed in the following proposition:

Proposition 4.4 (Positivity of densities)**.** *The scheme for ($\mathscr{S}_m$) proposed in (4.21) and (4.22) ensures the positivity of densities under the classical CFL condition:*

$$\frac{\Delta t}{\Delta x}\max_i\Big(\frac{r_{i+\frac{1}{2}} + r_{i-\frac{1}{2}}}{2}\Big) \leq 1, \tag{4.24}$$

which only implies the celerity of material and gravity waves.

Proof. The proof is classical. Applying (4.21) and (4.22) to the mass conservation equations, one readily obtains:

$$m^*_{k,i} = \big(1 - (r_{i+\frac{1}{2}} + r_{i-\frac{1}{2}})\frac{\Delta t}{2\Delta x}\big)m^n_{k,i} + (r_{i+\frac{1}{2}} - u^n_{k,i+1})\frac{\Delta t}{2\Delta x}m^n_{k,i+1} + (r_{i-\frac{1}{2}} + u_{k,i-1})\frac{\Delta t}{2\Delta x}m^n_{k,i-1},\ k = 1,2.$$

Seeing $m^*_{k,i}$ as a linear convex combination of $m^n_{k,j}$, $j \in \{i-1;i;i+1\}$, with $m^n_{k,j} \geq 0$ and $r_{i+\frac{1}{2}} \geq |u^n_{k,l}|$, $l \in \{i;i+1\}$, $\forall i$, a sufficient condition to ensure $m^*_{k,i} \geq 0$ is given by (4.24). □

The proposed scheme is also consistent with the relaxation property obtained at the continuous level, as presented in the next proposition:

Proposition 4.5 (Discrete pressure relaxation)**.** *The pressure relaxation property exposed in Section 4.2.2.a at the continuous level holds at the discrete level. Denoting $\Pi = P_I - P_2$, it writes $|\Pi^*| < |\Pi^n|$ for a flow homogeneous along x.*

Proof. As in the continuous case, one assumes a flow independent of space first. The semi-discrete equation verified by h_k reads:

$$\frac{(h_1^* - h_1^n)}{\Delta t} = -\frac{(h_2^* - h_2^n)}{\Delta t} = \lambda_p^n \Pi^*.$$

As ρ_k is a continuous and differentiable function of P_k, one can define two functions (η_1, η_2) such that $\rho_k^* = \rho_k^n + \rho_k'(\eta_k)(P_k^* - P_k^n)$, $k = 1,2$ (mean value theorem). With $m_k^* = m_k^n$ due to mass conservation without spatial derivatives, one obtains:

$$\Pi^* = \frac{(-1)^k}{\lambda_p^n \Delta t}\left(\frac{m_k^n}{\rho_k^n} - \frac{m_k^*}{\rho_k^*}\right) = (-1)^k \frac{m_k^n}{\lambda_p^n \Delta t}\left(\frac{\rho_k^* - \rho_k^n}{\rho_k^n \rho_k^*}\right) = (-1)^k \frac{m_k^n \rho_k'(\eta_k)}{\lambda_p^n \Delta t \rho_k^n \rho_k^*}(P_k^* - P_k^n),\ k = 1,2.$$

Using $\Pi^* - \Pi^n = (P_1^* - P_1^n) + \frac{g}{2}(m_1^n - m_1^*) - (P_2^* - P_2^n) = (P_1^* - P_1^n) - (P_2^* - P_2^n)$, the equation above with $k = 1,2$ yields:

$$\Pi^* - \Pi^n = -\lambda_p \Delta t \left(\frac{\rho_1^*}{h_1^n \rho_1'(\eta_1)} + \frac{\rho_2^*}{h_2^n \rho_2'(\eta_2)}\right)\Pi^*, \tag{4.25}$$

which provides:

$$|\Pi^*| \leq |\Pi^n|, \tag{4.26}$$

since $\lambda_P > 0$ and $\rho_k'(P_k) > 0$. Considering spatial derivatives, one obtains a discrete equivalent of (4.9) where convective terms vanish when $\tau_p \to 0$. □

Remark 4.4 (Discrete pressure relaxation in pressurized and dry regimes)**.** *According to the definition (4.8) of λ_p, one observes that $\lambda_p \to 0$ when $h_k \to 0$, $k = 1$ or 2. Nonetheless, discrete relaxation effects may be still present as the associated time scale, i.e. τ_p defined (4.7), vanishes very slowly due to the high celerity and density values of the water phase. Note that this discrete pressure relaxation brings dissipation and thus robustness in pressurized and dry regimes.*

At last, this first step deals with the slow dynamics of ($\mathscr{S}$) ensuring the positivity of heights and densities under the CFL condition (4.24) based on the celerity of material and gravity waves.

4.3.4 Step 2: implicit approach for the fast dynamics

This second step deals with ($\mathscr{S}_a$) and updates $\mathbf{W}_i$ from $\mathbf{W}_i^*$ to $\mathbf{W}_i^{**}$. In particular, all the variables are kept constant except the velocities. As all the eigenvalues of this system are zero, see proposition (4.2), one cannot apply a classical numerical method relying on the spectral radius of the Jacobian matrix. Thus, a relaxation method which consists in considering a larger system easier to solve is developed, see [18, 19, 21, 2, 8] for a related framework.

One introduces the system ($\mathscr{S}_a^r$) which relaxes towards ($\mathscr{S}_a$) in the limit $\varepsilon \to 0$:

$$\begin{cases} \partial_t h_1 = 0, \\ \partial_t m_k = 0,\ k = 1,2, \\ \partial_t m_1 u_1 + h_1 \partial_x \Pi_I = 0, \\ \partial_t m_2 u_2 + h_2 \partial_x \Pi_2 + (\Pi_2 - \Pi_I)\partial_x h_2 = 0, \\ \partial_t m_k \Pi_k + a_k^2 h_k \partial_x u_k + a_k^2 (u_k - u_2)\partial_x h_k = \dfrac{1}{\varepsilon} m_k (P_k - \Pi_k),\ k = 1,2. \end{cases} \tag{$\mathscr{S}_a^r$}$$

Π_k is an additional unknown which relaxes towards P_k as $\varepsilon \to 0$ and $\Pi_I = \Pi_1 - \rho_1 g \frac{h_1}{2}$. The PDE verified by Π_k is derived from the PDE verified by P_k in ($\mathscr{S}$) without the convective terms. In addition, a_k are positive numerical parameters used to ensure the stability of the relaxation approximation in the regime of small ε, their definition is provided later according to the flow regime. The structure of the convective part of ($\mathscr{S}_a^r$) is studied in the following proposition and results from immediate calculations not detailed herein.

Proposition 4.6 (Structure of the convective part of ($\mathscr{S}_a^r$))**.** *When $a_k > 0$, the convective part of ($\mathscr{S}_a^r$) is strictly hyperbolic. Its eigenvalues are given by $\{0; \pm\frac{a_1}{\rho_1}; \pm\frac{a_2}{\rho_2}\}$, and all associated characteristic fields are linearly degenerate.*

4.3.4.a Time discretization

In order to keep a CFL condition based on the slow dynamics, the time discretization proposed for the convective part of ($\mathscr{S}_a^r$) is mainly implicit:

$$\begin{cases} h_k^{**} = h_k^*, m_k^{**} = m_k^*,\ k=1,2, \\ (m_1^{**}u_1^{**} - m_1^*u_1^*)/\Delta t + h_1^{**}\partial_x\Pi_I^{**} = 0, \\ (m_2^{**}u_2^{**} - m_2^*u_2^*)/\Delta t + h_2^{**}\partial_x\Pi_2^{**} + (\Pi_2^* - \Pi_I^*)\partial_x h_2^* = 0, \\ (m_k^{**}\Pi_k^{**} - m_k^*\Pi_k^*)/\Delta t + a_k^{2^*}h_k^{**}\partial_x u_k^{**} + a_k^{2^*}(u_k^* - u_2^*)\partial_x h_k^* = 0,\ k=1,2. \end{cases} \tag{4.27}$$

The explicit treatment of $(\Pi_2^* - \Pi_I^*)\partial_x h_2^*$ in the air momentum equation is justified by the pressure relaxation solved in the previous step. Regarding the semi-discrete equation verified by Π_1, the term $a_1^{2^*}(u_1^* - u_2^*)\partial_x h_1^*$ may be treated implicitly solving the air phase first. In practice, this treatment seems needless as the explicit approach does not induce any additional CFL constraint. At last, note that relaxation parameters depend only on h_k and m_k (see Definition 4.3.1) leading to $a_k^* = a_k^{**}$.

In the following, an instantaneous relaxation ($\varepsilon \to 0$) between Π_k and P_k is assumed and writes $\Pi_k^* = P_k^*$. Performing classical combinations on (4.27), the proposed scheme for ($\mathscr{S}_a$) reduces to the following semi-discrete equations on $u_k,\ k=1,2$:

$$\frac{u_1^{**} - u_1^*}{\Delta t} - \frac{\Delta t}{\rho_1^*}\partial_x\Big(\frac{a_1^{2^*}}{\rho_1^*}\partial_x u_1^{**}\Big) = -\frac{1}{\rho_1^*}\partial_x P_I^* + \frac{\Delta t}{\rho_1^*}\partial_x\Big(\frac{a_1^{2^*}(u_1^* - u_2^*)}{m_1^*}\partial_x h_1^*\Big), \tag{4.28a}$$

$$\frac{u_2^{**} - u_2^*}{\Delta t} - \frac{\Delta t}{\rho_2^*}\partial_x\Big(\frac{a_2^{2^*}}{\rho_2^*}\partial_x u_2^{**}\Big) = -\frac{1}{\rho_2^*}\partial_x P_2^* - \frac{(P_2^* - P_I^*)}{m_2^*}\partial_x h_2^*. \tag{4.28b}$$

One may notice that the relaxation variable does not appear in (4.28). Furthermore, in comparison with ($\mathscr{S}_a$), the proposed implicit relaxation approach acts as a stabilization process adding diffusion terms weighted by a_k at the discrete level.

4.3.4.b Space discretization

Considering the space discretization of (4.28), a classical two-point flux approximation is used for the diffusion terms and centered fluxes are used for the pressure gradients of the RHS. Furthermore, in order to improve the robustness of the scheme when $h_k \to 0,\ k=1,2$, the following is applied in the RHS of (4.28) before space integration:

$$\frac{\partial_x h_k^*}{m_k^*} = \frac{1}{\rho_k^*}\partial_x \ln(h_k^*). \tag{4.29}$$

Integrating (4.28) on a cell $C_i = [x_{i-\frac{1}{2}}, x_{i+\frac{1}{2}}[$ yields an implicit system for each phase which may be written under matrix form:

$$A_k^*\mathbb{U}_k^{**} = \mathbb{S}_k^*, \tag{4.30}$$

where A_k^* is defined as:

$$A_{k,ij}^* = \begin{cases} 1 + \frac{1}{\rho_{k,i}^*}(\frac{\Delta t}{\Delta x})^2\Big((\frac{a_k^2}{\rho_k})_{i+\frac{1}{2}}^* + (\frac{a_k^2}{\rho_k})_{i-\frac{1}{2}}^*\Big) & \text{if } i=j, \\ -\frac{1}{\rho_{k,i}^*}(\frac{a_k^2}{\rho_k})_{i+\frac{1}{2}}^* & \text{if } j=i+1, \\ -\frac{1}{\rho_{k,i}^*}(\frac{a_k^2}{\rho_k})_{i-\frac{1}{2}}^* & \text{if } j=i-1, \\ 0 & \text{elsewhere.} \end{cases} \tag{4.31}$$

The integrated source terms $\mathbb{S}_k^*,\ k=1,2$, write:

$$\mathbb{S}_{1,i}^* = u_{1,i}^* - \frac{\Delta t}{2\Delta x}\Big(\frac{P_{I,i+1}^* - P_{I,i-1}^*}{\rho_{1,i}^*}\Big) + (\frac{\Delta t}{\Delta x})^2\frac{1}{\rho_{1,i}^*}\Big((\frac{a_1^2(u_1-u_2)}{\rho_1})_{i+\frac{1}{2}}^*\ln(\frac{h_{1,i+1}^*}{h_{1,i}^*}) - (\frac{a_1^2(u_1-u_2)}{\rho_1})_{i-\frac{1}{2}}^*\ln(\frac{h_{1,i}^*}{h_{1,i-1}^*})\Big), \tag{4.32}$$

$$\mathbb{S}_{2,i}^* = u_{2,i}^* - \frac{\Delta t}{2\Delta x}\Big(\frac{P_{2,i+1}^* - P_{2,i-1}^*}{\rho_{2,i}^*}\Big) - \frac{\Delta t}{\Delta x}\Big(\frac{P_{2,i}^* - P_{I,i}^*}{\rho_{2,i}^*}\Big)\ln\Big(\frac{1+\frac{h_{2,i+1}^*}{h_{2,i}^*}}{1+\frac{h_{2,i-1}^*}{h_{2,i}^*}}\Big). \tag{4.33}$$

Proposition 4.7 (Non-singularity of the implicit system)**.** *The system* (4.30) *is non-singular as* A_k^* *has an M-matrix structure.*

Proof. Regarding (4.31), A_k^* verifies:

$$A_{k,ii}^* > 0, \qquad A_{k,i\neq j}^* \leq 0, \qquad |A_{k,ii}^*| - \sum_{j\neq i} |A_{k,ij}^*| > 0. \tag{4.34}$$

Thus, A_k^* has an M-matrix structure and (4.30) admits a unique solution. □

Remark 4.5 (Non-singularity with vanishing phases)**.** *In addition to Proposition 4.7, note that* A_k^* *remains non-singular when* $h_k \to 0$*. This is a substantial property when dealing with pressurized and dry regimes which is not obtained with the implicit system derived in Chapter 3.*

The definition of the relaxation parameters and the correlated diffusion coefficients is addressed in the next section.

4.3.4.c Definition of relaxation parameters

At the continuous level, the relaxation parameters a_k must typically follow the so-called Whitham condition:

$$a_k > \max_{\rho_k}(\rho_k c_k), \; k = 1,2, \tag{4.35}$$

in order to prevent the relaxation system ($\mathscr{S}_a^r$) from instabilities in the regime of small values of ε, see [9, 18] for instance. In particular, it ensures the stability of acoustic waves propagating at $\sqrt{P_k'(\rho_k)} = c_k$. As stated throughout this chapter, mixed flows involve stratified regimes driven by gravity waves as well as pressurized and dry regimes driven by acoustic waves. Thus, regarding (4.28), a definition of relaxation parameters according to the flow regime is proposed below.

Definition 4.3.1 (Relaxation parameters according to the flow regime)**.** *Under the light of* (4.28)*,* a_k *is defined according to the flow regime:*

- *In the stratified and dry regimes* ($h_1 < H$)*: the pressure gradient* $h_1 \partial_x P_I$ *in* ($\mathscr{S}_a$) *is treated as a source term. It accounts for variable interfacial pressure which can be interpreted as air phase pressure due to the fast pressure relaxation solved in the first step. Thus,* a_1 *is set to zero in* (4.28a)*.*
- *In the pressurized regime* ($h_1 = H$)*: the stabilization process for acoustic waves is applied and* a_1 *must follow the so-called Whitham condition:* $a_1 > \max_{\rho_1}(\rho_1 c_1)$ *in* (4.28a)*.*
- *In all the regimes,* a_2 *follows the Whitham condition* $a_2 > \max_{\rho_2}(\rho_2 c_2)$ *in* (4.28b)*.*

According to Definition 4.3.1, a_1 switches between the stratified and the pressurized regime from 0 to $\eta_1 \max_{\rho_1}(\rho_1 c_1)$ where η_1 is a constant greater than one (typically $\eta_1 = 1.01$). In practice, it is proposed to identify each regime using a threshold h_s on h_1 so that a_1 is defined as:

$$a_1 = f(h_1) \max_{\rho_1}(\rho_1 c_1), \tag{4.36}$$

where:

$$f(h_1) = \begin{cases} 0, & \text{if } h_1 < h_s, \\ \eta_1 \left(\frac{h_1 - h_s}{H - h_s} \right)^2, & \text{if } h_s \leq h_1 \leq H. \end{cases} \tag{4.37}$$

Therefore, a_1 is a continuous differentiable function which ensures the stability of (4.28a) in every regime as particularly observed in Chapter 6. The threshold h_s is typically set to $(1-\delta)H$ with $\delta = 10^{-3}$ for mixed flow simulations, more details are provided in Section 4.4.3 regarding this setting.

Remark 4.6 (Simplification for constant pipe heights)**.** *On the RHS of* (4.28a)*, the diffusion term provided by the relaxation approach writes* $\frac{\Delta t}{\rho_1^*} \partial_x \left(\frac{a_1^{2^*}(u_1^* - u_2^*)}{m_1^*} \partial_x h_1^* \right)$*. In view of Definition 4.3.1, this term is zero in the stratified and dry regimes* ($a_1 = 0$) *but also in the pressurized regime when considering constant pipe heights* ($\partial_x h_1 = 0$)*. This term is thus not considered in the mixed flow simulations presented in Section 4.4 and Chapter 6.*

At the the discrete level, the value $a_{1,i}$ is defined through a simplified version of (4.36) which reads:

$$a_{1,i} = f(h_{1,i})\rho_{1,i}c_{1,i}.$$

The latter is less restrictive than (4.36) but in our framework, c_1 is a constant, see (4.2a), and the water density ρ_1 experiences small variations. An arithmetic mean is then used to define the interfacial diffusion coefficient involved in A_1^* (see (4.31)):

$$\left(\frac{a_1^2}{\rho_1}\right)^*_{i+\frac{1}{2}} = \frac{1}{2}\left(\frac{a_{1,i}^2}{\rho_{1,i}} + \frac{a_{1,i+1}^2}{\rho_{1,i+1}}\right)^*.$$

This relation ensures a smoother transition between the regimes compared to an harmonic mean. The other interfacial diffusion coefficient arising in the RHS (4.32), i.e. $\left(\frac{a_1^2(u_1-u_2)}{\rho_1}\right)^*_{i+\frac{1}{2}}$, may be defined equivalently. Regarding the air phase, one directly defines $a_{2,i+\frac{1}{2}}$ in order to be consistent with (4.35) but only on two adjacent cells:

$$a_{2,i+\frac{1}{2}} = \eta_2 \max_{j\in\{i,i+1\}}(\rho_{2,j}c_{2,j}),$$

where η_2 is a constant greater than one (typically $\eta_2 = 1.01$). This discrete definition is more classical when using relaxation schemes, see [19, 21] for instance. An arithmetic mean is then used for $\rho_{2,i+\frac{1}{2}}$, leading to the following definition for the interfacial diffusion coefficient involved in A_2^* (see (4.31)):

$$\left(\frac{a_2^2}{\rho_2}\right)^*_{i+\frac{1}{2}} = a^{*^2}_{2,i+\frac{1}{2}}\left(\frac{2}{\rho_{2,i}+\rho_{2,i+1}}\right)^*.$$

This relation closes the second step which does not require any condition on the time step.

4.3.5 Step 3: implicit approach for the velocity relaxation

This third step deals with ($\mathscr{S}_u$) and updates $\mathbf{W}_i$ from $\mathbf{W}_i^{**}$ to $\mathbf{W}_i^{n+1}$. Noticeably, all variables are kept constant except the velocities. As for the pressure relaxation, the source term is treated implicitly except for the λ_u parameter. Indeed, the latter may include complex functions depending on the state variable and accounting for friction effects, see (4.14). Using the fact that m_k is constant w.r.t. time in this step, the proposed semi-discrete implicit scheme writes:

$$m_k^{**}(u_k^{n+1} - u_k^{**}) = (-1)^k \Delta t \lambda_u^{**}(u_1^{n+1} - u_2^{n+1}). \tag{4.38}$$

Combining (4.38) for $k = 1, 2$, one obtains the following non-singular 2×2 system:

$$\begin{pmatrix} m_1^{**} + \Delta t\lambda_u^{**} & -\Delta t\lambda_u^{**} \\ -\Delta t\lambda_u^{**} & m_2^{**} + \Delta t\lambda_u^{**} \end{pmatrix}\begin{pmatrix} u_1^{n+1} \\ u_2^{n+1} \end{pmatrix} = \begin{pmatrix} (m_1u_1)^{**} \\ (m_2u_2)^{**} \end{pmatrix},$$

which yields:

$$\begin{pmatrix} u_1^{n+1} \\ u_2^{n+1} \end{pmatrix} = \frac{1}{\Lambda^{**}}\begin{pmatrix} m_2^{**} + \Delta t\lambda_u^{**} & \Delta t\lambda_u^{**} \\ \Delta t\lambda_u^{**} & m_1^{**} + \Delta t\lambda_u^{**} \end{pmatrix}\begin{pmatrix} (m_1u_1)^{**} \\ (m_2u_2)^{**} \end{pmatrix}. \tag{4.39}$$

where $\Lambda^{**} = m_1^{**}m_2^{**} + \Delta t\lambda_u^{**}(m_1^{**} + m_2^{**})$.

Proposition 4.8 (Discrete velocity relaxation)**.** *The velocity relaxation property exposed in Section 4.2.2.b at the continuous level holds at the discrete level. Denoting $\mathscr{U}^{**} = u_1^{**} - u_2^{**}$, it writes $|\mathscr{U}^{n+1}| < |\mathscr{U}^{**}|$.*

Proof. Using (4.39), one readily obtains:

$$\mathscr{U}^{n+1} = \frac{m_1^{**}m_2^{**}}{\Lambda^{**}}\mathscr{U}^{**},$$

where $m_1^{**}m_2^{**} < \Lambda^{**}$. □

Remark 4.7 (Discrete velocity relaxation in pressurized and dry regimes)**.** *As already mentioned in Remark 4.2, the chosen definition (4.14) for λ_u, i.e. $\lambda_u = \frac{1}{2}f_i\rho_2|u_1 - u_2|$, does not vanish when $h_k \to 0$. This definition is relevant at the discrete level as it keeps (4.39) non-singular in pressurized and dry regimes ($\Lambda_u^{**} > 0$). Note also that this discrete velocity relaxation brings dissipation and thus robustness in these regimes. The corresponding parametric study is presented in Section 4.4.3.*

To summarize, the proposed fractional step method is a three-step scheme ensuring the positivity of heights and densities under the CFL condition (4.24) based on the celerity of material and gravity waves. In particular, the stable resolution of acoustic waves in the second step is obtained thanks to diffusion terms arising from a relaxation approach. For the water phase, these terms are activated only in the pressurized regime following a criterion on the water height. Indeed, in the stratified regime, the corresponding convective term to stabilize is treated as a source term accounting for variable air pressure due to the fast pressure relaxation. In the presence of vanishing phases, the overall scheme does not involve any singular system to solve. Furthermore, the dissipative relaxation processes (pressure and velocity) are ensured at the discrete level. In the next section, numerical experiments are performed, beginning with Riemann problems for the convective part and moving to canonical mixed flow configurations.

Remark 4.8 (CFL number and linear stability)**.** *In the proposed scheme, the only CFL condition comes from a positivity requirement for heights and densities in the first step. However, stability issues regarding IMEX schemes have been recently pointed out in [15, 16]. Thus, a linear stability analysis is performed in Chapter 5 at the discrete level and an additional constraint on the CFL number is obtained. The latter only involves the ratio* $\frac{\sqrt{gH}}{c_1}$*. For instance, considering realistic pipe heights satisfying* $H \in [0.1;10]$*, the maximum CFL number ensuring the linear stability is an increasing function of* $\frac{\sqrt{gH}}{c_1}$ *which belongs to* $[0.086;0.67]$*. In practice, this range of CFL numbers still makes the scheme interesting, as presented in Section 4.4.*

4.4 Numerical experiments

In this section, several test cases are performed in order to evaluate the ability of the CTL model associated with the proposed scheme to handle mixed flows. From now on, the proposed scheme is referred to as the SPR scheme for *SPlitting with Relaxation*. Firstly, one considers in Section 4.4.1 a Riemann problem to make sure that the SPR scheme is stable and converges towards relevant shock solutions of the homogeneous convective problem. Secondly, the accuracy in the stratified regime is studied in Section 4.4.2 regarding a dambreak problem. Thirdly, canonical mixed flow configurations are considered. The goal is to provide a first assessment of the SPR scheme ability to handle pressurized as well as dry flows, which inherently lead to vanishing phases. More complex mixed flow test cases are extensively studied in Chapter 6.

4.4.1 Shock waves and contact discontinuity: a Riemann problem

4.4.1.a Global setting and objectives

This section focuses on the convective part of ($\mathscr{S}$). As stated in section (4.2.4), the jump conditions and all the Riemann invariants can be detailed so that one can build analytical solutions including the contact discontinuity, shock waves and rarefaction waves. Thus, one considers in the following an analytical solution which involves the five waves of the system: two shocks in each phase propagating at speed $u_k \pm c_k,\ k = 1,2$, and a contact discontinuity propagating at speed u_2 where h_1 jumps, see Figure 4.2.

As we want to approximate *fast* acoustic waves (shock waves) in both phases with the SPR scheme, the two relaxation parameters $a_k,\ k = 1,2$, follow the Whitham condition. The solutions are computed over the domain $[0,1]$ of the x-space where homogeneous Neumann conditions are imposed at both boundaries, see Appendix 4.A. The time step is denoted Δt_{m} and is computed from the CFL condition (4.24) where the so-called *material* CFL number denoted $\mathrm{CFL}_{\mathrm{m}}$ verifies:

$$\mathrm{CFL}_{\mathrm{m}} = \frac{\Delta t_{\mathrm{m}}}{\Delta x} \max_i \left(\frac{r_{\mathrm{m},i+\frac{1}{2}} + r_{\mathrm{m},i-\frac{1}{2}}}{2} \right), \tag{4.40}$$

with $\mathrm{CFL}_{\mathrm{m}} \leq 1$ and $r_{\mathrm{m},i+\frac{1}{2}} = \max_{j\in\{i;i+1\}} \left(|u^n_{2,j}|; \left| \left(u_1 \pm \sqrt{g\tfrac{h_1}{2}}\right)^n_j \right| \right)$ at the nth iteration.

A mesh refinement is also performed in order to check the numerical convergence of the method. For this purpose, the discrete L^1-error between the approximate solution and the exact one at the final time T, normalized by the discrete L^1-norm of the exact solution, is computed on regular meshes:

$$\mathrm{error}_{\mathscr{U}}(\Delta x, T) = \frac{\sum_j |\mathscr{U}^N_j - \mathscr{U}_{ex}(x_j,T)|}{\sum_j |\mathscr{U}_{ex}(x_j,T)|}, \tag{4.41}$$

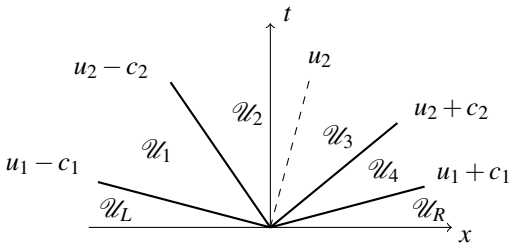

Variable	$\mathscr{U}_L$	$\mathscr{U}_1$	$\mathscr{U}_2$	$\mathscr{U}_3$	$\mathscr{U}_4$	$\mathscr{U}_R$
h_1	0.5	0.5	0.5	0.5023747	0.5023747	0.5023747
ρ_1	998.11150	998.16140	998.16140	998.16240	998.16240	998.06259
u_1	10.0	9.9254584	9.9254584	9.8225555	9.82255555	9.6734610
ρ_2	1.204	1.204	1.2642	1.2601362	1.2349335	1.2349335
u_2	5.0	5.0	-11.838960	-11.838960	-18.826134	-18.826134

Figure 4.2: Wave structure, initial conditions ($\mathscr{U}_L$, $\mathscr{U}_R$) and intermediate states $(\mathscr{U}_k)_{k=1,4}$.

where $\mathscr{U}$ denotes the state vector in non conservative variables, $\mathscr{U}^N$ the discrete approximation at final time and $\mathscr{U}_{ex}$ stands for the exact solution. In the refinement process, the coarser mesh is composed of 100 cells and the most refined one contains 200000 cells.

The results obtained with a classical explicit Rusanov scheme applied on the non-split convective part of ($\mathscr{S}$) are added for comparison. The time step of this second scheme is denoted Δt_{a} and is computed from a CFL condition similar to (4.24) which involves the spectral radius of ($\mathscr{S}$) and thus acoustic waves, see Property 4.2. In that framework, the so-called *acoustic* CFL number is denoted $\mathrm{CFL_a}$ and is defined by:

$$\mathrm{CFL_a} = \frac{\Delta t_{\mathrm{a}}}{\Delta x} \max_i \left(\frac{r_{\mathrm{a},i+\frac{1}{2}} + r_{\mathrm{a},i-\frac{1}{2}}}{2} \right), \tag{4.42}$$

with $\mathrm{CFL_a} \leq 1$ and $r_{\mathrm{a},i+\frac{1}{2}} = \max_{j\in\{i;i+1\}} \left(|u^n_{2,j}|; |\left(u_1 \pm c_1\right)^n_j|; |\left(u_2 \pm c_2\right)^n_j| \right)$ at the nth iteration.

For a certain time step computed from a given *material* CFL number $\mathrm{CFL_m}$, one can compute the corresponding *acoustic* CFL number $\mathrm{CFL_a}'$ from the relation:

$$\mathrm{CFL_a}' = \frac{\max_i \left(\frac{r_{\mathrm{a},i+\frac{1}{2}} + r_{\mathrm{a},i-\frac{1}{2}}}{2} \right)}{\max_i \left(\frac{r_{\mathrm{m},i+\frac{1}{2}} + r_{\mathrm{m},i-\frac{1}{2}}}{2} \right)} \mathrm{CFL_m}. \tag{4.43}$$

Focusing on the Riemann problem depicted in Figure 4.2, the SPR scheme is assessed in the sequel setting $\mathrm{CFL_m} = 0.5$ and $\mathrm{CFL_m} = 0.01$ which corresponds respectively to $\mathrm{CFL_a}' \sim 40$ and $\mathrm{CFL_a}' \sim 0.8$. The Rusanov scheme is used setting $\mathrm{CFL_a} = 0.5$.

Remark 4.9 (SPR scheme with small CFL numbers)**.** *When setting a small CFL number with the SPR scheme, typically $CFL_a' = CFL_a$ which yields $\Delta t_m = \Delta t_a$, one expects a better resolution of fast propagation phenomena. Furthermore, one also expects a lower numerical diffusion on slow propagation phenomena compared to the full explicit Rusanov scheme as the spectral radius of their explicit part are different. In particular, $r_{m,i+\frac{1}{2}} \ll r_{a,i+\frac{1}{2}}$ when $|u_k| \ll c_k$ and $\sqrt{g\frac{h_1}{2}} \ll c_1$.*

4.4.1.b Results and comments

The fields at $T = 23.10^{-5}\,s$ with 1000 cells and the errors are displayed respectively on Figures 4.3 and 4.4. Efficiency results are displayed on Figure 4.5. Despite the great complexity of this test case, one observes that the intermediate states are correctly captured by the two schemes. The latter are stable and converge towards the relevant shock solutions. Note that this property is obtained despite the presence of non-conservative products in ($\mathscr{S}$), ($\mathscr{S}_m$) and ($\mathscr{S}_a$). Indeed, as seen in Property 4.3, these non-conservative products are actually well-defined for shock waves as they involve $\partial_x h_k$ where h_k does not jump across the shocks. The contact discontinuity is also well captured and an expected convergence rate of $\frac{1}{2}$ is obtained, see Figure 4.4.

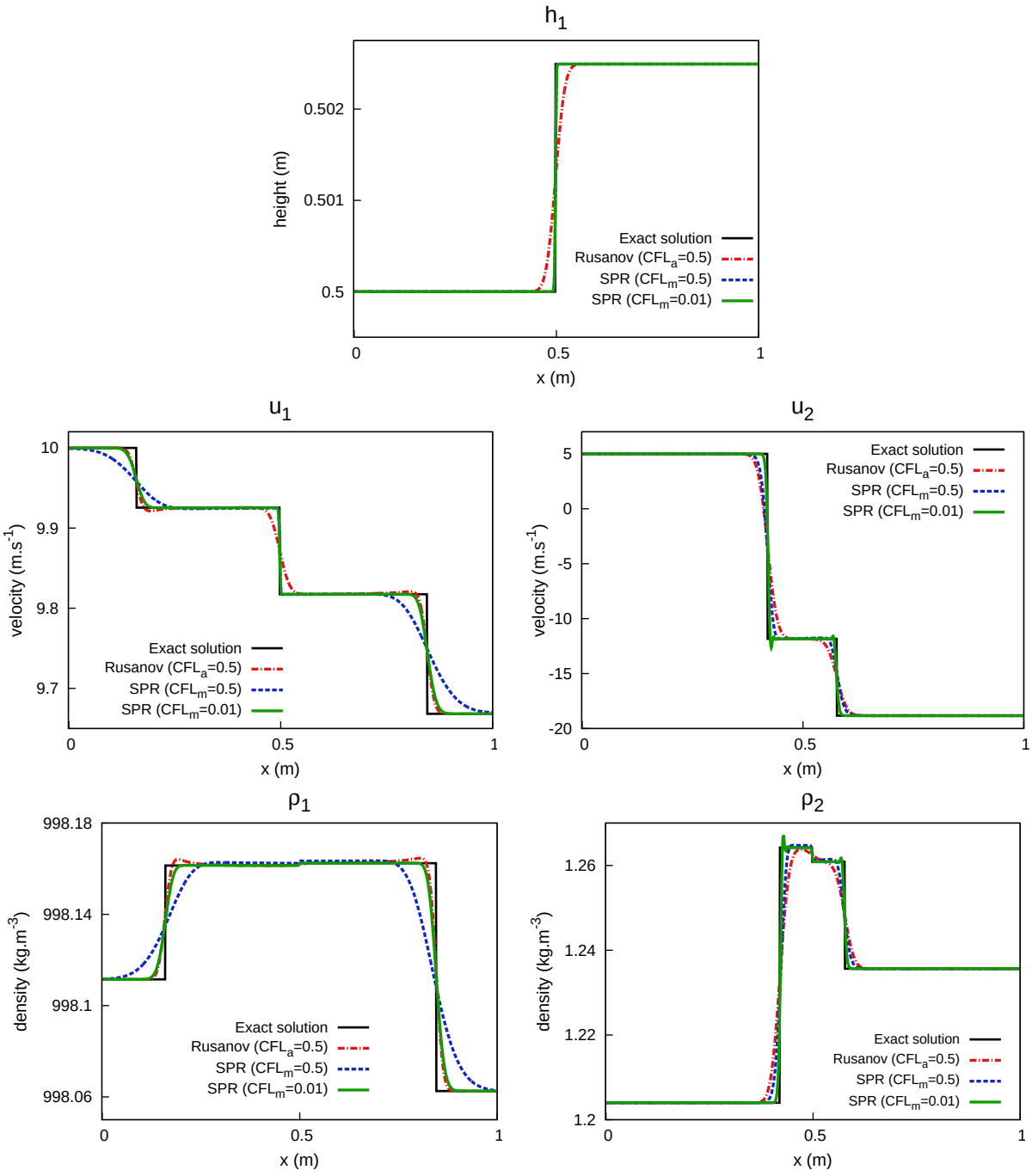

Figure 4.3: Approximate solutions for the Riemann problem at $T = 23.10^{-5}$ s. with 1000 cells.

Focusing on the fastest shock waves, i.e. the shock waves of phase 1, the Rusanov scheme is the best suited to approximate them as its CFL condition (4.42) is based on the celerity of these fastest shocks waves ($u_1 \pm c_1$). As expected, the SPR scheme with $\mathrm{CFL_m} = 0.5$ is the most diffusive as its CFL condition (4.40) is based on the celerity of slow waves. However, setting $\mathrm{CFL_m} = 0.01$ improves notably the results which compare well with the Rusanov scheme. These comments are comforted on Figures 4.4 and 4.5 where the SPR scheme with $\mathrm{CFL_m} = 0.01$ is equivalent to the Rusanov scheme in terms of errors and efficiency for the variables (ρ_1, u_1).

Focusing on the slowest shock waves, i.e. the shock waves of phase 2, the best results are obtained with the SPR scheme setting $\mathrm{CFL_m} = 0.01$. Small overshoots are observed on Figure 4.3 but they are bounded in L^1-norm and do not preclude the convergence. The Rusanov scheme is the most diffusive and less efficient than the SPR scheme at $\mathrm{CFL_m} = 0.5$, see Figure 4.5. Regarding error and efficiency curves, the SPR scheme with $\mathrm{CFL_m} = 0.01$ is the best choice for the variables (ρ_2, u_2).

Focusing on the slow contact discontinuity where h_1 jumps, the best results are obtained with the SPR scheme at $\mathrm{CFL_m} = 0.5$. Indeed, the latter follows the best suited CFL condition for slow propagation phenomena. As expected, the full explicit Rusanov scheme is not adapted for capturing slow waves and provides the most diffusive results with the lowest efficiency, see Figure 4.5. The SPR scheme with $\mathrm{CFL_m} = 0.01$ and $\mathrm{CFL_m} = 0.5$ compares well in terms of errors, see Figure 4.4, but the second setting is more efficient as larger time steps are used.

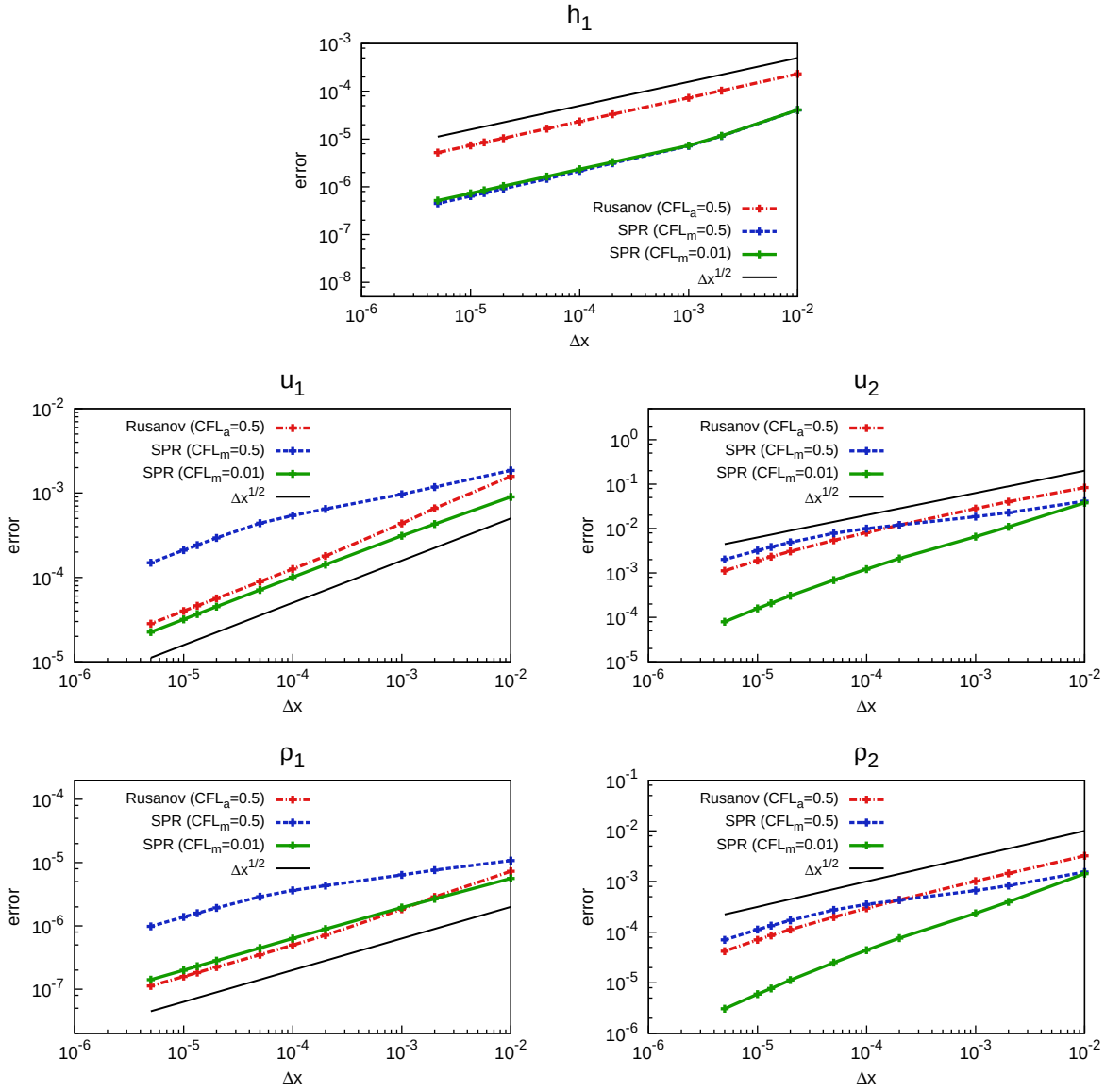

Figure 4.4: Errors in L^1-norm for the Riemann problem.

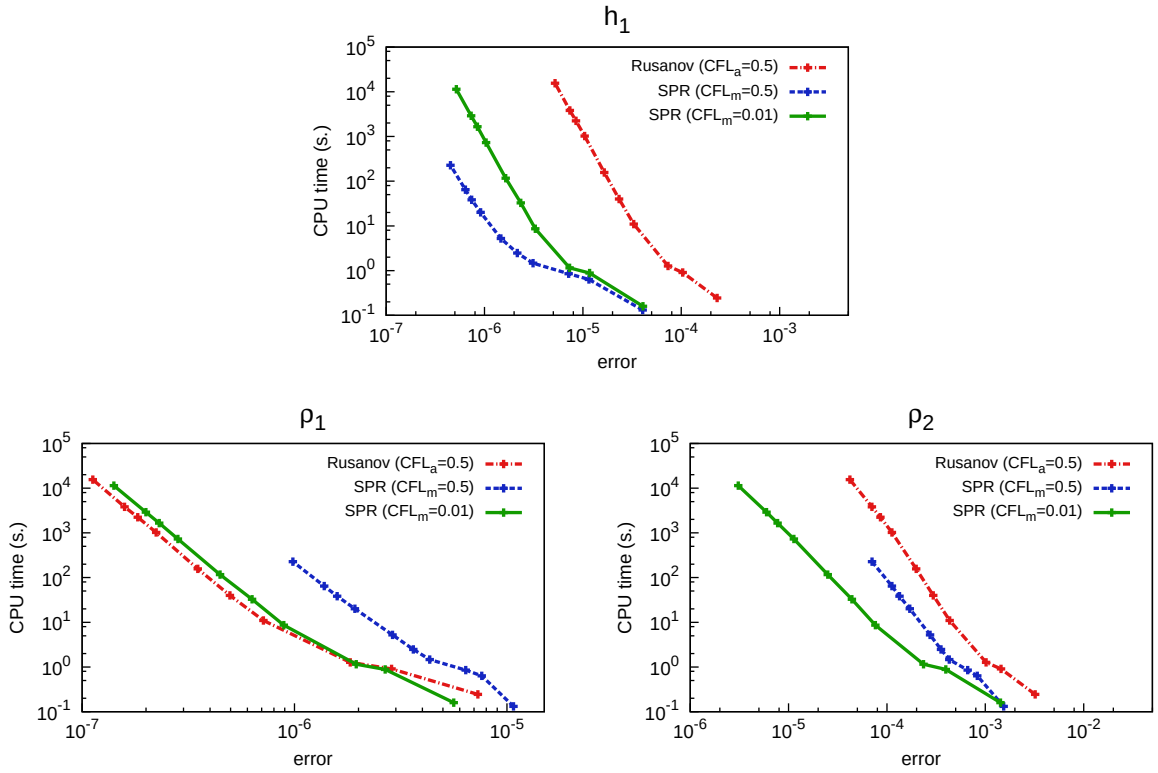

Figure 4.5: Errors in L^1-norm against CPU time for the Riemann problem.

In summary, the SPR scheme is a convergent and stable scheme for the convective part of ($\mathscr{S}$). It yields better accuracy and efficiency compared to a classical explicit Rusanov scheme, in particular when setting $\mathrm{CFL_m} = 0.01$. In the next section, these conclusions are confronted to a dambreak test case which involves the full system with pressure and velocity relaxation source terms.

Remark 4.10 (Comparison with the results of Chapter 3)**.** *Regarding Riemann problems for the convective part of* ($\mathscr{S}$)*, one obtains the same trends as above with the implicit-explicit scheme developed in Chapter 3.*

4.4.2 Stratified regime: a dambreak problem

A common way to deal with free-surface flows is to use the well-known Saint-Venant or shallow water equations, see [29]. In a few words, this model is a one-layer model resulting from a depth averaging of the Euler set of equations and assuming a thin layer of incompressible fluid with hydrostatic pressure law. Particularly, it admits an analytical solution for the so-called dambreak problem. As detailed below, this configuration is relevant regarding stratified regimes. Thus, it is proposed to consider the dambreak test case for the CTL model and to compare the results with the reference solution provided by the shallow water equations. Indeed, one can expect to obtain the same kind of solution for the water layer as the derivation processes are very close and the compressibility of water as well as the additional air layer are expected to have a minor influence here.

4.4.2.a Global setting and objectives

The initial condition for the dambreak problem is a discontinuity on h_1 with uniform density and zero speed, see Figure 4.6. In order to get meaningful results in a short simulation time, hereafter $T = 24.10^{-2}\,s$, a pipe of height $H = 10\,m$ and length $L = 1\,m$ is considered (the same trends are obtained with smaller pipes). This configuration provides a low speed flow representative of practical configurations with $\frac{|u_1|}{c_1} \sim 10^{-3}$ and $\frac{\sqrt{gH}}{c_1} \sim 7.10^{-3}$. The solutions are computed over the domain $[0,1]$ of the x-space where wall boundary conditions are imposed at the inlet and outlet, see Appendix 4.A.

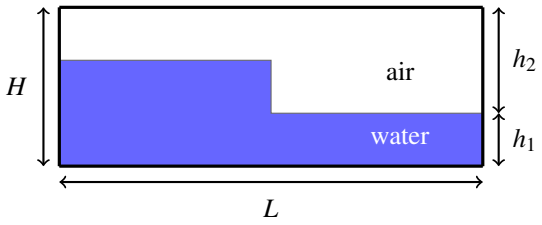

Variable	$0 \leq x \leq L/2$	$L/2 < x \leq L$
h_1/H	0.6	0.4
ρ_1	$998.1115 kg.m^{-3}$	$998.1115 kg.m^{-3}$
u_1	$0 m.s^{-1}$	$0 m.s^{-1}$
ρ_2	$1.204 kg.m^{-3}$	$1.204 kg.m^{-3}$
u_2	$0 m.s^{-1}$	$0 m.s^{-1}$

Figure 4.6: Initial conditions for the dambreak problem.

Contrary to the previous test case, the full system with pressure and velocity relaxation source terms is now involved. Regarding the SPR scheme, the relaxation parameters are set according to the definition (4.3.1) for the stratified regimes ($h_1 < H$): $a_1 = 0$ whereas a_2 follows the Whitham condition. The time step is computed using (4.40) for a given *material* CFL number denoted CFL_m.

As previously, a mesh refinement is also performed in order to check the stability and numerical convergence of the method when considering the full system. For this purpose, the obtained solution is compared with the analytical solution of the shallow water equations denoted SW_{ref} hereafter. The latter provides the evolution in time and space for h_1 and u_1 which contains a rarefaction wave propagating to the left and a shock wave propagating to the right. Thus, we compute the deviation in L^1-norm from this reference solution on regular meshes:

$$\Delta S(\Delta x, T) = \frac{\sum_j |\mathscr{U}_j^N - SW_{ref}(x_j, T)|}{\sum_j |SW_{ref}(x_j, T)|}, \tag{4.44}$$

where $\mathscr{U} = (h_1, u_1)$ and $\mathscr{U}^N$ denotes the discrete approximation at final time. We emphasize that (4.44) is not an error estimate as the analytical solution of the shallow water equations for the dambreak problem is not an analytical solution for the CTL model. In the refinement process, the coarser mesh is composed of 100 cells while the most refined one contains 200000 cells.

The results obtained with a classical explicit Rusanov scheme are added for comparison. The latter is applied on the non-split convective part of ($\mathscr{S}$) while the source terms are treated in a second homogeneous step as in [33]. Its time step is computed with an *acoustic* CFL number defined in (4.42) and set to $\text{CFL}_\text{a} = 0.5$. Concerning the SPR scheme, it is assessed setting $\text{CFL}_\text{m} = 0.5$ and $\text{CFL}_\text{m} = 0.01$ which corresponds respectively to $\text{CFL}_\text{a}^{'} \sim 100$ and $\text{CFL}_\text{a}^{'} \sim 2$ for the considered dambreak problem.

4.4.2.b Results and comments

The fields at $T = 24.10^{-2} s$ with 1000 cells and the deviations ΔS are displayed respectively on Figures 4.7 and 4.8. Deviations against CPU times are displayed on Figure 4.9.

As observed on Figure 4.7, the reference solution is accurately captured by the SPR scheme. It confirms that the compressibility of water as well as the additional air layer have minor influence here. The expected behavior is however obviously not captured by the Rusanov scheme which provides very diffusive results.

The deviation estimates on Figure 4.8 show that the SPR scheme is stable in the stratified regime ($a_1 = 0$) and converges. Indeed, a plateau is obtained for the finest meshes ($\Delta x < 2.10^{-5} m$), which highlights the fact that the reference solution is not an analytical solution for the CTL model. Regarding the CPU times on Figure 4.9, one observes that the practical simulation of a dambreak with the Rusanov scheme is out of reach. Indeed, even for the worst deviation obtained with the SPR scheme, the Rusanov scheme needs a CPU time 10^6 times larger. Small deviations with low CPU times are obtained using the SPR scheme, see the table Figure 4.7. The two CFL number values yield close results but, in terms of efficiency, the best choice seems to be $\text{CFL}_\text{m} = 0.5$. However, this last comment may be biased as we do not compare with an exact solution of the target set of PDEs.

This test case illustrates the difficulties to simulate low speed stratified regimes, in the sense $\sqrt{gH} \ll c_1$, with the CTL model using a classical explicit scheme. The proposed SPR scheme is not only stable and convergent but also provides interesting results as it accurately captures the expected behavior with low CPU time. The next step is to handle mixed flow configurations which involve transitions between stratified and pressurized or dry regimes.

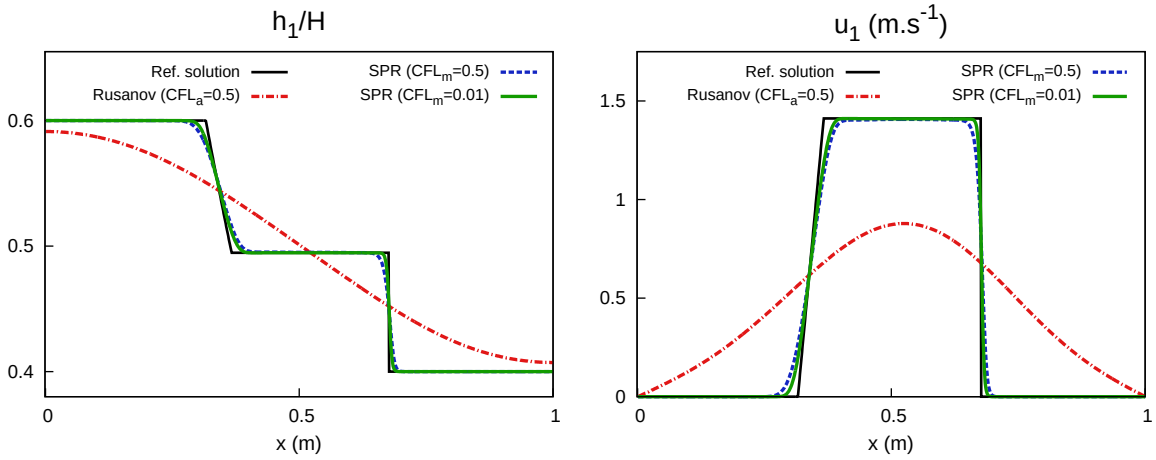

Scheme	Rusanov with $CFL_a = 0.5$	SPR with $CFL_m = 0.01$	SPR with $CFL_m = 0.5$
CPU time	$150\,s$	$30\,s$	$1\,s$

Figure 4.7: Approximate solutions and CPU times for the dambreak problem at $T = 24.10^{-2}\,s$ with 1000 cells.

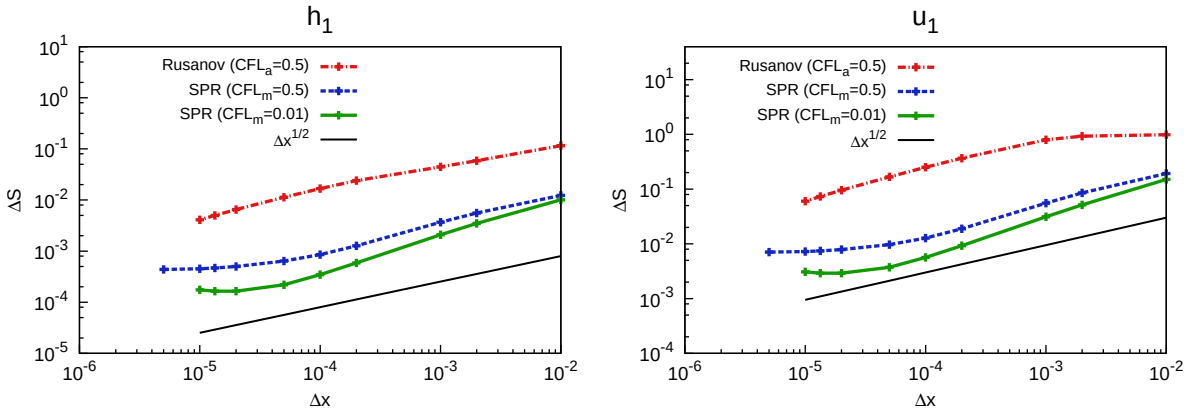

Figure 4.8: Deviation in L^1-norm from the shallow water solution for the dambreak problem.

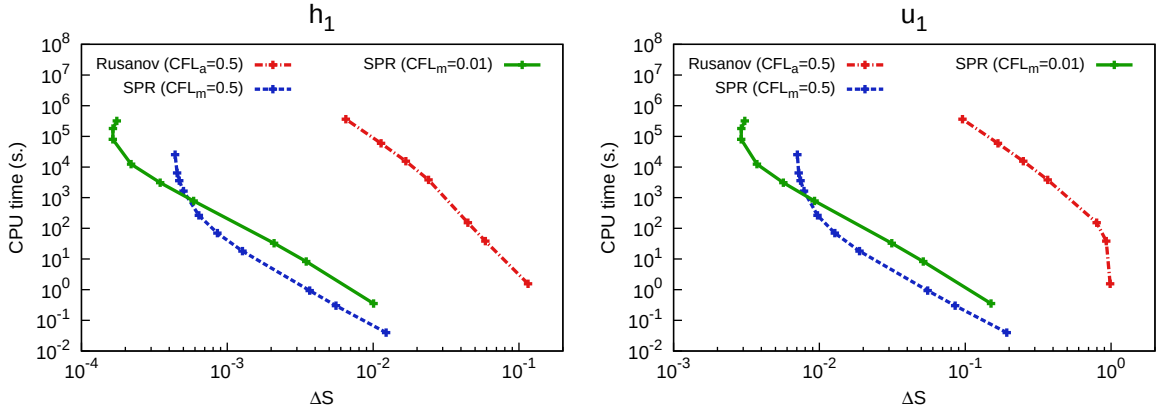

Figure 4.9: Deviation in L^1-norm against CPU time for the dambreak problem.

Remark 4.11 (Whitham condition on the water phase in the stratified regime)**.** *When the Whitham condition is applied on the water phase in the stratified regime, see Figure 4.10, one observes that the scheme is unable to capture the expected behavior. Indeed, the additional numerical diffusion based on the celerity of fast acoustic waves is not adapted to the propagation of slow gravity waves. This assesses the strategy proposed in Definition 4.3.1 for the relaxation parameter a_1. Note that the scheme developed in Chapter 3 yields similar results for the dambreak problem, meaning that it is not suited for the propagation of slow gravity waves.*

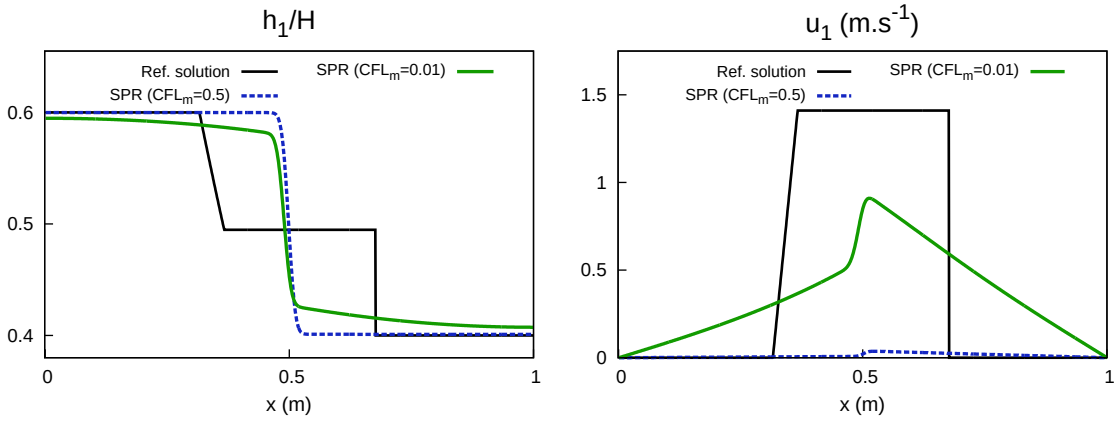

Figure 4.10: Approximate solutions for the dambreak problem at $T = 24.10^{-2}\,s$ with 1000 cells applying the Whitham condition on water phase.

4.4.3 Preliminary results on canonical mixed flow configurations

Before several mixed flow validation test cases in Chapter 6, canonical test cases are considered herein. The goal is to provide a first assessment of the SPR scheme ability to handle pressurized as well as dry flows, which inherently lead to vanishing phases. In this framework, the influence of the threshold value h_s, defined in Section 4.3.4.c to ensure the stability of the scheme in pressurized regimes ($h_1 \to H$), is studied. In addition, the importance of relaxation source terms on the scheme stability in the presence of vanishing phases is emphasized. To this aim, three test cases are presented: a pressurized dambreak which involves a transition from the pressurized to the stratified regime, a pipe filling which involves a transition from the stratified to the pressurized regime and a pipe drying which involves a transition from the stratified to the dry regime.

4.4.3.a Pressurized dambreak

A transition from the pressurized to the stratified regime is considered in the sequel. It consists in a dambreak problem, as in Section 4.4.2, where the left part of the initial condition is in charge, see Figure 4.11. A realistic rectangular pipe is chosen whose height is set to $H = 0.2\,m$ and length is set to $L = 10\,m$. The solution is computed on a regular mesh composed of 1000 cells ($\Delta x = 10^{-2}\,m$) where a wall boundary condition is applied to the left end and an homogeneous Neumann boundary condition is applied to the right end, see Appendix 4.A. The simulation time is set to $T = 2.2\,s$ and the (material) CFL number is set to 0.01.

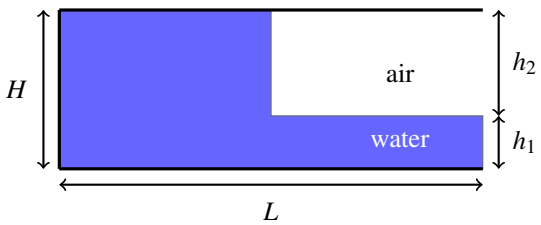

Variable	$0 \le x \le L/2$	$L/2 < x \le L$
h_1/H	$1 - 10^{-5}$	10^{-1}
ρ_1	$998.1115\,kg.m^{-3}$	$998.1115\,kg.m^{-3}$
u_1	$0\,m.s^{-1}$	$0\,m.s^{-1}$
ρ_2	$1.204\,kg.m^{-3}$	$1.204\,kg.m^{-3}$
u_2	$0\,m.s^{-1}$	$0\,m.s^{-1}$

Figure 4.11: Initial conditions for the pressurized dambreak problem.

The first objective of this test case is to evaluate the influence of the threshold value h_s which triggers the *acoustic* stabilization terms in the pressurized regime, see Section 4.3.4.c and definition (4.36). Several threshold values are compared:

$$h_s = (1-\delta)H,\ \delta \in \{10^{-2}, 10^{-3}, 10^{-4}\}. \tag{4.45}$$

The initial water height in charge is subsequently set to $h_1 = (1-10^{-5})H$, such that $h_1 > h_s$. The impact of the velocity relaxation source term, defined in (4.14) as:

$$\lambda_u = \frac{1}{2} f_i \rho_2 |u_1 - u_2|, \tag{4.46}$$

with f_i a constant friction factor, is also assessed. The latter does not vanish in pressurized and dry regimes where one would expect $\lambda_u \to 0$ to be fully consistent with the compressible Euler model, see (4.17). Thus, simulation results with a vanishing velocity relaxation parameter, defined as:

$$\lambda_u^{'} = \frac{h_1 h_2}{H^2} \lambda_u, \tag{4.47}$$

are also presented. The numerical solutions of this pressurized dambreak problem using the CTL model are referred hereafter as the *pressurized* solutions whereas a *free surface* solution, obtained by setting $H^{'} = 2H$ (no pressurized part in the initial condition) is provided for comparison. Indeed, it is assumed that the solution should behave as if there were no roof, so that the water phase fields are also compared with a reference solution given by an analytical solution of the shallow water system (without roof). The results of this parametric study are displayed on Figure 4.12.

As already discussed in Section 4.4.2, the *free surface* solution is close to the reference solution whereas the *pressurized* solutions display a noticeable disparity depending on the threshold value and on the definition of the velocity relaxation parameter. Indeed, focusing on the height and velocity fields, all the *pressurized* solutions display a delay at the transition between the pressurized and stratified part in comparison with the *free surface* solution. It highlights the fact that both stability terms and velocity relaxation source terms bring dissipation through friction effects along the walls where one phase is vanishing. As expected, the highest delay is obtained with the lowest threshold value, corresponding to $\delta = 10^{-2}$, combined with a non-vanishing velocity relaxation parameter. The vanishing relaxation parameter $\lambda_u^{'}$ allows to reduce this delay when setting the highest thresholds values, corresponding to $\delta = 10^{-3}$ and $\delta = 10^{-4}$. However, focusing on the pressure field, non-expected oscillations are observed at the transition point when setting the highest threshold value ($\delta = 10^{-4}$), with both vanishing and non-vanishing velocity relaxation parameter. Numerical results on finer meshes are not presented herein as they display similar trends.

This test case illustrates the necessity to set sufficiently low threshold values, typically $\delta \geq 10^{-3}$, to guarantee the stability of the scheme at transition points between pressurized and stratified parts. Nonetheless, low threshold values combined with a non-vanishing velocity relaxation parameter, typically with $\delta = 10^{-2}$, seem to bring too much dissipation. Finally, the best compromise for the considered test case is given by $\delta = 10^{-3}$ using the vanishing velocity relaxation parameter $\lambda_u^{'}$. This conclusion is confronted to another test case in the next section which involves a transition from the stratified to the pressurized regime.

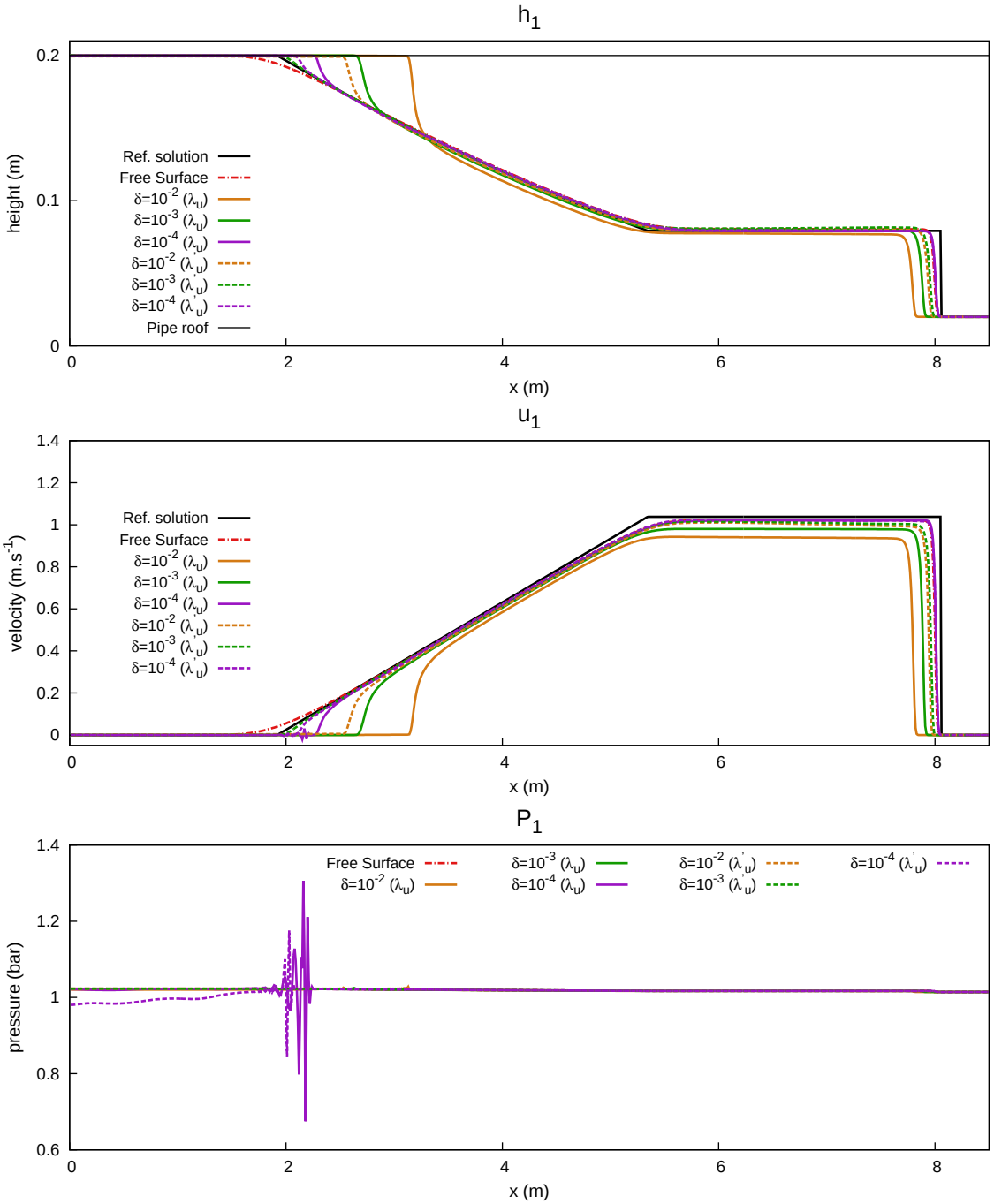

Figure 4.12: Influence of the threshold value and the velocity relaxation parameter for the pressurized dambreak problem (1000 cells, $t = 2.2\,s$).

4.4.3.b Pipe filling

A transition from the stratified to the pressurized regime ($h_2 \to 0$) is investigated in the sequel through a so-called pipe filling. This configuration is deeply studied in Chapter 6 while the present section focuses on the influence of the threshold value h_s and the definition of the velocity relaxation parameter. A rectangular sloping pipe is thus considered where the initial condition is a static condition with uniform water height, uniform density and zero speed, see Figure 4.13. In that framework, the CTL model is defined in the inclined frame. The pipe height is set to $H = 0.2\,m$, its length is set to $L = 2\,m$ and its angle from the horizontal is $\theta = -30^o$. The solution is computed on a regular mesh composed of 1000 cells ($\Delta x = 2.10^{-3}\,m$) where wall boundary conditions are applied to both ends of the pipe, see Appendix 4.A. The simulation time is set to $T = 0.3\,s$ and the (material) CFL number is set to 0.01.

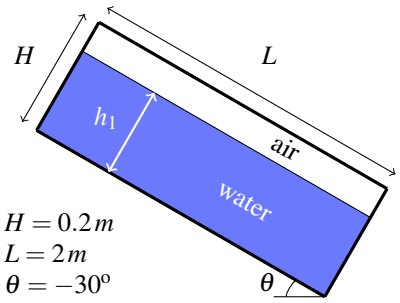

Variable	$0 \leq x \leq 2\,m$
h_1/H	0.8
ρ_1	$998.1115\,kg.m^{-3}$
u_1	$0\,m.s^{-1}$
ρ_2	$1.204\,kg.m^{-3}$
u_2	$0\,m.s^{-1}$

Figure 4.13: Initial conditions for the pipe filling test case.

As in the previous section, several threshold values are compared, see (4.45), with vanishing and non-vanishing velocity relaxation parameter, recalled in (4.46) and (4.47) respectively. Regarding the vanishing relaxation parameter $\lambda_u^{'}$, only the results with $\delta = 10^{-3}$ are presented as the other values display the same trends. Results are plotted on Figure 4.14.

In this proposed framework, a mixed flow is obtained with a stratified and a pressurized part separated by a jump. All the settings yield a similar solution in the stratified part while a large disparity may be observed in the pressurized part. Regarding the water phase, even if height and velocity fields are comparable, pressure oscillations depending on the setting are observed in the pressurized region. The latter are commonly encountered when dealing with mixed flows, they are studied more precisely in Chapter 6 and it is shown that they vanish when the mesh is refined. Thus, the discussion focuses here on the air phase fields in the pressurized part. Indeed, when using a vanishing velocity relaxation parameter, spurious velocity and pressure oscillations are obtained for the computed thin air layer. In particular, the air height h_2 tends to zero and reaches the machine precision so that the air phase solution degenerates. Note that the sole meaningful air phase fields in the pressurized part are given by h_2u_2 and h_2P_2 which effectively vanish, but it is also important to monitor (u_2, P_2) as they are involved as such in the scheme, particularly in the source terms and the time step computation, see (4.24). As observed, this prejudicial behavior is not obtained when using a non vanishing velocity relaxation parameter which brings more robustness, thus ensuring $u_2 \sim u_1$ when $h_2 \to 0$. The pressure relaxation source term also contributes to this robustness ensuring $P_2 \sim P_I$, see Remark 4.4. Numerical results on finer meshes are not presented herein as they display similar trends.

This test case illustrates the necessity to use a non vanishing velocity relaxation parameter when considering transitions from the stratified to the pressurized regime. Indeed, it clearly brings more robustness without impacting negatively the solution. The threshold value seems to have little influence regarding such transitions. In the next section, transitions from stratified to dry regimes are investigated.

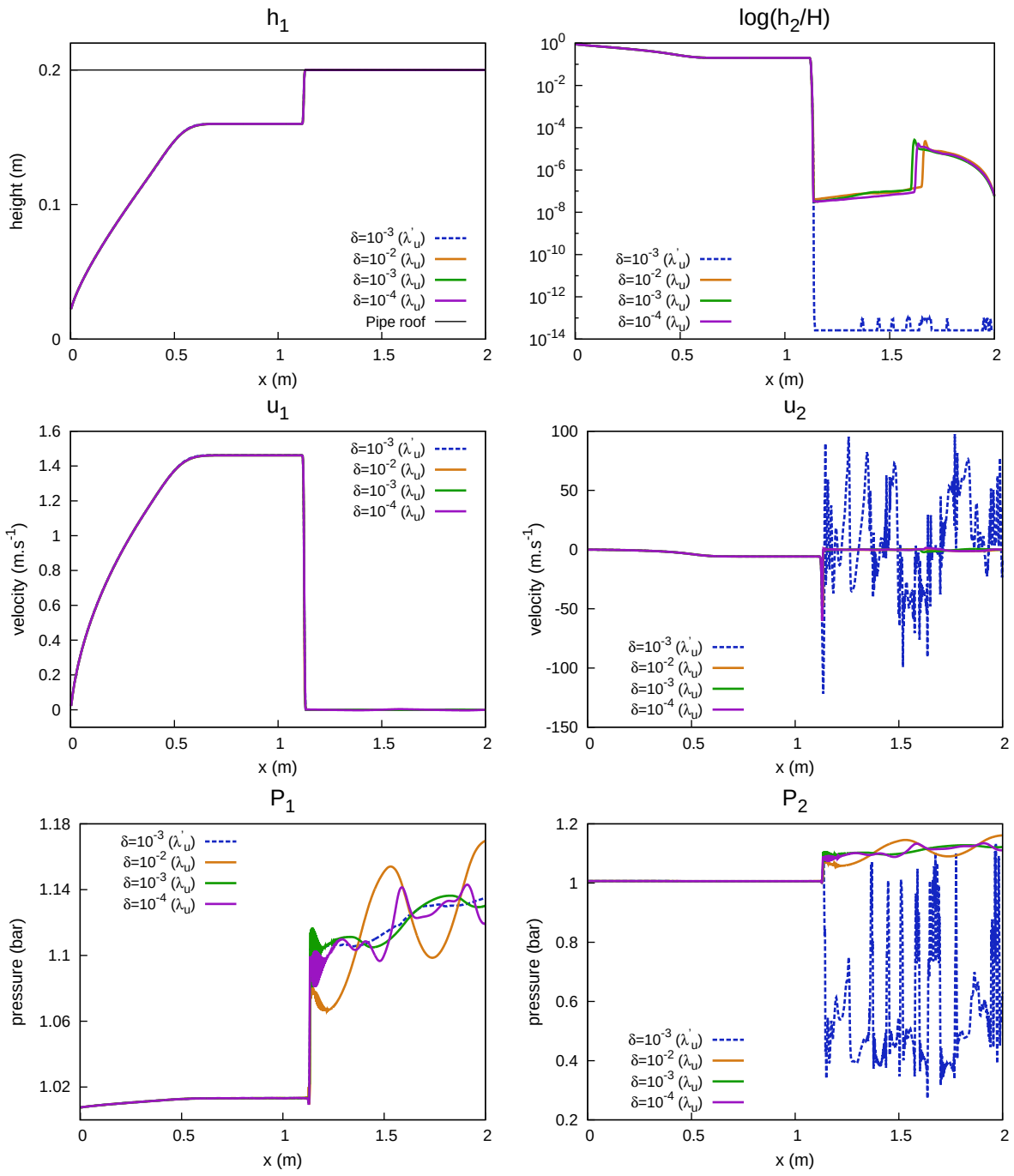

Figure 4.14: Influence of the threshold value and the velocity relaxation parameter for the pipe filling test case (1000 cells, $t = 0.3\,s$).

4.4.3.c Pipe drying

A transition from the stratified to the dry regime ($h_1 \to 0$) is investigated in the sequel through a pipe drying. In particular, the impact of the velocity relaxation in the dry regime is studied. A rectangular sloping pipe is thus considered where the initial condition is a static condition with uniform water height, uniform density and zero speed, see Figure 4.13. The pipe height is set to $H = 0.2\,m$, its length is set to $L = 2\,m$ and its angle from the horizontal is $\theta = -60^o$. The solution is computed on a regular mesh composed of 1000 cells ($\Delta x = 2.10^{-3}\,m$) where wall boundary conditions are applied to both ends of the pipe, see Appendix 4.A. The simulation time is set to $T = 0.8\,s$ and the (material) CFL number is set to 0.01.

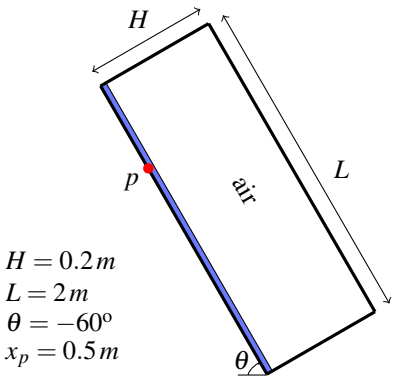

Variable	$0 \leq x \leq 2m$
h_1/H	10^{-4}
ρ_1	$998.1115 kg.m^{-3}$
u_1	$0 m.s^{-1}$
ρ_2	$1.204 kg.m^{-3}$
u_2	$0 m.s^{-1}$

Figure 4.15: Initial conditions for the pipe drying test case.

The time series of water phase fields at $x = 0.5m$ are presented on Figure 4.16 setting both vanishing and non vanishing velocity relaxation parameter. The water height is decreasing in both cases. As already observed with the pipe filling test case, the non vanishing velocity relaxation parameter λ_u provides more robustness ensuring $u_1 \sim u_2$ when $h_1 \to 0$. Combined with the pressure relaxation source terms which ensures $P_I \sim P_2$, physical results are obtained for the water phase in the dry part. When using the vanishing parameter $\lambda_u^{'}$, h_1 approaches the machine precision and non physical velocity and pressure fields are computed. Note that the sole meaningful water phase fields in the dry part are given by $h_1 u_1$ and $h_1 P_1$ which effectively vanish, but as for the air phase in the pressurized regime, it is also important to monitor (u_1, P_1) as they are involved as such in the scheme, particularly in the source terms and the time step computation, see (4.24). Numerical results on finer meshes are not presented herein as they display similar trends.

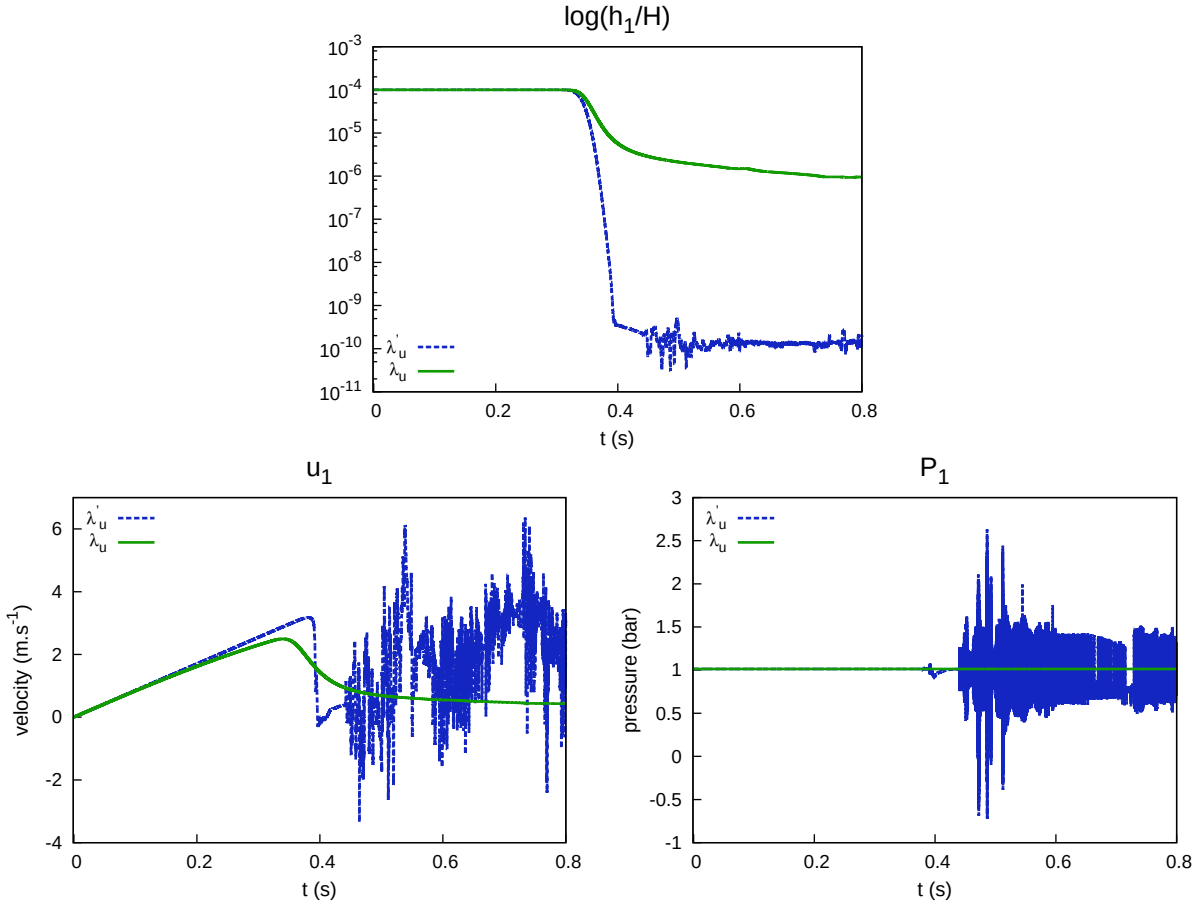

Figure 4.16: Influence of the velocity relaxation parameter for the pipe drying test case (1000 cells).

This test case illustrates the necessity to use a non vanishing velocity relaxation parameter when considering transitions from the stratified to the dry regime. Indeed, it clearly brings more robustness and allows to satisfactorily deal with dry regimes. Under the light of the above results, guidelines are provided in the next section in order to efficiently compute mixed flow configurations using the CTL model and the SPR scheme.

4.4.3.d Guidelines

When dealing with mixed flows using the CTL model, both **water and air phases are always calculated**, even in pressurized and dry regimes where $h_k \to 0$, $k = 1$ or 2. This configuration is known to raise robustness issues with most of classical schemes. As exposed above on a set of canonical test cases, one may correctly handle such regimes using the SPR scheme. Firstly, the importance of pressure and velocity relaxation source terms is highlighted. The latter bring more robustness providing dissipative effects, in particular in pressurized and dry regimes. In that sense, the two-layer framework is advantageous as the vanishing phase field is stabilized following the non-vanishing one. Secondly, the numerical treatment of pressurized regimes through dedicated stability terms for the water phase dynamics, see Section 4.3.4, is also an essential feature. The latter are triggered following a threshold value which should be low enough to effectively provide stability and high enough not to bring too much dissipation. Finally, the selected setting corresponds to a non vanishing velocity relaxation parameter, i.e. λ_u recalled in (4.46), and a threshold value set to $h_s = (1-\delta)H$ with $\delta = 10^{-3}$.

4.5 Conclusion

The numerical resolution of the Compressible Two-Layer model is addressed in this chapter with the aim of simulating mixed flows and entrapped air pockets in pipes. To this end, a fractional step method combined with an implicit-explicit time discretization is proposed. The latter relies on the fast pressure relaxation in addition to a mimetic approach with the shallow water equations for the slow dynamics of the water phase. It results in a three-step scheme, namely the SPR scheme, where the slow dynamics of the system is treated explicitly whereas the fast dynamics is treated implicitly. In particular, the slow dynamics includes the water hydrostatic gradient which corresponds to a driving term in the stratified regime. A classical explicit Rusanov scheme is used in this first step. The fast dynamics includes the pressure gradients in a second sub-system for which an original implicit relaxation approach is proposed. It ensures the stable resolution of acoustic waves through additional diffusion terms. For the water phase, these terms are only activated in the pressurized regime according to a criterion on the water height. The third sub-system deals with the velocity relaxation using a classical implicit approach. For the three steps, a particular attention is paid to the robustness in the presence of vanishing phases which occur in pressurized and dry flows. Finally, the overall scheme ensures the positivity of heights and densities under a CFL condition based on the celerity of material and gravity waves.

The stability and the convergence of the method towards relevant shock solutions is verified on a Riemann problem for the convective part of the model. The proposed scheme yields better accuracy and efficiency than a classical explicit Rusanov scheme, especially for the slow material wave of the system. Including the relaxation source terms, a dambreak problem relevant for the stratified regime is considered. The SPR scheme accurately captures the expected behavior with low CPU time whereas the Rusanov scheme is unable to approximate satisfactorily slow gravity waves. The ability of the scheme to handle canonical mixed flow configurations is then demonstrated. In particular, the importance of relaxation processes (pressure and velocity) regarding the robustness with vanishing phases is underlined and the criterion to active stabilization terms in the water phase is adjusted.

The numerical scheme developed in this chapter highlights the potential of the CTL model regarding the two-phase simulation of mixed flows and entrapped air pockets in pipes. In a larger extent, the general approach may be adapted for the simulation of low-speed flows with other isentropic two-fluid two-pressure models, for instance the isentropic version of the Baer and Nunziato model [6], accounting for the strong interactions between the relaxation source terms and the convective part. Note that the development of Dirichlet boundary conditions has not been considered in this work. It is still an open problem for two-phase two-pressure models in the general case due to the complexity of the waves structure. A possible approach may be to solve simplified partial Riemann problems on boundary cells assuming locally $\partial_x h_k = 0$. Doing so, the system reduces to two decoupled Euler system where *classical* methods could be applied. Simple boundary conditions are nonetheless described in the present work including homogeneous Neumann, wall and periodic boundary conditions.

In order to validate this overall approach, several mixed flow configurations are considered in Chapter 6. Prior to that, a linear stability of the SPR scheme is presented in Chapter 5.

4.A Boundary conditions for the SPR scheme

The CTL model is doted with a complex wave structure with source terms, see Proposition 4.2, which makes arduous the development of Dirichlet boundary conditions. Furthermore, the SPR scheme is based on a fractional step method combined with an implicit-explicit time discretization which is not a classical framework regarding such a goal. Thus, only elementary boundary conditions using a *ghost cell* approach are, for now, implemented, see [50] for instance.

4.A.1 Homogeneous Neumann boundary condition

The Homogeneous Neumann boundary condition consists in enforcing $\frac{\partial \mathbf{W}}{\partial \mathbf{n}} = 0$ at the boundaries where $\mathbf{n}$ is a normal vector to the boundary cells. At the discrete level, it resumes to impose $\mathbf{W}_{i+1} = \mathbf{W}_i,\ i \in \{0, N\}$, where N is the number of cells. Regarding the SPR scheme, this condition is easily applied in each step at the discrete level. In particular, the implicit system solved in step 2, see Section 4.3.4, preserves its M-matrix tridiagonal structure. Note that this kind of treatment is not really well suited for imposing non reflective boundary conditions, as some waves may be reflected in the computational domain.

4.A.2 Wall boundary condition

Wall boundary conditions are imposed using the classical mirror state approach. In practice, it consists in imposing $h_{k,i+1} = h_{k,i},\ \rho_{k,i+1} = \rho_{k,i},\ u_{k,i+1} = -u_{k,i},\ k = 1,2,\ i \in \{0, N\}$, where N is the number cells, see [50]. Regarding the SPR scheme, this condition is easily applied in each step at the discrete level. In particular, the implicit system solved in step 2, see Section 4.3.4, preserves its M-matrix tridiagonal structure.

4.A.3 Periodic boundary condition

The periodic boundary conditions consists in imposing $\mathbf{W}_0 = \mathbf{W}_N$ and $\mathbf{W}_{N+1} = \mathbf{W}_1$ at the discrete level, where N is the number of cells. Regarding the SPR scheme, this condition is easily applied in each step. In particular, the implicit system solved in step 2, see Section 4.3.4, preserves its M-matrix structure while the tridiagonal structure is lost.

References

[1] V.I. Agoshkov, D. Ambrosi, V. Pennati, A. Quarteroni, and F. Saleri. Mathematical and numerical modelling of shallow water flow. *Computational Mechanics*, 11(5):280–299, 1993.

[2] A. Ambroso, C. Chalons, F. Coquel, and T. Galié. Relaxation and numerical approximation of a two-fluid two-pressure diphasic model. *ESAIM: Mathematical Modelling and Numerical Analysis*, 43(6):1063–1097, 2009.

[3] A. Ambroso, C. Chalons, and P.-A. Raviart. A Godunov-type method for the seven-equation model of compressible two-phase flow. *Computers & Fluids*, 54:67–91, 2012.

[4] K. Arai and K. Yamamoto. Transient analysis of mixed free- surface-pressurized flows with modified slot model (part 1: Computational model and experiment). *Proc. FEDSM03 4th ASME-JSME Joint Fluids Engineering Conf.*, pages 2907–2913, 2003.

[5] F. Aureli, A. Dazzi, A. Maranzoni, and P. Mignosa. Validation of single- and two-equation models for transient mixed flows: a laboratory test case. *Journal of Hydraulic Research*, 53(4):440–451, 2015.

[6] M. R. Baer and J. W. Nunziato. A two phase mixture theory for the deflagration to detonation (DDT) transition in reactive granular materials. *International Journal of Multiphase Flow*, 12(6):861–889, 1986.

[7] A.J.C. Barré de Saint Venant. Théorie du mouvement non-permanent des eaux avec application aux crues des rivières et à l'introduction des marées dans leur lit. *C.R. Acad. Sc. Paris.*, 73:147–154, 1871.

[8] C. Berthon, B. Braconnier, and B. Nkonga. Numerical approximation of a degenerate non-conservative multifluid model: relaxation scheme. *International Journal for Numerical Methods in Fluids*, 48:85–90, 2005.

[9] F. Bouchut. *Nonlinear stability of finite volume methods for hyperbolic conservation laws, and well-balanced schemes for sources*. Birkhauser, 2004.

[10] C. Bourdarias, M. Ersoy, and S. Gerbi. Unsteady flows in non uniform closed water pipes: a full kinetic approach. *Numerische Mathematik*, 128(2):217–263, 2014.

[11] C. Bourdarias and S. Gerbi. A finite volume scheme for a model coupling free surface and pressurised flows in pipes. *Journal of Computational and Applied Mathematics*, 209:1–47, 2007.

[12] S. Bousso, M. Daynou, and M. Fuamba. Numerical modeling of mixed flows in storm water systems: Critical review of literature. *Journal of Hydraulic Engineering*, 139(4):385–396, 2013.

[13] R.P. Brent. An algorithm with guaranteed convergence for finding a zero of a function. *Computer Journal*, 14(4):422–425, 1971.

[14] H. Capart, X. Sillen, and Y. Zech. Numerical and experimental water transients in sewer pipes. *Journal of Hydraulic Research*, 35(5):659–672, 1997.

[15] C. Chalons, F. Coquel, S. Kokh, and N. Spillane. Large time-step numerical scheme for the seven-equation model of compressible two-phase flows. *Springer Proceedings in Mathematics and Statistics*, 4:225–233, 2011.

[16] C. Chalons, M. Girardin, and S. Kokh. Large time-step and asymptotic preserving numerical schemes for the gas dynamics equations with source terms. *SIAM Journal on Scientific Computing*, 35(6):a2874–a2902, 2013.

[17] F. Coquel, T. Gallouët, J.-M. Hérard, and N. Seguin. Closure laws for a two-fluid two-pressure model. *C. R. Acad. Sci. Paris*, 334(I):927–932, 2002.

[18] F. Coquel, E. Godlewski, and N. Seguin. Relaxation of fluid systems. *Mathematical Models and Methods in Applied Sciences*, 22(8), 2012.

[19] F. Coquel, J.-M. Hérard, and K. Saleh. A splitting method for the isentropic Baer-Nunziato two-phase flow model. *ESAIM: Proceedings*, 38(3):241–256, 2012.

[20] F. Coquel, J.-M. Hérard, and K. Saleh. A positive and entropy-satisfying finite volume scheme for the Baer-Nunziato model. *Journal of Computational Physics*, 330:401–435, 2017.

[21] F. Coquel, J.-M. Hérard, K. Saleh, and N. Seguin. A robust entropy-satisfying finite volume scheme for the isentropic Baer-Nunziato model. *ESAIM: Mathematical Modelling and Numerical Analysis*, 48:165–206, 2013.

[22] J.-A. Cunge and M. Wegner. Numerical integration of barré de Saint-Venant's flow equations by means of an implicit scheme of finite differences. *La Houille Blanche*, 1:33–39, 1964.

[23] P. Degond and M. Tang. All speed scheme for the low Mach number limit of the isentropic Euler equation. *Communications in Computational Physics*, 10:1–31, 2011.

[24] G. Dimarco, R. Loubère, and M.-H. Vignal. Study of a new asymptotic preserving scheme for the Euler system in the low Mach number limit. *Preprint*, 2016. URL: `https://hal.archives-ouvertes.fr/hal-01297238`.

[25] M. Ferrari, A. Bonzanini, and P. Poesio. A 5-equation, transient, hyperbolic, 1-dimensional model for slug capturing in pipes. *International Journal for Numerical Methods in Fluids*, pages 1–36, 2017.

[26] T. Gallouët, J.-M. Hérard, and N. Seguin. Numerical modeling of two-phase flows using the two-fluid two-pressure approach. *Mathematical Models and Methods in Applied Sciences*, 14(05):663–700, 2004.

[27] P. Garcia-Navarro, F. Alcrudo, and A. Priestley. An implicit method for water flow modelling in channels and pipes. *Journal of Hydraulic Research*, 32(5):721–742, 1994.

[28] S.L. Gavrilyuk. The structure of pressure relaxation terms : one-velocity case. *EDF report H-I83-2014-00276-EN*, 2014.

[29] J.-F. Gerbeau and B. Perthame. Derivation of viscous Saint-Venant system for laminar shallow water; numerical validation. *Discrete Contin. Dyn. Syst. Ser. B*, 1:89–102, 2001.

[30] J. Glimm, D. Saltz, and D. H. Sharp. Two phase flow modelling of a fluid mixing layer. *Journal of Fluid Mechanics*, 378:119–143, 1999.

[31] E. Godlewski, M. Parisot, J. Saint-Marie, and F. Wahl. Congested shallow water type model: roof modelling in free surface flow. *Preprint*, 2017. URL: `https://hal.archives-ouvertes.fr/hal-01368075v2`.

[32] J. Haack, S. Jin, and J.G. Liu. An all-speed asymptotic preserving method for the isentropic Euler and navier-stokes equations. *Communications in Computational Physics*, 12:955–980, 2012.

[33] J.-M. Hérard and O. Hurisse. A fractional step method to compute a class of compressible flows with micro-inertia. *Computers & Fluids*, 55:57–69, 2012.

[34] D. Iampietro, F. Daude, P. Galon, and J.-M. Hérard. A Mach-sensitive implicit-explicit scheme adapted to compressible multi-scale flows. *Preprint*, 2017. URL: `https://hal.archives-ouvertes.fr/hal-01531306`.

[35] R.I. Issa and M.H.W. Kempf. Simulation of slug flow in horizontal and nearly horizontal pipes with the two-fluid model. *International Journal of Multiphase Flow*, 29:69–95, 2003.

[36] A. K. Kapila, S. F. Son, J. B. Bdzil, R. Menikoff, and D. S. Stewart. Two-phase modeling of DDT: Structure of the velocity-relaxation zone. *Physics of Fluids*, 9(12):3885–3897, 1997.

[37] F. Kerger. *Modelling transient air-water flows in civil and environmental engineering*. PhD thesis, University of Liège, Liège, Belgium, 2010.

[38] F. Kerger, P. Archambeau, Erpicum S., B.J. Dewals, and M. Pirotton. An exact Riemann solver and a Godunov scheme for simulating highly transient mixed flows. *Journal of Computational and Applied Mathematics*, 235(8):2030–2040, 2011.

[39] D. Lannes. On the dynamics of floating structures. *Annals of PDE*, 3(1):11, 2017.

[40] A. Line and J. Fabre. Stratified gas liquid flow. *Encyclopedia of Heat Transfer*, pages 1097–1101, 1997.

[41] H. Lochon, F. Daude, P. Galon, and J.-M. Hérard. HLLC-type Riemann solver with approximated two-phase contact for the computation of the Baer-Nunziato two-fluid model. *Journal of Computational Physics*, 326:733–762, 2016.

[42] A.S. Léon, M.S. Ghidaoui, A.R. Schmidt, and M.H. Garcia. A robust two-equation model for transient-mixed flows. *Journal of Hydraulic Research*, 48(1):44–56, 2010.

[43] S. Noelle, G. Bispen, K. Arun, M. Lukacova-Medvidova, and C.D. Munz. A weakly asymptotic preserving all Mach number scheme for the Euler equations of gas dynamics. *SIAM Journal on Scientific Computing*, 36:B989–B1024, 2014.

[44] A. Preissmann and J.A. Cunge. Calcul des intumescences sur machines électroniques. *IX^e Assemblée Générale de l'A.I.R.H.*, Dubrovnik, 1961.

[45] L. Ramezani, B. Karney, and A. Malekpour. Encouraging effective air management in water pipelines: A critical review. *Journal of Water Resources Planning and Management*, 142(12), 2016.

[46] V. H. Ransom and D. L. Hicks. Hyperbolic two-pressure models for two-phase flow. *Journal of Computational Physics*, 53:124–151, 1984.

[47] V. V. Rusanov. Calculation of interaction of non-steady shock waves with obstacles. *Zh. Vychisl. Mat. Mat. Fiz.*, 1(2):267–279, 1961.

[48] Y. Taitel and A.E. Dukler. A model for predicting flow regime transitions in horizontal and near horizontal gas-liquid flow. *AIChE J.*, 22:47–55, 1976.

[49] S.-A. Tokareva and E.-F. Toro. HLLC-type Riemann solver for the Baer-Nunziato equations of compressible two-phase flow. *Journal of Computational Physics*, 229(10):3573–3604, 2010.

[50] E.F. Toro. *Riemann Solvers and Numerical Methods for Fluid Dynamics*. Springer-Verlag Berlin Heidelberg, 2009.

[51] B. Trajkovic, M. Ivetic, F. Calomino, and A. D'Ippolito. Investigation of transition from free surface to pressurized flow in a circular pipe. *Water science and technology*, 39(9):105–112, 1999.

[52] B.C. Trindade. Air pocket modeling in water mains with an air valve. Master's thesis, Auburn University, 2012.

[53] B.C. Trindade and J.G. Vasconcelos. Modeling of water pipeline filling events accounting for air phase interactions. *Journal of Hydraulic Engineering*, 139(9):921–934, 2013.

[54] J.G. Vasconcelos, S.J. Wright, and P.L. Roe. Improved simulation of flow regime transition in sewers: Two-component pressure approach. *Journal of Hydraulic Engineering*, 132(6):553–562, 2006.

[55] J.G. Vasconcelos, S.J. Wright, and P.L. Roe. Numerical oscillations in pipe-filling bore predictions by shock-capturing models. *Journal of Hydraulic Engineering*, 135(4):296–305, 2009.

Chapter 5

Linear stability analysis of the SPR scheme

Abstract: In the present chapter, a stability analysis is conducted on the implicit-explicit scheme proposed in Chapter 4 for the Compressible Two-Layer model developed in Chapter 2. This scheme, namely the SPR scheme, ensures the positivity of heights and densities under a CFL condition based on the celerity of material and gravity waves. However, some numerical experiments on dambreak problems display unstable behaviors when setting classically the related CFL number to $\frac{1}{2}$. The proposed analysis aims at clarifying an additional condition on this number to guarantee the scheme stability. It relies on a Von Neumann approach where each step of the scheme is linearized. In particular, the analysis is performed on a dimensionless version of the Compressible Two-Layer model and a critical threshold on the CFL number is identified. The latter depends on the ratio between the speed of slow gravity waves, involved in the explicit part of the scheme, and the speed of fast acoustic waves, involved in the implicit part of the scheme. Such stability issues regarding implicit-explicit schemes have been also recently highlighted in [12, 13] where the same kind of linear approach is proposed.

Contents

5.1 Introduction

The SPR scheme has been introduced in Chapter 4 to compute mixed flows with the Compressible Two-Layer model developed in Chapter 2. In the proposed scheme, one uses an implicit-explicit (IMEX) time discretization to deal explicitly with the slow propagation phenomena and implicitly with the fast ones. The stability of this IMEX approach is studied hereafter.

In the nonlinear framework, several difficulties are raised when studying the stability of a scheme. Two properties are usually targeted, namely the conservation of an invariant domain (typically the positivity of physical variables) and the existence of a discrete entropy inequality [1]. The first goal is reached with the SPR scheme which ensures the positivity of heights and densities through a *material* CFL condition based on the celerity of material and gravity waves. The second goal is *a priori* not reached with the SPR scheme due to the proposed splitting. However, the stability is checked experimentally refining the mesh and comparing with analytical or reference solutions. Doing so, the only constraint on the *material* CFL number is to be lower than 1. In practice, unstable results are obtained when considering some dambreak configurations and setting classically this CFL number to $\frac{1}{2}$. In order to exhibit an additional constraint, a linear stability analysis is led.

Indeed, stability issues regarding IMEX schemes have been recently pointed out in [12, 13]. In particular, several IMEX schemes have been derived for the compressible Euler system with the aim of dealing with low Mach number flows, see for instance [2, 7, 5, 11, 9, 8, 6]. Asymptotic consistency with the incompressible Euler system when the Mach number goes to zero is often studied while few details are provided about asymptotic (uniform) stability. However, the asymptotic stability is not necessarily ensured even if both explicit and implicit part of the scheme are individually stable. Using a linearized approach, the authors in [12, 13] give some examples where a coupling between both parts of the scheme may yield an non-uniform stability condition with a CFL number depending on the Mach number.

Thus, as in [12, 13] but considering the Compressible Two-Layer model, the work presented herein highlights stability issues arising from the SPR (IMEX) scheme. The latter is quickly recalled in Section 5.2 before presenting in Section 5.3 some simulation results where instabilities are observed. The linear stability analysis is performed in Section 5.4 using the Von Neumann approach. In Section 5.5, a dimensionless version of the Compressible Two-Layer model is proposed to identify parameters playing a leading role on the stability.

5.2 The SPR scheme

In this section, the Compressible Two-Layer model and the SPR scheme exposed in Chapters 2 and 4 respectively are quickly recalled.

5.2.1 The Compressible Two-Layer model

Considering a two-layer air-water flow through a pipe of height H, the Compressible Two-Layer model, referred to as the CTL model hereafter, reads:

$$\begin{cases} \partial_t h_1 + U_I \partial_x h_1 = \lambda_p (P_I - P_2(\rho_2)), \\ \partial_t m_k + \partial_x m_k u_k = 0, \ k = 1,2, \\ \partial_t m_k u_k + \partial_x m_k u_k^2 + \partial_x h_k P_k(\rho_k) - P_I \partial_x h_k = (-1)^k \lambda_u (u_1 - u_2), \ k = 1,2, \end{cases} \tag{$\mathscr{S}$}$$

where $k = 1$ for water, $k = 2$ for air, $m_k = h_k \rho_k$ and $h_1 + h_2 = H$. Here, h_k, ρ_k, $P_k(\rho_k)$ and u_k denote respectively the height, the mean density, the mean pressure and the mean velocity of phase k. The interfacial dynamics is represented by the transport equation on h_1 while the other two equations account for mass and momentum conservation in each phase. The interfacial pressure is denoted by P_I and closed by the hydrostatic constraint, while the interfacial velocity is denoted by U_I and closed following an entropy inequality, one obtains:

$$(U_I, P_I) = (u_2, P_1(\rho_1) - \rho_1 g \frac{h_1}{2}), \tag{5.1}$$

see Chapter 2 for details. In the following, one uses a linear gas law for water and a perfect gas law for air:

$$\begin{cases} P_1(\rho_1) = P_{1,\text{ref}} + c_{1,\text{ref}}^2 (\rho_1 - \rho_{1,\text{ref}}), \\ P_2(\rho_2) = P_{2,\text{ref}} \left(\dfrac{\rho_2}{\rho_{2,\text{ref}}} \right)^\gamma, \end{cases} \tag{5.2}$$

with some reference density $\rho_{k,\text{ref}}$ and pressure $P_{k,\text{ref}}$. The coefficient γ is set to 7/5 for air and the celerity c_k of pressure waves is defined by $c_k = \sqrt{P'(\rho_k)}$. The relaxation time scales are defined by $\lambda_p = \frac{3 h_1 h_2}{4\pi \mu_1 H}$ and $\lambda_u = \frac{h_1 h_2}{2H^2} f_i \rho_2 |u_2 - u_1|$, where μ_1 is the dynamic viscosity of water and f_i is a friction factor, see Chapter 4 for details.

5.2.2 A fractional step method adapted to mixed flows

The proposed fractional step method splits ($\mathscr{S}$) into three sub-systems. The *slow* dynamics of ($\mathscr{S}$) is treated in ($\mathscr{S}_m$) including the pressure relaxation source term and emphasizing the closeness with the shallow water equations for the water phase:

$$\begin{cases} \partial_t h_1 + u_2 \dfrac{\partial h_1}{\partial x} = \lambda_p (P_I - P_2), \\ \partial_t m_k + \partial_x m_k u_k = 0, \ k = 1,2, \\ \partial_t m_1 u_1 + \partial_x m_1 u_1^2 + \partial_x \rho_1 g \dfrac{h_1^2}{2} = 0, \\ \partial_t m_2 u_2 + \partial_x m_2 u_2^2 = 0. \end{cases} \tag{$\mathscr{S}_m$}$$

($\mathscr{S}_a$) refers to the *fast* dynamics of ($\mathscr{S}$) including the pressure gradients:

$$\begin{cases} \partial_t h_k = 0, \ \partial_t m_k = 0, \ k = 1,2, \\ \partial_t m_1 u_1 + h_1 \partial_x P_I = 0, \\ \partial_t m_2 u_2 + h_2 \partial_x P_2 + (P_2 - P_I) \dfrac{\partial h_2}{\partial x} = 0, \end{cases} \tag{$\mathscr{S}_a$}$$

where $P_I = P_1(\rho_1) - \rho_1 g \frac{h_1}{2}$. Finally, ($\mathscr{S}_u$) deals with the velocity relaxation source terms:

$$\partial_t h_k = 0, \ \partial_t m_k = 0, \ \partial_t m_k u_k = (-1)^k \lambda_u (u_1 - u_2), \ k = 1,2. \tag{$\mathscr{S}_u$}$$

In the discrete setting, the time step is denoted Δt and the space step Δx. The space is partitioned into cells $C_j = [x_{j-\frac{1}{2}}, x_{j+\frac{1}{2}}[$ where $x_{j+\frac{1}{2}} = (j+\frac{1}{2})\Delta x$ are the cell interfaces. For the iteration n, the solution is approximated on each cell C_j by:

$$\mathbf{W}_j^n = \Big((h_1)_j^n, (h_1\rho_1)_j^n, (h_1\rho_1 u_1)_j^n, (h_2\rho_2)_j^n, (h_2\rho_2 u_2)_j^n\Big)^T.$$

A suitable numerical scheme is associated to each sub-system whose details are provided below.

5.2.2.a Step 1: Explicit approach for ($\mathscr{S}_m$)

In this step, $\mathbf{W}_j$ is updated from $\mathbf{W}_j^n$ to $\mathbf{W}_j^*$. A classical explicit finite-volume scheme with Rusanov fluxes is used on the convective part while the pressure relaxation source term is treated implicitly. It writes:

$$\mathbf{W}_j^* = \mathbf{W}_j^n - \frac{\Delta t}{\Delta x}\Big(\mathbf{F}(\mathbf{W}_{j+\frac{1}{2}}^n) - \mathbf{F}(\mathbf{W}_{j-\frac{1}{2}}^n)\Big) - \frac{\Delta t}{2\Delta x}\mathbf{B}(\mathbf{W}_j^n)\Big(\mathbf{W}_{j+1}^n - \mathbf{W}_{j-1}^n\Big) + \Delta t\mathbf{S}(\mathbf{W}_j^*), \tag{5.3}$$

where:

$$\begin{cases} \mathbf{F}(\mathbf{W}) = (0, m_1u_1, m_1u_1^2 + m_1g\dfrac{h_1}{2}, m_2u_2, m_2u_2^2)^T, \\ \mathbf{B}(\mathbf{W}) = (u_2, 0, 0, 0, 0)^T, \\ \mathbf{S}(\mathbf{W}) = (\lambda_p(P_I - P_2), 0, 0, 0, 0)^T. \end{cases} \tag{5.4}$$

The fluxes are defined by:

$$\begin{cases} \mathbf{F}(\mathbf{W}_{j+\frac{1}{2}}^n) = \dfrac{1}{2}\Big(\mathbf{F}(\mathbf{W}_j^n) + \mathbf{F}(\mathbf{W}_{j+1}^n) - r_{j+\frac{1}{2}}(\mathbf{W}_{j+1}^n - \mathbf{W}_j^n)\Big), \\ r_{j+\frac{1}{2}} = \max\limits_{i\in\{j;j+1\}}\Big(|u_{2,i}^n|, |\big(u_1 \pm \sqrt{g\dfrac{h_1}{2}}\big)_i^n|\Big). \end{cases} \tag{5.5}$$

In order to solve implicitly the source term, the mass terms $m_{k,j}^n$ are updated first and the first equation in ($\mathscr{S}_m$) is solved under the form $f(h_{1,j}^*) = 0$ where:

$$f(y) = y - h_{1,j}^n + \Delta t\int_{x_{j-\frac{1}{2}}}^{x_{j+\frac{1}{2}}} u_2^n\frac{\partial h_1^n}{\partial x}dx - \Delta t\lambda_{p,j}^n\Big(P_I\Big(\frac{m_{1,j}^*}{y}\Big) - P_2\Big(\frac{m_{2,j}^*}{H-y}\Big)\Big).$$

One may easily demonstrate that f is strictly increasing on $[0;H]$ with the limits $f \underset{0^+}{\to} -\infty$ and $f \underset{H^-}{\to} +\infty$, such that $f(x) = 0$ admits a unique solution $h_{1,j}^*$ on $[0;H]$.

Proposition 5.1 (Positivity of heights and densities)**.** *The proposed scheme for ($\mathscr{S}_m$) ensures the positivity of heights and densities under the classical CFL condition:*

$$\frac{\Delta t}{\Delta x}\max_j\Big(\frac{r_{j+\frac{1}{2}} + r_{j-\frac{1}{2}}}{2}\Big) < 1, \tag{5.6}$$

which only implies material velocities.

In the following, the *material* CFL number is denoted ν and given by:

$$\nu = \frac{\Delta t}{\Delta x}\max_j\Big(\frac{r_{j+\frac{1}{2}} + r_{j-\frac{1}{2}}}{2}\Big). \tag{5.7}$$

5.2.2.b Step 2: Implicit approach for ($\mathscr{S}_a$)

In this step, only u_k is updated from u_k^* to u_k^{**}. A relaxation approach detailed in Chapter 4 is used so that the semi-discrete scheme writes:

$$\begin{cases} h_k^{**} = h_k^*, m_k^{**} = m_k^*,\ k = 1,2, \\ \dfrac{u_1^{**} - u_1^*}{\Delta t} - \dfrac{\Delta t}{\rho_1^*}\partial_x\Big(\dfrac{a_1^{2^*}}{\rho_1^*}\partial_x u_1^{**}\Big) = -\dfrac{1}{\rho_1^*}\partial_x P_I^* + \dfrac{\Delta t}{\rho_1^*}\partial_x\Big(\dfrac{a_1^{2^*}(u_1^* - u_2^*)}{m_1^*}\partial_x h_1^*\Big), \\ \dfrac{u_2^{**} - u_2^*}{\Delta t} - \dfrac{\Delta t}{\rho_2^*}\partial_x\Big(\dfrac{a_2^{2^*}}{\rho_2^*}\partial_x u_2^{**}\Big) = -\dfrac{1}{\rho_2^*}\partial_x P_2^* - \dfrac{(P_2^* - P_I^*)}{m_2^*}\partial_x h_2^*, \end{cases} \tag{5.8}$$

where $a_2 > \max_{\rho_2}(\rho_2 c_2)$ and a_1 is defined according to the flow regime. In the following, only the stratified regime is considered so that a_1 is set to zero. Integrating (5.8) on a cell C_j, one obtains for the velocities:

$$u_{1,j}^{**} = u_{1,j}^{*} - \frac{\Delta t}{2\Delta x}\left(\frac{P_{I,j+1}^{*} - P_{I,j-1}^{*}}{\rho_{1,j}^{*}}\right), \tag{5.9}$$

$$\left(1 + \frac{1}{\rho_{2,j}^{*}}\left(\frac{\Delta t}{\Delta x}\right)^2\left(\left(\frac{a_2^2}{\rho_2}\right)_{j+\frac{1}{2}}^{*} + \left(\frac{a_2^2}{\rho_2}\right)_{j-\frac{1}{2}}^{*}\right)\right)u_{2,j}^{**} - \frac{1}{\rho_{2,j}^{*}}\left(\frac{\Delta t}{\Delta x}\right)^2\left(\frac{a_2^2}{\rho_2}\right)_{j+\frac{1}{2}}^{*} u_{2,j+1}^{**} - \frac{1}{\rho_{2,j}^{*}}\left(\frac{\Delta t}{\Delta x}\right)^2\left(\frac{a_2^2}{\rho_2}\right)_{j-\frac{1}{2}}^{*} u_{2,j-1}^{**} =$$
$$u_{2,j}^{*} - \frac{\Delta t}{2\Delta x}\left(\frac{P_{2,j+1}^{*} - P_{2,j-1}^{*}}{\rho_{2,j}^{*}} - \left(\frac{P_2 - P_I}{m_2}\right)_i^{*}\left(h_{2,j+1}^{*} - h_{2,j-1}^{*}\right)\right). \tag{5.10}$$

In practice, the definition $a_{2,j+\frac{1}{2}}^{*} = k_2 \max((\rho_2 c_2)_j^{*}, (\rho_2 c_2)_{j+1}^{*})$ is chosen with $k_2 = 1.01$.

5.2.2.c Step 3: Implicit approach for ($\mathscr{S}_u$)

In this step, only u_k is updated from u_k^{**} to u_k^{n+1}. The velocity relaxation source term is treated implicitly (except the λ_u coefficient) such that the following non-singular 2x2 system is obtained:

$$\begin{pmatrix} m_{1,j}^{**} + \Delta t \lambda_{u,j}^{**} & -\Delta t \lambda_{u,j}^{**} \\ -\Delta t \lambda_{u,j}^{**} & m_{2,j}^{**} + \Delta t \lambda_{u,j}^{**} \end{pmatrix} \begin{pmatrix} u_{1,j}^{n+1} \\ u_{2,j}^{n+1} \end{pmatrix} = \begin{pmatrix} (m_1 u_1)_j^{**} \\ (m_2 u_2)_j^{**} \end{pmatrix}. \tag{5.11}$$

This step concludes the overall scheme which ensures the positivity of heights and densities under the *material* CFL condition (5.6).

5.3 Numerical experiments

The CTL model ($\mathscr{S}$) is used hereafter to simulate a classical dambreak problem. The latter is a Riemann problem where the initial condition is a discontinuity on h_1 with constant density and zero speed, see Figure 5.1. Regarding the pressure laws (5.2), the reference states are given on Figure 5.2.

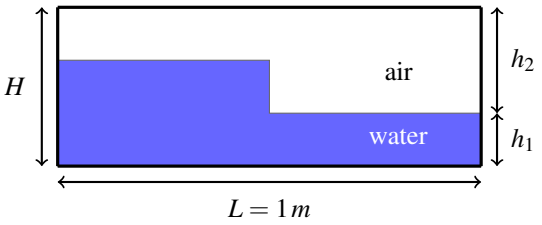

Variable	$0 \le x \le L/2$	$L/2 < x \le L$
h_1/H	0.6	0.4
ρ_1	$998.1115\,kg.m^{-3}$	$998.1115\,kg.m^{-3}$
u_1	$0\,m.s^{-1}$	$0\,m.s^{-1}$
ρ_2	$1.204\,kg.m^{-3}$	$1.204\,kg.m^{-3}$
u_2	$0\,m.s^{-1}$	$0\,m.s^{-1}$

Figure 5.1: Initial conditions for the dambreak problem.

Water	Air
$\rho_{1,\text{ref}} = 998.1115\,kg.m^{-3}$	$\rho_{2,\text{ref}} = 1.204\,kg.m^{-3}$
$P_{1,\text{ref}} = 1.0133\,bar$	$P_{2,\text{ref}} = 1.0141\,bar$
$c_{1,\text{ref}} = 1490.8697\,m.s^{-1}$	$c_{2,\text{ref}} = 343.4\,m.s^{-1}$

Figure 5.2: Reference states for pressure laws.

The solution of this problem for the water phase describes basically a rarefaction wave propagating to the left and a shock wave propagating to the right before reflecting against the walls. Indeed, strong similarities are found with the analytical solution provided by the Saint-Venant system, see Chapter 4. In the following, simulation results are displayed with several pipe heights. The length of the pipe is set to 1 meter and a 250 cells mesh is used so that $\Delta x = 4.10^{-3}$ for all simulations. In practice, the time step is calculated using (5.7) where the CFL number ν follows a ramp depending on the iteration number and starting from 0 to reach $\nu_{\max} < 1$.

5.3.1 Case 1: $H = 1\,m$

The height and the velocity of phase 1 are displayed for several times on Figure 5.3 where $\nu_{\max} = 0.5$. At $T = 1.5\,s$, instabilities are observed whereas the flow is supposed to reach calmly its equilibrium state given by $h_1 = 0.5\,m$ and $u_k = 0\,m.s^{-1}$.

The total simulation time is equal to 4 seconds. When setting $\nu_{max} = 0.5$, see Figure 5.4, instabilities are also observed on the time step from $T \approx 1.2\,s$, corresponding to a critical CFL number $\nu_c \approx 0.26$. Indeed, regarding (5.7), instabilities on the velocity field may directly impact the time step profile. In addition, note that the instabilities seem bounded in time. When setting $\nu_{max} = 0.2$, see Figure 5.5, instabilities are not observed. Thus, applying a smaller threshold on the CFL number than the classical $\nu_{max} = 0.5$ prevents instabilities from popping up.

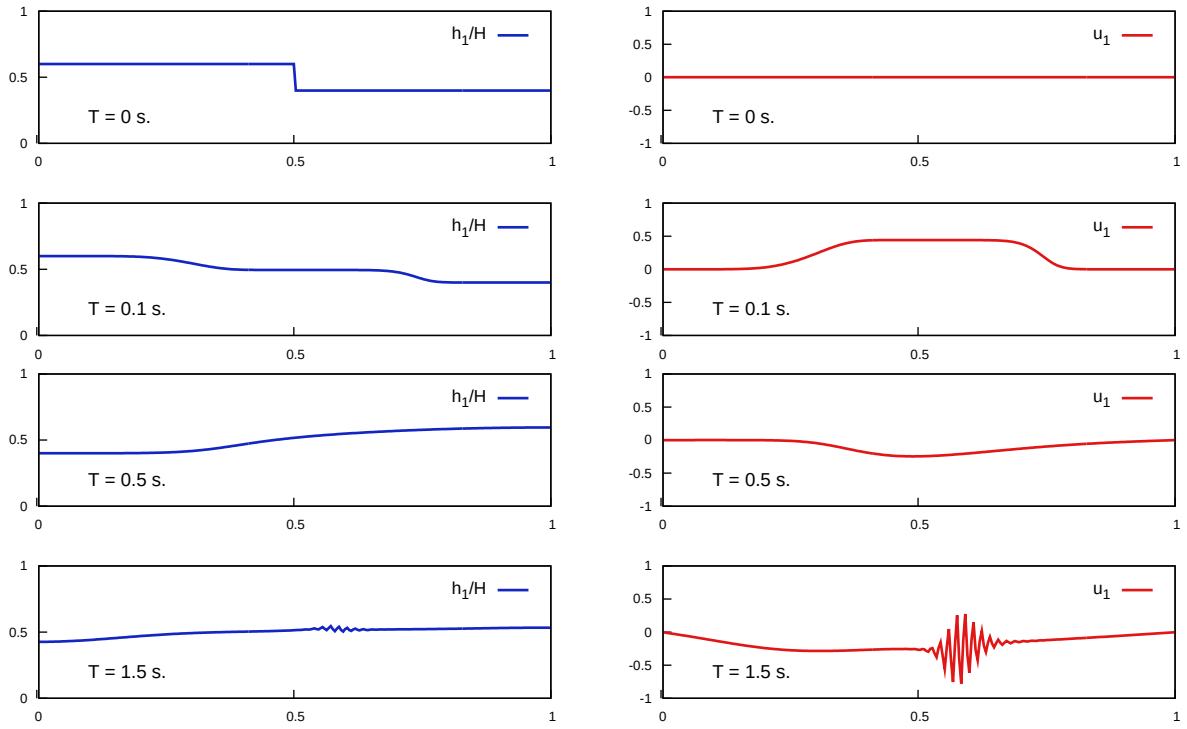

Figure 5.3: h_1 and u_1 fields at several times for $H = 1\,m$ and $\nu_{\max} = 0.5$.

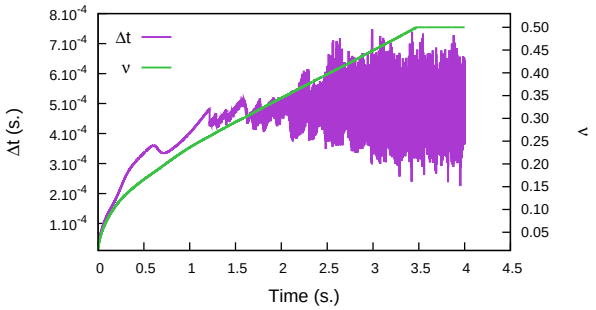

Figure 5.4: Δt and ν in function of time for $H = 1\,m$ and $\nu_{\max} = 0.5$.

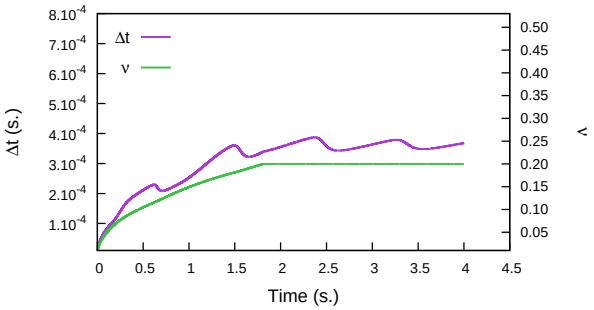

Figure 5.5: Δt and ν in function of time for $H = 1\,m$ and $\nu_{\max} = 0.2$.

5.3.2 Case 2: $H = 0.1\,m$

In this test case, the pipe height is changed to $H = 0.1\,m$ and the total simulation time is 2 seconds. As in the previous test case, instabilities are observed when $\nu_{max} = 0.5$. More precisely, regarding Figure 5.6, the instabilities pop up at

$T \approx 0.45\,s$ corresponding to a critical CFL number $\nu_c \approx 0.09$. Thus, the critical threshold is smaller than in Section 5.3.1 where $H = 1\,m$. When setting $\nu_{max} = 0.07$, see Figure 5.7, instabilities are not observed.

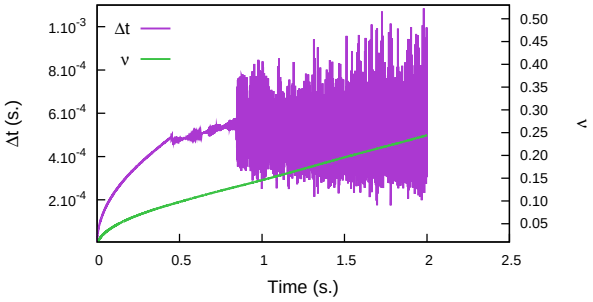

Figure 5.6: Δt and ν in function of time for $H = 0.1\,m$ and $\nu_{\max} = 0.5$.

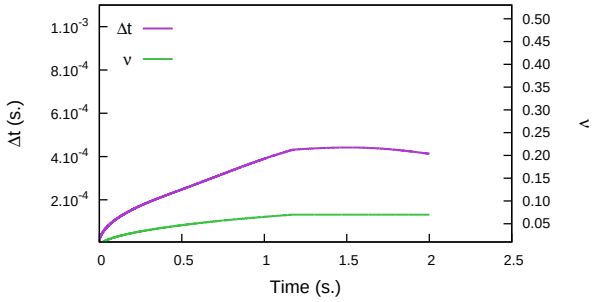

Figure 5.7: Δt and ν in function of time for $H = 1\,m$ and $\nu_{\max} = 0.07$.

5.3.3 Case 3: $H = 10\,m$

In this test case, the pipe height is set to $H = 10\,m$ and the total simulation time is 6 seconds. Contrary to the previous test cases, instabilities do not pop up with $\nu_{max} = 0.5$, see Figure 5.8. Indeed, at $T = 6\,s$, the flow has nearly reached its steady state at rest, see Figure 5.9.

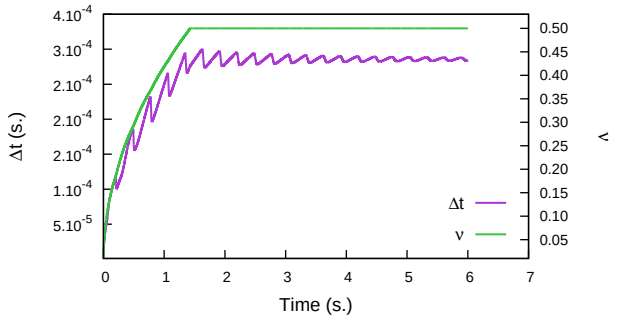

Figure 5.8: Δt and ν in function of time for $H = 10\,m$ and $\nu_{\max} = 0.5$.

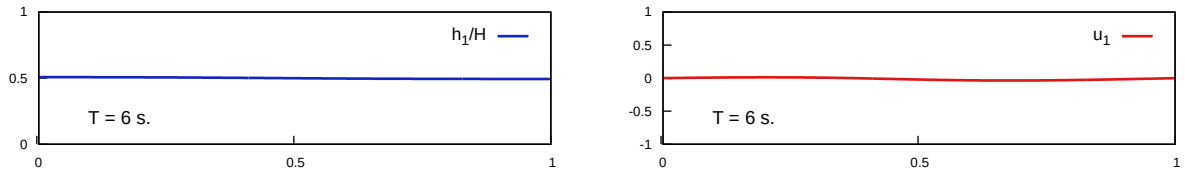

Figure 5.9: h_1 and u_1 fields at $T = 6\,s$ for $H = 10\,m$ and $\nu_{\max} = 0.5$.

Depending on the test case, different critical thresholds on the CFL number have been obtained to guarantee the stability of the scheme. Therefore, in addition to the CFL condition (5.6) which ensures the positivity of heights and densities, an other constraint on the CFL number ν should be applied. As a first approach, a linear stability analysis is performed on ($\mathscr{S}$) in the following section. The goal is to find correlations between the presented numerical results derived from the nonlinear system and stability results derived from the linearized version of the SPR scheme. In a second time, the stability analysis is performed on a dimensionless form of ($\mathscr{S}$) to highlight dimensionless quantities playing a leading role on the stability.

5.4 Linear stability analysis

The linear stability analysis is performed at the discrete level using the Von Neumann approach, see [3, 4]. Thus, the SPR scheme is linearized around a constant state and the stability of Fourier modes is studied. The Von Neumann framework is recalled hereafter before computing the amplification matrix associated to each step of the algorithm. Finally, stability results are provided considering the test cases of Section 5.3.

5.4.1 Von Neumann framework

In order to linearize the SPR scheme, the state $\mathbf{W}_j^n$ is decomposed into a constant state

$$\mathbf{W}_0 = (h_{1,0}, m_{1,0}, m_{1,0}u_{1,0}, m_{2,0}, m_{2,0}u_{2,0}),$$

and a perturbation $\mathbf{w}_j^n$, it reads:

$$\mathbf{W}_j^n = \mathbf{W}_0 + \mathbf{w}_j^n, \tag{5.12}$$

where:

$$\mathbf{w}_j^n = \left(\mathrm{h}_{1,j}^n, \mathrm{m}_{1,j}^n, (\mathrm{m}_1\mathrm{u}_1)_j^n, \mathrm{m}_{2,j}^n, (\mathrm{m}_2\mathrm{u}_2)_j^n\right)^T. \tag{5.13}$$

Note that the field notations for $\mathbf{W}_j^n$ and $\mathbf{w}_j^n$ only differ by straight characters in the second one. Regarding the Von Neumann framework, $\mathbf{w}_j^n$ is then decomposed into Fourier modes. In particular, for a given Fourier mode of wavelength $k \in \mathbb{Z}$, it writes:

$$\mathbf{w}_j^n = \widehat{\mathbf{w}}^n(k, \nu, \mathbf{W}_0) e^{ijk\Delta x}, \tag{5.14}$$

where the associated amplitude $\widehat{\mathbf{w}}^n(k, \nu, \mathbf{W}_0)$ also depends on the state $\mathbf{W}_0$ and the CFL number ν. The stability of the mode k is then studied regarding the spectral radius of the amplification matrix $G(k, \nu, \mathbf{W}_0)$ defined by:

$$\widehat{\mathbf{w}}^{n+1}(k, \nu, \mathbf{W}_0) = G(k, \nu, \mathbf{W}_0)\widehat{\mathbf{w}}^n(k, \nu, \mathbf{W}_0). \tag{5.15}$$

Proposition 5.2. *Denoting $\rho(G(k, \nu, \mathbf{W}_0))$ the spectral radius of $G(k, \nu, \mathbf{W}_0)$, i.e. the eigenvalue of $G(k, \nu, \mathbf{W}_0)$ with the largest modulus, the SPR scheme is linearly stable around $\mathbf{W}_0$ at CFL ν if and only if $\rho(G(k, \nu, \mathbf{W}_0)) \leq 1 \; \forall k \in \mathbb{Z}$.*

Proof. Using (5.15), $\widehat{\mathbf{w}}^{n+1} = G\widehat{\mathbf{w}}^n = G^{n+1}\widehat{\mathbf{w}}^0$. A geometric sequence is obtained which is bounded if and only if $\rho(G) \leq 1$. □

In practice, an amplification matrix is associated to each step of the algorithm such that G is decomposed into the product of three matrices:

$$G = G_3 G_2 G_1, \tag{5.16}$$

where $G_p, \; p = 1..3$, refers to the step p, see Section 5.2.2. The amplification matrices are calculated in the following section.

5.4.2 Linearization and amplification matrices

The linearization of the SPR scheme is derived hereafter step by step using the conservative variables $(h_1, m_1, m_1u_1, m_2, m_2u_2)$.

5.4.2.a Linearization of step 1

In this step, one focuses on ($\mathscr{S}_m$). As in practice $\lambda_p \gg 1$, it is chosen to impose $P_I = P_2$ in the linearized version of the scheme. Thus, the first step is divided into two sub-steps. The first one updates $\mathbf{W}_j$ from $\mathbf{W}_j^n$ to $\mathbf{W}_j^{n+}$ and is associated to the convective part of ($\mathscr{S}_m$) at the continuous level:

$$\begin{cases} \partial_t h_1 + u_2 \dfrac{\partial h_1}{\partial x} = 0, \\ \partial_t m_k + \partial_x m_k u_k = 0, \; k = 1, 2, \\ \partial_t m_1 u_1 + \partial_x m_1 u_1^2 + \partial_x \rho_1 g \dfrac{h_1^2}{2} = 0, \\ \partial_t m_2 u_2 + \partial_x m_2 u_2^2 = 0. \end{cases} \tag{5.17}$$

The second sub-step updates $\mathbf{W}_j$ from $\mathbf{W}_j^{n+}$ to $\mathbf{W}_j^*$ and is associated to:

$$\begin{cases} P_I = P_2, \\ \partial_t m_k = 0, \ k = 1,2, \\ \partial_t m_k u_k = 0, \ k = 1,2. \end{cases} \tag{5.18}$$

Regarding (5.17), the linearization of the classical explicit finite-volume scheme with Rusanov fluxes used in step 1, see (5.3) and (5.5), is equivalent to consider the same scheme applied to the following linearized system:

$$\partial_t \mathbf{w} + J_0 \partial_x \mathbf{w} = 0, \tag{5.19}$$

where $\mathbf{w}$ is the perturbation and J_0 is the jacobian of (5.17) evaluated in $\mathbf{W}_0$:

$$J_0 = \begin{pmatrix} u_{2,0} & 0 & 0 & 0 & 0 \\ 0 & 0 & 1 & 0 & 0 \\ m_{1,0}\frac{g}{2} & -u_{1,0}^2 + g\frac{h_{1,0}}{2} & 2u_{1,0} & 0 & 0 \\ 0 & 0 & 0 & 0 & 1 \\ 0 & 0 & 0 & -u_{2,0}^2 & 2u_{2,0} \end{pmatrix}. \tag{5.20}$$

Thus, in the first sub-step, $\mathbf{w}_j^{n+}$ satisfies:

$$\mathbf{w}_j^{n+} = \mathbf{w}_j^n - \frac{\Delta t}{\Delta x}\Big(\mathbf{f}(\mathbf{w}_{j+\frac{1}{2}}^n) - \mathbf{f}(\mathbf{w}_{j-\frac{1}{2}}^n)\Big), \tag{5.21}$$

where:

$$\begin{cases} \mathbf{f}(\mathbf{w}_{j+\frac{1}{2}}^n) = \dfrac{1}{2}\Big(J_0(\mathbf{w}_{j+1}^n + \mathbf{w}_j^n) - r_0(\mathbf{w}_{j+1}^n - \mathbf{w}_j^n)\Big), \\ r_0 = \max\Big(|u_{2,0}|, |\big(u_{1,0} + \sqrt{g\dfrac{h_{1,0}}{2}}\big)|\Big). \end{cases} \tag{5.22}$$

Note that the positivity of heights and densities is now ensured under the CFL condition :

$$\nu < 1, \tag{5.23}$$

where:

$$\nu = \frac{\Delta t}{\Delta x} r_0. \tag{5.24}$$

Using (5.22) and (5.24), (5.21) reads:

$$\mathbf{w}_j^{n+} = \mathbf{w}_j^n - \frac{\nu}{2r_0}\Big(J_0(\mathbf{w}_{j+1}^n - \mathbf{w}_{j-1}^n) - r_0(\mathbf{w}_{j+1}^n + \mathbf{w}_{j-1}^n - 2\mathbf{w}_j^n)\Big). \tag{5.25}$$

Turning into Fourier modes decomposition, (5.25) yields:

$$\widehat{\mathbf{w}}^{n+} = G_1^+ \widehat{\mathbf{w}}^n, \tag{5.26}$$

with:

$$G_1^+(k, \nu, \mathbf{W}_0) = \Big(1 - 2\nu \sin^2(\frac{k\Delta x}{2})\Big)\mathrm{Id} - i\frac{\nu}{r_0}\sin(k\Delta x) J_0, \tag{5.27}$$

where Id is the identity matrix.

In the second sub-step, see (5.18), only the density of each phase is updated through the pressure equality $P_I = P_2$. The latter is treated implicitly and writes at the discrete level:

$$P_{I,j}^* = P_{2,j}^*. \tag{5.28}$$

Using $m_{k,j}^* = m_{k,j}^{n+}$ and the closure for P_I, (5.28) yields:

$$P_1\Big(\frac{m_{1,j}^{n+}}{h_{1,j}^*}\Big) - m_{1,j}^{n+}\frac{g}{2} - P_2\Big(\frac{m_{2,j}^{n+}}{h_{2,j}^*}\Big) = 0. \tag{5.29}$$

Remark 5.1. (5.29) *ensures the positivity of heights and densities without any CFL condition. Indeed, as in Section 5.2.2.a where the relaxation time scale is finite, one may easily demonstrate that* (5.29) *admits a unique solution* $h_{1,j}^*$ *on* $[0; H]$.

Regarding (5.2), P_1 is linear with a constant celerity for pressure waves denoted $c_1 = c_{1,\text{ref}} = c_{1,0}$. For phase 2, the perfect gas law verifies $P_2(\frac{m_2}{h_2}) = \frac{c_2^2(\rho_2)}{\gamma}\frac{m_2}{h_2}$ which is approximated as $P_2(\frac{m_2}{h_2}) = \frac{c_{2,0}^2}{\gamma}\frac{m_2}{h_2}$ in the linearized scheme. Thus, (5.29) becomes:

$$c_{1,0}^2\frac{m_{1,j}^{n+}}{h_{1,j}^*} - m_{1,j}^{n+}\frac{g}{2} - \frac{c_{2,0}^2}{\gamma}\frac{m_{2,j}^{n+}}{h_{2,j}^*} + (P_{1,\text{ref}} - c_{1,0}^2\rho_{1,ref}) = 0. \tag{5.30}$$

In order to linearize the above equation in terms of conservative variables, $\frac{m_{k,j}^{n+}}{h_{k,j}^*}$ is expanded at first order around $\mathbf{W}_0$:

$$\frac{m_{k,j}^{n+}}{h_{k,j}^*} = \frac{m_{k,0}}{h_{k,0}} - \frac{m_{k,0}}{h_{k,0}^2}\mathrm{h}_{k,j}^* + \frac{1}{h_{k,0}}\mathrm{m}_{k,j}^{n,+} + o(\mathrm{h}_{k,j}^*, \mathrm{m}_{k,j}^{n+}). \tag{5.31}$$

Consequently, the linearized version of (5.30) reads:

$$-\Big(c_{1,0}^2\frac{m_{1,0}}{h_{1,0}^2} + \frac{c_{2,0}^2}{\gamma}\frac{m_{2,0}}{h_{2,0}^2}\Big)\mathrm{h}_{1,j}^* + \Big(\frac{c_{1,0}^2}{h_{1,0}} - \frac{g}{2}\Big)\mathrm{m}_{1,j}^{n+} - \frac{c_{2,0}^2}{\gamma h_{2,0}}\mathrm{m}_{2,j}^{n+} + K = 0,$$

where $K = P_{I,0} - P_{2,0} + \frac{H}{h_{2,0}}P_{2,0}$. In the Fourier space, the latter equation yields:

$$\widehat{\mathrm{h}}_1^* = \frac{1}{c_{1,0}^2\frac{m_{1,0}}{h_{1,0}^2} + \frac{c_{2,0}^2}{\gamma}\frac{m_{2,0}}{h_{2,0}^2}}\Big((\frac{c_{1,0}^2}{h_{1,0}} - \frac{g}{2})\widehat{\mathrm{m}}_1^{n+} - \frac{c_{2,0}^2}{\gamma h_{2,0}}\widehat{\mathrm{m}}_2^{n+}\Big) + \frac{K}{c_{1,0}^2\frac{m_{1,0}}{h_{1,0}^2} + \frac{c_{2,0}^2}{\gamma}\frac{m_{2,0}}{h_{2,0}^2}}. \tag{5.32}$$

As the constant term does not contribute to the amplification matrix, G_1^* writes:

$$G_1^*(k,\nu,\mathbf{W}_0) = \begin{pmatrix} 0 & \frac{\frac{c_{1,0}^2}{h_{1,0}} - \frac{g}{2}}{c_{1,0}^2\frac{m_{1,0}}{h_{1,0}^2} + \frac{c_{2,0}^2}{\gamma}\frac{m_{2,0}}{h_{2,0}^2}} & 0 & \frac{\frac{-c_{2,0}^2}{\gamma h_{2,0}}}{c_{1,0}^2\frac{m_{1,0}}{h_{1,0}^2} + \frac{c_{2,0}^2}{\gamma}\frac{m_{2,0}}{h_{2,0}^2}} & 0 \\ 0 & 1 & 0 & 0 & 0 \\ 0 & 0 & 1 & 0 & 0 \\ 0 & 0 & 0 & 1 & 0 \\ 0 & 0 & 0 & 0 & 1 \end{pmatrix}. \tag{5.33}$$

Finally, the amplification matrix of the first step is given by:

$$G_1 = G_1^* G_1^+. \tag{5.34}$$

5.4.2.b Linearization of step 2

In this step, only the velocities of each phase are updated while the other variables are constant. Regarding phase 1, (5.9) is first multiplied by $m_{1,j}^{**} = m_{1,j}^*$ to write it in conservative variables, and using (5.28), it provides:

$$(m_1u_1)_j^{**} = (m_1u_1)_j^* - h_{1,j}^*\frac{\Delta t}{2\Delta x}\Big(P_2\Big(\frac{m_2}{h_2}\Big)_{j+1}^* - P_2\Big(\frac{m_2}{h_2}\Big)_{j-1}^*\Big). \tag{5.35}$$

Using the linearized pressure law $P_2(\frac{m_2}{h_2}) = \frac{c_{2,0}^2}{\gamma}\frac{m_2}{h_2}$ and the first order expansion (5.31) applied to $(\frac{m_2}{h_2})_{j+1}^*$ and $(\frac{m_2}{h_2})_{j-1}^*$, (5.35) is linearized as:

$$(\mathrm{m}_1\mathrm{u}_1)_j^{**} = (\mathrm{m}_1\mathrm{u}_1)_j^* - h_{1,0}\frac{\Delta t}{2\Delta x}\Big(\frac{c_{2,0}^2}{\gamma h_{2,0}}(\mathrm{m}_{2,j+1}^* - \mathrm{m}_{2,j-1}^*) + \frac{c_{2,0}^2 m_{2,0}}{\gamma h_{2,0}^2}(\mathrm{h}_{1,j+1}^* - \mathrm{h}_{1,j-1}^*)\Big).$$

With $\frac{\Delta t}{\Delta x} = \frac{\nu}{r_0}$, the above equation reads in the Fourier space:

$$\widehat{\mathrm{m}_1\mathrm{u}_1}^{**} = \widehat{\mathrm{m}_1\mathrm{u}_1}^{*} - i\frac{\nu}{r_0}\frac{c_{2,0}^2 h_{1,0}}{\gamma h_{2,0}}\sin(k\Delta x)\Big(\widehat{\mathrm{m}}_2^* + \rho_{2,0}\widehat{\mathrm{h}}_1^*\Big). \tag{5.36}$$

Regarding phase 2, (5.10) with $P^*_{I,j} = P^*_{2,j}$ writes:

$$\Big(1+\frac{1}{\rho^*_{2,j}}\Big(\frac{\Delta t}{\Delta x}\Big)^2\Big(\Big(\frac{a_2^2}{\rho_2}\Big)^*_{j+\frac{1}{2}}+\Big(\frac{a_2^2}{\rho_2}\Big)^*_{j-\frac{1}{2}}\Big)\Big)\frac{(m_2u_2)^{**}_j}{m^{**}_{2,j}}-\frac{1}{\rho^*_{2,j}}\Big(\frac{\Delta t}{\Delta x}\Big)^2\Big(\frac{a_2^2}{\rho_2}\Big)^*_{j+\frac{1}{2}}\frac{(m_2u_2)^{**}_{j+1}}{m^{**}_{2,j+1}}$$
$$-\frac{1}{\rho^*_{2,j}}\Big(\frac{\Delta t}{\Delta x}\Big)^2\Big(\frac{a_2^2}{\rho_2}\Big)^*_{j-\frac{1}{2}}\frac{(m_2u_2)^{**}_{j-1}}{m^{**}_{2,j-1}}=\frac{(m_2u_2)^*_j}{m^*_{2,j}}-\frac{\Delta t}{2\Delta x}\Big(\frac{P^*_{2,j+1}-P^*_{2,j-1}}{\rho^*_{2,j}}\Big). \quad (5.37)$$

In order to linearize (5.37) in terms of conservative variables, $\frac{(m_2u_2)^{**}_j}{m^{**}_{2,j}}$ is expanded at first order around $\mathbf{W}_0$:

$$\frac{(m_2u_2)^{**}_j}{m^{**}_{2,j}}=\frac{(m_2u_2)_0}{m_{2,0}}-\frac{(m_2u_2)_0}{m^2_{2,0}}\mathrm{m}^{**}_{2,j}+\frac{1}{m_{2,0}}(\mathrm{m_2u_2})^{**}_j+o(\mathrm{m}^{**}_{2,j},(\mathrm{m_2u_2})^{**}_j). \quad (5.38)$$

Thus, denoting $\mu_{2,0}=\frac{a^2_{2,0}}{\rho^2_{2,0}}$ and injecting (5.24), the linearization of the left-hand side (*LHS*) of (5.37) gives:

$$LHS=\Big(1+2\mu_{2,0}\frac{\nu^2}{r_0^2}\Big)\frac{(\mathrm{m_2u_2})^{**}_j}{m_{2,0}}-\mu_{2,0}\frac{\nu^2}{r_0^2}\frac{(\mathrm{m_2u_2})^{**}_{j+1}}{m_{2,0}}-\mu_{2,0}\frac{\nu^2}{r_0^2}\frac{(\mathrm{m_2u_2})^{**}_{j-1}}{m_{2,0}}$$
$$-\Big(\Big(1+2\mu_{2,0}\frac{\nu^2}{r_0^2}\Big)\frac{u_{2,0}}{m_{2,0}}\mathrm{m}^{**}_{2,j}-\mu_{2,0}\frac{\nu^2}{r_0^2}\frac{u_{2,0}}{m_{2,0}}\mathrm{m}^{**}_{2,j+1}-\mu_{2,0}\frac{\nu^2}{r_0^2}\frac{u_{2,0}}{m_{2,0}}\mathrm{m}^{**}_{2,j-1}\Big).$$

Turning into Fourier modes decomposition, the above equation with $\mathrm{m}^{**}_{2,j}=\mathrm{m}^*_{2,j}$ yields:

$$\widehat{LHS}=\Big(1+4\mu_{2,0}\frac{\nu^2}{r_0^2}\sin^2(\frac{k\Delta x}{2})\Big)\Big(\frac{1}{m_{2,0}}\widehat{\mathrm{m_2u_2}}^{**}-\frac{u_{2,0}}{m_{2,0}}\widehat{\mathrm{m}}^*_2\Big)+u_{2,0}.$$

The right-hand side (*RHS*) of (5.37) is linearized in the same way as (5.35) for the pressure gradient and using (5.38) for $\frac{(m_2u_2)^*_j}{m^*_{2,j}}$, one obtains:

$$RHS=u_{2,0}-\frac{u_{2,0}}{m_{2,0}}\mathrm{m}^*_{2,j}+\frac{1}{m_{2,0}}(\mathrm{m_2u_2})^*_j-\frac{\nu}{2r_0\rho_{2,0}}\Big(\frac{c^2_{2,0}}{\gamma h_{2,0}}(\mathrm{m}^*_{2,j+1}-\mathrm{m}^*_{2,j-1})+\frac{c^2_{2,0}m_{2,0}}{\gamma h^2_{2,0}}(\mathrm{h}^*_{1,j+1}-\mathrm{h}^*_{1,j-1})\Big).$$

In the Fourier space, it reads:

$$\widehat{RHS}=\frac{1}{m_{2,0}}\widehat{\mathrm{m_2u_2}}^*-\frac{u_{2,0}}{m_{2,0}}\widehat{\mathrm{m}}^*_2-i\frac{\nu}{r_0}\frac{c^2_{2,0}}{\gamma m_{2,0}}\sin(k\Delta x)(\widehat{\mathrm{m}}^*_2+\rho_{2,0}\widehat{\mathrm{h}}^*_1)+u_{2,0}.$$

Consequently, $\widehat{LHS}=\widehat{RHS}$ provides:

$$\widehat{\mathrm{m_2u_2}}^{**}=\frac{1}{1+4\mu_{2,0}\frac{\nu^2}{r_0^2}\sin^2(\frac{k\Delta x}{2})}\Big(\widehat{\mathrm{m_2u_2}}^*+\Big(4\mu_{2,0}u_{2,0}\frac{\nu^2}{r_0^2}\sin^2(\frac{k\Delta x}{2})-i\frac{\nu}{r_0}\frac{c^2_{2,0}}{\gamma}\sin(k\Delta x)\Big)\widehat{\mathrm{m}}^*_2$$
$$-i\frac{\nu}{r_0}\frac{c^2_{2,0}\rho_{2,0}}{\gamma}\sin(k\Delta x)\widehat{\mathrm{h}}^*_1\Big). \quad (5.39)$$

Lastly, gathering (5.36) and (5.39), the amplification matrix G_2 of step 2 writes:

$$G_2(k,\nu,\mathbf{W}_0)=\begin{pmatrix}1&0&0&0&0\\0&1&0&0&0\\-i\frac{\nu}{r_0}\frac{c^2_{2,0}h_{1,0}\rho_{2,0}}{\gamma h_{2,0}}\sin(k\Delta x)&0&1&-i\frac{\nu}{r_0}\frac{c^2_{2,0}h_{1,0}}{\gamma h_{2,0}}\sin(k\Delta x)&0\\0&0&0&1&0\\\frac{-i\frac{\nu}{r_0}\frac{c^2_{2,0}\rho_{2,0}}{\gamma}\sin(k\Delta x)}{1+4\mu_{2,0}\frac{\nu^2}{r_0^2}\sin^2(\frac{k\Delta x}{2})}&0&0&\frac{4\mu_{2,0}u_{2,0}\frac{\nu^2}{r_0^2}\sin^2(\frac{k\Delta x}{2})-i\frac{\nu}{r_0}\frac{c^2_{2,0}}{\gamma}\sin(k\Delta x)}{1+4\mu_{2,0}\frac{\nu^2}{r_0^2}\sin^2(\frac{k\Delta x}{2})}&\frac{1}{1+4\mu_{2,0}\frac{\nu^2}{r_0^2}\sin^2(\frac{k\Delta x}{2})}\end{pmatrix}. \quad (5.40)$$

5.4.2.c Linearization of step 3

As in step 2, only the velocities of each phase are updated in the current step. The velocity relaxation is treated implicitly such that the scheme in conservative variables writes:

$$(m_k u_k)_j^{n+1} - (m_k u_k)_j^{**} = (-1)^k \lambda_u^{**} \Delta t \Big(\frac{(m_1 u_1)_j^{n+1}}{m_{1,j}^{n+1}} - \frac{(m_2 u_2)_j^{n+1}}{m_{2,j}^{n+1}} \Big),\ k = 1,2.$$

Using (5.38) for both phases and $m_{k,j}^{n+1} = m_{k,j}^{**}$, the right-hand side is linearized around $\mathbf{W}_0$ considering a constant relaxation parameter $\lambda_{u,0}$. One readily obtains in the Fourier space:

$$\widehat{m_k u_k}^{n+1} - \widehat{m_k u_k}^{**} = (-1)^k \lambda_{u,0} \Delta t \Big(\frac{1}{m_{1,0}} \widehat{m_1 u_1}^{n+1} - \frac{1}{m_{2,0}} \widehat{m_2 u_2}^{n+1} - (\frac{u_{1,0}}{m_{1,0}} \widehat{m}_1^{**} - \frac{u_{2,0}}{m_{2,0}} \widehat{m}_2^{**}) + (u_{1,0} - u_{2,0}) \Big).$$

In matrix form, the amplification part writes:

$$\begin{pmatrix} 1 + \Delta t \frac{\lambda_{u,0}}{m_{1,0}} & -\Delta t \frac{\lambda_{u,0}}{m_{2,0}} \\ -\Delta t \frac{\lambda_{u,0}}{m_{1,0}} & 1 + \Delta t \frac{\lambda_{u,0}}{m_{2,0}} \end{pmatrix} \begin{pmatrix} \widehat{m_1 u_1}^{n+1} \\ \widehat{m_2 u_2}^{n+1} \end{pmatrix} = \begin{pmatrix} \widehat{m_1 u_1}^{**} + \Delta t \lambda_u \frac{u_{1,0}}{m_{1,0}} \widehat{m}_1^{**} - \Delta t \lambda_u \frac{u_{2,0}}{m_{2,0}} \widehat{m}_2^{**} \\ \widehat{m_2 u_2}^{**} - \Delta t \lambda_u \frac{u_{1,0}}{m_{1,0}} \widehat{m}_1^{**} + \Delta t \lambda_u \frac{u_{2,0}}{m_{2,0}} \widehat{m}_2^{**} \end{pmatrix}.$$

The above 2x2 system is easily inverted such that injecting $\Delta t = \frac{\nu}{r_0} \Delta x$, G_3 reads:

$$G_3(k, \nu, \mathbf{W}_0) = \begin{pmatrix} 1 & 0 & 0 & 0 & 0 \\ 0 & 1 & 0 & 0 & 0 \\ 0 & \nu \frac{\lambda_{u,0} u_{1,0}}{r_0 m_{1,0}} \frac{\Delta x}{\chi} & (1 + \nu \frac{\lambda_{u,0}}{r_0 m_{2,0}} \Delta x) \frac{1}{\chi} & -\nu \frac{\lambda_{u,0} u_{2,0}}{r_0 m_{2,0}} \frac{\Delta x}{\chi} & \nu \frac{\lambda_{u,0}}{r_0 m_{2,0}} \frac{\Delta x}{\chi} \\ 0 & 0 & 0 & 1 & 0 \\ 0 & -\nu \frac{\lambda_{u,0} u_{1,0}}{r_0 m_{1,0}} \frac{\Delta x}{\chi} & \nu \frac{\lambda_{u,0}}{r_0 m_{1,0}} \frac{\Delta x}{\chi} & \nu \frac{\lambda_{u,0} u_{2,0}}{r_0 m_{2,0}} \frac{\Delta x}{\chi} & (1 + \nu \frac{\lambda_{u,0}}{r_0 m_{1,0}} \Delta x) \frac{1}{\chi} \end{pmatrix}, \tag{5.41}$$

where $\chi = 1 + \nu \frac{\lambda_{u,0}}{r_0} (\frac{1}{m_{1,0}} + \frac{1}{m_{2,0}}) \Delta x$.

Finally, using (5.34), (5.40) and (5.41), one can compute the amplification matrix $G = G_3 G_2 G_1$ associated to a constant state $\mathbf{W}_0$, a CFL number ν and a wavenumber k.

5.4.3 Stability results

Regarding Proposition 5.2, the process is the following:

- A constant state $\mathbf{W}_0$ is chosen in the region where instabilities seem to pop up (if applicable).
- Starting from $\nu = 10^{-2}$ to $\nu = 1$, a CFL number is set.
  - $G(k, \nu, \mathbf{W}_0)$ and its spectral radius $\rho(G(k, \nu, \mathbf{W}_0))$ are computed for a wavenumber k, $k = 1, .., 1000$.
  - The highest spectral radius $\rho_{\max}(\nu, \mathbf{W}_0) = \max_{k \in \{1,..,1000\}} \rho(G(k, \nu, \mathbf{W}_0))$ is stored.
- If $\rho_{max}(\nu, \mathbf{W}_0) > 1$, the corresponding CFL number is denoted ν_c^{lin} and compared to the critical value ν_c observed in the results exposed in Section 5.3.

5.4.3.a Case 1: $H = 1\,m$

For this test case, instabilities are observed in Section 5.3.1 setting $v_{\max} = 0.5$. The fields values of the chosen $\mathbf{W}_0$ are given on Figure 5.10 and the stability results are given on Figure 5.11. Thus, one obtains $0.24 < \nu_c^{lin} \leq 0.25$ which is very close to the results exposed in Section 5.3.1 where $\nu_c \approx 0.26$.

Variable	Value
$h_{1,0}/H$	0.52258750
$\rho_{1,0}$	$998.11280\,kg.m^{-3}$
$u_{1,0}$	$4.1794280\times10^{-3}\,m.s^{-1}$
$\rho_{2,0}$	$1.2042155\,kg.m^{-3}$
$u_{2,0}$	$-6.8358296\times10^{-4}\,m.s^{-1}$

Figure 5.10: Constant state $\mathbf{W}_0$ for case 1.

ν	$\rho_{\max}$	ν	$\rho_{\max}$	ν	$\rho_{\max}$
0.01	0.99999992	0.11	0.99999579	0.21	0.99998561
0.02	0.99999978	0.12	0.99999504	0.22	0.99998427
0.03	0.99999958	0.13	0.99999424	0.23	0.99998286
0.04	0.99999931	0.14	0.99999337	0.24	0.99998138
0.05	0.99999899	0.15	0.99999244	**0.25**	**1.22488823**
0.06	0.99999861	0.16	0.99999146	0.26	1.53162575
0.07	0.99999816	0.17	0.99999041	0.27	1.82311507
0.08	0.99999766	0.18	0.99998930	0.28	2.11116586
0.09	0.99999710	0.19	0.99998813	0.29	2.40055364
0.10	0.99999647	0.20	0.99998690	0.30	2.69371724

Figure 5.11: $\rho_{\max}$ in function of ν for case 1.

5.4.3.b Case 2: $H = 0.1\,m$

For this test case. instabilities are observed in Section 5.3.2 setting $\nu_{\max} = 0.5$. The fields values of the chosen $\mathbf{W}_0$ are given on Figure 5.10 and the stability results are give on Figure 5.13. One obtains $0.08 < \nu_c^{lin} < 0.09$ with $\nu_c \approx 0.09$.

Variable	Value
$h_{1,0}/H$	0.51344995
$\rho_{1,0}$	$998.11165\,kg.m^{-3}$
$u_{1,0}$	$5.0913423\times10^{-4}\,m.s^{-1}$
$\rho_{2,0}$	$1.2037687\,kg.m^{-3}$
$u_{2,0}$	$-7.2361372\times10^{-4}\,m.s^{-1}$

Figure 5.12: Constant state $\mathbf{W}_0$ for case 2.

ν	$\rho_{\max}$
0.01	0.999999643
0.02	0.999998674
0.03	0.999997093
0.04	0.999994899
0.05	0.999992093
0.06	0.999988675
0.07	0.999984644
0.08	0.999980001
0.09	**1.665513685**
0.10	2.607954694

Figure 5.13: $\rho_{\max}$ in function of ν for case 2.

As in the previous test case, the linear stability results are in agreement with the simulation results.

5.4.3.c Case 3: $H = 10\,m$

For this test case, instabilities are not observed in Section 5.3.3 setting $\nu_{\max} = 0.5$. One chooses the first cell of the mesh at $T = 6\,s$ to define $\mathbf{W}_0$, see Figure 5.14. The spectral radius of G is displayed on Figure 5.15 for $0.6 \leq \nu \leq 0.7$ and one observes that $0.66 < \nu_c^{lin} \leq 0.67$. This result is consistent as $\nu_c^{lin} > \nu_{\max}$. Several remarks regarding the above results are gathered in the following section.

Variable	Value
$h_{1,0}/H$	0.49740926
$\rho_{1,0}$	$998.12270\,kg.m^{-3}$
$u_{1,0}$	$1.9884389\times10^{-4}\,m.s^{-1}$
$\rho_{2,0}$	$1.2039472\,kg.m^{-3}$
$u_{2,0}$	$-1.8598072\times10^{-4}\,m.s^{-1}$

Figure 5.14: Constant state $\mathbf{W}_0$ for case 3.

ν	$\rho_{\max}$
0,60	0,999989846
0,61	0,999989556
0,62	0,999989262
0,63	0,999988965
0,64	0,999988663
0,65	0,999988358
0,66	0,999988048
0,67	**1,088466568**
0,68	1,186869198
0,69	1,281790999
0,70	1,374451430

Figure 5.15: $\rho_{\max}$ in function of ν for case 3.

5.4.4 Remarks

- Following the numerical results presented in Section 5.3, the linear stability analysis also provides critical CFL numbers depending on the considered test case. Indeed, correct agreements are found between the two approaches. Thus, it is obvious that an additional condition on the CFL number ν has to be applied. However, the complexity of the amplification matrix G makes inconceivable the computation of an analytical expression for ρ_{max} even with a dedicated software (unsuccessful attempt with *Maxima*). In order to identify dimensionless parameters playing a leading role in the stability, the same analysis is performed in the next section on a dimensionless version of the CTL model.

- In the provided results, it is interesting to notice that each step is individually stable ($\rho_{\max}(G_p)\leq 1, p=1,..,3$) while $\rho_{\max}(G)$ may be strictly greater than 1. It illustrates the fact that in general, for two matrices (A_1,A_2), $\rho(A_1A_2)$ is not necessarily bounded by $\rho(A_1)\rho(A_2)$. The previous inequality is nonetheless verified when A_1 and A_2 commute, see [10] for some properties on spectral radii. In particular, note that in the work presented in [12, 13], the authors introduce the notion of characteristic splittings for which the matrices associated to the implicit and explicit part commute. In this framework, there is no interaction between both parts of the scheme and the uniform stability is obtained.

- The considered test cases deal with stratified flows where $a_1=0$, see (5.8). Regarding the pressurized regime, numerical diffusion is added through a_1 imposing the Whitham condition, i.e. $a_1>\max_{\rho_1}(\rho_1 c_1)$, to ensure stability. If the latter condition is applied for the stratified regime, the instabilities do not pop up but the solution is largely affected by the numerical diffusion.

5.5 Dimensionless analysis

A dimensionless version of the CTL model ($\mathscr{S}$) is proposed in this section. Dealing with two phases, several dimensionless models could be derived as several characteristic quantities have to be defined. One approach is detailed below in order to identify key parameters playing a leading role in the stability of the SPR scheme.

5.5.1 A dimensionless Compressible Two-Layer model

In order to rescale the CTL model ($\mathscr{S}$), the following dimensionless quantities are introduced:

$$\tilde{t}=\frac{t}{T},\ \tilde{x}=\frac{x}{L},\ U=\frac{L}{T},\ \tilde{h}_k=\frac{h_k}{H},\ \tilde{\rho}_k=\frac{\rho_k}{\rho_k^*},\ \ \tilde{u}_k=\frac{u_k}{u_k^*},\ \tilde{P}_k=\frac{P_k}{P_k^*}, \tag{5.42}$$

where one has to define the characteristic quantities (ρ_k^*,u_k^*,P_k^*) for both phases.

5.5.1.a Dimensionless mass conservation

Using (5.42), the mass conservation equation for each phase writes:

$$\frac{\partial \tilde{m}_k}{\partial \tilde{t}} + \frac{u_k^*}{U}\frac{\partial \tilde{m}_k \tilde{u}_k}{\partial \tilde{x}} = 0.$$

Hereafter, the same characteristic velocity is chosen for both phases:

$$u_1^* = u_2^* = U. \tag{5.43}$$

This choice is suggested by the velocity relaxation in the momentum conservation equations, see ($\mathscr{S}$), which yields $u_1 - u_2 \underset{t\to+\infty}{\to} 0$. Although it would be possible to specify an individual characteristic velocity for each phase, physical arguments to close u_k^* in this framework are clearly not obvious. Therefore, thanks to (5.43), the dimensionless mass conservation equations write:

$$\frac{\partial \tilde{m}_k}{\partial \tilde{t}} + \frac{\partial \tilde{m}_k \tilde{u}_k}{\partial \tilde{x}} = 0. \tag{5.44}$$

5.5.1.b Dimensionless momentum conservation

Using (5.42) and (5.43), the momentum conservation equation for each phase writes:

$$\frac{\partial \tilde{m}_k \tilde{u}_k}{\partial \tilde{t}} + \frac{\partial \tilde{m}_k \tilde{u}_k^2}{\partial \tilde{x}} + \frac{P_k^*}{\rho_k^* U^2}\frac{\partial \tilde{h}_k \tilde{P}_k}{\partial \tilde{x}} - \left(\frac{P_1^*}{\rho_k^* U^2}\tilde{P}_1 - \frac{\rho_1^* g H}{\rho_k^* U^2}\tilde{\rho}_1 \frac{\tilde{h}_1}{2}\right)\frac{\partial \tilde{h}_k}{\partial \tilde{x}} = (-1)^k \frac{\lambda_u^* T}{\rho_k^* H}\tilde{\lambda}_u(\tilde{u}_1 - \tilde{u}_2).$$

An individual characteristic pressure P_k^* is chosen for each phase and reads:

$$P_k^* = \rho_k^* c_k^{*^2}, \tag{5.45}$$

where $c_k^* = c_k(\rho_k^*)$. This choice is arguable regarding the pressure relaxation which yields $P_l \underset{t\to+\infty}{\to} P_2$. However, in order to respect the hierarchy in terms of densities, i.e. $\rho_1^* > \rho_2^*$, as well as in terms of pressure wave celerity, i.e. $c_1^* > c_2^*$, the choice $P_1^* = P_2^*$ cannot be considered. Other dimensionless quantities are therefore introduced, such as the Mach number of each phase:

$$M_k = \frac{U}{c_k^*},\ k = 1,2, \tag{5.46}$$

the Froude number:

$$Fr = \frac{U}{\sqrt{gH}}, \tag{5.47}$$

and the ratio between the characteristic density of each phase:

$$\mathscr{R} = \frac{\rho_2^*}{\rho_1^*}. \tag{5.48}$$

Note that imposing $c_2^* < c_1^*$, (5.46) yields $M_1 < M_2$. The velocity relaxation parameter λ_u^* is defined as:

$$\lambda_u^* = \frac{\rho_2^* H}{\tau_u}, \tag{5.49}$$

where τ_u is a characteristic time scale. Thus, defining $k_u = \tau_u / T$, the dimensionless momentum conservation equations write:

$$\begin{cases} \dfrac{\partial \tilde{m}_1 \tilde{u}_1}{\partial \tilde{t}} + \dfrac{\partial \tilde{m}_1 \tilde{u}_1^2}{\partial \tilde{x}} + \dfrac{1}{M_1^2}\dfrac{\partial \tilde{h}_1 \tilde{P}_1}{\partial \tilde{x}} - \dfrac{1}{M_1^2}\left(\tilde{P}_1 - \dfrac{M_1^2}{Fr^2}\tilde{\rho}_1 \dfrac{\tilde{h}_1}{2}\right)\dfrac{\partial \tilde{h}_1}{\partial \tilde{x}} = \dfrac{\mathscr{R}\tilde{\lambda}_u}{k_u}(\tilde{u}_2 - \tilde{u}_1), \\ \dfrac{\partial \tilde{m}_2 \tilde{u}_2}{\partial \tilde{t}} + \dfrac{\partial \tilde{m}_2 \tilde{u}_2^2}{\partial \tilde{x}} + \dfrac{1}{M_2^2}\dfrac{\partial \tilde{h}_2 \tilde{P}_2}{\partial \tilde{x}} - \dfrac{1}{\mathscr{R}M_1^2}\left(\tilde{P}_1 - \dfrac{M_1^2}{Fr^2}\tilde{\rho}_1 \dfrac{\tilde{h}_1}{2}\right)\dfrac{\partial \tilde{h}_2}{\partial \tilde{x}} = \dfrac{\tilde{\lambda}_u}{k_u}(\tilde{u}_1 - \tilde{u}_2). \end{cases} \tag{5.50}$$

5.5.1.c Dimensionless transport equation on water height

Using the characteristic quantities defined so far, the transport equation on water height writes:

$$\frac{\partial \tilde{h}_1}{\partial \tilde{t}} + \tilde{u}_2 \frac{\partial \tilde{h}_1}{\partial \tilde{x}} = \frac{\lambda_p^* T}{H} \tilde{\lambda}_p (\rho_1^* c_1^{*^2} \tilde{P}_1 - \rho_1^* g H \tilde{\rho}_1 \frac{\tilde{h}_1}{2} - \rho_2^* c_2^{*^2} \tilde{P}_2).$$

The pressure relaxation parameter λ_p^* is defined as:

$$\lambda_p^* = \frac{H}{\tau_p \Pi}, \tag{5.51}$$

where τ_p and Π are respectively a characteristic time scale and a characteristic pressure scale. Thus, with $k_p = \tau_p / T$ and $\Pi = P_1^* = \rho_1^* c_1^{*^2}$, one obtains:

$$\frac{\partial \tilde{h}_1}{\partial \tilde{t}} + \tilde{u}_2 \frac{\partial \tilde{h}_1}{\partial \tilde{x}} = \frac{\tilde{\lambda}_p}{k_p} \Big(\tilde{P}_1 - \frac{M_1^2}{Fr^2} \tilde{\rho}_1 \frac{\tilde{h}_1}{2} - \mathscr{R} \frac{M_1^2}{M_2^2} \tilde{P}_2 \Big). \tag{5.52}$$

5.5.1.d Resulting dimensionless model

The proposed dimensionless CTL model is a five-equation system corresponding to the five dimensionless unknowns $(\tilde{h}_1, \tilde{\rho}_1, \tilde{u}_1, \tilde{\rho}_2, \tilde{u}_2)$ which writes:

$$\begin{cases} \dfrac{\partial \tilde{h}_1}{\partial \tilde{t}} + \tilde{u}_2 \dfrac{\partial \tilde{h}_1}{\partial \tilde{x}} = \dfrac{\tilde{\lambda}_p}{k_p} \Big(\tilde{P}_1 - \dfrac{M_1^2}{Fr^2} \tilde{\rho}_1 \dfrac{\tilde{h}_1}{2} - \mathscr{R} \dfrac{M_1^2}{M_2^2} \tilde{P}_2 \Big), \\ \dfrac{\partial \tilde{m}_1}{\partial \tilde{t}} + \dfrac{\partial \tilde{m}_1 \tilde{u}_1}{\partial \tilde{x}} = 0, \\ \dfrac{\partial \tilde{m}_2}{\partial \tilde{t}} + \dfrac{\partial \tilde{m}_2 \tilde{u}_2}{\partial \tilde{x}} = 0, \\ \dfrac{\partial \tilde{m}_1 \tilde{u}_1}{\partial \tilde{t}} + \dfrac{\partial \tilde{m}_1 \tilde{u}_1^2}{\partial \tilde{x}} + \dfrac{1}{M_1^2} \dfrac{\partial \tilde{h}_1 \tilde{P}_1}{\partial \tilde{x}} - \dfrac{1}{M_1^2} \Big(\tilde{P}_1 - \dfrac{M_1^2}{Fr^2} \tilde{\rho}_1 \dfrac{\tilde{h}_1}{2} \Big) \dfrac{\partial \tilde{h}_1}{\partial \tilde{x}} = \dfrac{\mathscr{R} \tilde{\lambda}_u}{k_u} (\tilde{u}_2 - \tilde{u}_1), \\ \dfrac{\partial \tilde{m}_2 \tilde{u}_2}{\partial \tilde{t}} + \dfrac{\partial \tilde{m}_2 \tilde{u}_2^2}{\partial \tilde{x}} + \dfrac{1}{M_2^2} \dfrac{\partial \tilde{h}_2 \tilde{P}_2}{\partial \tilde{x}} - \dfrac{1}{\mathscr{R} M_1^2} \Big(\tilde{P}_1 - \dfrac{M_1^2}{Fr^2} \tilde{\rho}_1 \dfrac{\tilde{h}_1}{2} \Big) \dfrac{\partial \tilde{h}_2}{\partial \tilde{x}} = \dfrac{\tilde{\lambda}_u}{k_u} (\tilde{u}_1 - \tilde{u}_2). \end{cases} \tag{$\tilde{\mathscr{S}}$}$$

Proposition 5.3. *Defining $\tilde{c}_k^2 = \tilde{P}_k'(\tilde{\rho}_k)$, the convective part of ($\tilde{\mathscr{S}}$) is hyperbolic under the non-resonant condition:*

$$|\tilde{u}_1 - \tilde{u}_2| \neq \frac{\tilde{c}_1}{M_1}. \tag{5.53}$$

Its eigenvalues are unconditionally real and given by:

$$\tilde{\lambda}_1 = \tilde{u}_2,\ \tilde{\lambda}_2 = \tilde{u}_1 - \frac{\tilde{c}_1}{M_1},\ \tilde{\lambda}_3 = \tilde{u}_1 + \frac{\tilde{c}_1}{M_1},\ \tilde{\lambda}_4 = \tilde{u}_2 - \frac{\tilde{c}_2}{M_2},\ \tilde{\lambda}_5 = \tilde{u}_2 + \frac{\tilde{c}_2}{M_2}. \tag{5.54}$$

Proof. The calculations are identical as those presented in Chapter 2 for the dimensional model. □

At the discrete level the counterpart of the CFL condition (5.6) in the dimensionless framework writes:

$$\frac{\Delta \tilde{t}}{\Delta \tilde{x}} \max_j \Big(\frac{\tilde{r}_{j+\frac{1}{2}} + \tilde{r}_{j-\frac{1}{2}}}{2} \Big) = \nu, \tag{5.55}$$

where $\Delta \tilde{t}$ and $\nu < 1$ denote respectively the *material* time step and CFL number. In addition, $\tilde{r}_{j+\frac{1}{2}}$ is defined by:

$$\tilde{r}_{j+\frac{1}{2}} = \max_{i \in \{j; j+1\}} \Big(|\tilde{u}_{2,i}^n|, |(\tilde{u}_1 \pm \frac{1}{Fr} \sqrt{\frac{\tilde{h}_1}{2}})_i^n| \Big). \tag{5.56}$$

In the following, the amplification matrix associated to ($\tilde{\mathscr{S}}$) is computed and the stability analysis is performed focusing on the influence of Fr and M_1 on ν.

5.5.2 Amplification matrix

Without detailing the calculations, the same derivation as in Section 5.4.2 is performed on ($\tilde{\mathscr{S}}$). One defines the dimensionless constant state $\tilde{\mathbf{W}}_0 = (\tilde{h}_{1,0}, \tilde{m}_{1,0}, \tilde{m}_{1,0}\tilde{u}_{1,0}, \tilde{m}_{2,0}, \tilde{m}_{2,0}\tilde{u}_{2,0})$ where one sets $\tilde{h}_{k,0} = \frac{1}{2}$ and $\tilde{\rho}_{k,0} = 1$. Thus, for step 1, G_1^+ in (5.27) becomes:

$$\tilde{G}_1^+(k, \nu, \tilde{\mathbf{W}}_0, Fr, M_1, M_2, \mathscr{R}) = \left(1 - 2\nu \sin^2\left(\frac{k\Delta\tilde{x}}{2}\right)\right)\mathrm{Id} - i\frac{\nu}{\tilde{r}_0}\sin(k\Delta\tilde{x})\tilde{J}_0, \tag{5.57}$$

where:

$$\tilde{r}_0 = \max\left(|\tilde{u}_{2,0}|, |\tilde{u}_{1,0} \pm \frac{1}{2Fr}|\right), \tag{5.58}$$

and:

$$\tilde{J}_0 = \begin{pmatrix} \tilde{u}_{2,0} & 0 & 0 & 0 & 0 \\ 0 & 0 & 1 & 0 & 0 \\ \frac{1}{4Fr^2} & -\tilde{u}_{1,0}^2 + \frac{1}{4Fr^2} & 2\tilde{u}_{1,0} & 0 & 0 \\ 0 & 0 & 0 & 0 & 1 \\ 0 & 0 & 0 & -\tilde{u}_{2,0}^2 & 2\tilde{u}_{2,0} \end{pmatrix}. \tag{5.59}$$

G_1^* in (5.33) becomes:

$$\tilde{G}_1^*(k, \nu, \tilde{\mathbf{W}}_0, Fr, M_1, M_2, \mathscr{R}) = \begin{pmatrix} 0 & \frac{1-\frac{M_1^2}{4Fr^2}}{1+\frac{\mathscr{R}}{\gamma}\frac{M_1^2}{M_2^2}} & 0 & \frac{-\frac{R}{\gamma}\frac{M_1^2}{M_2^2}}{1+\frac{\mathscr{R}}{\gamma}\frac{M_1^2}{M_2^2}} & 0 \\ 0 & 1 & 0 & 0 & 0 \\ 0 & 0 & 1 & 0 & 0 \\ 0 & 0 & 0 & 1 & 0 \\ 0 & 0 & 0 & 0 & 1 \end{pmatrix}. \tag{5.60}$$

Regarding step 2, G_2 in (5.40) becomes:

$$\tilde{G}_2(k, \nu, \tilde{\mathbf{W}}_0, Fr, M_1, M_2, \mathscr{R}) = \begin{pmatrix} 1 & 0 & 0 & 0 & 0 \\ 0 & 1 & 0 & 0 & 0 \\ -i\frac{\nu}{\tilde{r}_0}\frac{\mathscr{R}}{\gamma M_2^2}\sin(k\Delta\tilde{x}) & 0 & 1 & -i\frac{\nu}{\tilde{r}_0}\frac{\mathscr{R}}{\gamma M_2^2}\sin(k\Delta\tilde{x}) & 0 \\ 0 & 0 & 0 & 1 & 0 \\ \frac{-i\frac{\nu}{\tilde{r}_0}\frac{1}{\gamma M_2^2}\sin(k\Delta\tilde{x})}{1+4\frac{k_2^2}{M_2^2}\frac{\nu^2}{\tilde{r}_0^2}\sin^2(\frac{k\Delta\tilde{x}}{2})} & 0 & 0 & \frac{4\frac{k_2^2}{M_2^2}\frac{\nu^2}{\tilde{r}_0^2}\tilde{u}_{2,0}\sin^2(\frac{k\Delta\tilde{x}}{2}) - i\frac{\nu}{\tilde{r}_0}\frac{1}{\gamma M_2^2}\sin(k\Delta\tilde{x})}{1+4\frac{k_2^2}{M_2^2}\frac{\nu^2}{\tilde{r}_0^2}\sin^2(\frac{k\Delta\tilde{x}}{2})} & \frac{1}{1+4\frac{k_2^2}{M_2^2}\frac{\nu^2}{\tilde{r}_0^2}\sin^2(\frac{k\Delta\tilde{x}}{2})} \end{pmatrix}. \tag{5.61}$$

Regarding the last step, G_3 in (5.41) becomes:

$$\tilde{G}_3(k, \nu, \tilde{\mathbf{W}}_0, Fr, M_1, M_2, \mathscr{R}) = \begin{pmatrix} 1 & 0 & 0 & 0 & 0 \\ 0 & 1 & 0 & 0 & 0 \\ 0 & 2\frac{\nu}{\tilde{r}_0}\frac{\tilde{u}_{1,0}\tilde{\lambda}_{u,0}}{k_u}\tilde{\Lambda}\frac{\Delta\tilde{x}}{\tilde{\chi}} & (1 + 2\frac{\nu}{\tilde{r}_0}\frac{\tilde{\lambda}_{u,0}}{k_u}\Delta\tilde{x})\frac{1}{\tilde{\chi}} & -2\frac{\nu}{\tilde{r}_0}\frac{\tilde{u}_{2,0}\tilde{\lambda}_{u,0}}{k_u}\tilde{\Lambda}\frac{\Delta\tilde{x}}{\tilde{\chi}} & 2\frac{\nu}{\tilde{r}_0}\frac{\tilde{\lambda}_{u,0}}{k_u}\mathscr{R}\frac{\Delta\tilde{x}}{\tilde{\chi}} \\ 0 & 0 & 0 & 1 & 0 \\ 0 & -2\frac{\nu}{\tilde{r}_0}\frac{\tilde{u}_{1,0}\tilde{\lambda}_{u,0}}{k_u}\tilde{\Lambda}\frac{\Delta\tilde{x}}{\tilde{\chi}} & 2\frac{\nu}{\tilde{r}_0}\frac{\tilde{\lambda}_{u,0}}{k_u}\frac{\Delta\tilde{x}}{\tilde{\chi}} & 2\frac{\nu}{\tilde{r}_0}\frac{\tilde{u}_{2,0}\tilde{\lambda}_{u,0}}{k_u}\tilde{\Lambda}\frac{\Delta\tilde{x}}{\tilde{\chi}} & (1 + 2\frac{\nu}{\tilde{r}_0}\frac{\tilde{\lambda}_{u,0}}{k_u}\mathscr{R}\Delta\tilde{x})\frac{1}{\tilde{\chi}} \end{pmatrix}, \tag{5.62}$$

where $\tilde{\chi} = 1 + 2\frac{\nu}{\tilde{r}_0}\frac{\tilde{\lambda}_{u,0}}{k_u}(\mathscr{R}+1)\Delta\tilde{x}$ and $\tilde{\Lambda} = 1 + 2\frac{\nu}{\tilde{r}_0}\frac{\tilde{\lambda}_{u,0}}{k_u}(\mathscr{R}-1)\Delta\tilde{x}$.

Finally, the amplification matrix $\tilde{G}$ of the dimensionless model is given by:

$$\tilde{G} = \tilde{G}_3\tilde{G}_2\tilde{G}_1^*\tilde{G}_1^+. \tag{5.63}$$

5.5.3 Stability results

In this section, the influence of dimensionless parameters on ν_c^{lin}, the highest CFL number which guarantees $\rho_{\max}(\tilde{G}) \leq 1$, is studied. Accordingly, the four dimensionless parameters $(Fr, M_1, M_2, \mathscr{R})$ have to be specified. In practice, ρ_1^* and ρ_2^* are given such that one deduces $\mathscr{R} = \frac{\rho_2^*}{\rho_1^*}$ and $c_k^* = c_k(\rho_k^*)$. M_2 is then defined from M_1 using the relation:

$$M_2 = \frac{c_1^*}{c_2^*} M_1. \tag{5.64}$$

The Froude number Fr and the Mach number M_1 are linked by the relation:

$$Fr = \frac{c_1^*}{\sqrt{gH}} M_1, \tag{5.65}$$

such that Fr is deduced from M_1 specifying $\frac{M_1}{Fr}$ through the value of H. Note that $\frac{M_1}{Fr}$ corresponds to the ratio between the celerity of gravity waves and the celerity of the fastest acoustic waves. Thus, the chosen degrees of freedom are given by $(H, M_1, \rho_1^*, \rho_2^*)$. More precisely, one considers $\rho_k^* = \rho_{k,\text{ref}}$ which yields $c_k^* = c_{k,\text{ref}}$ and using the numerical values provided in Figure 5.2, one obtains $\mathscr{R} \sim 10^{-3}$ and $\frac{c_1^*}{c_2^*} \sim 4$. Therefore, $\tilde{G}$ is read as $\tilde{G}(k, \nu, \tilde{\mathbf{W}}_0, M_1/Fr, M_1)$ and the influence of $\frac{M_1}{Fr}$ and M_1 on the linear stability is regarded hereafter.

5.5.3.a Influence of M_1 on ν_c^{lin} keeping $\frac{M_1}{Fr}$ frozen

The goal of this section is to study the behavior of ν_c^{lin} as a function of the Mach number M_1 keeping $\frac{M_1}{Fr}$, or equivalently H, frozen. This framework is relevant as $\frac{M_1}{Fr} = \frac{\sqrt{gH}}{c_1^*}$ can be considered constant in practice. Regarding (5.65), note also that the Froude number Fr follows the monotony of M_1. The dimensionless velocity is set to $\tilde{u}_{k,0} = 1$ such that $\tilde{\mathbf{W}}_0$ is completely defined with $\tilde{h}_{k,0} = \frac{1}{2}$ and $\tilde{\rho}_{k,0} = 1$. For numerical applications, one considers $H \in \{0.1, 1, 10\}$, or equivalently (approximately) $\frac{M_1}{Fr} \in \{6.10^{-4}, 2.10^{-3}, 6.10^{-3}\}$. Therefore, for a given Mach number M_1, the highest CFL number ν verifying $\rho_{\max}(\nu, M_1) = \max_{k \in \{1,..,1000\}} \rho(\tilde{G}(k, \nu, M_1)) \leq 1$ is denoted ν_c^{lin}. On Figure 5.16, ν_c^{lin} is displayed in function of M_1 for the given set of pipe heights.

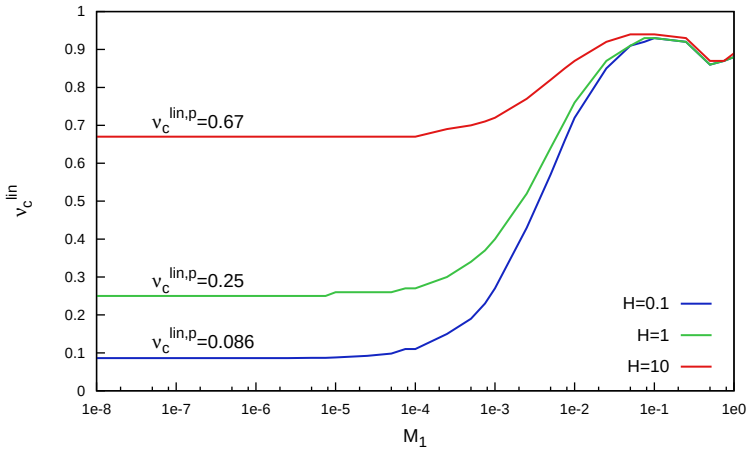

Figure 5.16: ν_c^{lin} as a function of M_1.

One observes that ν_c^{lin} reaches a plateau when $M_1 \to 0$. For a given value of H, the plateau value denoted $\nu_c^{lin,p}$ is very close to the value of ν_c obtained in Section 5.3. Moreover, the dimensional results provided in Section 5.4.3 are consistent with these results as $M_1 < 10^{-5}$ in the three test cases. Therefore, the linear stability analysis gives accurate results. In addition, $\nu_c^{lin,p}$ spans a wide range of Mach numbers, at least for $M_1 \in [10^{-8}; 10^{-5}]$, which makes it only dependent on H (or $\frac{M_1}{Fr}$). The next section aims at clarifying this dependency.

5.5.3.b Influence of $\frac{M_1}{Fr}$ on $\nu_c^{lin,p}$

In order to characterize the plateau value $\nu_c^{lin,p}$ corresponding to $M_1 \to 0$, $\tilde{u}_{k,0}$ is set to zero in this section such that $\nu_c^{lin} = \nu_c^{lin,p}$. Thus, for a given Mach number, one studies $\nu_c^{lin,p}$ in function of $\frac{M_1}{Fr}$, see Figure 5.17. One observes

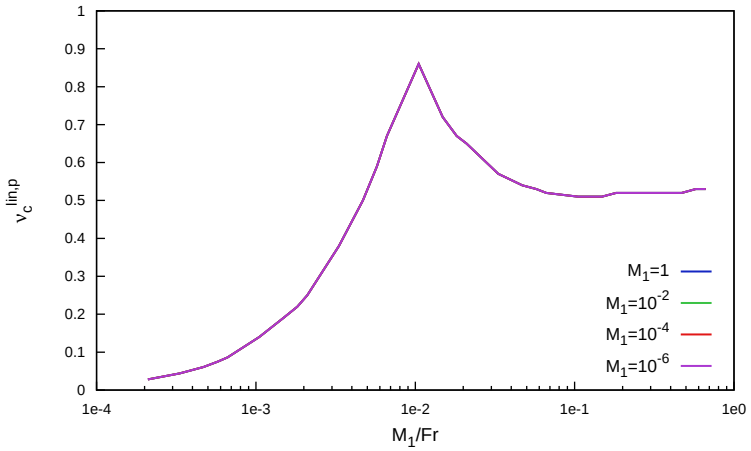

Figure 5.17: $\nu_c^{lin,p}$ in function of $\frac{M_1}{Fr}$.

that the plateau value is indeed only depending on $\frac{M_1}{Fr}$ as the curves are superposed for all Mach number values, $M_1 \in \{10^{-6}, 10^{-4}, 10^{-2}, 1\}$. Furthermore, for $\frac{M_1}{Fr} \leq 10^{-2}$ corresponding to $H \lesssim 20m$, $\nu_c^{lin,p}$ is a monotonically increasing function with an upper limit of 0.86. When $\frac{M_1}{Fr} > 10^{-2}$, the function has a lower limit of approximately 0.5. Thus, focusing on real applications where $0.1\,m \leq H \leq 10\,m$, one obtains $0.086 < \nu_c^{lin,p} < 0.67$.

5.5.3.c Interpretation in terms of acoustic CFL number

Focusing on the lower bound $\nu_c^{lin,p} = 0.086$, one may wonder if the SPR scheme is still advantageous compared to a classical explicit scheme in terms of time step magnitude. Indeed, regarding the eigenvalues detailed in (5.54), a classical explicit scheme applied to ($\tilde{\mathscr{S}}$) leads formally to the CFL condition:

$$\frac{\Delta\tilde{t}_a}{\Delta\tilde{x}} \max\left(|\tilde{u}_2|, |\tilde{u}_1 \pm \frac{\tilde{c}_1}{M_1}|, |\tilde{u}_2 \pm \frac{\tilde{c}_2}{M_2}|\right) = \nu_a, \tag{5.66}$$

where $\Delta\tilde{t}_a$ and $\nu_a < 1$ denote respectively the *acoustic* time step and CFL number. Thus, using (5.55), the corresponding *acoustic* CFL number ν_a for a given *material* CFL number ν in the linearized framework writes:

$$\nu_a = \frac{\max\left(|\tilde{u}_{2,0}|, |\tilde{u}_{1,0} \pm \frac{\tilde{c}_{1,0}}{M_1}|, |\tilde{u}_{2,0} \pm \frac{\tilde{c}_{2,0}}{M_2}|\right)}{\max\left(|\tilde{u}_{2,0}|, |\left(\tilde{u}_{1,0} \pm \frac{1}{Fr}\sqrt{\frac{\tilde{h}_{1,0}}{2}}\right)|\right)} \nu,$$

where one expects $\nu_a \gg 1$ for a so-called large time-step scheme. With $\tilde{u}_{k,0} = 1$, $\tilde{c}_{k,0} = 1$ and $\tilde{h}_{1,0} = \frac{1}{2}$, one obtains:

$$\nu_a = \frac{M_1 + 1}{M_1 + \frac{M_1}{2Fr}} \nu. \tag{5.67}$$

Considering practical applications where $\frac{M_1}{Fr} \leq 10^{-2}$ ($H \lesssim 20m$), $U \leq 10m.s^{-1}$ ($M_1 \leq 6.10^{-3}$), (5.67) writes:

$$\nu_a \geq 10^2 \nu. \tag{5.68}$$

For the lower bound $\nu_c^{lin,p} = 0.086$, one obtains $\nu_a \geq 8.6$ which makes the SPR scheme computationally interesting regarding low speed flows.

5.6 Conclusion

In the present chapter, a linear stability analysis is performed on the SPR scheme developed in Chapter 4 for the Compressible Two-Layer model proposed in Chapter 2. Focusing on a dambreak problem, the analysis highlights the need for an extra CFL condition ensuring the stability of scheme. Despite the linear framework, the results matches remarkably well with numerical experiments performed on the non-linear system. In particular, a critical threshold on the CFL number is experimentally identified. The latter only depends on the ratio between the speed of slow gravity waves, involved in the explicit part of the scheme, and the speed of fast acoustic waves, involved in the implicit part of the scheme.

Thus, the proposed linear analysis confirms that in the context of implicit-explicit schemes, the CFL condition applied on the explicit part of the scheme may not be sufficient to ensure the stability of the overall scheme. Indeed, as underlined in [12, 13], some coupling between both parts of the scheme may influence the stability of the resulting method. Dealing with the compressible Euler model, the authors warn peculiarly about the non-uniform stability of some splittings when the Mach number tends to zero. In the framework of linearized flux-vector splitting schemes, this negative coupling does not occur when the matrices associated to each part of the scheme commute. In our case, the additional constraint on the CFL number cannot be given analytically due to the complexity of the model. However, focusing on practical applications, the stability results for the dimensionless model show that the computational gain is still significant using the SPR scheme as the corresponding *acoustic* CFL number may be set greatly above 1. Even if the extension of those results to the nonlinear system is not straightforward, guidelines are proposed and should be kept in mind when considering other test cases such as mixed flows and entrapped air pockets.

References

[1] F. Bouchut. *Nonlinear stability of finite volume methods for hyperbolic conservation laws, and well-balanced schemes for sources*. Birkhauser, 2004.

[2] C. Chalons, M. Girardin, and S. Kokh. Large time-step and asymptotic preserving numerical schemes for the gas dynamics equations with source terms. *SIAM Journal on Scientific Computing*, 35(6):a2874–a2902, 2013.

[3] J.-G. Charney, R. Fjörtoft, and J. Von Neumann. Numerical integration of the barotropic vorticity equation. *Tellus*, 2:237–254, 1950.

[4] J. Crank and P. Nicolson. A practical method for numerical evaluation of solutions of partial differential equations of the heat-conduction type. *Mathematical Proceedings of the Cambridge Philosophical Society*, 43:50–67, 1947.

[5] P. Degond and M. Tang. All speed scheme for the low Mach number limit of the isentropic Euler equation. *Communications in Computational Physics*, 10:1–31, 2011.

[6] G. Dimarco, R. Loubère, and M.-H. Vignal. Study of a new asymptotic preserving scheme for the Euler system in the low Mach number limit. *Preprint*, 2016.

[7] J. Haack, S. Jin, and J.G. Liu. An all-speed asymptotic preserving method for the isentropic Euler and navier-stokes equations. *Communications in Computational Physics*, 12:955–980, 2012.

[8] D. Iampietro, F. Daude, P. Galon, and J.-M. Hérard. A weighted splitting approach adapted to low Mach number flows. *Springer Proceedings in Mathematics and Statistics*, 200:3–11, 2017.

[9] K. Kaiser, J. Schütz, R. Schöbel, and S. Noelle. A new stable splitting for the isentropic euler equations. *SIAM Journal on Scientific Computing*, 70:1390–1407, 2017.

[10] F. Kittaneh. Spectral radius inequalities for hilbert space operators. *Proceedings of the American Mathematical Society*, 134(2):385–390, 2005.

[11] S. Noelle, G. Bispen, K. Arun, M. Lukacova-Medvidova, and C.D. Munz. A weakly asymptotic preserving all Mach number scheme for the Euler equations of gas dynamics. *SIAM Journal on Scientific Computing*, 36:B989–B1024, 2014.

[12] J. Schütz and S. Noelle. Flux splitting for stiff equations: A notion on stability. *SIAM Journal on Scientific Computing*, 64:522–540, 2015.

[13] H. Zakerzadeh and S. Noelle. A note on the stability of implicit-explicit flux splittings for stiff hyperbolic systems. *IGPM report 449*, 2016.

Chapter 6

Simulations of mixed flows and entrapped air pockets in pipes with a compressible two-layer model

Abstract: Focusing on mixed flows, this chapter is dedicated to the validation of the Compressible Two-Layer model presented in Chapter 2 using the numerical scheme proposed in Chapter 4 (SPR scheme). Three test cases involving the specific features of mixed flows are studied. The first one is an elementary test case which involves a transition from the stratified to the pressurized regime without significant air influence. A mesh sensitivity analysis is led and the results are compared with those obtained with a reference single-phase mixed flow model (the PFS model [5]) and with some analytical results provided by a simplified approach. The second one is an experimental test case proposed recently in the literature [2] for the validation of single-phase mixed flow models. It is closer to industrial applications involving a circular pipe with slope changes and several regime transitions. The last test case is an oscillating manometer which involves air pocket entrapment. In particular, a reference solution is developed and the influence of air pressurization on the flow dynamics is emphasized. This bench of test cases highlights the ability of the Compressible Two-Layer model to provide a relevant two-phase description of mixed flows. Furthermore, the associated numerical method is particularly robust and the CPU cost is very reasonable. These features demonstrate that the Compressible Two-Layer model associated with the SPR scheme results in an original contribution to the two-phase modelling of mixed flows and entrapped air pockets in pipes.

Note: A paper in preparation is made up of the numerical results exposed in this chapter in addition to the numerical method developed in Chapter 4.

Contents

Three test cases involving mixed flows are considered in this chapter. They are simulated with the Compressible Two-Layer model (CTL model) presented in Chapter 2 using the numerical scheme proposed in Chapter 4 (SPR scheme). An elementary pipe filling is first studied in Section 6.1 before moving to more complex configurations including experimental validation in Section 6.2 and air pocket entrapment in Section 6.3.

6.1 Elementary mixed flow: a pipe filling

The so-called pipe filling test case is an elementary test case which involves transitions between stratified and pressurized regimes. It is simple to implement and allows to assess the ability of the SPR scheme to handle flow regime transitions and vanishing phases. As presented below, the presence of air has little influence in the proposed configuration.

6.1.1 Global setting and objectives

In the following, a sloping pipe is considered where the initial condition is a static condition with uniform water height, uniform density and zero speed, see Figure 6.1. A realistic rectangular pipe is chosen whose height H is $0.2\,m$, length is $2\,m$, and θ, its angle from the horizontal, is -30^o. In this framework, the CTL model is defined in the inclined frame. Thus, gravity source terms are added, see Appendix 6.A.1 for details. The total simulation time is set to $T = 2\,s$ with wall boundary conditions at the inlet and outlet, see Appendix 4.A.

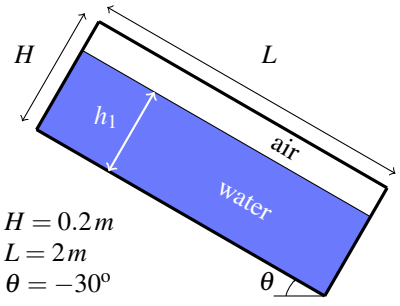

Variable	$0 \leq x \leq 2\,m$
h_1/H	0.8
ρ_1	$998.1115\,kg.m^{-3}$
u_1	$0\,m.s^{-1}$
ρ_2	$1.204\,kg.m^{-3}$
u_2	$0\,m.s^{-1}$

Figure 6.1: Initial conditions for the pipe filling test case.

As this test case includes regime transitions, the adaptive stabilization process exposed in Section 4.3.4.c of Chapter 4 is assessed hereafter. To say it briefly, stabilization terms for the water phase are activated when $h_1 \geq h_s$, where

$h_s = (1-\delta)H$ and $\delta = 10^{-3}$. The time step is computed using (4.40) for a given *material* CFL number denoted $\mathrm{CFL_m}$. The latter is set to 0.01 to get accuracy with fair efficiency as observed in the previous test cases, see also Remarks 4.8 and 4.9. In order to check the stability and the convergence of the method, a mesh refinement is performed considering regular meshes from 160 cells to 10240 cells, which corresponds to a space step range from $\Delta x \sim 1\,cm$ to $\Delta x \sim 0.02\,cm$.

The results obtained with the SPR scheme associated with the CTL model are compared with those obtained with the *Pressurized Free Surface* (PFS) model developed in [5]. This other model is also dedicated to mixed flows in pipes but only computes the water phase neglecting the presence of air. It is a one-layer model which couples the shallow-water equations in the free-surface regime with the isentropic Euler set of equations in the pressurized regime. At the discrete level, a Roe-type scheme is proposed in [5] and a kinetic scheme has also been recently derived in [4]. Both schemes are explicit in time with a CFL condition depending on the celerity of fast acoustic waves arising in the pressurized regime. The comparison between the two models is relevant as the PFS model is validated against several experimental data. Furthermore, the presence of air should have minor influence in the proposed configuration.

6.1.2 Results and comments

Results with the CTL model

The evolution of the water height is depicted on Figure 6.2 through some snapshots along the simulation. The pipe is actually filling with a pressurized water front propagating towards the top of the pipe. When the front stops, one obtains a dry area ($h_1 \simeq 0$) and a pressurized area ($h_1 \simeq H$) separated by an oscillating free surface in the absence of wall friction effects.

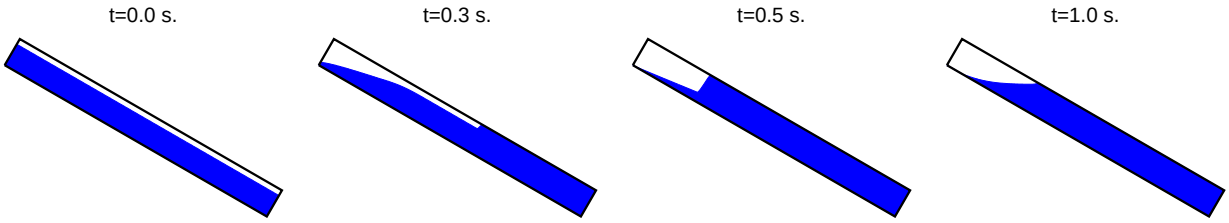

Figure 6.2: Snapshots of water height with 640 cells.

The fields at $t = 0.3\,s$ are detailed on Figure 6.3 with a mesh sensitivity analysis. A mixed flow is obtained with a jump between the stratified and the pressurized part. The water height h_1, as well as the flow rate $h_k u_k$, $k = 1,2$, display a fast mesh convergence. However, the convergence appears more difficult to reach for the water pressure. Indeed, although they vanish when the mesh is refined, spurious oscillations are observed at the transition point where the pressure jumps as well as in the pressurized part. This numerical behavior is associated to the brutal transition in terms of wave speed between the stratified and the pressurized part, expressed by the ratio $\frac{\sqrt{gH}}{c_1} \sim 10^{-4} \ll 1$ in the present case. It is a common feature when dealing numerically with mixed flow, see [22] for a related study. Note that the PFS model does not yield either converged pressure fields.

The air height is depicted in log scale on Figure 6.4 at $t = 0.3\,s$. The robustness of the SPR scheme regarding vanishing phases is thus illustrated as $\frac{h_2}{H}$ may reach 10^{-9} in the pressurized part for the finest mesh. A very thin air layer is then solved but dissipative effects provided by the relaxation source terms bring stability. Note that the thickness of this air layer is independent of the threshold value h_s as it tends to zero when the mesh is refined while the threshold is kept constant.

Focusing on the water pressure behavior, the associated pressure jump at the interface between both regimes may be estimated using (6.B.12), see Appendix 6.B for details. Thus, (6.B.12) yields $\Delta P_1 \sim 0.080\,\mathrm{bar}$ while one measures $\Delta P_1 \sim 0.081\,\mathrm{bar}$ on the finest mesh, see Figure 6.3. One may also predict the slope in the pressurized part. Indeed, as the flow is static with uniform height, i.e. $u_k = 0$ and $h_1 = H$, the conservation equation for the water phase, see (6.A.2), yields the equilibrium between the pressure gradient and gravity terms:

$$\partial_x P_1 = -\rho_1 g \sin(\theta).$$

Despite the spurious oscillations, the expected slope is obtained in the transient regime, as observed on Figure 6.3 for the pressure field. Furthermore, summing the momentum conservation equations for both phases, the gradient of the total mean pressure, defined as $P_{\mathrm{tot}} = \frac{1}{h_1+h_2}(h_1P_1 + h_2P_2)$, also verifies an equilibrium with gravity terms for static

flows:

$$\partial_x P_{\text{tot}} = -\frac{m_1+m_2}{h_1+h_2} g \sin(\theta).$$

In particular, at $t = 2\,s$ when the pipe is filled and the free surface slightly oscillates, this equilibrium is verified, see Figure 6.5. In this configuration, there are no more oscillations in the pressurized part. Spurious oscillations are still observed at the transition point for coarser meshes but they disappear when the mesh is refined. Note that this total pressure is the sole meaningful pressure when one phase vanishes.

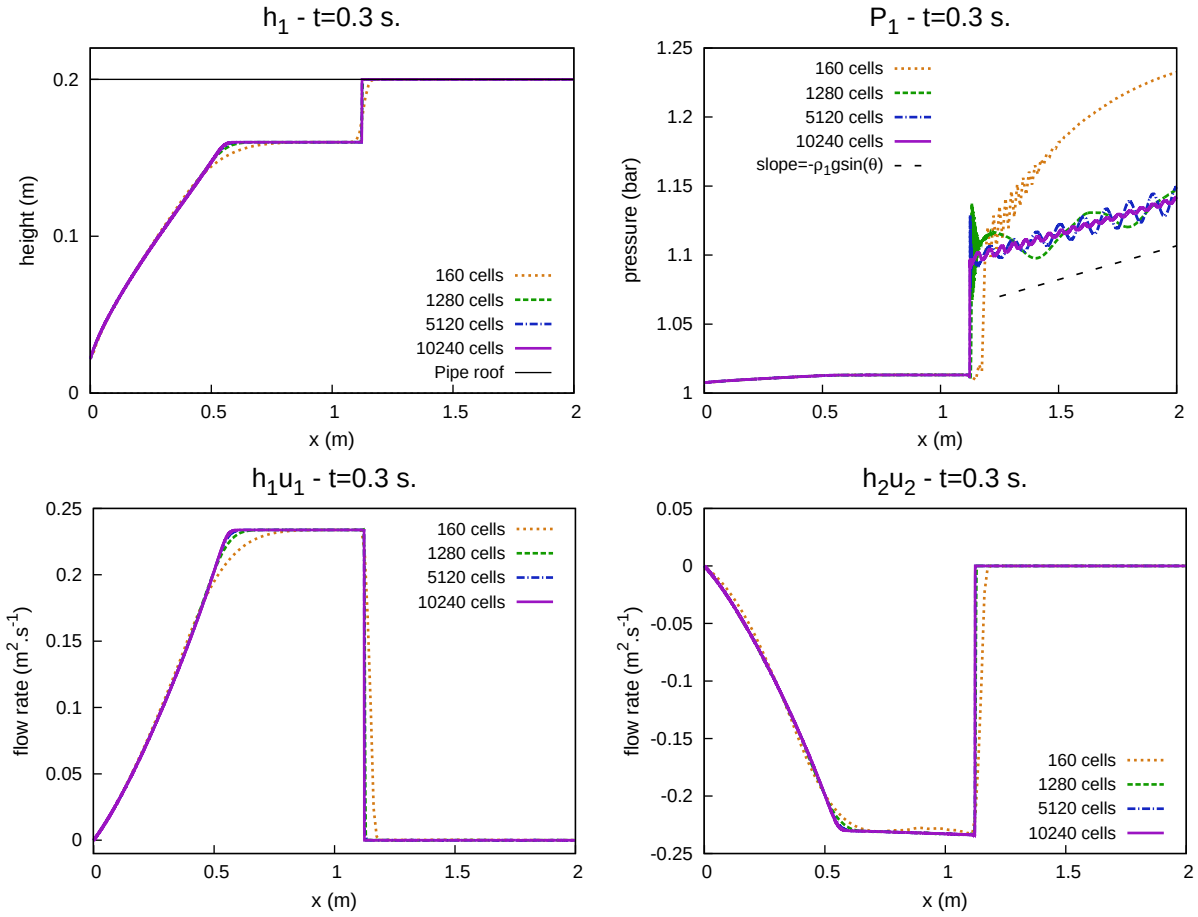

Figure 6.3: Approximate solutions for the pipe filling test case at $t = 0.3\,s$.

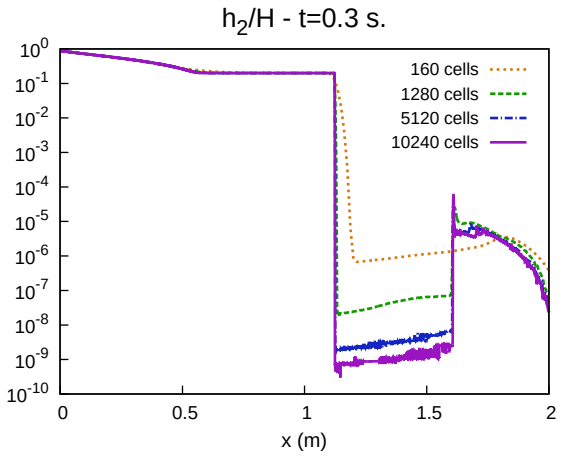

Figure 6.4: Air height in log scale at $t = 0.3\,s$.

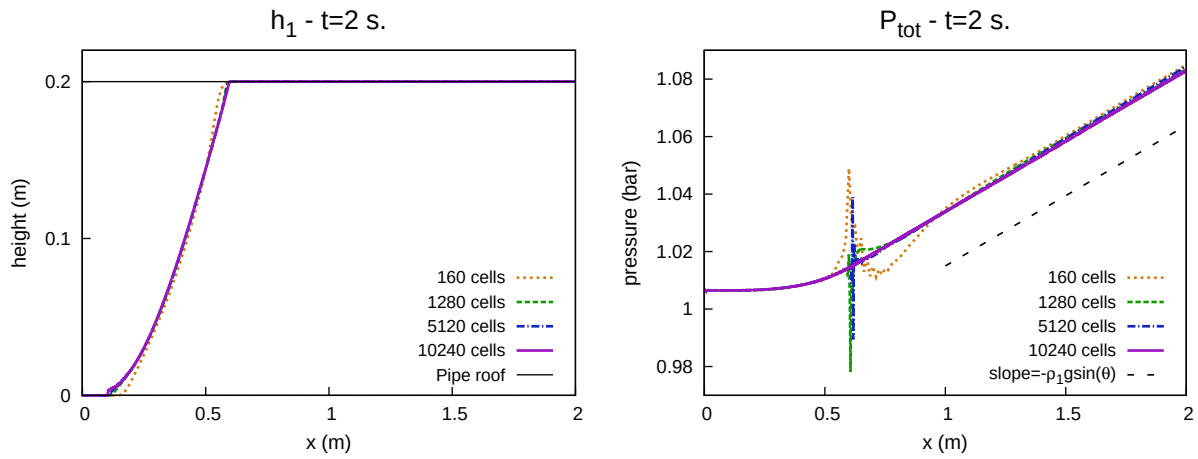

Figure 6.5: h_1 and $P_{\text{tot}} = \frac{1}{H}(h_1 P_1 + h_2 P_2)$ at $t = 2\,s$.

The pressure signal is analyzed more precisely through the water pressure time series at $x = 1\,m$ plotted on Figure 6.6. Oscillations are also observed in time. They are attenuated with the mesh refinement and as expected, a jump is observed when the front is coming. The time signal in charge is clarified hereafter using a lower acoustic wave celerity in the water phase.

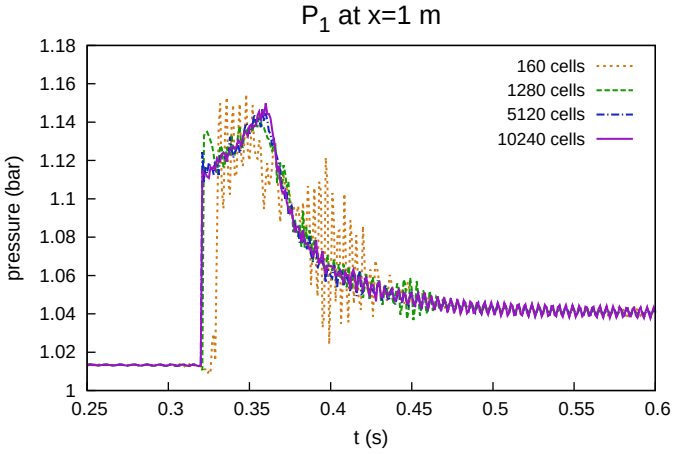

Figure 6.6: Pressure probe for water phase at $x = 1\,m$.

Lower acoustic waves celerity in the water phase

A classical and widely used trick to smoothen the transition between the stratified and the pressurized regime is to decrease the celerity of acoustic waves in the water phase, i.e. decrease $c_{1,\text{ref}}$ in the pressure law (4.2a). This strategy can be physically justified as the reference celerity, that is $c_{1,\text{ref}} = 1500 m.s^{-1}$, corresponds to a pure water phase in a rigid pipe. In practice, dealing with air-water flows, the mixing between the phases in addition to pipe elasticity effects may strongly reduce the celerity of acoustic waves in the water phase, see respectively [9] and [16] for example. Thus, $c_{1,\text{ref}}$ is set to $200 m.s^{-1}$ hereafter. As an illustration, this order of magnitude is experimentally measured in [6] for a PVC pipe whose diameter is $0.16 m$. The water pressure at $t = 0.3\,s$ as well as its time evolution at $x = 1\,m$ are presented on Figure 6.7.

It is observed that the mesh convergence of the pressure field at $t = 0.3\,s$ is quite fast, canceling the spurious oscillations when the mesh is refined. The expected slope in charge is again well approximated. Regarding the pressure time series, the signal is also clarified. In particular, well structured oscillations are observed for $t \gtrsim 0.4\,s$ The period may be estimated considering the propagation of acoustic waves in the water medium, see Appendix 6.C. It yields $T = \frac{4L_w}{c_1}$ where L_w is the length filled by the water phase. With $L_w = 1.6 m$ in the present case, it results in an expected period $T = 0.032\,s$, while numerical approximations yield $T \sim 0.03\,s$ on Figure 6.7. Regarding the amplitude, it seems to result from a combination between hydrostatic effects due to free surface oscillations and acoustic effects due to acoustic waves propagation. Note that when using $c_{1,\text{ref}} = 1500 m.s^{-1}$, the correct period is also captured but

with a weaker amplitude so that is does not clearly appear on Figure 6.6. The other fields, which concern heights and velocities, are not affected by this celerity change, nor the pressure jump in the present case. Finally, physically relevant and converged results are obtained using $c_{1,\text{ref}} = 200 m.s^{-1}$. They are compared hereafter with those obtained with the PFS model.

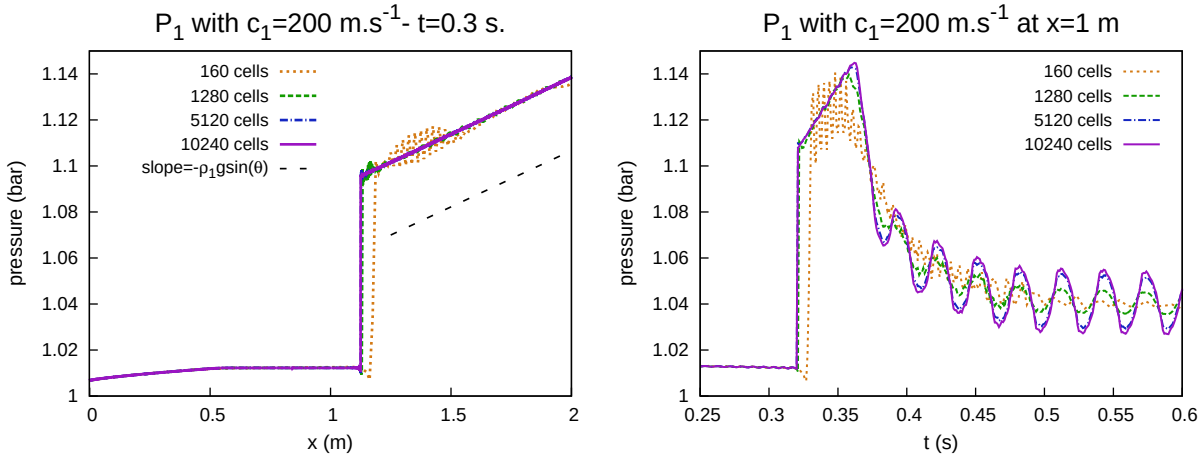

Figure 6.7: Water pressure with $c_1 = 200 m.s^{-1}$.

Comparison with the PFS model

As revealed on Figure 6.8, the CTL and the PFS models yield very close results on the same mesh (5120 cells) using $c_{1,\text{ref}} = 200 m.s^{-1}$. This confirms that the air phase has not real influence here. Furthermore, it also emphasizes the fact that the thin air layer computed with the CTL model in the pressurized part, see Figure 6.4, does not affect the pressurized dynamics. Regarding the pressure fields, the PFS model yields spurious oscillations at the transition point while the CTL model does not. It seems that the unified description of the CTL model in addition to its dissipative relaxation source terms brings more stability. Thus, in some sense, the additional air layer is beneficial.

Regarding the CPU times, it needs 20 minutes to compute the solution over 2 seconds on a 640 cells mesh with the CTL model. This computation time is independent of the celerity c_1 as the latter is not involved in the CFL condition (4.24). Using the explicit scheme developed in [4] for the PFS model, the CFL condition actually depends on c_1. A reduction of c_1 is therefore profitable for the PFS model in terms of CPU time. Thus, it requires 13 minutes when $c_1 = 1500 m.s^{-1}$ and 2 minutes when $c_1 = 200 m.s^{-1}$. The CTL model is naturally more computationally demanding as it involves a larger system with implicit parts. However, the CPU time is not prohibitive compared to the PFS model statistics. Furthermore, higher acoustic waves celerity can be chosen with more stability.

Remark 6.1 (Time steps when dealing with mixed flows)**.** *The CFL condition* (4.24) *of the SPR scheme recalled below:*

$$\frac{\Delta t}{\Delta x} \max_i \left(\frac{r_{i+\frac{1}{2}} + r_{i-\frac{1}{2}}}{2} \right) \leq 1,$$

with $r_{i+\frac{1}{2}} = \max_{j \in \{i;i+1\}} \left(|u^n_{2,j}|; \left| \left(u_1 \pm \sqrt{g \tfrac{h_1}{2}} \right)^n_j \right| \right)$*, involves the speed of both phases. When dealing with mixed flows, pressure jumps may occur between the stratified and the pressurized regime as observed with the pipe filling test case. In particular, a jump on* P_1 *induces a jump* P_2 *due to the pressure relaxation, see 4.2.2.a. Consequently, this jump on* P_2 *induces a jump on* u_2 *which may be strong due to the high compressibility of the air phase. The time step may be then governed by this local over-speed on the air phase whereas the latter should not exist in the pressurized part. This is an intrinsic feature of the CTL model which may lead to small time steps. In addition, small CFL numbers have to be chosen to guarantee the stability of the interface. Nonetheless, note that comparable CPU times with the PFS model have been obtained using* $c_1 = 1500 m.s^{-1}$.

Lastly, the ability of the CTL model to handle mixed flows is highlighted with this test case. Indeed, one obtains physically relevant results in agreement with the PFS results and analytical results provided by a simplified approach. The CPU time is comparable with the one of the PFS and seems totally tractable for practical applications of industrial interest. Transitions between the regimes are correctly handled with the SPR scheme where dissipative effects ensured by relaxation source terms bring stability. In the next section, a more severe mixed flow test case is considered and the results are compared against experimental data.

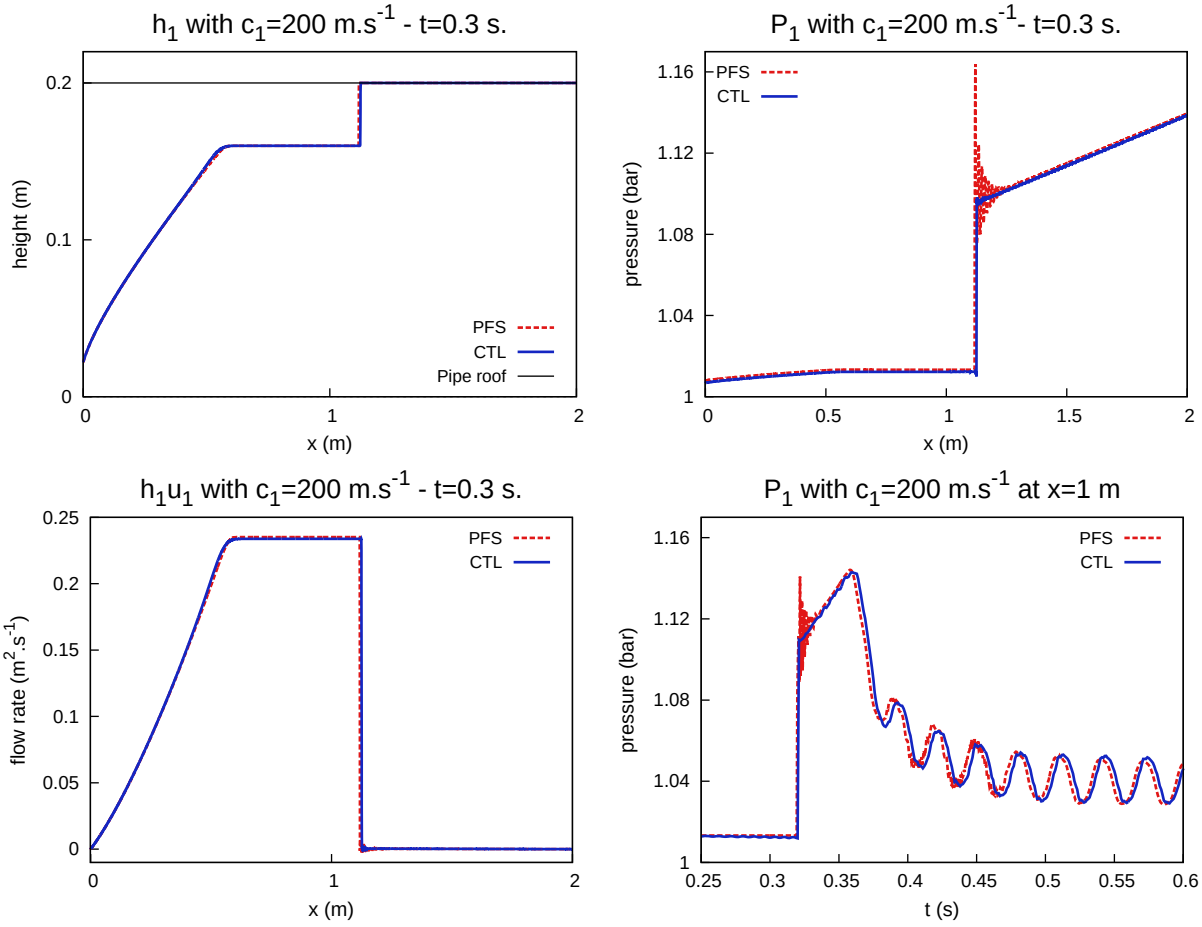

Figure 6.8: Comparison with the PFS model using $c_1 = 200 m.s^{-1}$, 5120 cells.

6.2 Mixed flow with experimental validation: a laboratory test case (Aureli *et al.* (2015))

In this section, a recent experimental test case dedicated to the validation of *single-phase* mixed flow models is considered, see [2]. The latter is closer to industrial applications as it involves a circular pipe with slope changes and several regime transitions. It can effectively be seen as a *single-phase* mixed flow due to the presence of vents at the upstream and downstream end of the pipe to avoid air pocket entrapment.

6.2.1 Global setting and objectives

The experimental configuration is depicted on Figure 6.9. It consists in a sloped PVC circular pipe of diameter $H = 0.192 m$ and length $L = 12.12 m$. A slope change occurs at $L_1 = 7 m$, switching from $\theta_1 = -4.8^o$ to $\theta_2 = 15.48^o$. The pipe is opened at the inlet and outlet to avoid air pocket entrapment effects. Thus, atmospheric pressure is maintained at the two ends. The pipe is initially partially filled by water until a closed gate located at $x = 5 m$ (x is the distance along the pipe axis). The experiment begins when the gate opens. It gives rise to a transient mixed flow with several transitions in both parts of the pipe. Pressure and velocity measurements are performed along the pipe during 30 seconds.

The pressure gauges are located at six points: G1 ($x = 1 m$), G2 ($x = 3 m$), G3 ($x = 4.5 m$), G4 ($x = 6.80 m$), G5 ($x = 7.32 m$) and G6 ($x = 8.52 m$). The velocity gauges are located just before the pressure gauges on the following points: V1 ($x = 0.94, m$), V2 ($x = 2.94 m$), V3 ($x = 4.44 m$), V4 ($x = 6.74 m$), V5 ($x = 7.26 m$) and V6 ($x = 8.46 m$). All the experimental data are provided with the related article [2] under data files. Numerical results are also presented in the latter using a simpler discretization of the PFS model than the one detailed in [5], and a Preissmann slot model [8]. Comments on these results results are provided hereafter.

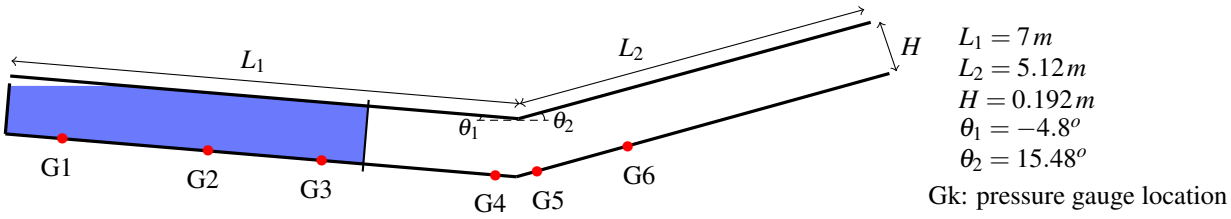

Figure 6.9: Configuration and initial condition and for the Aureli *et al.* test case.

Dealing with circular pipes, the CTL model is slightly modified due to the 2D integration on a cross-section, see Appendix 6.A.2 for details. Furthermore, friction effects occur between the pipe walls and the water phase. They are modeled by a Manning-Strickler law, see (6.A.5). In particular, the Manning roughness coefficient is set to $n_m = 5.0\,m^{-\frac{1}{3}}s$ hereafter. The celerity of acoustic waves in the water phase is initially set to $c_{1,\text{ref}} = 300\,m.s^{-1}$ in the linear pressure law (4.2a). The latter is physically relevant for the considered PVC pipe and makes the numerical convergence faster, see Section 6.1. Results with $c_{1,\text{ref}} = 1500\,m.s^{-1}$ are also displayed.

Regarding the boundary conditions, the air phase should be in equilibrium with the atmospheric pressure at the two ends. In practice, a vertical event is added at the left end of the pipe and periodic boundary conditions are imposed, see Appendix 4.A. This vertical event is only filled by air and acts as a wall for the water phase. The air phase is then maintained in equilibrium at both ends of the pipe and its initial value is given by the atmospheric pressure. For the other initial conditions, the water height is set to $h_1 = (1-10^{-4})H$ in the pressurized part and $h_1 = 10^{-5}H$ in the dry part, the water density is set to $\rho_{1,\text{ref}}$ neglecting hydrostatic effects and the flow is static. Focusing on the SPR scheme, the same setting as for the pipe filling test case of Section 6.1 is used. In particular, the threshold is set to $h_s = (1-\delta)H$ with $\delta = 10^{-3}$ and the (material) CFL number is set to 0.01. The same mesh size as in [2] is initially used, that is 300 cells which yields $\Delta x \sim 4\,cm$. Results with 1000 cells are also displayed.

6.2.2 Results and comments

The evolution of water height is depicted on Figure 6.10 through some snapshots along the simulation. A water front is propagating towards the upward part of the pipe where a first transition to a pressurized regime occurs. A mixed flow is thus generated which oscillates between both part of the pipe with transitions from stratified to pressurized flow and vice versa. Note also that this test case involves dry areas.

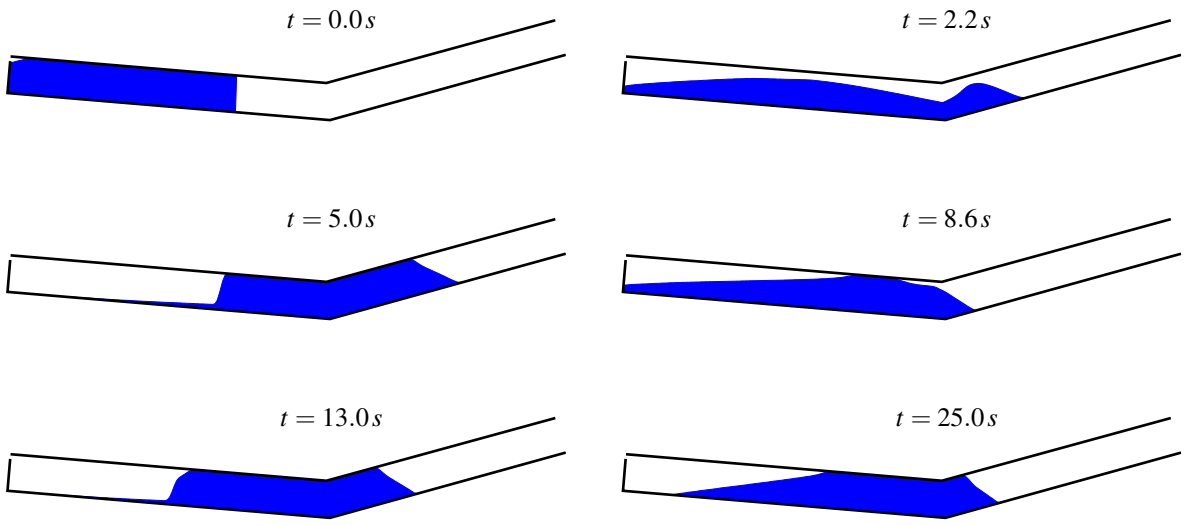

Figure 6.10: Snapshots of water height with 300 cells for the experimental test case.

The pressure head time series are displayed on Figure 6.11. In the related paper [2], the pressure head is derived from pressure measurements assuming an hydrostatic pressure distribution over the pipe section. In the CTL

framework, the latter is denoted $\mathscr{H}$ and defined as:

$$\mathscr{H} = h_1 + \frac{P_1 - P_{hydro}}{\rho_{1,\text{ref}} g}, \tag{6.1}$$

where P_{hydro} corresponds to the supposed mean hydrostatic pressure on a cross section. It writes $P_{hydro} = P_{atm} + \rho_{1,\text{ref}} g \ell_1 \cos(\theta)$ for circular pipes where P_{atm} is the air pressure at the outlet (or inlet) and ℓ_1 is the distance between the free surface and the center of mass of the wet section, see (6.A.4). In the stratified regime, $\rho_1 \sim \rho_{1,\text{ref}}$ and $P_2 \sim P_{\text{atm}}$, such that $P_1 - P_{hydro}$ may be rewritten as $P_I - P_2 \sim 0$ due to pressure relaxation. Therefore, $\mathscr{H} \sim h_1$ in the stratified regime. In the pressurized regime, $\mathscr{H}$ computes the equivalent height corresponding to an overpressure or subpressure in comparison to the hydrostatic reference. As displayed on Figure 6.11, the CTL model is able to reproduce faithfully the experimental observations on pressure head time series. Indeed, the pressure heads in both stratified and pressurized regimes are correctly captured. Transitions between the regimes are also particularly well apprehended, see gauges G4 and G5 for instance.

The water velocity time series are displayed on Figure 6.12. Even if the authors in [2] temper about the quality of velocity measurements, the obtained numerical results also highlight the good behavior of the CTL model. Some velocity peaks may be overestimated, in particular on gauges V2 and V6, but the results are globally very satisfactory.

It is recalled that the above results are obtained on a coarse mesh ($\Delta x = 4\,cm$) with a physically relevant acoustic wave celerity in the water phase ($c_{1,\text{ref}} = 300\,m.s^{-1}$). The required CPU time to perform a 30 seconds simulation is 25 minutes, which seems reasonable regarding the fidelity of the results and the complexity of the model. Indeed, the air phase dynamics is also calculated but seems to have a weak influence on the results, as expected for this configuration.

Focusing on gauges G5 and V5 where transitions occur, both influences of the mesh size and the acoustic wave celerity in the water phase are assessed on Figure 6.13. In particular, pressure heads and water velocity profiles are compared using $c_{1,\text{ref}} = 300\,m.s^{-1}$ and $c_{1,\text{ref}} = 1500\,m.s^{-1}$ on a 300 cells ($\Delta x \sim 4\,cm$) and 1000 cells ($\Delta x \sim 1\,cm$) mesh. All the obtained results are very close and in good agreement with experimental measurements. As already observed with the pipe filling test case in Section 6.1, the highest acoustic wave celerity associated to the coarser mesh displays some spurious oscillations on the pressure head. However, the global trends are well captured and the spurious oscillations are strongly attenuated on the finest mesh for both values of acoustic waves celerity. Finally, these results confirm the stability of the SPR scheme when using high acoustic wave celerity values.

Comparable numerical results are obtained in [2] when using *single-phase* mixed flow models, i.e. the PFS model [5] and the Preissmann slot model [8]. However, the authors illustrate the lack of robustness of the latter models when using a physically relevant acoustic waves celerity. Indeed, the latter is set to $c_{1,\text{ref}} = 12\,m.s^{-1}$ in [2] to get satisfactory results whereas $c_{1,\text{ref}} = 200\,m.s^{-1}$ leads to strong spurious oscillations, in particular with the Preissmann slot model. This drawback is tempered in the related paper as only a weak influence of this celerity value is identified. Nonetheless, when dealing with longer pipes encountered in industrial configurations, typically $L \sim 100\,m$, such a low value of $c_{1,\text{ref}}$ may provide non physical results.

The results obtained for this experimental test case validate the CTL model in the configuration of mixed flow where the air phase has a weak influence. Indeed, pressure heads and velocity time series are correctly captured at several locations along the pipe where transitions from stratified to pressurized regimes and vice versa occur. Furthermore, the stability and the efficiency of the SPR scheme are also highlighted as a high acoustic wave celerity in the water phase may be chosen with non prohibitive CPU time. The next step is to consider mixed flow configurations featuring a strong influence of the air phase. To this end, a so-called U-tube test case involving air pocket entrapment is detailed in the next section.

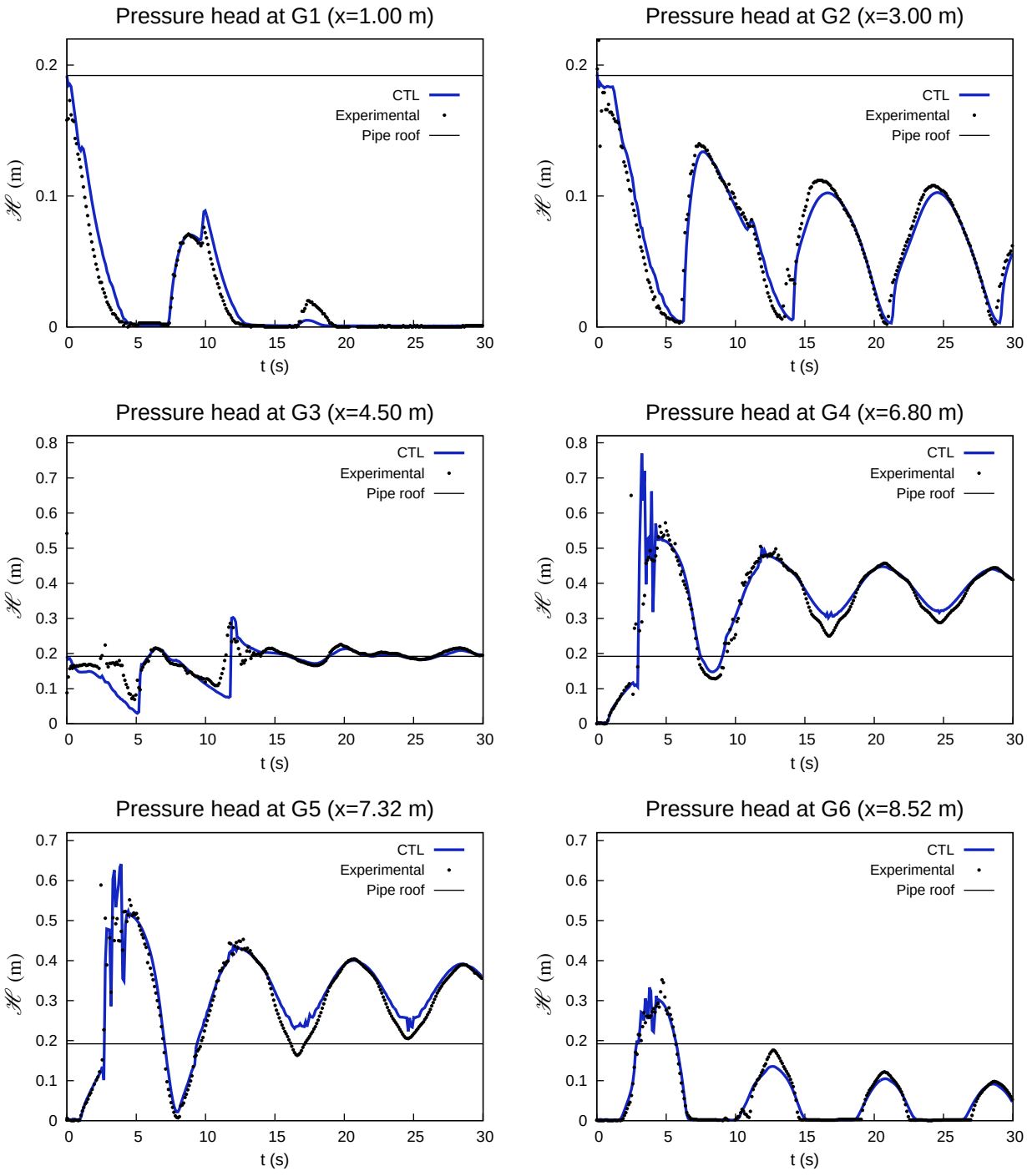

Figure 6.11: Comparison between experimental and numerical pressure head time series using 300 cells.

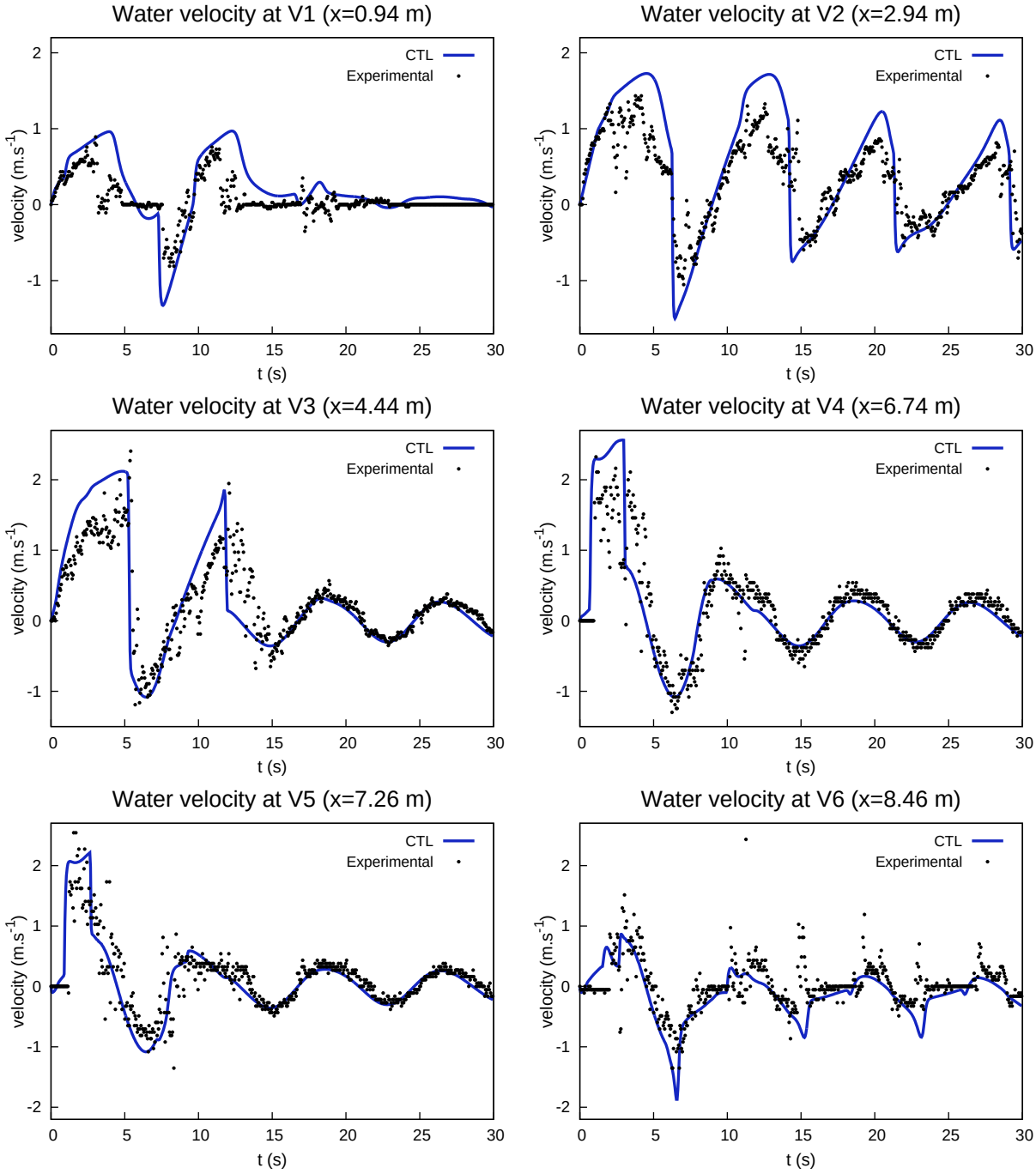

Figure 6.12: Comparison between experimental and numerical water velocity time series using 300 cells.

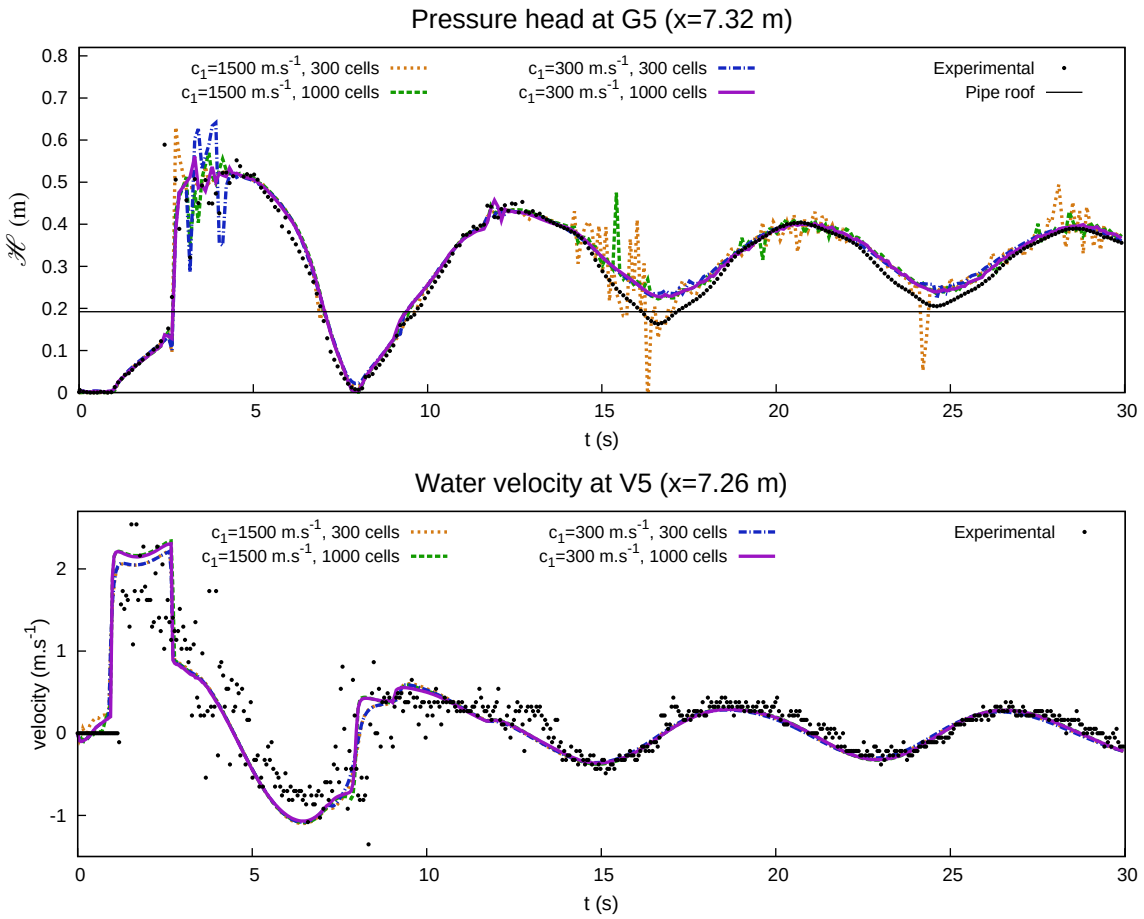

Figure 6.13: Mesh and water acoustic wave celerity sensitivity.

Remark 6.2 (Influence of air pocket entrapment)**.** *The proposed pipe configuration in [2] is endowed with open boundary conditions in order to avoid air pocket entrapment and air pressurization. The influence of air pocket entrapment on this test case has been nevertheless highlighted with the CTL model when setting wall boundary conditions instead of periodic boundary conditions, see Figure 6.14. Even if the air phase is initialized at atmospheric pressure, strong disparities are observed between both configurations. Indeed, it appears that the air phase entrapment prevents the water phase from oscillating between both parts of the pipe. This influence is studied in more detail in Section 6.3.*

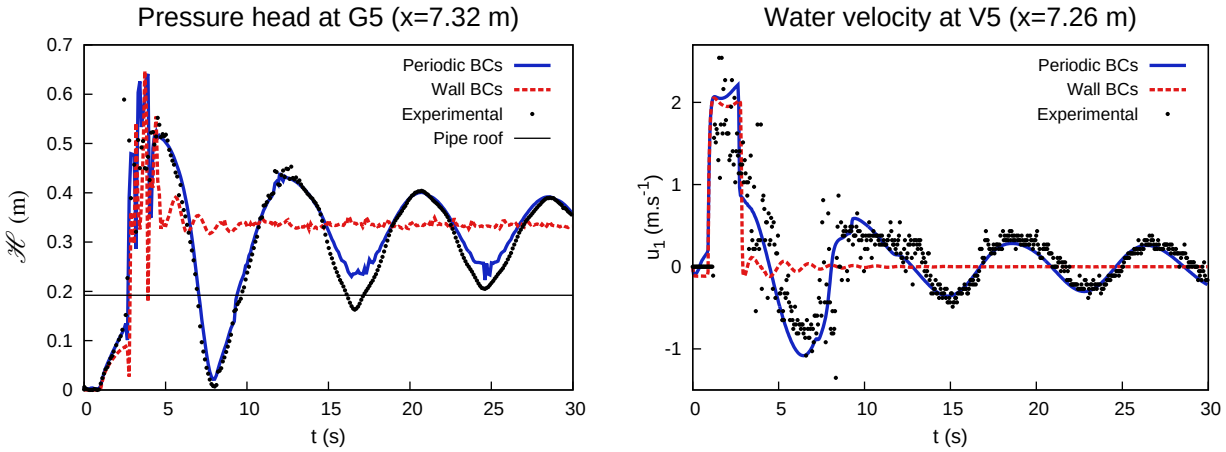

Figure 6.14: Influence of air pocket entrapment through the choice of boundary conditions (300 cells, $c_{1,\text{ref}} = 300 m.s^{-1}$).

6.3 Mixed flow with air pocket entrapment: a U-Tube test case

In this section, the ability of CTL model to handle air pocket entrapment and air pressurization is assessed. A *two-phase* mixed flow configuration is thus considered through a closed pipe describing a U-shape filled by water and air. In particular, the air phase is pressurized and entrapped at the two ends of the pipe. A reference solution is first derived and numerical results are compared for several air pressures. The case where the pipe is open at the boundaries is also considered, as initially proposed in [18].

6.3.1 Reference solution

A reference solution for the so-called U-Tube test case is derived in this section. This derivation is proposed in a general framework where the sloped branches of the pipe are inclined from an angle θ compared to the horizontal reference, as depicted on Figure 6.15 ($\theta = \frac{\pi}{2}$ for the U-Tube). Thus, the configuration under consideration consists in a symmetric closed rectangular pipe of total length L_t and height H describing a V-shape filled by water and air. The length of both sloped parts of the pipe is denoted L and the center part length is denoted D such that $L_t = D + 2L$.

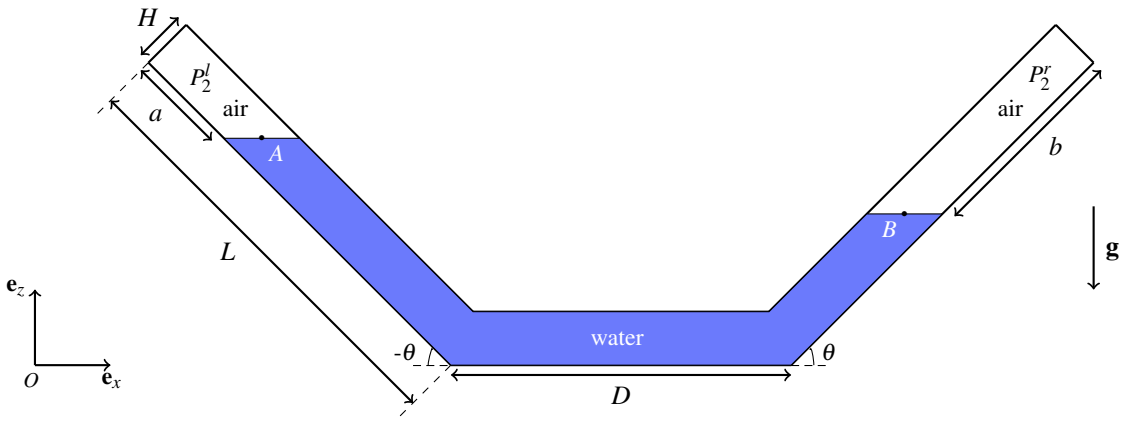

Figure 6.15: Geometric description of the V-Tube.

The water elevation is measured from the two ends of the pipes, respectively a from the left side and b for the right side. The air pressure is denoted $P_2^l(t)$ in the left air pocket and $P_2^r(t)$ in the right one. In the initial state, the flow is kept static. This system may enter in an oscillatory mixed flow regime depending on initial air pressures $(P_{2,0}^l, P_{2,0}^r)$ and water elevations (a_0, b_0). The goal is to obtain a reference solution depending on this initial state.

Governing equation for $a(t)$

The unsteady equation verified by $a(t)$ is derived hereafter. To this aim, a thin pipe compared to its length is considered, i.e. $H \ll L_t$, so that a 1D model is built assuming that the water phase is incompressible. It is also assumed that the water phase cannot touch the boundary walls, i.e. the water elevations remain positive:

$$a(t) > 0,\ b(t) > 0,\ \forall t. \tag{6.2}$$

In the reference frame $(0, \mathbf{e}_x, \mathbf{e}_z)$ and neglecting friction effects, the incompressible Euler set of equations writes:

$$\mathrm{div}(\mathbf{v_1}) = 0, \tag{6.3a}$$

$$\frac{\partial \mathbf{v}_1}{\partial t} + \nabla\left(\frac{v_1^2}{2}\right) + \mathbf{rot}\,\mathbf{v}_1 \wedge \mathbf{v}_1 + \frac{1}{\rho_{1,\mathrm{ref}}}\nabla P_1 = \mathbf{g}, \tag{6.3b}$$

where $\mathbf{v}_1$ is the local velocity vector of the water phase ($v_1^2 = \mathbf{v_1}.\mathbf{v_1}$), P_1 the local pressure, $\rho_{1,\mathrm{ref}}$ the water density assumed constant and $\mathbf{g}$ the gravity field.

Let be A and B, two points belonging to the free surface on each side of the pipe. The momentum conservation equation (6.3b) is integrated along a streamline going from A to B oriented by an elementary displacement vector $\mathbf{dl} = dx\mathbf{e}_x + dz\mathbf{e}_z$. By definition, $\mathbf{v}_1 \wedge \mathbf{dl} = \mathbf{0}$, such that it provides:

$$\int_A^B \frac{\partial \mathbf{v}_1}{\partial t}.\mathbf{dl} + \int_A^B \nabla\left(\frac{v_1^2}{2} + \frac{P_1}{\rho_{1,\mathrm{ref}}} + gz\right).\mathbf{dl} = 0, \tag{6.4}$$

which can be rewritten as:

$$\int_A^B \frac{\partial \mathbf{v}_1}{\partial t}.\mathbf{dl} + \frac{v_1^2(z=z_B^-) - v_1^2(z=z_A^-)}{2} + \frac{P_1(z=z_B^-) - P_1(z=z_A^-)}{\rho_{1,\text{ref}}} + g(z_B - z_A) = 0. \tag{6.5}$$

The z coordinates are given by $z_A = (L-a)\sin(\theta)$ and $z_b = (L-b)\sin(\theta)$ where L is the length of both sloped part of the pipe. The water phase is considered in pressure equilibrium with the air phase at the free-surface such that $P_1(z=z_A^-) = P_2(z=z_A^+)$ and $P_1(z=z_B^-) = P_2(z=z_B^+)$ (surface tension effects are neglected here). Furthermore, the air pressure is assumed uniform in each air pocket. Due to the incompressible framework, the divergence free condition (6.3a) yields a uniform flow rate along the pipe. In particular, for a thin pipe with constant cross-section, it is assumed that:

$$\mathbf{v}_1 = \dot{a}\mathbf{u}, \tag{6.6}$$

everywhere in the water medium where $\mathbf{u}$ is a unitary vector oriented by $\mathbf{dl}$. Therefore, $v_1^2(z=z_B^-) = v_1^2(z=z_A^-)$ and (6.5) provides:

$$L_w\ddot{a} + g(a-b)\sin(\theta) + \frac{P_2^r - P_2^l}{\rho_{1,\text{ref}}} = 0, \tag{6.7}$$

where L_w length is the length of a streamline connecting A with B. For a thin pipe, it is assumed that $L_w = L_t - (a+b)$.

The mass conservation of the water phase in the incompressible framework writes:

$$a(t) + b(t) = a_0 + b_0, \ \forall t. \tag{6.8}$$

Regarding the air phase, the air pockets are assumed to be kept separated by the water medium. Therefore, the mass conservation applies in each of them and yields $\rho_2^l a = \rho_{2,0}^l a_0$ and $\rho_2^r b = \rho_{2,0}^b b_0$ due to the uniform pressure assumption. Using a prefect gas law for the air phase, see (3.3b), one obtains:

$$\begin{cases} P_2^l = P_{2,0}^l \left(\frac{a_0}{a}\right)^{\gamma_2}, \\ P_2^r = P_{2,0}^r \left(\frac{b_0}{b}\right)^{\gamma_2}. \end{cases} \tag{6.9}$$

Denoting $l_0 = a_0 + b_0$, $a(t)$ finally complies with:

$$\ddot{a} + \frac{2g\sin(\theta)}{L_w}a + \frac{1}{L_w\rho_{1,\text{ref}}}\left(P_{2,0}^r\left(\frac{b_0}{l_0-a}\right)^{\gamma_2} - P_{2,0}^l\left(\frac{a_0}{a}\right)^{\gamma_2}\right) = \frac{gl_0\sin(\theta)}{L_w}. \tag{6.10}$$

A non-linear ordinary differential equation is obtained which may be solved numerically using a classical Runge-Kutta method. Once $a(t)$ is known, $b(t)$ is deduced from $b(t) = l_0 - a(t)$, the air pressures are calculated from 6.9 and the water velocity verifies $v_1 = \dot{a}$.

Remark 6.3 (Open pipe)**.** *When the pipe is open at the boundaries, the air pressure satisfies $P_2^r(t) = P_2^l(t) = P_{atm}$, $\forall t$, so that (6.10) writes:*

$$\ddot{a} + \frac{2g\sin(\theta)}{L_w}a = \frac{gl_0\sin(\theta)}{L_w}. \tag{6.11}$$

An harmonic oscillator is obtained whose solution is:

$$a(t) = a_{eq} + (a_0 - a_{eq})\cos(\omega_0 t), \tag{6.12}$$

where $a_{eq} = \frac{l_0}{2}$ is the equilibrium position and $\omega_0 = \sqrt{\frac{2g\sin(\theta)}{L_w}}$ is the pulsation of oscillations.

In order to go further in the analysis of the solution of (6.10), the latter is studied around its equilibrium state.

Equilibrium state

The equilibrium state of (6.10) is characterized by $\ddot{a} = \dot{a} = 0$ so that the equilibrium position a_{eq} complies with the following non-linear equation:

$$a_{eq} + \frac{1}{2\rho_{1,\text{ref}}g\sin(\theta)}\left(P_{2,0}^r\left(\frac{b_0}{l_0-a_{eq}}\right)^{\gamma_2} - P_{2,0}^l\left(\frac{a_0}{a_{eq}}\right)^{\gamma_2}\right) = \frac{l_0}{2}. \tag{6.13}$$

The analytical solution of the above equation is clearly not obvious. It may nonetheless be estimated under the assumption $|\varepsilon| \ll a_0$ where:

$$a_{eq} = a_0 + \varepsilon. \tag{6.14}$$

Indeed, an asymptotic expansion of (6.13) at order 1 in ε readily yields:

$$\varepsilon = \frac{(b_0 - a_0) - \frac{1}{\rho_{1,\text{ref}} g \sin(\theta)}(P^r_{2,0} - P^l_{2,0})}{2 + \frac{\gamma_2}{\rho_{1,\text{ref}} g \sin(\theta)}\left(\frac{P^r_{2,0}}{b_0} + \frac{P^l_{2,0}}{a_0}\right)}. \tag{6.15}$$

ε is equivalently defined as $\varepsilon = b_0 - b_{eq}$ due to (6.8) such that the validity range of (6.15) is described by $|\varepsilon| \ll b_0$ and $|\varepsilon| \ll a_0$. In this framework, a first order approximation of the equilibrium air pressures in each air pocket, defined analytically as $P^l_{2,eq} = P^l_{2,0}\left(\frac{a0}{a_{eq}}\right)^{\gamma_2}$ and $P^r_{2,eq} = P^r_{2,0}\left(\frac{b0}{b_{eq}}\right)^{\gamma_2}$ due to mass conservation, takes the following form:

$$\begin{cases} P^l_{2,eq} = P^l_{2,0}\left(1 - \dfrac{\gamma_2 \varepsilon}{a_0}\right), \\ P^r_{2,eq} = P^r_{2,0}\left(1 + \dfrac{\gamma_2 \varepsilon}{b_0}\right). \end{cases} \tag{6.16}$$

These equilibrium pressures must be strictly positive such that ε must satisfy $-\frac{b_0}{\gamma_2} < \varepsilon < \frac{a_0}{\gamma_2}$. The latter condition is automatically verified under the initial assumptions $|\varepsilon| \ll b_0$ and $|\varepsilon| \ll a_0$ as $\gamma_2 = 1.4$ for air.

Remark 6.4. *The equilibrium position may also be exactly calculated solving (6.13) numerically. However, due to the high numbers of free parameters, namely $(a_0, b_0, P^l_{2,0}, P^r_{2,0})$, the existence and the uniqueness of the solution cannot be simply guaranteed in the general case. For instance, a profitable framework is to consider an identical air mass in both air pockets and initial water elevations satisfying $L \leq a_0 + b_0 \leq 2L$.*

Oscillations around the equilibrium state

The initial non linear equation (6.10) is now expanded around its equilibrium state taking $a(t)$ under the form:

$$a = a_{eq} + \delta, \tag{6.17}$$

where δ is assumed to satisfy $|\delta| \ll |a_{eq}|$ and $|\delta| \ll |b_{eq}|$. Therefore, up to first order w.r.t. δ, one obtains:

$$\ddot{\delta} + \omega^2 \delta = 0, \tag{6.18}$$

where:

$$\begin{cases} \omega^2 = \omega_0^2 + \omega_a^2, \\ \omega_0^2 = \dfrac{2g\sin(\theta)}{L_w}, \\ \omega_a^2 = \dfrac{\gamma_2}{L_w \rho_{1,\text{ref}}}\left(\dfrac{P^l_{2,eq}}{a_{eq}} + \dfrac{P^r_{2,eq}}{b_{eq}}\right). \end{cases} \tag{6.19}$$

Thus, an harmonic oscillator is obtained whose pulsation features an additional contribution ω_a due to air pocket entrapment. Indeed, the pulsation ω_0 is the corresponding pulsation when the pipe is open, see Remark 6.3.

Remark 6.5 (Influence of air pocket entrapment on oscillations)**.** *Considering $P^l_{2,eq} \sim P^r_{2,eq} \sim P_{2,d}$, $a_{eq} \sim b_{eq} \sim d$ and $\theta = 90^o$, one obtains:*

$$\frac{\omega}{\omega_0} = \sqrt{1 + \frac{\gamma_2 P_{2,d}}{\rho_{1,\text{ref}} g d}} \tag{6.20}$$

The air entrapment has no influence on the pulsation of oscillations when $\omega \sim \omega_0$, which also writes $d \gg \frac{\gamma_2 P_{2,d}}{\rho_{1,\text{ref}} g}$. With $P_{2,d} \sim 1\,\text{bar}$, it yields $d \gg 15\,m$. Therefore, the effects of air pocket entrapment are experienced in a closed pipe even if the boundaries are taken far from the liquid phase. This comment is confirmed by the results presented in Remark 6.2, where the setting of wall boundary conditions with $d < 10\,m$ does not allow to reproduce the experimental behavior.

Finally, the solution of (6.10) in agreement with the initial conditions $a(0) = a_0$ and $\dot{a}(0) = 0$ may be estimated as:

$$a(t) = a_{eq} + (a_0 - a_{eq})\cos(\omega t), \tag{6.21}$$

where a_{eq} and ω are defined in (6.14) and (6.19) respectively. The water velocity, namely $v_1 = \dot{a}$, consequently verifies:

$$v_1(t) = (a_{eq} - a_0)\omega \sin(\omega t), \tag{6.22}$$

and the air pressures in each air pocket comply with:

$$\begin{cases} P_2^l(t) = P_{2,eq}^l\Big(1 - \dfrac{\gamma_2\big(a(t) - a_{eq}\big)}{a_{eq}}\Big), \\ P_2^r(t) = P_{2,eq}^r\Big(1 + \dfrac{\gamma_2\big(a(t) - a_{eq}\big)}{b_{eq}}\Big). \end{cases} \tag{6.23}$$

In the next section, several initial states are proposed for a U-Tube pipe ($\theta = \frac{\pi}{2}$). Numerical results are then presented in Section 6.3.3 comparing the CTL model with the reference solution built in this section. In particular, the *reference solution* refers to the estimated solution exposed above while the *NL reference solution* refers to the solution obtained with a Runge-Kutta method of order 4 applied to (6.10).

6.3.2 Global setting and objectives

For the numerical tests, the U-Tube pipe depicted on Figure 6.16 is considered. Realistic dimensions are chosen with $H = 0.1\,m$, $L = 4.5\,m$ and $D = 1\,m$ such that $L_t = 2L + D = 10\,m$.

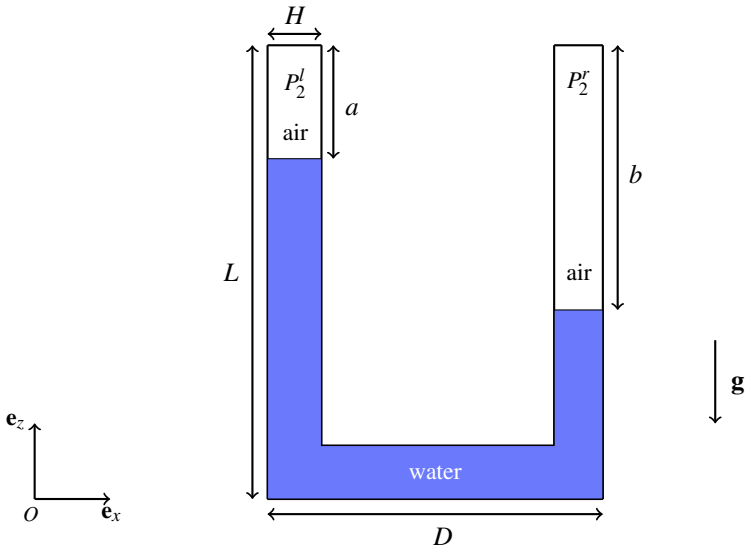

Figure 6.16: Geometric description of the U-Tube test case.

It is proposed to handle this configuration with the CTL model studying the influence of the initial state. Therefore, three different settings detailed on Table 6.1 are considered. Initial water elevations are identical while initial air pressures and boundary conditions vary. Air pockets with different pressures are thus entrapped in the C1 and C2 settings while the OP setting refers to an open pipe without any air pocket entrapment. For the other initial conditions, the water height is set to $h_1 = (1 - 10^{-4})H$ in the pressurized part and $h_1 = 10^{-5}H$ in the dry part, the water density is set to $\rho_{1,\text{ref}}$ neglecting hydrostatic effects and the flow is static. The total simulation time is set to 10 seconds.

Id	$P_{2,0}^l$	$P_{2,0}^r$	a_0	b_0	BCs
C1	$1.1\,atm$	$1\,atm$	$0.3L$	$0.6L$	Wall
C2	$1.8\,atm$	$1\,atm$	$0.3L$	$0.6L$	Wall
OP	$1\,atm$	$1\,atm$	$0.3L$	$0.6L$	Periodic

Table 6.1: Initial and boundary conditions for U-Tube test cases.

In practice, the CTL model is defined along the pipe axis, see Appendix 6.A.1, without any treatment for the slope change, simply accounted for by a discontinuity on θ. Note that the CTL model is well defined for $\theta \in [-\frac{\pi}{2}, \frac{\pi}{2}]$ such that right angle bends may be handled. The celerity of acoustic waves in the water phase is set to $c_{1,\text{ref}} = 1500\,m.s^{-1}$. Focusing on the SPR scheme, the same setting as for the previous mixed flow test cases is used. In particular, the threshold is set to $h_s = (1 - \delta)H$ with $\delta = 10^{-3}$ and the (*material*) CFL number is set to 0.01. Several mesh sizes are

considered from 300 cells ($\Delta x \sim 3.3\,cm$) to 3000 cells ($\Delta x \sim 0.33\,cm$). The numerical results are compared with the *reference solution* and the *NL reference solution* defined in the previous section.

6.3.3 Results and comments

For each setting exposed on Table 6.1, the air pressure at $x = 0$ (i.e. $P_{2,l}$) as well as the water velocity at $x = L_t/2$ (middle of the pipe) are evaluated with the CTL model. The setting C1 is considered first on Figure 6.17 using a coarse mesh ($\Delta x \sim 3.3\,cm$). The CTL model compares very well with the *reference solution* both in terms of amplitude and frequency. Due to numerical diffusion, a slight shift associated to an amplitude damping is observed in the long time evolution. However, the air pocket entrapment influence is accurately restored. Note that in this configuration, the *reference solution* and the *NL reference solution* are almost identical.

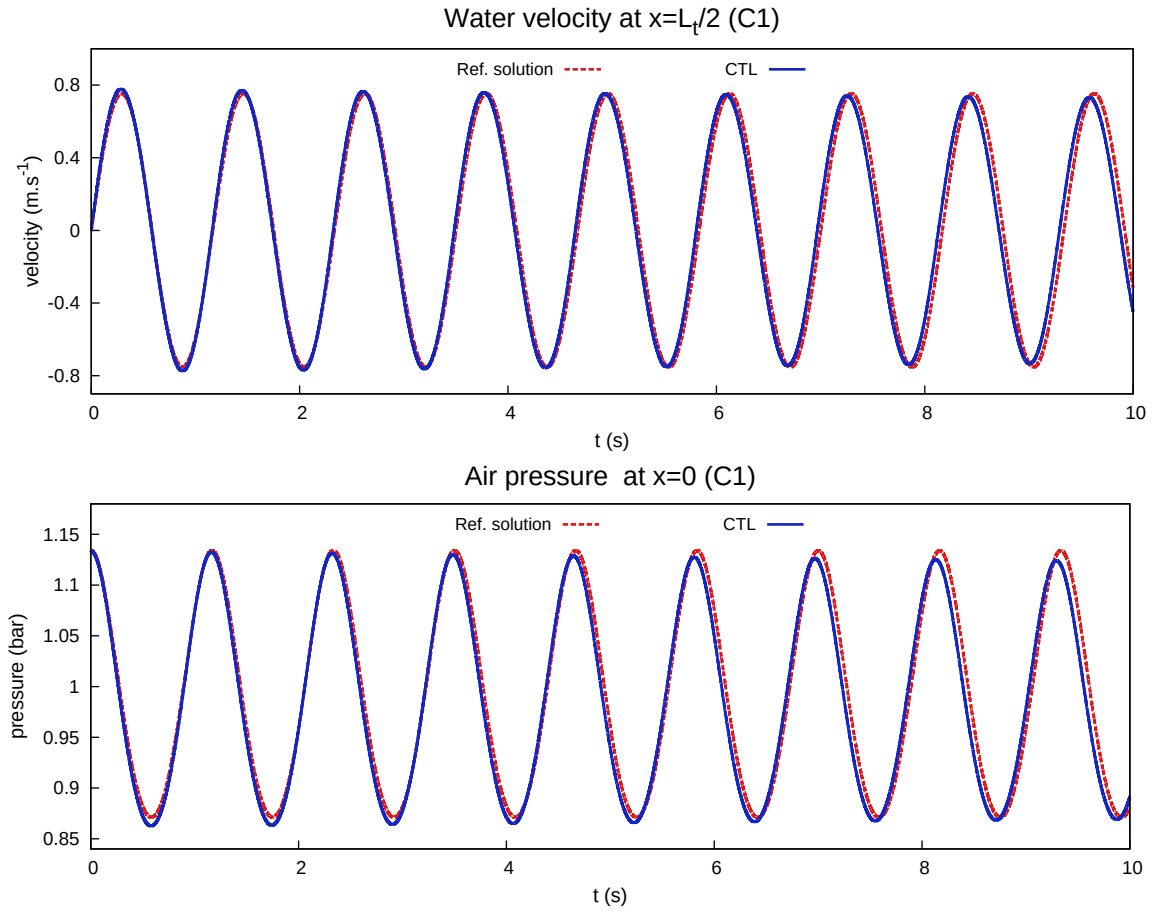

Figure 6.17: Comparison between the reference solution and numerical results for the C1 setting using 300 cells.

The setting C2 is more severe as the left-side air pocket is more pressurized. In this context, the *NL reference solution* differs from the *reference solution*, see Figure 6.18. The CTL model is nonetheless able to catch the correct frequency and amplitude although numerical diffusion is observed for long simulation times. When refining the mesh, see Figure 6.19 for the air pressure field, this numerical diffusion naturally diminishes and the results are improved. The open boundary case (OP setting) is also assessed on Figure 6.20. The CTL model accurately restores the expected behavior for the velocity field setting periodic boundary conditions.

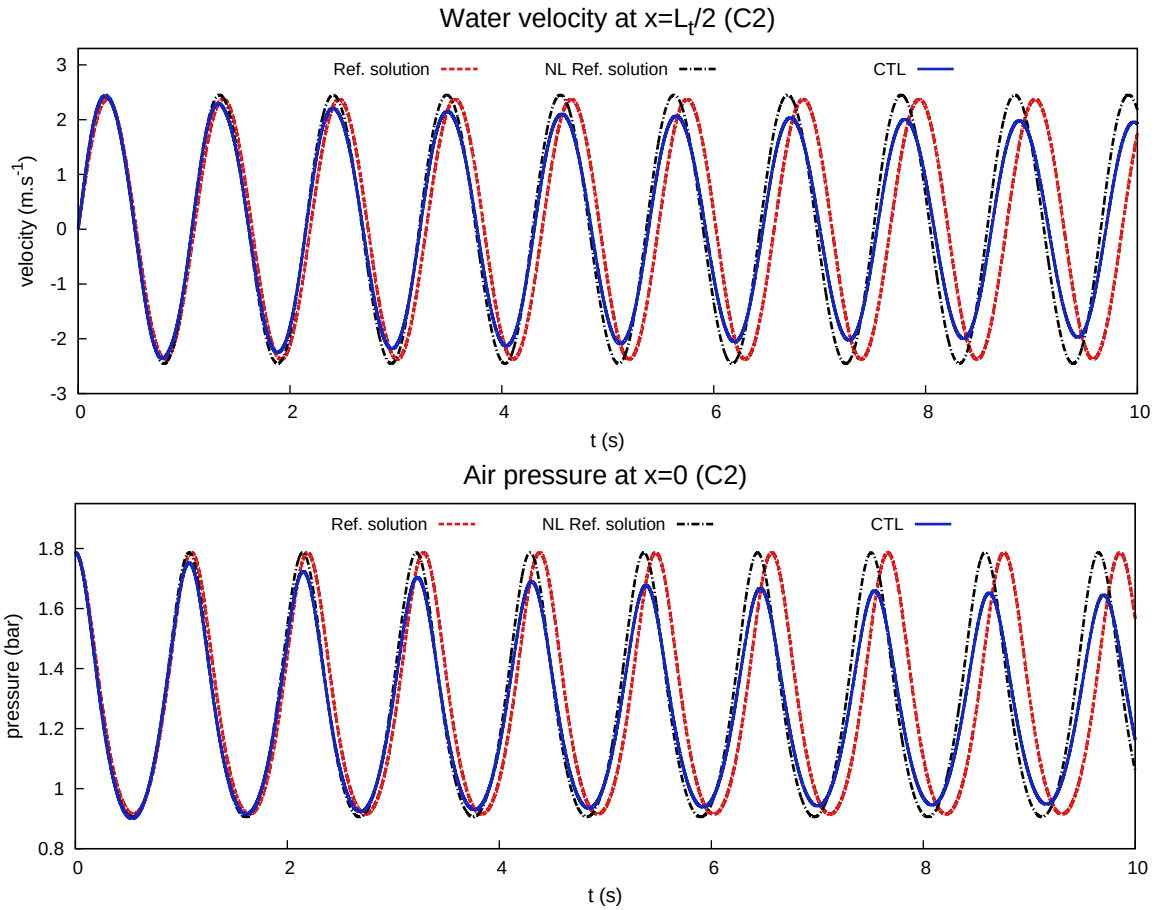

Figure 6.18: Comparison between the reference solution and numerical results for the C2 setting using 300 cells.

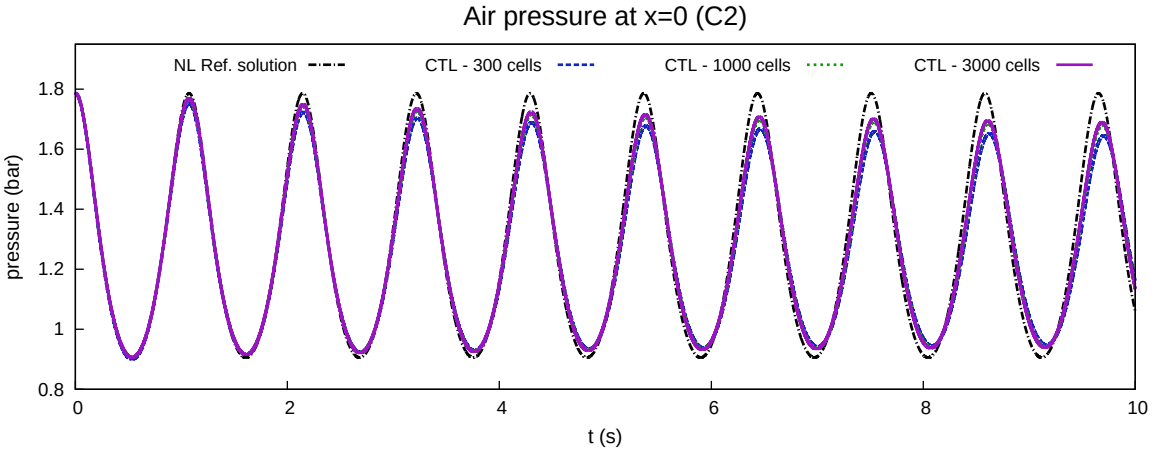

Figure 6.19: Mesh sensitivity on air pressure for the C2 setting.

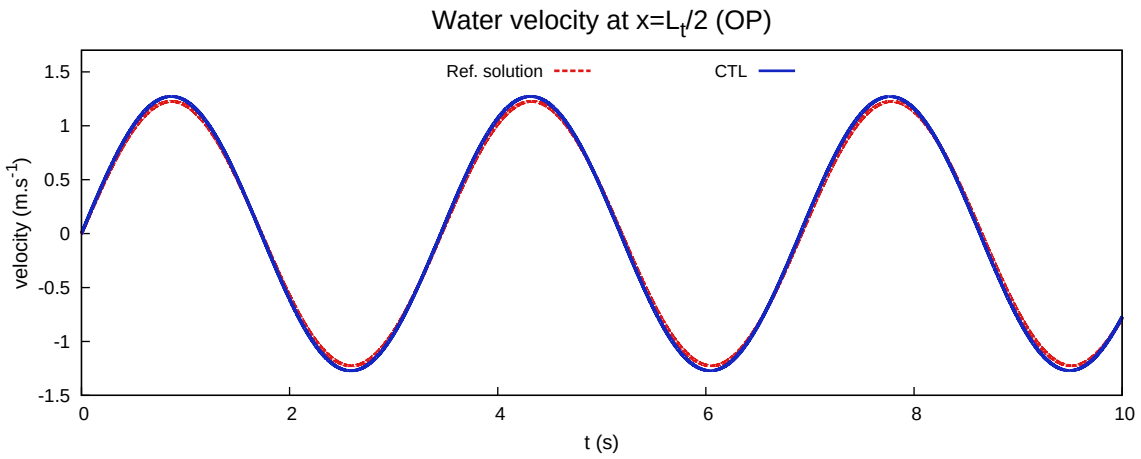

Figure 6.20: Comparison between the reference solution and numerical results for the OP setting using 300 cells.

Finally, the different settings illustrate the ability of the CTL model to handle air pocket entrapment in pipes with different degrees of pressurization. This last feature is a key point regarding the two-phase modelling of mixed flows. Indeed, as highlighted on Figure 6.21, the solution strongly depends on the air pressurization level where a large disparity both in terms of frequency and amplitude is observed. In addition, the considered configuration is relevant regarding industrial facilities. Similar settings have been studied experimentally in [23, 24, 13, 7] featuring the same kind of oscillatory pressure behavior in entrapped air pockets.

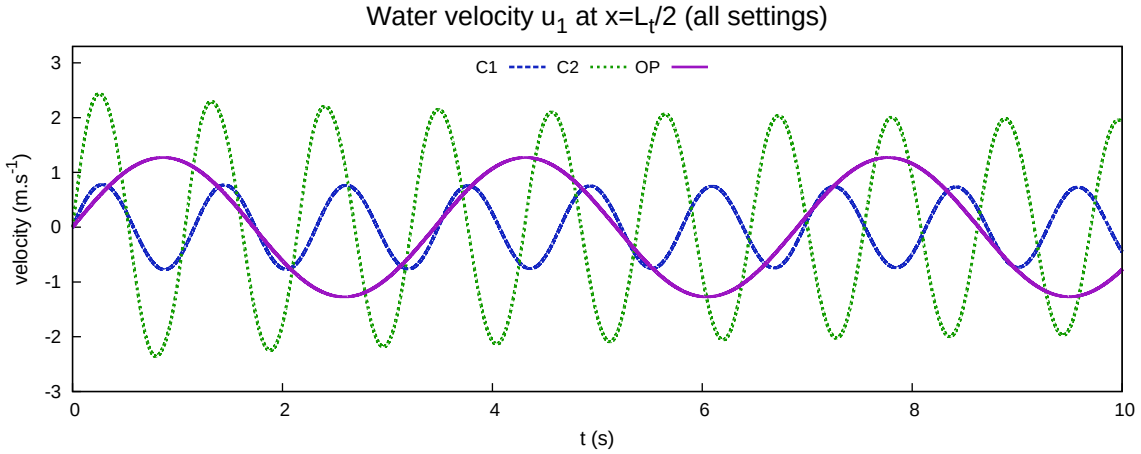

Figure 6.21: Comparison of the water velocity between the different settings using the CTL model with 300 cells.

6.4 Conclusion and perspectives

The three test cases presented herein clearly illustrate the ability of the Compressible Two-Layer model associated with the SPR scheme to deal with mixed flows in pipes including air-water interactions. Firstly, physically relevant results are obtained considering the typical single-phase dynamics of a mixed flow which concerns transitions between stratified regimes and pressurized or dry regimes. It is addressed through an elementary pipe filling and an experimental test case. In the first case, the results are satisfactorily compared with those given by a reference single-phase mixed flow model, namely the PFS model [5], and with analytical results provided by a simplified approach. In the second case, the results are in good agreement with pressure and velocity time series coming from experimental measurements. Secondly, the two-phase description of the CTL model is validated on a U-tube test case which involves entrapped air pockets with a strong influence on the flow dynamics. Comparing with a built reference solution, both the period and the amplitude of the phenomenon are very accurately captured.

Beyond this physical validation, the efficiency and the robustness of the method regarding transitions between the regimes are highlighted. In particular, realistic values for the celerity of acoustic waves in the water phase may be chosen, typically between $200 m.s^{-1}$ and $1500 m.s^{-1}$, whereas lower non-physical values have to be set with com-

mon single-phase mixed flow models [21, 5] to avoid detrimental oscillations when transitions occur. Moreover, the corresponding CPU times are totally tractable.

It is important to note that all the above attractive features are obtained with a two-phase description in every regime, particularly in pressurized and dry regimes where a thin-layer of vanishing fluid is computed. This challenging approach is the most natural regarding the unified formulation of the CTL model and turns out to be beneficial with the proposed SPR scheme as soon as relaxation source terms provide dissipation and robustness.

To the best knowledge of the authors, the CTL model is thus the only validated 1D two-phase model for mixed flows in pipes providing an accurate compressible description of both phases in every regime. Therefore, numerous two-phase transient mixed flow configurations including air pockets entrapment seem achievable. Further validations are needed in that sense. In particular, we are interested in the estimation of the so-called *clearing velocity* which corresponds to the required water velocity to transport entrapped air pockets downstream. This configuration is deeply studied experimentally [10, 17, 15] and is of particular interest for industrial applications regarding the clearing of air pockets from hydraulic pipes. Another complex application is the simulation of *slug flows* which may be seen as highly intermittent gas-liquid mixed flows in pipes mainly resulting from growing instabilities at the interface between both phases. They are particularly involved in the petroleum industry and they are also widely studied analytically [11, 20] and experimentally [3, 14, 1].

6.A Sloping pipes and wall friction

This appendix aims at providing some additional features of the CTL model when dealing with more complex pipe configurations. In particular, sloping pipes (rectangular and circular) as well as wall friction are taken into account.

6.A.1 Sloping rectangular pipes

Sloping pipes are frequently encountered in industrial configurations. Considering a constant slope of angle $\theta \in [-\frac{\pi}{2};\frac{\pi}{2}]$, a description of the geometry is presented on Figure 6.22.

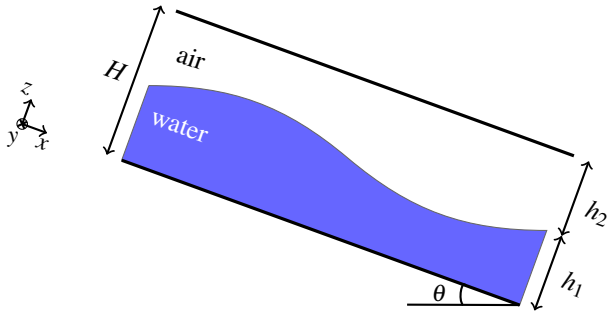

Figure 6.22: Geometric description for sloped pipes.

The frame of reference is the inclined frame (O,x,y,z) so that the closure relations (3.2) for interfacial variables readily become:

$$(U_I,P_I) = (u_2, P_1 - \rho_1 g \frac{h_1}{2}\cos(\theta)). \tag{6.A.1}$$

Thus, gravity source terms are also added and the CTL model in the inclined frame writes:

$$\begin{cases} \dfrac{\partial h_1}{\partial t} + U_I \dfrac{\partial h_1}{\partial x} = \lambda_p (P_I - P_2(\rho_2)), \\ \dfrac{\partial m_k}{\partial t} + \dfrac{\partial m_k u_k}{\partial x} = 0, \ k = 1,2, \\ \dfrac{\partial m_k u_k}{\partial t} + \dfrac{\partial m_k u_k^2}{\partial x} + \dfrac{\partial h_k P_k(\rho_k)}{\partial x} - P_I \dfrac{\partial h_k}{\partial x} = (-1)^k \lambda_u (u_1 - u_2) - m_k g \sin(\theta), \ k = 1,2. \end{cases} \tag{6.A.2}$$

At the discrete level, the gravity source terms are treated implicitly in the first step of the SPR scheme, see Section 4.3.3. The partial mass m_k^* are indeed available from the mass conservation equations.

If the slope of the pipe is varying in space, i.e. $\theta(x)$, one still uses (6.A.2) imposing a discontinuity on θ at the discrete level without any additional treatment. In particular, curvature effects are not taken into account.

6.A.2 Sloping circular pipes

In the framework of circular pipes, the CTL model results from a 2D integration of the isentropic Euler set of equations for both phases over a cross-section. It reads as (6.A.2) except that h_k is replaced by A_k, the area filled by the phase k in the cross section and the interfacial closure laws becomes:

$$(U_I, P_I) = (u_2, P_1 - \rho_1 g \ell_1). \tag{6.A.3}$$

The length ℓ_1 represents the distance between the interface and the center of mass of the wet section, it writes for circular pipes:

$$\ell_1 = \frac{R^3}{A_1}\Big(\frac{2}{3}\sin^3\frac{\theta_1}{2} - \frac{1}{2}\cos\frac{\theta_1}{2}(\theta_1 - \sin\theta_1)\Big), \tag{6.A.4}$$

where $A_1 = \frac{R^2}{2}(\theta_1 - \sin(\theta_1))$ and R is the radius of the pipe, see Chapter 2 for details.

6.A.3 Wall friction

In order to take into account friction effects between the pipe walls and the water phase, a source term in the momentum conservation equation for the water water phase is added:

$$F_1 = -m_1 g S_f, \tag{6.A.5}$$

where S_f is a friction factor assumed to be given by the Manning-Strickler law:

$$S_f = n_m^2 \frac{u_1|u_1|}{R_h^{4/3}}, \tag{6.A.6}$$

with n_m the Manning roughness coefficient and R_h the so-called hydraulic radius, see [19]. For circular pipes, $R_h(A_1) = \frac{A_1}{P_m}$, where P_m is the wet perimeter, i.e. the length in contact with the water phase on a given cross-section. In the computations presented in Section 6.3, F_1 is treated explicitly in a homogeneous additional step which occurs after the velocity relaxation.

6.B Estimation of the pressure jump for the pipe filling test case

The pipe filling test case addressed in Section 6.1 is characterized by a jump between the stratified and the pressurized part. In particular, on may estimate the related pressure jump for the water phase. The state close to the jump location in the stratified part is denoted $\mathbf{W}^-$ while the state in the pressurized part is denoted $\mathbf{W}^+$, see Figure 6.23.

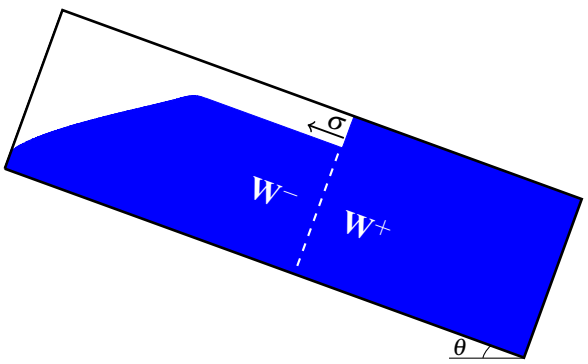

Figure 6.23: Water height front in the pipe filling test case.

Denoting σ the speed of the jump, the Rankine-Hugoniot jump conditions applied to the mass conservation equation in the water phase, see (2.20), yield:

$$\sigma = \frac{[\rho_1 h_1 u_1]_-^+}{[\rho_1 h_1]_-^+}, \tag{6.B.7}$$

where the brackets $[.]$ denote the difference between the states on both sides of the discontinuity, see [12]. It is assumed that the water density is almost constant through the jump, i.e. $\rho_1^- \sim \rho_1^+ \sim \rho_{1,\text{ref}}$. In addition, one has $u_1^+ = 0$ and $h_1^+ = H$ such that:

$$\sigma = \frac{h_1^-}{h_1^- - H} u_1^-. \tag{6.B.8}$$

The same approach on the air phase where $h_2^+ = 0$ and $u_2^+ = 0$ yields:

$$\sigma = u_2^-. \tag{6.B.9}$$

Summing the momentum conservation equation of each phase, a conservative equation is obtained where the Rankine-Hugoniot jump conditions yield:

$$-\sigma[m_1 u_1 + m_2 u_2]_-^+ + [m_1 u_1^2 + m_2 u_2^2 + h_1 P_1 + h_2 P_2]_-^+ = 0. \tag{6.B.10}$$

In the pressurized part, one has $u_1^+ = u_2^+ = 0$, $h_2^+ = 0$, such that we are left with:

$$(m_1 u_1)^- \left(\sigma - u_1^-\right) + (m_2 u_2)^- \left(\sigma - u_2^-\right) + H P_1^+ - \left((h_1 P_1)^- + (h_2 P_2)^-\right) = 0. \tag{6.B.11}$$

An instantaneous pressure relaxation is assumed in the stratified part such that one obtains $P_2^- = P_I^- = P_1^- - m_1^- \frac{g}{2}\cos(\theta)$. Denoting $\Delta P_1 = P_1^+ - P_1^-$ and using (6.B.8) and (6.B.9), (6.B.11) provides:

$$\Delta P_1 = \rho_1^- \left(\frac{h_1^-}{H - h_1^-} (u_1^-)^2 - \frac{g}{2} \frac{h_1^- (H - h_1^-)}{H} \cos(\theta) \right), \tag{6.B.12}$$

where one reasonably assumes $\rho_1^- = \rho_{1,\text{ref}}$ and $h_1^- = h_{1,\text{init}}$. The value u_1^- may be estimated considering that the flow in the stratified part is uniform along x close to the jump. Thus, neglecting the friction with the air phase, u_1^- complies with $\partial_t u_1^- = -\rho_1 g \sin(\theta)$ which yields $u_1^-(t) = -\rho_1 g t \sin(\theta)$. Therefore, (6.B.12) provides an analytical estimation of the pressure jump ΔP_1. Note that this estimation does not involve the air phase nor the celerity of acoustic waves in the water phase.

6.C Period of pressure waves oscillations for the pipe filling test case

Regarding the pipe filling test case, one observes oscillations on the pressure time series when the pipe is filled, see Figure 6.7. The period of these oscillations may be estimated considering the propagation of a pressure pulse along a static fluid, between the free surface and the bottom end of the pipe, see Figure 6.24 for a sketch of the configuration.

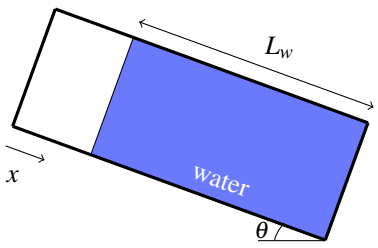

Figure 6.24: Sketch of the filled pipe.

In the water medium, assumed static, the water pressure classically verifies a wave equation:

$$\frac{\partial^2 P_1}{\partial t^2} - c_1^2 \frac{\partial^2 P_1}{\partial x^2} = 0, \tag{6.C.13}$$

which is derived from the isentropic Euler set of equations without source term. It can formally be rewritten as $(\partial_t P_1 + c_1 \partial_x P_1)(\partial_t P_1 - c_1 \partial_x P_1) = 0$ such that the general solution of (6.C.13) reads:

$$P_1(x,t) = F(x + c_1 t) + G(x - c_1 t), \tag{6.C.14}$$

where (F,G) are differentiable functions complying with:

$$\begin{cases} \partial_t F - c_1 \partial_x F = 0, \\ \partial_t G + c_1 \partial_x G = 0. \end{cases} \tag{6.C.15}$$

In the following, the origin of space is taken at the free surface. Let us consider a pulse emanating from this free surface propagating positively at speed c_1. The goal is to estimate the needed time to recover the same pulse at the same spot. To this end, boundary conditions have to be specified. An analogous configuration may be a mechanical pulse traveling through a string with a free boundary condition at the free surface and a fixed endpoint.

Dirichlet boundary condition at the bottom end

At the bottom end, one assumes that the pressure is constant and given by the hydrostatic equilibrium. A Dirichlet boundary condition of value P_h is imposed:

$$P_1(x = L_w, t) = P_h, \ \forall t. \tag{6.C.16}$$

The incoming pulse may be written under the form $G(x - c_1 t)$ and should verify $G(L_w - c_1 t) = P_h$, $\forall t$. This condition cannot be satisfied by a non uniform pressure. Thus, a reflection occurs through a pulse $F(x + c_1 t)$ propagating at speed $-c_1$. The boundary condition then writes $F(L_w + c_1 t) + G(L_w - c_1 t) = P_h$ and the amplitude of the reflected pulse is $P_h - G_0$, where G_0 is the amplitude of the incoming pulse.

Homogeneous Neumann boundary condition at the free surface

The free surface boundary condition is modeled by an homogeneous Neumann boundary condition:

$$\frac{\partial P_1(x,t)}{\partial x}\Big|_{x=0} = 0, \ \forall t. \tag{6.C.17}$$

The incoming pulse may be written under the form $F(x + c_1 t)$ and should verify $\frac{\partial F(x+c_1 t)}{\partial x}\big|_{x=0} = 0$, $\forall t$. As below, this condition cannot be satisfied by a non uniform pressure. Thus, a reflection occurs through a pulse $G(x - c_1 t)$ propagating at speed c_1. The boundary condition then writes $\frac{\partial F(x+c_1 t) + G(x-c_1 t)}{\partial x}\big|_{x=0} = 0$, $\forall t$. Using (6.C.15), the latter may be rewritten in time derivatives: $\frac{\partial F(x+c_1 t) - G(x-c_1 t)}{\partial t}\big|_{x=0} = \frac{\partial F(c_1 t) - G(-c_1 t)}{\partial t} = 0$, $\forall t$. Therefore, $G(-c_1 t) = F(c_1 t)$ and the reflected pulse has the same amplitude than the incoming pulse.

Period of pressure waves

Consider a pulse of amplitude G_0 emanating from the free surface and traveling at speed c_1. It travels the distance L_w before being reflected at the pipe end. The reflected pulse has the amplitude $P_h - G_0$ and travels at speed $-c_1$ the distance L_w before being reflected on the free surface. The reflected pulse has the same amplitude, i.e. $P_h - G_0$, and travels the distance L_w at speed c_1 before being reflected at the pipe end. The reflected pulse has the amplitude $P_h - (P_h - G_0) = G_0$ and travels at speed $-c_1$ the distance L_w before being reflected on the free surface. The reflected pulse has the same amplitude, i.e. G_0, and matches with the initial pulse. Finally, the period T of the phenomenon verifies:

$$T = \frac{4 L_w}{c_1}. \tag{6.C.18}$$

References

[1] M. Abdulkadir, V. Hernandez-Perez, I.S. Lowndes, B.J. Azzopardi, and E. Sam-Mbomah. Experimental study of the hydrodynamic behaviour of slug flow in a horizontal pipe. *Chemical Engineering Science*, 156:147–161, 2016.

[2] F. Aureli, A. Dazzi, A. Maranzoni, and P. Mignosa. Validation of single- and two-equation models for transient mixed flows: a laboratory test case. *Journal of Hydraulic Research*, 53(4):440–451, 2015.

[3] D. Barnea, Y. Luninski, and Y. Taitel. Flow pattern in horizontal and vertical two phase flow in small diameter pipes. *The Canadian Journal of Chemical Engineering*, 61(5):617–620, 1983.

[4] C. Bourdarias, M. Ersoy, and S. Gerbi. Unsteady flows in non uniform closed water pipes: a full kinetic approach. *Numerische Mathematik*, 128(2):217–263, 2014.

[5] C. Bourdarias and S. Gerbi. A finite volume scheme for a model coupling free surface and pressurised flows in pipes. *Journal of Computational and Applied Mathematics*, 209:1–47, 2007.

[6] J.A. Cardle, C.C.S. Song, and M. Yuan. Measures of mixed transient flows. *Journal of Hydraulic Engineering*, 115(2):169–182, 1989.

[7] M.A. Chaiko and K.W. Brinckman. Models for analysis of water hammer in piping with entrapped air. *Journal of Fluids Engineering*, 124:194–215, 2002.

[8] J.-A. Cunge and M. Wegner. Numerical integration of barré de Saint-Venant's flow equations by means of an implicit scheme of finite differences. *La Houille Blanche*, 1:33–39, 1964.

[9] S.N. Domenico. Acoustic wave propagation in air-bubble curtains in water - part I: History and theory. *Geophysics*, 47(3):345–353, 1982.

[10] M. Escarameia. Investigating hydraulic removal of air from water pipelines. *Proceedings of the Institution of Civil Engineers-Water Management.*, 160(1):25–34, 2007.

[11] J. Fabre and A. Liné. Modeling of two-phase slug flow. *Annual review of fluid mechanics*, 24(1):21–46, 1992.

[12] E. Godlewski and P.-A. Raviart. *Numerical approximation of hyperbolic systems of conservation laws*. Springer New York, 1996.

[13] N. H. Lee. *Effect of pressurization and expulsion of entrapped air in pipelines*. PhD thesis, Georgia Institute of Technology, United States, 2005.

[14] Z.S. Mao and A.E. Dukler. An experimental study of gas-liquid slug flow. *Experiments in Fluids*, 8(3-4):169–182, 1989.

[15] I.W.M. Pothof and F.H.L.R. Clemens. Experimental study of air-water flow in downward sloping pipes. *International Journal of Multiphase Flow*, 37(3):278–292, 2011.

[16] I. Pothov and B. Karney. *Water Supply System Analysis - Selected Topics*, chapter Guidelines for transient analysis in water transimission and distribution systems. 2012.

[17] O Pozos, C. Gonzalez, J. Giesecke, W. Marx, and E. Rodal. Air entrapped in gravity pipeline systems. *Journal of Hydraulic Research*, 48(3):338–347, 2010.

[18] V. H. Ransom. Numerical benchmark test no. 2.2: Oscillating manometer. *Multiphase Science and Technology*, 3:468–470, 1987.

[19] V.L. Streeter, E.B. Wylie, and K.W. Bedford. *Fluid Mechanics*. McGraw-Hill, 1998.

[20] Y. Taitel and D. Barnea. Two-phase slug flow. *Advances in heat transfer*, 20:83–132, 1990.

[21] J.G. Vasconcelos, S.J. Wright, and P.L. Roe. Improved simulation of flow regime transition in sewers: Two-component pressure approach. *Journal of Hydraulic Engineering*, 132(6):553–562, 2006.

[22] J.G. Vasconcelos, S.J. Wright, and P.L. Roe. Numerical oscillations in pipe-filling bore predictions by shock-capturing models. *Journal of Hydraulic Engineering*, 135(4):296–305, 2009.

[23] F. Zhou, F. E. Hicks, and P. M. Steffler. Transient flow in a rapidly filling horizontal pipe containing trapped air. *Journal of Hydraulic Engineering*, 128(3):625–634, 2002.

[24] L. Zhou, D. Liu, B. Karney, and Q. Zhang. Influence of entrapped air pockets on hydraulic transients in water pipelines. *Journal of Hydraulic Engineering*, 137(12):1686–1692, 2011.

Conclusions et perspectives

Les travaux menés au cours de cette thèse portent sur la modélisation des écoulements mixtes eau-air en conduite. Ces derniers présentent un enjeu industriel important puisqu'ils sont au cœur de nombreuses installations telles que les centrales de production d'énergie ou les réseaux urbains d'assainissement. La dynamique de tels écoulements est complexe à appréhender en raison notamment de son aspect multi-régime. Ils font ainsi l'objet d'études expérimentales, analytiques et numériques depuis plusieurs décennies. En utilisant une approche 1D, de nombreux modèles ont été proposés dans la littérature. Ils sont essentiellement monophasiques avec pour objectif de décrire les régimes à surface libre, en charge et les transitions associées. En pratique, les interactions eau-air peuvent modifier significativement la dynamique de l'écoulement, particulièrement en présence de poches d'air piégées. Certaines approches monophasiques ont alors été étendues à la prise en compte de ces poches sur des configurations simplifiées mais la communauté scientifique souligne la nécessité de développer un modèle capable de rendre compte des interactions eau-air dans tous les régimes. Les contributions de cette thèse s'inscrivent dans ce contexte avec l'élaboration d'un nouveau modèle 1D diphasique pour les écoulements mixtes eau-air en conduite. Une méthode numérique dédiée et des éléments de validation sur des cas tests représentatifs accompagnent cette proposition.

Le modèle proposé, dénommé CTL pour *Compressible Two-Layer*, est un modèle bifluide résultant de l'intégration des équations d'Euler isentropiques sur chaque phase dans une configuration bicouche. Il est composé de cinq équations dont les cinq inconnues principales correspondent à la hauteur d'une des phases en plus de la vitesse et de la pression de chaque phase. La configuration bicouche est pertinente pour les écoulements mixtes en conduite puisqu'elle permet de décrire naturellement le régime stratifié, le régime en charge (ou sec) et les poches d'air piégées. On parle alors d'un modèle bicouche compressible qui appartient par nature à la classe des modèles bifluide bipression initialement introduits par Ransom et Hicks [8]. Ce type de modèle nécessite des lois de fermeture pour les variables d'interface (vitesse, pression) et les termes sources. Dans notre contexte d'écoulements mixtes eau-air, des lois de fermetures originales sont proposées, notamment pour la pression d'interface. Elles s'appuient sur la contrainte hydrostatique imposée sur la phase eau et sur une caractérisation entropique du modèle comme initialement suggéré par Coquel *et al.* dans [4]. Le modèle ainsi fermé répond aux spécificités d'un écoulement mixte, à savoir l'importance des effets gravitaires à surface libre et l'importance des effets acoustiques en charge. En effet, il dégénère par construction vers une description monophasique compressible adaptée aux régimes en charge et sec. De plus, des propriétés mathématiques notables sont obtenues telles que l'hyperbolicité, l'unicité des relations de saut, la positivité des hauteurs et des densités. La formulation du modèle est également étendue pour traiter des conduites circulaires à section variable. La proposition résultante est en rupture par rapport aux modèles 1D d'écoulements mixtes disponibles dans la littérature. Au-delà de l'approche diphasique qui permet de rendre compte des interactions entre les phases, l'originalité tient dans la modélisation compressible de la phase eau à surface libre et dans la description unifiée des différents régimes qui permet une gestion naturelle des transitions associées.

La simulation de ce modèle bicouche compressible soulève de nombreux challenges pour les applications visées. Le développement de méthodes numériques pour les modèles bifluide est intrinsèquement source de difficultés en raison de la structure complexe du système d'ondes sous-jacent et des termes sources de relaxation en interaction forte avec la partie convective. Les difficultés additionnelles relatives aux écoulements mixtes correspondent à la coexistence d'une dynamique lente à surface libre avec une dynamique rapide en charge, et à la gestion de phases évanescentes inhérentes aux régimes en charge et sec. Afin de répondre à ces problématiques, on s'est intéressé au développement d'un schéma implicite-explicite (IMEX) avec splitting d'opérateur. Une méthode performante a ainsi été proposée. Elle repose sur une gestion explicite de la dynamique gravitaire et une gestion implicite de la dynamique acoustique via un splitting approprié. Une méthode originale de relaxation a notamment été développée pour la partie implicite en proposant une stabilisation adaptée au régime d'écoulement. Enfin, un intérêt particulier a été porté sur la robustesse du schéma en présence de phases évanescentes.

Une démarche de vérification et de validation de l'approche générale a été élaborée. Le schéma proposé est stable et converge vers les bonnes solutions de choc. En considérant un cas de rupture de barrage représentatif du régime

stratifié, l'intérêt de la méthode numérique développée par rapport à une approche explicite classique est clairement illustré. Le bon comportement du modèle CTL dans ce régime est ainsi mis en évidence. La simulation d'écoulements mixtes a ensuite été abordée. Une configuration canonique de remplissage de conduite est d'abord étudiée. Elle permet de démontrer la capacité du modèle et du schéma associé à gérer une configuration impliquant les spécificités monophasiques d'un écoulement mixte. De plus, une comparaison avec un modèle monophasique référence de la littérature, i.e. le modèle PFS [3], est proposée. Un comportement plus robuste dans les transitions entre régimes est alors obtenu tout en garantissant un temps de calcul raisonnable malgré la complexité accrue du système à résoudre. Ce bon comportement est ensuite confirmé sur une configuration expérimentale impliquant de nombreuses transitions [1]. La qualité des résultats obtenus sur ces deux cas tests permet de placer le modèle CTL à l'état de l'art dans la modélisation 1D des écoulements mixtes monophasiques. Enfin, une configuration répondant à l'influence de poches d'air piégées est considérée. En particulier, une solution de référence est construite analytiquement. Le très bon accord avec les résultats numériques obtenus en utilisant le modèle CTL illustre sa capacité à rendre compte des interactions eau-air pouvant fortement influencer la dynamique des écoulements mixtes.

Les trois volets abordés dans cette thèse, en l'occurrence le développement d'un modèle, sa discrétisation et sa validation, constituent une contribution originale pour la modélisation des écoulements mixtes eau-air en conduite. Des perspectives sont envisageables sur ces trois aspects, notamment dans le but d'étendre les champs d'action du modèle CTL.

La formulation du modèle proposé n'impose pas de restrictions quant à la gestion de configurations diphasiques complexes telles que le transport forcé ou la coalescence de poches d'air. Cette étape de validation supplémentaire doit être menée. De plus, l'utilisation du modèle dans un contexte industriel nécessite le développement de conditions limites adaptées. Pour les écoulements en conduite, il semble en effet essentiel de pouvoir imposer un débit ou une pression en entrée/sortie. Dans le cadre des modèles bifluide bipression, le développement de ces conditions limites de type Dirichlet est très peu abordé dans la littérature en raison de la complexité du système d'ondes sous-jacent. Une stratégie envisageable est de résoudre un demi-problème de Riemann aux cellules frontières en appliquant une série d'hypothèses pour faciliter sa résolution. En particulier, l'hypothèse $\partial_x h_k = 0$ appliquée localement à la frontière permet de découpler les deux phases en se ramenant à deux systèmes d'Euler isentropique. Des méthodes *classiques* pourraient alors être utilisées. Cette stratégie suppose toutefois une méthode numérique explicite appliquée au système non découpé. Son extension au schéma SPR développé dans cette thèse, qui repose sur une approche implicite-explicite associée à un splitting d'opérateur, exige donc une étude complémentaire.

Le modèle CTL a été établi à partir d'une description bicouche des écoulements eau-air en conduite. En pratique, ce type d'écoulement peut présenter des transitions, parfois brutales, vers des régimes ne tombant pas dans le formalisme bicouche, en particulier le régime dispersé. Il serait alors intéressant d'évaluer la capacité du modèle à représenter ce type de régime. Cette perspective s'appuie sur la structure commune des modèles bifluide bipression indépendamment du type de moyenne utilisée (spatiale, temporelle, statistique). Ainsi, une interprétation appropriée du taux de présence $\alpha_k = \frac{h_k}{H}$ ouvre la porte vers un modèle 1D multi-régime traduisant effectivement les effets gravitaires à surface libre. Dans un registre similaire, la présence de contraintes géométriques dans les installations industrielles, telles que des coudes, peut engendrer des dynamiques intrinsèquement 2D alors que le niveau de description du modèle CTL est par construction 1D. En s'appuyant également sur la structure commune des modèles bifluide bipression, un couplage de modèles 1D-2D peut être étudié pour gérer ce type de configuration en s'inspirant de travaux existants dans la littérature [7, 6]. Une autre extension naturelle en terme de représentativité physique consiste à intégrer des équations de conservation d'énergie au modèle. Comme pour les équations de conservation de masse et de quantité de mouvement, elles résultent de l'intégration des équations de conservation d'énergie locales écrites pour chaque phase. Elles sont notamment présentes dans le modèle introduit par Ransom et Hicks [8] et dans le modèle de Baer et Nunziato [2]. Ces équations augmentent la complexité du système au niveau continu et au niveau discret. Il s'agira alors d'établir des lois de fermetures en accord avec la contrainte hydrostatique et d'étudier l'adaptabilité du schéma SPR. Ainsi, des dynamiques complexes eau-vapeur impliquant des transferts de masse et d'énergie entre les phases pourraient être considérées.

D'un point de vue analytique, il serait intéressant d'étudier le lien entre les équations de la phase eau dans le modèle CTL et les équations de Saint-Venant. La mise en place d'une approche asymptotique permettant de lier les deux systèmes soulève toutefois de nombreuses difficultés. En effet, il s'agit de passer d'une description diphasique compressible à une description monophasique incompressible. Cela impose d'établir un adimensionnement bien choisi afin de prendre en compte d'une part une asymptotique de relaxation entre les phases et d'autre part une asymptotique bas Mach. En particulier, se pose la question de la compatibilité de l'équation de transport sur la hauteur d'eau. Enfin, un travail de modélisation doit être mené afin d'établir une expression analytique du temps de relaxation associé à la relaxation en pression. L'expression utilisée dans cette thèse provient d'une des seules contributions de la littérature sur ce sujet [5] et concerne les écoulements dispersés.

Références

[1] F. Aureli, A. Dazzi, A. Maranzoni, and P. Mignosa. Validation of single- and two-equation models for transient mixed flows: a laboratory test case. *Journal of Hydraulic Research*, 53(4):440–451, 2015.

[2] M. R. Baer and J. W. Nunziato. A two phase mixture theory for the deflagration to detonation (DDT) transition in reactive granular materials. *International Journal of Multiphase Flow*, 12(6):861–889, 1986.

[3] C. Bourdarias and S. Gerbi. A finite volume scheme for a model coupling free surface and pressurised flows in pipes. *Journal of Computational and Applied Mathematics*, 209:1–47, 2007.

[4] F. Coquel, T. Gallouët, J.-M. Hérard, and N. Seguin. Closure laws for a two-fluid two-pressure model. *C. R. Acad. Sci. Paris*, 334(I):927–932, 2002.

[5] S.L. Gavrilyuk. The structure of pressure relaxation terms : one-velocity case. *EDF report H-I83-2014-00276-EN*, 2014.

[6] E. Godlewski. Coupling fluid models. *Exploring some features of interfacial coupling, in "Finite Volumes for Complex Applications V" (eds. R. Eymard and J.-M. Hérard), ISTE-Wiley*, pages 87–102, 2008.

[7] J.-M. Hérard and O. Hurisse. Some attempts to couple distinct fluid models. *NHM*, 5(3):649–60, 2010.

[8] V. H. Ransom and D. L. Hicks. Hyperbolic two-pressure models for two-phase flow. *Journal of Computational Physics*, 53:124–151, 1984.